COMPOSITION AND STRUCTURAL CONTROL OF ALLOY ANODES FOR HIGH-ENERGY ALKALI-ION BATTERIES.

by

Amine Daali

A Dissertation Submitted in
Partial Fulfillment of the
Requirements for the Degree of

Doctor of Philosophy in
Engineering

at

The University of Wisconsin-Milwaukee
May 2024

ABSTRACT

COMPOSITION AND STRUCTURAL CONTROL OF ALLOY ANODE FOR HIGH-ENERGY ALKALI-ION BATTERIES.

by

Amine DAALI

The University of Wisconsin-Milwaukee, 2024
Under the supervision of Professor Wilkistar Otieno

Modern human societies will not be able to thrive without reliable, cost-effective, and safe energy storage methods. Alkali-ion batteries, a frontier in energy storage systems, have been in the limelight due to their promising specific capacities and low electrochemical potentials. However, State-of-the-art lithium-ion batteries cannot satisfy the worldwide increasing energy demand because of the low specific capacity of the graphite anode. Alloying anode materials are considered among the best candidates for replacing graphite due to their much higher specific capacity. However, their potential is hampered by the significant volume changes experienced during cycling, leading to mechanical degradation and short cycle life. Many structural and design strategies have been utilized to mitigate volume changes and enhance battery performance. Yet, an optimized design and an intensive understanding of the underlying alloying mechanism continue to be debatable and ambiguous due to a lack of operando and in-situ characterization. In this thesis, multiscale synchrotron X-ray diffraction and absorption spectroscopies coupled with in-situ and ex-situ characterization have been used to understand the role of carbon, different composite, different structures, and different electrolytes in the alloying process and in mitigating volume expansion of alloy anode for Li-and Na-ion battery systems.

Firstly, Carbon-sandwiched SnS_2, obtained through a hydrogel-embedding method, to confine the growth of few-layer SnS_2 nanosheets between nitrogen- and sulfur-doped carbon nanotube (NS-CNT) and amorphous carbon, demonstrate excellent sodium storage properties. In operando small-angle X-ray (SAX) scattering combined with the ex-situ X-ray absorption near edge spectra (XANES) reveal that the redox reactions between SnS_2/NS-CNT and the sodium ion are highly reversible. On the contrary, the nanostructure evolution is found to be irreversible, in which the SnS_2 nanosheets collapse, followed by the regeneration of SnS_2 nanoparticles. This work provides operando insights into the chemical environment evolution and structure change of SnS_2-based anodes, elucidating its reversible reaction mechanism, and illustrates the significance of engineered carbon support in ensuring the electrode structure stability.

Silicon and phosphorus both show much higher specific capacity than graphite; however, their practical use is significantly hindered by their large volume changes during cycling. Although significant efforts have been made to improve their cycle life, the initial coulombic efficiencies of the reported Si-based and P-based anodes are still unsatisfactory (<84%). Here, by using a scalable high-energy ball milling approach, we report a practical hierarchical micro/nano-structured P-based anode material for high-energy lithium-ion batteries, which possesses a high initial coulombic efficiency of 91% and a high specific capacity of 2500 $mAh.g^{-1}$ together with long cycle life and fast charging capability. In-situ high-energy X-ray diffraction and in-situ single-particle charging/discharging were used to understand its superior lithium storage performance. Moreover, proof-of-concept full-cell lithium-ion batteries using such an anode and a $LiNi_{0.6}Co_{0.2}Mn_{0.2}O_2$ commercial battery grade cathode were assembled to show their practical use.

Starting from micrometer-sized silicon and black phosphorus, we have also reported a high-energy silicon-phosphorus/ carbon anode (denoted as mSPC) via a high-energy ball milling process, which demonstrates an average discharge working potential of 0.3 V versus lithium, together with a high reversible capacity of > 2000 $mAh.g^{-1}$, high initial coulombic

efficiency of 84%, excellent cycle stability, and superior rate capability up to 15 $A.g^{-1}$. Furthermore, in-situ focused ion-beam scanning electron microscopy (FIB-SEM) reveals that the volume change of the mSPC anode during repeated (de) lithiation is effectively alleviated. In contrast, starting from nanometer-sized silicon, the resulting anode (denoted as nSPC) not only presents a lower reversible capacity (1200 $mAh.g^{-1}$) but also exhibits a higher charge/discharge working potential, leading to reduced energy density. Our results indicate the importance of composition/structure control in tailoring the working potential and specific capacity of alloying-type anodes toward high-energy lithium-ion batteries.

Lastly, micro-sized Sn is a promising anode material for sodium-ion batteries in terms of cost, specific capacity, and volumetric energy density, which, however, suffers from huge volume changes and rapid cell degradation upon cycling. Despite recent advances via nano-structured electrode design and interface engineering, the correlation between mechanical stability, solid-electrolyte interphase (SEI), and reaction kinetics/reversibility remains controversial and elusive. Here, by combining in-situ scanning electron microscopy (SEM) and X-ray absorption spectroscopy (XAS) as well as X-ray photoelectron spectroscopy (XPS), we have investigated the underlying electro-chemo-mechanical behavior and their coupling effects during charge/discharge of micro-sized Sn anode. Our results revealed that micro-sized Sn is pulverized into nano-particles with simultaneous formation of numerous voids and pores upon the 1st charge/discharge, while the electrolytes composition plays a critical role in the consequent parasitic reactions and eventually the sodiation/desodiation reversibility. In contrast to carbonate-based electrolytes, ether-based electrolytes enabled the formation of inorganic species dominated SEI with improved mechanical strength, thus leading to higher specific capacity and improved cycling stability. The present findings are crucial for future development of micro-sized anode materials for rechargeable batteries with high volumetric energy density.

In conclusion, this research offers a holistic view of the design, optimization, and challenges of alloy electrodes for alkali-ion batteries. The findings pave the way for next-generation

battery systems with improved stability, longevity, and energy output.

TABLE OF CONTENTS

LIST OF FIGURES

LIST OF TABLES

Nomenclature

P_{red} Red Phosphorus

T_g Transition Temperature

2-MeTHF 2-Methyl Tetrahydrofuran

AFM Atomic Froce Microscopy

AIB Alkali Ion Battery

AM Active Material

BET-surface Brunner-Emmet-Teller Surface

BP Black Phosphorus

BPC Black Phosphorus Carbon

CBE Carbonate Based Electrolyte

CE Coulombic Efficiency

CMC Carboxymethyl Cellulose

CNT Carbon Nanotube

COP 21 Conference of the Parties

CV Cyclic Voltammetry

DMC Dimethyl Carbonate

DME Dimethoxyethane

EC Ethylene Carbonate

EDX Energy Dispersive X-ray

EES Electrochemical energy storage

EGDEE Ethylene Glycol Diethyl Ether

EOL End Of Life

ESD Energy Stroage Device

EV Electric Vehicule

EXAFS Extended X-Ray absorption Fine Structure

FEC Fluoroethylene carbonate

FIB-SEM Focuses Ion-Beam Scanning Electron Microscopy

G1 Dimethoxyethane

G2 Diglyme

G4 Tetraglyme

GelMa Methacrylated Gelatin

GWP Global Warming Potential

HAADF-STEM High-Angle Annular Dark-Field Scanning Transmission Electron Microscopy

HEBM High Energy Ball Milling

HEXRD High Energy X-ray Diffraction

HFE Hydrofluoroether

HR-STEM High Resolution Scanning Transmission Electron Microscopy

ICE Initial Coulombic Efficiency

IEA International Energy Agency

ILE Ionic Liquid Electrolyte

KB Ketjen Black carbon

LCA Life Cycle Assessement

LCI Life Cycle Inventory

LFP $LiFePO_4$, Lithium Iron (II) Phosphate

LIB Lithium Ion Battery

LiPAA Poly (acrylic acid)

LMO Lithium Managnese Oxide

MWCNT Micro Wall Carbon Nanotube

NCA Nickel Cobalt Aluminium

NMC Nickel Manganese Cobalt

NMP N-Methyl Pyrrolidone

NZE Net Zero Emissions

PAA poly(acrylicacid)

PC Propylene Carbonate

PDF Pair Distribution Function Analysis

PIB Potassium Ion Battery

PPM Part Per Million

PVDF Poly(Vinylidene Difluoride)

RP Red Phosphorus

RPC Red Phosphorus Carbon

SA Sodium Alginate

SAED Selected Area Electron Diffraction

SAXS Small Angle X-ray Scattering

SBR Styrene Butadine Rubber

SEI Solid Electrolyte Interphase

SEM Scanning Electron Microscopy

SHP Self Healing Polymer

SIB Sodium Ion Battery

SOC State of Charge

SPC Silicon Phosphorus Carbon

SSA Specific Surface Area

SSB Solid State ion Battery

SSE Solid State electrolyte

SVR Surface to Volume Ratio

TEGDME Tetraglyme

TEM Transmission Electron Microscopy

TFEP Fluorinated Cyclic Phosphate Solvent

TGA Thermo-Gravimetric Analysis

THF Tetrahydrofuran

TWh Terawatt hours

UNFCCC United Nation Framework Convention on Climate Change

WMO World Meteorological Organisation

XANES X-ray Absorption Near Edge Spectra

XAS X-ray Absorption Spectroscopy

XPS X-Ray Photoelectron Spectroscopy

XRD X-ray Diffraction

ACKNOWLEDGEMENTS

First and foremost, I am sincerely grateful to God for bestowing upon me the strength, wisdom, and perseverance required to complete this Ph.D. It is with a humble heart that I recognize the opportunities granted to me, not only in pursuing and achieving this academic milestone but also in the countless blessings that have been granted upon my life, including the gift of my supportive and loving family.

Embarking on this Ph.D. journey, akin to running a marathon, has been an expedition enriched by the invaluable support and contributions of many remarkable individuals. Their collective wisdom, guidance, and encouragement have been the wind beneath my wings, enabling me to climb to new academic heights. I stand on the shoulders of giants, and it is with deep gratitude that I acknowledge their pivotal roles in this academic voyage.

Foremost, my heartfelt appreciation extends to my advisor, Dr. Wilkistar Otieno, and my supervisors at Argonne National Laboratory, Dr. Guiliang Xu and Dr. Khalil Amine. Your mentorship was the lighthouse guiding me through the treacherous waters of research. Your patience, your gentle yet firm guidance, and your critical insights have been instrumental in refining my abilities as both a scientist and a researcher. The encouragement you provided was the beacon of hope during challenging times, fostering my growth from the early stages of research formulation to overcoming the hurdles encountered along the way. The analytical prowess, creative thinking, and resilience I have cultivated under your tutelage are treasures I will carry forth into my future endeavors. Your unwavering support and belief in my capabilities have been the cornerstone of my achievements. For this, I am eternally thankful.

My gratitude also flows to Dr. Rachid Amine, whose support and guidance were invaluable. Your expertise in analysis tools and the warmth of your familial welcome have enriched my research journey significantly.

A special thanks to Dr. Krishna Pillai, Dr. Hamid Seifoddini, and Dr. Dah-Chuan Gong, for their interest in my research and their invaluable insights as part of my candidacy and dissertation committees. Your probing questions and insightful suggestions were instrumental in refining my proposal.

I am deeply appreciative of my collaborators, including Dr. Zonghai Chen, Dr. Chen Zhao, Dr. Mohammed Khamechian, Dr. Xiang Liu, Dr. Ahmed Shabbir, Dr. Wenhua Zuo, Dr. Tongchao Liu, Dr. Phillip LaCasse, Ms. Madiha Ahmed, and Mr. Khan Iftekharudin, for their sage advice and feedback on experimental design, execution, analytical outcomes, and publications. Collaborating with you has been a highlight of my research experience.

To my friends from Marrakesh, Montreal, Paris, Milwaukee, Chicago, Casablanca and beyond, your support and encouragement were the pillars of strength that sustained me through the tests and tribulations of this journey, fostering personal growth and learning

beyond my imagination.

To my siblings, Dr. Salma Daali, Dr. Khalil Daali, Dr. Yasmina Daali, Zyad Daali, Oussama Idouissaaden, and Aya Idouissaaden, your unconditional love and unwavering support have been foundational to my perseverance and success.

Special thanks to Mounir Berrad, Nabil Karimi, Abdelhak Idouissaaden, and Andrew Trumbull. Your encouragement and belief in my potential have been helpful in navigating many challenges.

I am grateful to my wife, Mounia, for the love, support, and patience. Your willingness to listen and offer solace during my moments of stress and your unconditional care and love in countless ways have been instrumental to my journey. I could not have finished this strong without your support.

Lastly, I owe my deepest gratitude to my parents, Aziz and Mina, Mustapha and Fatiha, whose endless love, patience, and support have been my guiding stars. Your encouragement has fueled my aspirations, helping me transition from one chapter of my life to the next with courage and determination. Your sacrifices, love, and special care package have been the bedrock of my success.

In loving memory of RKIA BAHA.

This acknowledgment, while an attempt to encapsulate my gratitude, falls short of truly conveying the depth of my appreciation for everyone who has been a part of my journey. Thank you all, from the bottom of my heart.

Chapter 1

Introduction

Climate disturbance, global warming, and environmental crises are the new normal in our era. Fossil fuels and greenhouse gas emissions play a major role in increasing the earth's temperatures, leading to major and, most times, catastrophic environmental events. In July 2023, the UN secretary-general stated: "The era of global warming has ended; the era of global boiling has arrived. Climate change is here. It is terrifying, and it is just the beginning. However, limiting global temperature rise to $1.5°C$ [above pre-industrial levels] and avoiding the very worst of climate change is still possible. But only with dramatic, immediate climate action." These comments came after the release of yet another alarming report about the record temperature of the earth and the oceans by the World Meteorological Organization (WMO) [**Figure 1.1**].

During the Paris Agreement, which was adopted at the 21^{st} Conference of the Parties (COP 21) to the United Nations Framework Convention on Climate Change (UNFCCC) in 2015, policymakers and the International Energy Agency (IEA) presented the Net Zero Emissions by 2050 Scenario (NZE). This plan presents a pathway for the global energy sector to achieve net zero CO_2 emissions by 2050, and its primary goal is to limit global warming to well below $2°C$ above pre-industrial levels and to pursue efforts to limit the temperature increase to $1.5°C$. Awareness is building up, but there still needs to be more radical actions.

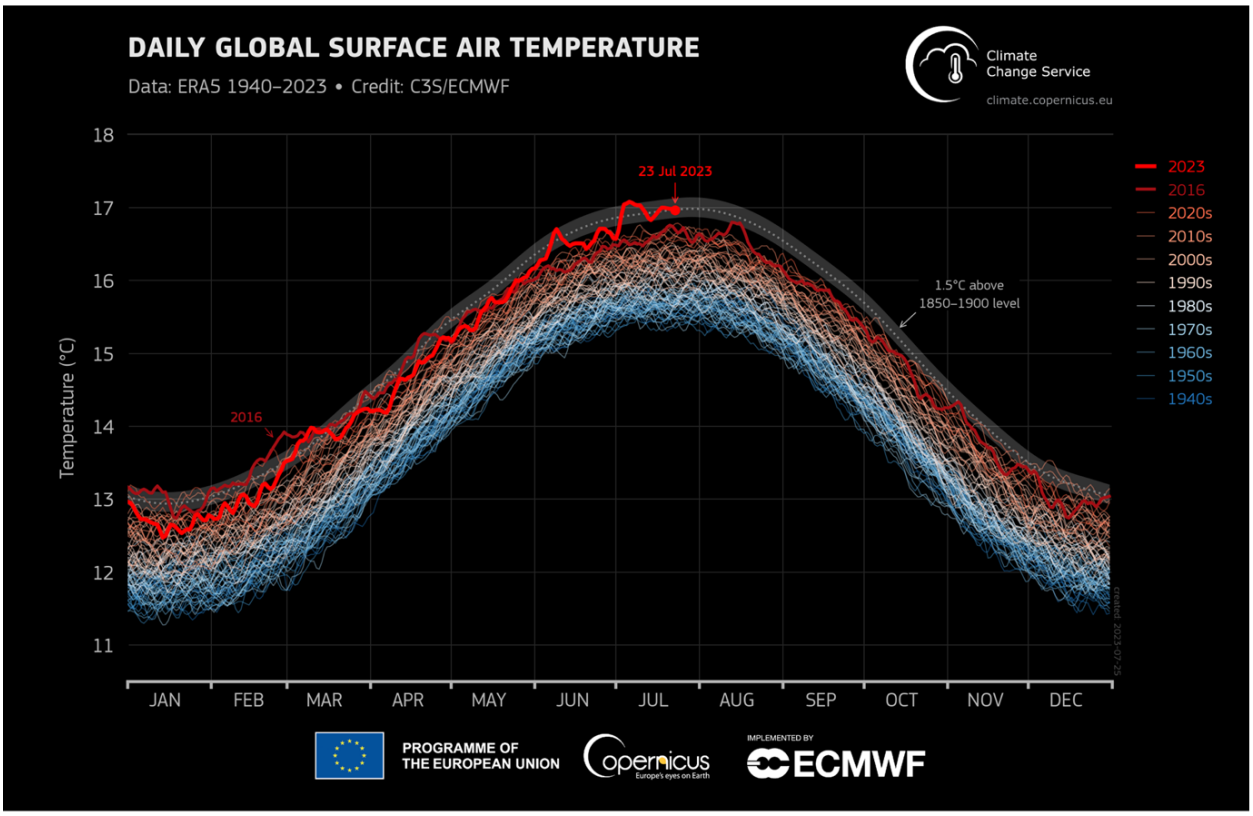

Figure 1.1: Global daily surface air temperature (°C) from 1 January 1940 to 23 July 2023 *plotted as time series for each year. 2023 and 2016 are shown with thick lines shaded in bright red and dark red, respectively. Other years are shown with thin lines and shaded according to the decade, from blue (1940s) to brick red (2020s). The dotted line and grey envelope represent the 1.5°C threshold above preindustrial level (1850–1900) and its uncertainty. Data: ERA5. Credit: C3S/ECMWF.*

The digital era we live in is highly energy-demanding, leading to over-consumption of fossil fuels. Mostly accused of all our wrongdoings, they are becoming more scarce, expensive, and subject to geopolitical influences and supply chain distortion. This continuous exponential growth in global energy demand is causing many unbalance but also opportunities for more investment and research toward sustainable and clean energy sources and efficient storage systems. Solar, wind, and tidal serve as good alternatives to fossil fuels. Different methods exist for storing that energy, but only a small portion is utilized. The total amount of energy utilized strongly depends on the technology used for the conversion from the original source [1]. The mass storage of energy could significantly increase efficiency and productivity, particularly for applications involving the electrical grid and transportation, while also allowing for a more considerable utilization of low-carbon energy conversion methods and a significant reduction in environmental impacts [2, 3]. A decrease in the utilization of fossil-fueled energy and an increase in energy flexibility could significantly impact the global economy by decreasing the amount of carbon pollution and human contribution to climate change [4].

Solar energy, for instance, can generate an annual power supply of 50 terawatt hours (TWh) through light irradiance, approximately three times the global energy requirements, which is around 17.7 TWh per year [5]. While other renewable energy sources still need to catch up to meet our current and projected societal needs, the sun stands as the most abundant energy reservoir capable of providing a substantially higher power output than what is presently demanded. Nevertheless, the limited duration of sunlight during the day, coupled with the uneven distribution of light across the earth's surface, imposes constraints on the widespread application of solar energy. Despite these limitations, recent advancements in photovoltaic technology have yielded devices with reported conversion efficiencies as high as 25.6% [6]. As a result, it becomes imperative to explore alternative methods and apparatus for energy storage systems that can efficiently harness and store solar energy, considering its diffuse and intermittent nature.

In tandem, the transportation and automotive sectors are undergoing a profound trans-

formation. Electrification is now spreading rapidly in almost all road transport segments, from passenger cars to commercial vehicles, buses, and two- and three-wheelers. Electric vehicle (EV) sales continue to surge, rising from 10.5 million in 2022 to almost 27 million in 2026. The EV share of global new passenger vehicle sales will jump from 14% in 2022 to 30% in 2026. Shares in some markets are much higher, with EVs reaching 52% of sales in China and 42% in Europe. Some European car markets move even faster, with the Nordics at 89% and Germany at 59%. In the US, a significant push from the Inflation Reduction Act means EVs make up nearly 28% of passenger vehicle sales by 2026, up from 7.6% in 2022. The fleet grows even faster, rising from 27 million passenger EVs on the road at the end of 2022 to over 100 million by 2026 [7][**Figure 1.2**].

This rapid industrialization is raising significant concerns. Consequently, high-performance energy storage devices have become a hot research topic in recent years. Developing low-cost and large-scale electrical energy storage (EES) is considered the necessary strategy and key enabler for future smart and green grids [8, 9]. All these products need a high energy density power source for longer endurance and better efficiency. This is the premise and motivation for this research on the design and structural optimization of alkali ion batteries.

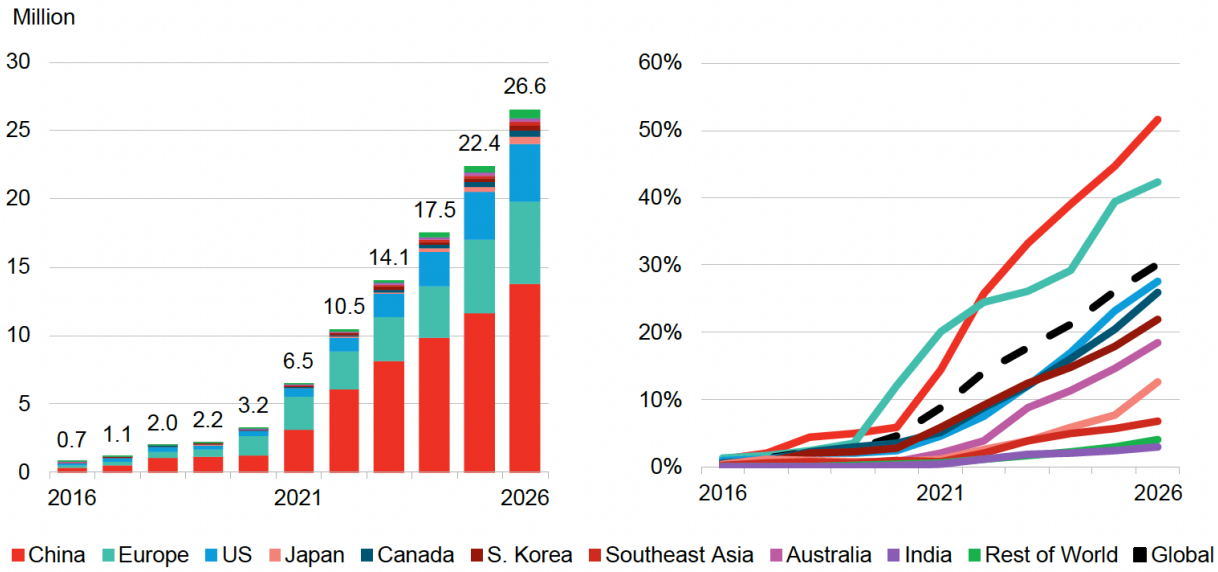

Source: BloombergNEF. Note: Europe includes the EU, the UK and EFTA countries. EV includes BEVs and PHEVs.

Figure 1.2: Global near-term passenger EV sales and share of new passenger vehicle sales by market.(Source: BloombergNEF [7])

1.1 Alkali Ion Batteries

Battery energy storage system has achieved great success in portable electronics and electronic vehicles and is supposed to have the capability to carry this responsibility, given their appealing advantages of high energy density, rational working voltage, and good cyclability [10]. Among various battery electrode materials, lithium metal is regarded as the "Holy Grail" electrode due to the extra-high capacity (3860 $mAh.g^{-1}$) and the lowest negative electrochemical potential (–3.040 V vs. the standard hydrogen electrode) [11, 12]. Lithium Ion Battery (LIB) has become an indispensable part of daily life and is currently the dominant energy storage solution [13, 14]. During the 1970s to 1980s, there was significant research conducted on LIBs. These batteries became commercially successful when SONY introduced them in 1991 [15]. Since then, they have been widely used in electronic devices, electric vehicles, and hybrid electric vehicles [16]. However, there are concerns regarding the limited availability of lithium resources and the high cost of energy storage in LIBs, particularly when considering large-scale renewable energy storage. As a result, there has been a renewed focus on developing rechargeable batteries that utilize more abundant alkali elements such as sodium and potassium [17, 18]. Sodium, in particular, is much more abundant in the earth's crust compared to lithium (23600ppm vs. 20ppm); the US alone possesses around 23 billion tons of soda ash. Given the advantages of sodium and potassium over lithium, there is great potential for the development of cost-effective sodium-ion batteries (SIBs) and potassium-ion batteries (PIB) for renewable energy storage [19, 20]. Sodium, with its smaller atomic radius compared to potassium, offers feasible exploration of suitable cathodes and anodes for SIBs. In terms of commercial considerations, copper current collector, which is an essential component of anode materials in LIBs, can be substituted with a significantly less expensive alternative, namely aluminum, in SIBs. This substitution is viable since sodium does not form alloys with aluminum [20]. Additionally, SIBs can leverage the existing infrastructure and well-established manufacturing technologies of LIBs, given their similar

chemistry and manufacturing processes [21]. Furthermore, the modest $330mV$ difference in the potential between the $Na/Na^{+}(-2.71V)$ and $Li/Li^{+}(-3.04V)$ redox couples allows for the potential development of high-voltage SIBs [22, 23]. However, from an R&D standpoint, sodium's larger Shannon ionic radius (1.02 Å) compared to lithium (0.76 Å) poses challenges in identifying suitable crystalline host materials for Na^{+} that possess sufficient capacity and exhibit good cycling stability. It will mostly lead to a lattice distortion in the crystal structure and cause a large volume change [24]. Despite the overwhelming number of publications on LIBs compared to SIBs, there has been a significant increase in the number of publications on SIBs in recent years **[Figure 1.3]**.

Like other alkali rechargeable intercalation batteries, converting stored chemical energy into electrical energy involves three essential components. The cathode is responsible for the insertion and extraction of working ions, the electrolyte facilitates the movement of ions between the anode and cathode, and the anode serves as the site where ions are stored and released during charging and discharging, respectively, while also donating electrons to the external circuit. In this chemical process, mobile ions (e.g., Li^{+}, Na^{+}) are reversibly shuttled between two electrodes through an electronically insulating and ionically conducting electrolyte. Typically, the electrodes are intercalation compounds that store the mobile ions in a topotactic manner within a host lattice [25], although some electrodes operate via a conversion/alloying mechanism [26]. During discharge, the ions are transported from the anode through the electrolyte to the cathode, releasing electrons to perform electrical work in an external circuit. During charge, an applied voltage reverses this ion migration process [27] **[Figure 1.4]**.

The majority of cathodes are transition metal oxides, chalcogenides, fluoride, phosphates, and sulfates, where the insertion/removal of the ion is accompanied by the reduction/oxidation of a transition metal ion. They have been developed, and plenty exhibit desirable energy density and cycling performances. However, progress on the research for anode counterpart remains slow [28].

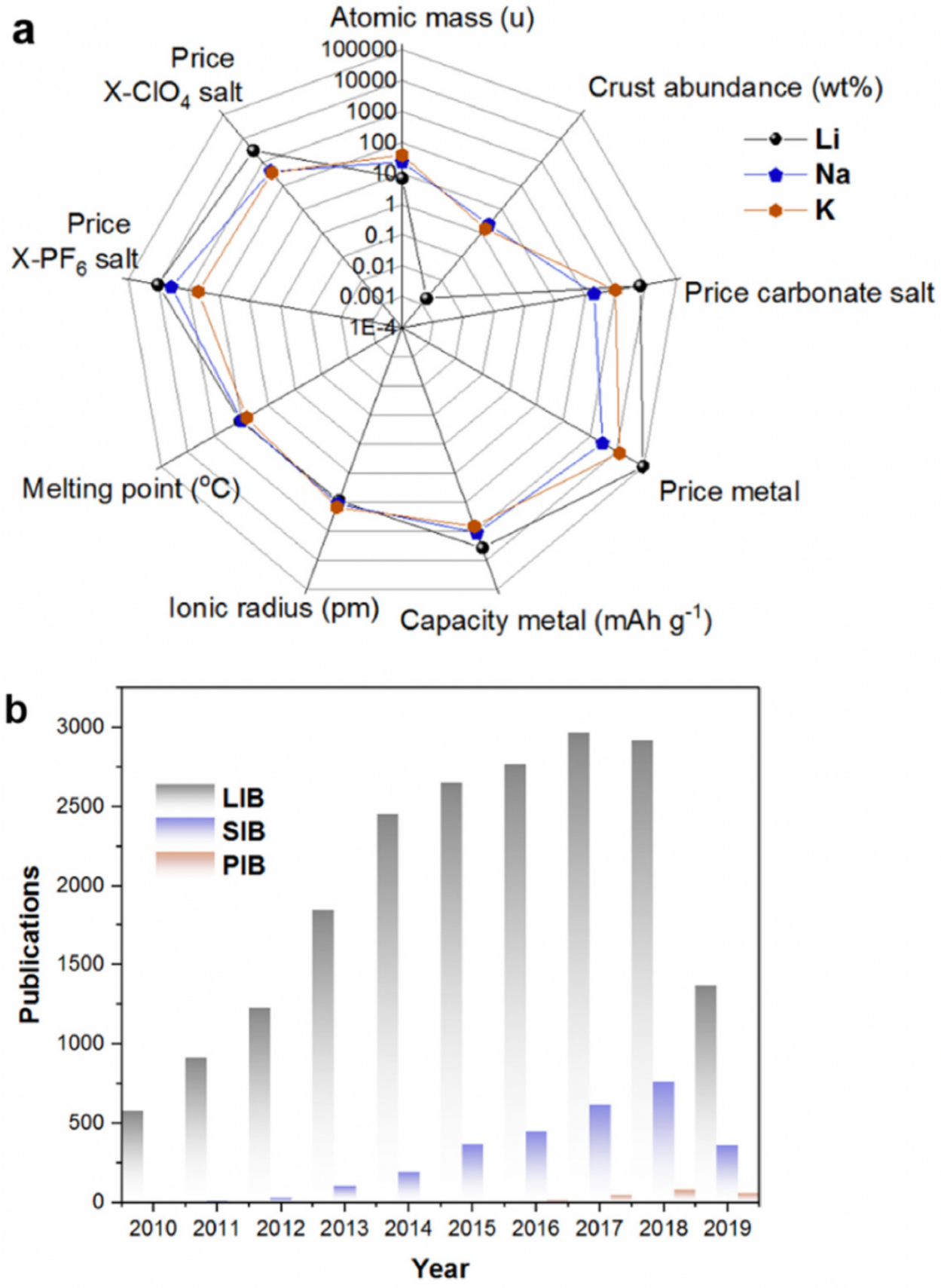

Figure 1.3: (a) Comparative chart of Li, Na and K for rechargeable batteries, the axes values are logarithmically plotted in its absolute value. (b) Number of publications by topic over time, data from Web of Science July 2019 by searching "metal ion battery" for each battery chemistry (Li, Na, and K). (Zhang et al. [23])

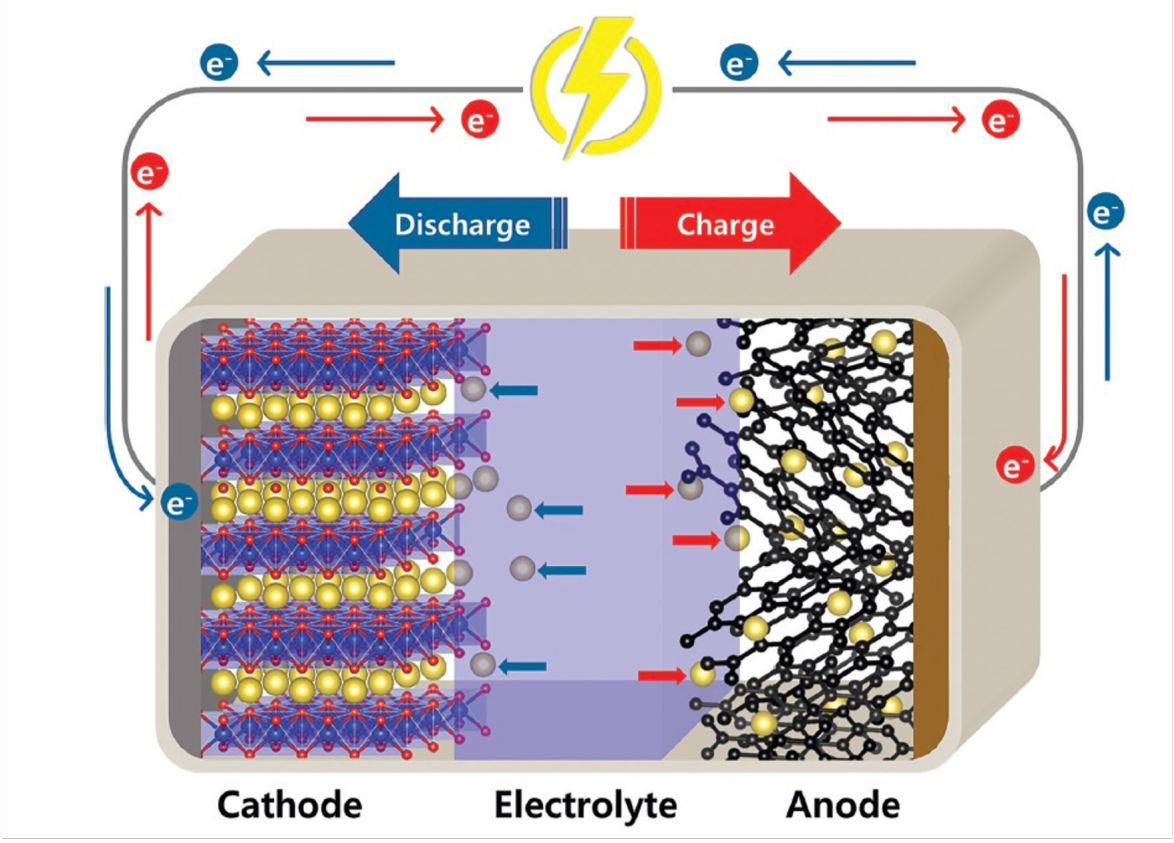

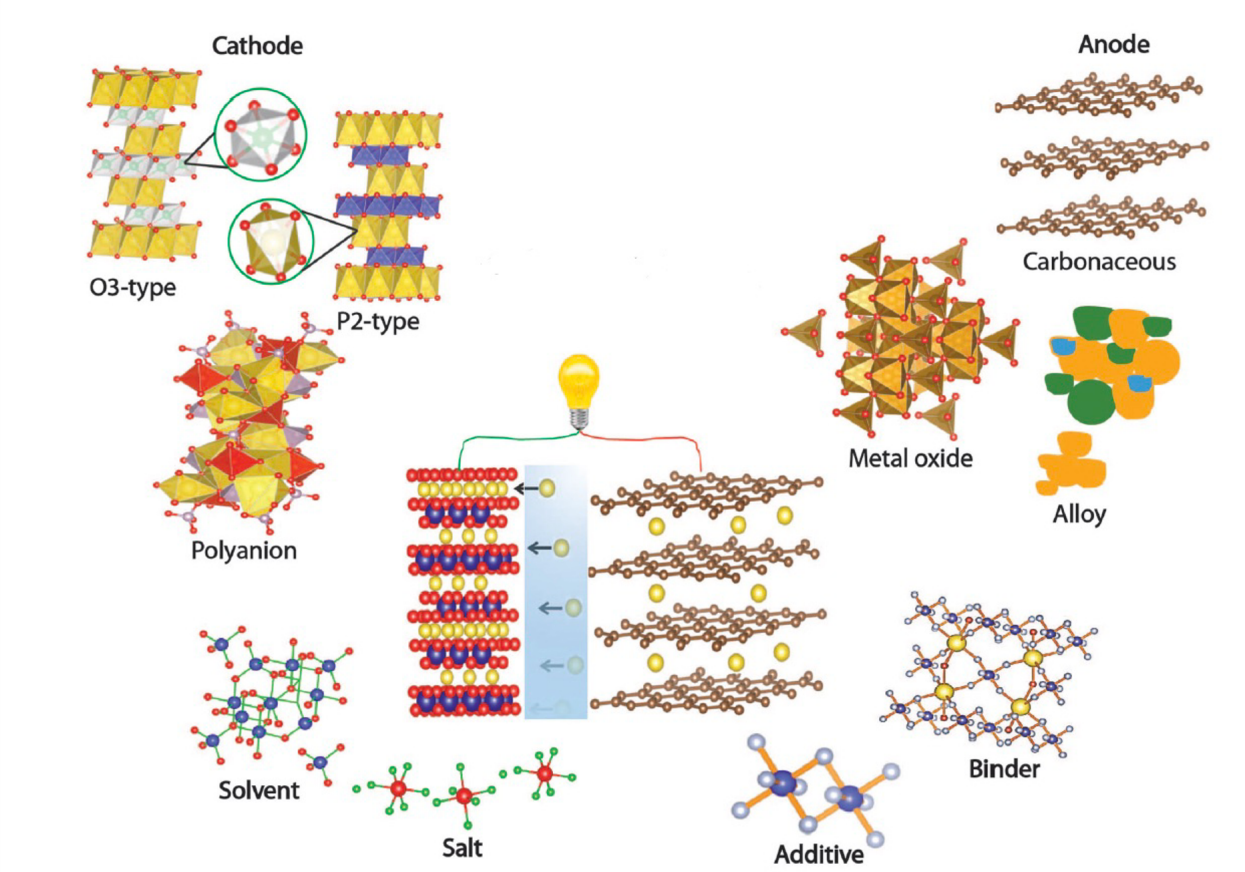

Figure 1.4: Schematic of the working principle of an Alkali-ion battery. (Singh et al. [27])

The electrolyte is usually an organic solvent (e.g., carbonates or ethers) with an added salt (e.g., $LiPF_6$, $NaPF_6$) [29]. More recently, polymers, ceramic, and superionic conductors [30, 31] can be used in an all-solid-state battery architecture. Although there have been various efforts to develop innovative electrodes, there is a limited amount of research dedicated to comprehending the interaction between ions (specifically Na^+) and solvents, which have the potential to impact the amount of energy required for desolvation at the electrolyte/electrode interface [32]. Nevertheless, considering the advancements made in LIB, it is undeniable that electrolytes play a crucial role in achieving optimal performance in conjunction with electrode selection when it comes to operating SIBs. Electrolytes are known to react with electrode surfaces during battery cycling to form a Solid Electrolyte Interphase (SEI). Stabilizing the SEI, especially on the anode electrode surface, was a key factor for the commercialization of LIBs and will also be so for SIBs in the rechargeable battery market [33]. Consequently, there is a pressing need to identify a stable electrolyte for high-performing SIB that is commercially viable. It is widely recognized that SIB is a maturing technology. Thus, we can draw inspiration and techniques from those commonly utilized in LIB. Several carbonate-based electrolytes face challenges in commercial SIB applications due to the formation of a soluble SEI layer that thickens continuously and inferior electrode stability [34]. Conversely, ether-based electrolytes are emerging as a promising alternative offering intriguing features to enhance battery performance, particularly in SIB. The solvation structures of these materials are stable, allowing for highly reversible reactions involving solvents and intercalation. This leads to the formation of a thin and stable SEI. While ether-based electrolytes have improved the stability and kinetics of sodiation, there is still much to be understood about their wetting properties, chemical compatibility, and electrode interactions. A thorough investigation of these aspects is necessary before these electrolytes can be successfully commercialized. Water-based electrolytes are also considered a cost-effective alternative for energy storage systems that have been successfully brought to market. It is important to note that the overall performance of an electrolyte is closely tied to the properties of the salts and solvents used.

The salts should have high solubility in the solvent to facilitate favorable ionic conductivity, exhibit chemical inertness to various components within the cell, remain stable across a wide range of applied voltages, and demonstrate desirable oxidation and reduction behavior, as well as thermal stability. On the other hand, the solvents must possess polar characteristics and high dielectric constants, have lower viscosity to enhance ionic conductivity, have low melting and high boiling points, and remain inert towards the charged cathode/anode surfaces during cell operations. Requirements for liquid electrolytes in SIBs are similar to those required for LIBs. The electrolyte challenges can be summarized as follows [35, 36, 37]:

(i) A big difference between the energy levels for the lowest unoccupied molecular orbital and highest occupied molecular orbital in the extended voltage window stability of $0 - 5.5V$,

(ii) High ionic conductivity ($> 5\ mS.cm^{-1}$) with low viscosity,

(iii) Compatibility problems between anode-based materials and cathode materials,

(iv) Thermal instability and degradation with cycling,

(v) High cost.

1.2 Anode Alloys

Moving on to the opposite end of the cathode, we encounter the anode, which is also referred to as the negative battery terminal. To develop a promising anode material, it must meet specific criteria. First, it should incorporate an element with a lower atomic mass and low density, allowing for a substantial number of metal ions per formula unit. These characteristics ensure stable and high gravimetric ($mAh.g^{-1}$) and volumetric capacities ($mAh.cm^{-3}$). Second, it must not display reactivity or any tendency to dissolve within the electrolyte solvent. Third, it must possess a potential close to the specific alkali metal, which should not fluctuate with changes in content, in order to maintain the working voltage when combined with the cathode. Fourth, it should be environmentally friendly, less hazardous, and possess high electronic and ionic conductivity. In addition to these fundamental requirements, other practical challenges exist, such as operating under high cut-off potentials that result in volume expansion and material pulverization, lower energy density, and low Coulombic efficiencies during the initial cycles. Moreover, the continuous demands placed on the SIB anode by the EVs market to enhance energy limits and compete with the dominance of LIBs present further challenges.

The battery's average voltage and discharge capacity are directly related to the chemistry involved. A higher voltage and capacity would provide more significant energy. The specific capacity of the electrode refers to the capacity per mass of active electrode materials without considering the mass of other electrode components such as binder and conductive additive materials. Specific energy refers to energy per unit mass, while energy density is the amount of energy stored per unit volume. The electrochemical capacity and energy in batteries are dependent on the constant current rate, which is often referred to as C-rate. In battery technology, the term C-rate refers to the rate at which a battery is discharged relative to its maximum capacity. It helps determine how quickly power can be drawn from a battery. A 1C discharge rate means the discharge current will completely deplete the battery in one hour. C-rate and other essential testing terms and formulas are summarized and defined below:

1. C-rate:

$$C - rate = \frac{C}{t_{rates}} \tag{1.1}$$

(where t is the time for a complete charge or discharge in hours)

2. Specific Capacity

$$Specific\ Capacity\ (mAh/g) = \frac{Current\ (mA) * time\ (h)}{Active\ Mass\ (g)} \tag{1.2}$$

3. Specific Energy

$$Specific\ Energy\ (Wh/kg) = \frac{Capacity\ (Ah) * Voltage\ (V)}{Total\ cell\ Mass\ (kg)} \tag{1.3}$$

4. Energy Density

$$Energy\ Density\ (Wh/L) = \frac{Capacity\ (Ah) * Voltage\ (V)}{Total\ cell\ Volume} \tag{1.4}$$

Energy density is one of the most critical parameters for battery systems, and from eq. 1.4, it can be roughly calculated by the following formula:

$$E_m = (\frac{Q_c * Q_a}{Q_c + Q_a}) * (U_c - U_a) * K \tag{1.5}$$

Em, Q_c, Q_a, U_c, U_a, and K are the energy density, specific capacity of cathode and anode, average potential of cathode and anode, and the proportion of active materials in the battery, respectively [38]. In LIBs, the K value is usually between 0.42 and 0.61.

It can be seen from the above formula that strategies to improve energy density mainly include enhancing the specific capacity of the cathode or anode, using higher potential material for the cathode or lower one for the anode, and increasing the K value. (The K value is mainly

related to the battery manufacturing process)[39].

In comparison to cathode materials, the anode materials used in LIBs or SIBs offer a greater potential for achieving higher energy densities due to their diverse nature and high theoretical capacity. The emerging anode materials can be classified into three categories based on their interaction mechanisms with Li and Na ions: intercalation, conversion, and alloying [40, 41].

Intercalation compounds can be characterized as materials that possess the ability to incorporate guest species into their lattice structure with minimal disturbance to their crystalline parameters. The most commonly used LIB anode intercalation material is graphite, which has a theoretical specific capacity of 372 $mAhg^{-1}$ [42]. However, its reversible capacity in SIBs is only 35 $mAhg^{-1}$ due to limited interlayer spacing [28]. Hard carbon, derived from biomass or other organic sources, has a larger disordered layer distance and can store additional Na ions. However, its capacity is still unsatisfactory. Additionally, carbonaceous anodes exhibit a relatively low reaction potential with Li and Na, resulting in the dendritic deposition of Li and Na metals during the electrochemical process and posing safety concerns [16].

Conversion types are a class of electrode materials that undergo a distinct electrochemical reaction mechanism. Unlike intercalation compounds, where ions are inserted into a host lattice without significantly altering its structure, conversion-type anodes involve a more substantial chemical transformation. In these anodes, during the charge and discharge cycles, the active material undergoes a conversion reaction with lithium or sodium ions, leading to the formation and decomposition of new compounds. Conversion-type anode materials primarily consist of transition metal oxides [43], sulfides [44], selenides [45], and phosphides. Despite having higher specific capacities than carbonaceous anodes, these compounds still face challenges such as low conductivity and significant irreversible capacities [46, 47].

In contrast to intercalation- and conversion-type anodes, alloying materials react with Li and Na ions to form alloys. This results in higher theoretical capacities, larger molar ratios,

safer potentials, and lower costs. Consequently, alloying materials have garnered significant interest for their potential applications in LIBs and SIBs [48]. Several Group IV (like Si, Ge, Sn) and Group V (like P, Sb, Bi) possess higher theoretical specific capacities based on the alloying mechanism and proper working potential in rechargeable alkali metal ion batteries [49, 50, 51]. Some examples and their particular features are summarized as follows: **[Figure 1.5]**

1. Silicon (Si) is one of the most promising anodes for lithium-ion batteries (LIBs) due to the high theoretical specific capacity (4200 $mAh.g^{-1}$ according to the formation of $Li_{4.4}Si$, 3579 $mAh.g^{-1}$ for $Li_{3.75}Si$ alloy at mild temperature), low working potential ($0.2 - 0.3$ $vs.$ Li/Li^{+}), low cost, nontoxicity, high abundance. However, capacity fading occurs due to volume expansion/contraction (300%) during the discharge/charge reaction [52, 53, 54, 55].

2. Phosphorus (P) is one of the highest-capacity alloy anodes for(SIBs) and(PIBs) [56, 57, 58, 39]. There are three types of P allotropes, including white phosphorus (P_{white}), red phosphorus (P_{red}), and black phosphorus (P_{black}). Among these allotropes, P_{white} has a low melting point and presents a safety issue associated with self-ignition at room temperature, thereby being excluded as a potential alloy anode. P_{red} possesses a high theoretical specific capacity, moderate working voltage (≈ 0.4 V $vs.$ Na/Na^{+}), low cost, nontoxic, and safe nature [59]. Nevertheless, it suffers from significant volume change (>400%), low electronic conductivity ($\approx 10^{14}$ Scm^{-1}), unstable SEI layer, and poor cycling performance. P_{black} is a 2D anisotropic layered material with a 5.2 Å interlayer distance. P_{black} possesses superior thermal stability, relatively high electronic conductivity ($0.2 - 3.3.10^{2}$ Scm^{-1}), and high charge-carrier mobility [60, 61]. Notably, P_{black} can be fabricated from P_{red} under high-pressure and high-temperature conditions [62] or through high-energy ball milling [60, 61, 62].

3. Metallic tin (Sn) is a low-cost, environmentally friendly material that is abundant in

nature [63, 64]. It shows a high theoretical capacity and proper average reaction potential, 994 $mAhg^{-1}$ and $\approx 0.55\ V\ vs.\ Li/Li^{+}$; 847 $mAhg^{-1}$ and $\approx 0.35\ V\ vs.\ Na/Na^{+}$. Sn also suffers from huge volume change during the discharge/charge process, around 260 % for LIB and 420 % for SIB [65, 66].

4. Metallic antimony (Sb) is also a promising anode candidate owing to decent theoretical specific capacity (660 $mAh.g^{-1}$), proper reaction potential ($\approx 0.4-0.8\ V\ for\ Na\ and\ \approx 0.4-0.5\ V\ for\ K$), and relatively high electronic conductivity ($2.5.10^{4}\ Scm^{-1}$). Same as all other alloys, Sb suffers from massive volume expansion [67].

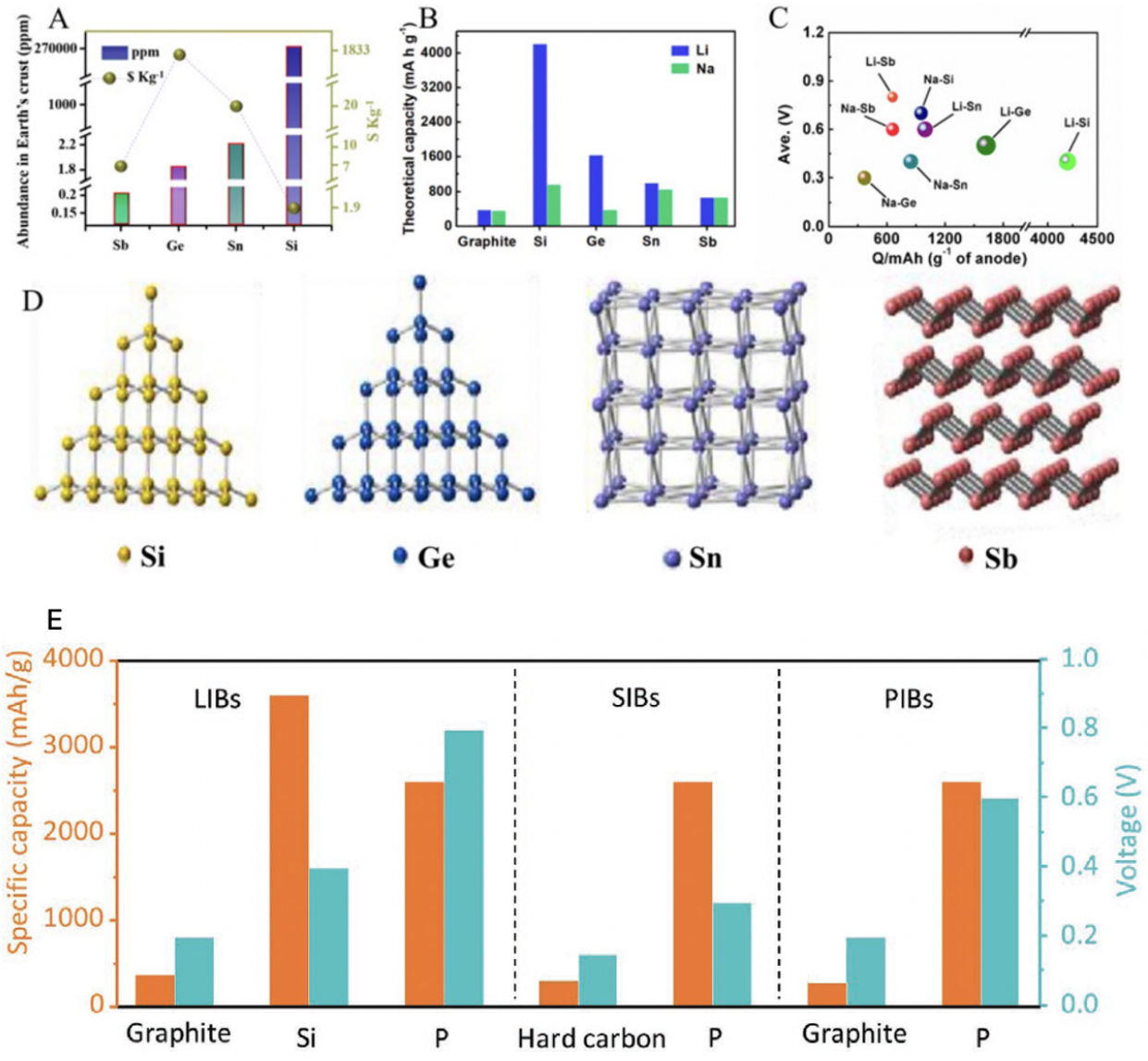

Figure 1.5: (A) Crustal abundance (ppm) and cost of alloying-type anodes (data for Sb, Ge, Sn, and Si costs taken from Shanghai Metals Market, Kitco Metals, London metal exchange, and Deutsche Rohstoffagentu, respectively). (B) Theoretical lithiation capacities of graphite, Si, Ge, and Sn for LIBs and SIBs. (C) Average potential of various alloy materials in LIBs and SIBs. (D) Crystal structures of Si, Ge, Sn, and Sb. (Li et al. [48]) (E) Theoretical specific capacity and average working voltage of typical anodes in LIBs, SIBs, and PIBs.(Zhou et al. [39])

.

1.3 Challenges

The electrochemical reaction of alloys is as follows: $xLi + M \rightleftharpoons Li_xM$ or $xNa + M \rightleftharpoons Na_xM$ where (M= Si, Ge, Sn, Sb, etc.), which differs from insertion/desertion in carbon-based anodes. However, the alloying reaction results in severe volume expansion and internal stress, leading to serious pulverization of the electrode materials. The frequent volumetric change during cycling also results in repeated formation and destruction of the SEI, which is the main reason for fast electrolyte consumption and capacity degradation [26, 28]. Moreover, some nonmetallic alloys of Si and P show relatively low conductivity and poor C-rate capabilities. These limitations stem from the intrinsic electronic properties of these materials. The low conductivity hinders the efficient movement of electrons during the charge and discharge cycles, which is crucial for high-performance battery operation. Furthermore, the poor C-rate capability, which refers to the speed at which the battery can be charged and discharged, is also a consequence of this limited electron mobility, as well as sluggish ion diffusion within the alloy structure.

To address the issues of bulk alloying materials, nano-engineering is adopted to increase the active sites, decrease the Li- and Na-ion diffusion distance, and mitigate the volume expansion and resulting stress [68]. Nano-structured alloys can be endowed with high gravimetric capacities and C-rates, and superior fracture toughness. However, because of the large specific Brunner-Emmet-Teller (BET) surface, low tap density, and complex fabrication process, some obstacles, such as the low initial Coulombic efficiency (ICE), inferior volumetric capacity, and high manufacturing costs, safety and health concerns, hinder the development and subsequent replacement for traditional electrode materials. Nevertheless, research into micro-scale alloying anode material continues because compared to nano-scale materials, they have higher ICE, volumetric capacity, and mass loading due to the high tap density and small BET surface. However, micro-scale alloys with large particle sizes have drawbacks, such as large ion and electron diffusion distances, pulverization, significant volumetric expansion,

and poor C-rates. Ideal alloying-type anode materials should combine the advantages of both nano and micro-scale materials by incorporating an overall micro-scale morphology and built-in nano-scale features.

Micro-sized materials demonstrate greater potential for practical applications than nano-materials in the aspects of areal mass loading, volumetric energy density, Coulombic efficiency, fabrication process, and cost [69, 70, 60, 71]. The booming publications on micro-sized anodes for rechargeable batteries in recent years reflect the keen interest of the scientific community. Briefly: **[Figure 1.6]**

- Owing to the large size, micro-sized materials have high tap density. It means that electrode composed of micro-sized materials has higher mass loadings at a certain thickness than nano-counterparts, leading to higher volumetric capacity and energy density, which is promising to satisfy the demand for portable energy storage devices [72].

- The low specific surface of micro-sized materials significantly decreases contact area with electrolytes, which mitigates capacity loss in the initial cycle and enhances the initial Coulombic efficiency (ICE) [69, 70, 73].

- Micro-sized materials are easily fabricated, simplifying the fabrication process and presenting remarkably cost advantages [74]. Therefore, from the practical application perspective, micro-sized alloy anodes with a high specific capacity, low reaction potential, and high tap density are promising candidates for the commercial implementation of high-energy batteries.

The expansion in the volume of alloy anodes, commonly used in LIBs, SIBs, and PIBs, is a significant issue that hinders their practical application [49, 75, 76]. For instance, the high-capacity P_{red} anode undergoes a volume change of 499% during the sodiation processes [59]. Similarly, the Sn anode experiences volume expansion of approximately 260% and $\approx 430\%$ as it undergoes phase transformations from Sn to $Li_{4.4}Sn$ and $Na_{15}Sn_4$, respectively.

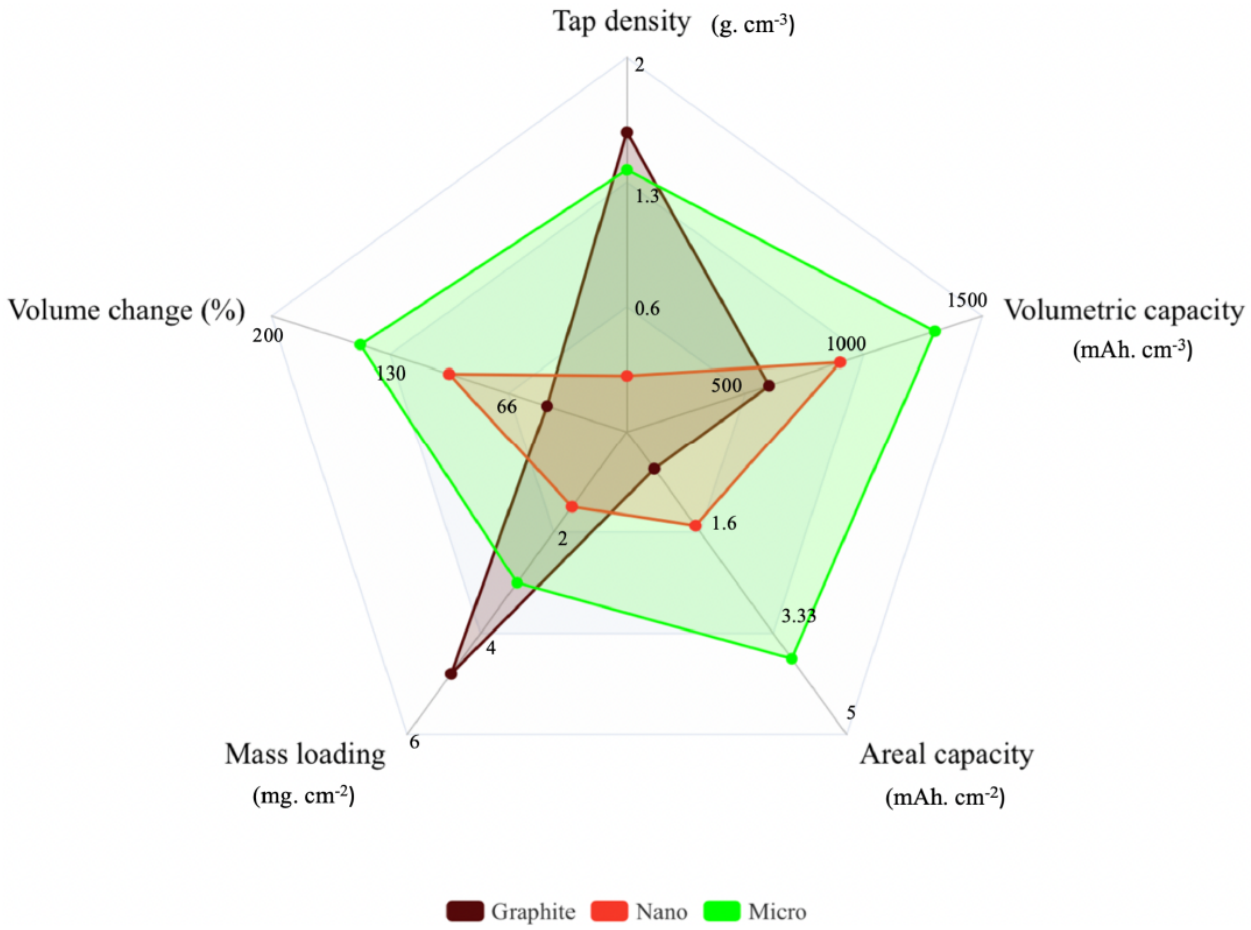

Figure 1.6: Comparison of critical practical metrics of Graphite, Nano-, and Micro-size anode materials.

This substantial increase in volume can lead to severe pulverization of the active materials [77]. The extensive volume expansion of alloy anodes presents a major challenge in maintaining an intact SEI layer [76, 78].

The formation of the M_xA_y alloy phase is responsible for this significant volume increase. Simultaneously, excessive electrolyte consumption results due spontaneous generation of an SEI protective layer on the surface of the alloy anode. If the SEI layer is compromised due to the strain caused by the volume expansion, the electrolyte will react with the exposed anode surface, leading to further electrolyte consumption [79]. This newly formed SEI layer can isolate the fragmented active materials, resulting in the loss of compact electrical contact. One notable aspect is the occurrence of these issues throughout each cycle, resulting in repeated failures and the continuous development of the SEI layer, as well as the severe pulverization of the electrode. Consequently, the SEI layer becomes thicker and more uneven while the electrolyte experiences significant depletion. Furthermore, the excessive consumption of charges from the cathodes leads to decreased reversible capacity. This situation places considerable stress on the SEI layer that forms on the micro-sized alloy particles, creating additional difficulties in maintaining its stability.

It is evident that various factors, such as the electrolytes, binders, and architectural structure of the anode, influence the performance of these anodes. Chapter 2 is a literature review of the leading solution proposed to alleviate this volume expansion issue.

Chapter 2

Literature Review

This review has been published[1].

This smart and digital era is highly energy-consuming and demanding. The depletion of fossil fuels has heightened concerns over energy security, leading to increased research into developing energy storage devices (ESDs) [80]. These ESDs play a vital role in our daily lives by powering an array of electrical devices, from mobile phones to electric vehicles. Furthermore, they are crucial in addressing the intermittency issues associated with emerging natural resources of energy (tidal, solar, wind, etc). Over the past few decades, alkali-ion batteries (LIB, SIB, ...) have garnered significant attention for their potential in energy storage applications. LIBs, with their high energy capacity, superior long lifespan, and adaptable design, have emerged as the market leader [81]. However, the cost of LIBs remains a concern owing to the limited and uneven distribution of lithium resources on Earth. On the other hand, SIBs offer a promising alternative for large-scale energy storage, given the abundance of sodium resources and competitive pricing. As SIBs exhibit electrochemical properties akin to LIBs, it is anticipated that the development of SIBs is expected to leverage the well-mature lithium-ion manufacturing and industry [41, 82].

Modern electronic devices, especially electric vehicles, demand LIBs/SIBs that possess

[1]DOI: 10.1039/d3im00126a

both high energy density and enhanced safety. This has driven the development of electrode materials with substantial capacity and sustained stability [83]. Interestingly, when compared to cathode materials, the anode materials in LIBs and SIBs show a higher promise for achieving superior energy densities. This is attributed to their varied nature and impressive theoretical capacity [48].

Typically, anodes are categorized into three main types based on their charge storage mechanism: insertion, conversion, and alloying [84]:

Materials of the insertion variety, like carbon and those based on titanium, support the reversible (de-) insertion of alkali metal ions without harming their crystalline frameworks, resulting in impressive durability and stability during repeated cycles. Graphite, having a capacity of 372 $mAh.g^{-1}$, is the primary choice for LIB anodes due to its consistent performance and superb cycling stability. However, its low discharge plateau ($0.2V$ vs Li/Li^{+}) leads to Li dendrite growth during fast charging processes [85].

On the other hand, conversion materials, such as phosphide, sulfide, and transition metal oxides, undergo multiple electron reactions with Li/Na. This leads to the formation of metallic particles and alkali metal compounds and, thus, exhibit high specific capacities. However, the challenge of initiating nucleation in mixed phases causes notable voltage hysteresis, substandard reversibility, and a drop in coulombic efficiency (CE), in which the CE is defined as the ratio of the charge-specific capacity over the discharge-specific capacity. Furthermore, the volume change during the cycling process leads to expedited structural degradation and reduced capacity retention [86].

Due to their alloying mechanism with Li/Na, alloy-based anode materials tend to display 3 times higher specific capacity than conversion materials, forming stable Li- or Na-rich phase alloys. At room temperature, many metals or metalloids exhibit alloying activity towards Li or Na, including but not limited to Si, Ge, Sn, Sb, Bi, and P [87, 88]. These alloying materials offer great commercial potential due to their high storage capacities, excellent electronic properties, and appropriate discharge plateaus. Si/C composites with

minimal Si content lead the pack as potential anodes for LIBs. However, a loss of capacity is inevitable due to the volume change caused by the high capacity, leading to three major challenges. Firstly, the structural breakdown from expansion disrupts internal electrical connectivity, diminishing the capacity. Next, shattered fragments tend to aggregate and clump together, obstructing ion movement. Lastly, an increase in the charge transfer impedance due to the continuous reactions between active material and electrolytes forming unstable SEI. Additionally, repetitive volume alteration makes electrode films prone to distortion, detachment, and delamination from current collectors. Even though the active material has not collapsed entirely, the detached electrode film ceases to contribute to the system's capacity. This event is a critical factor that hinders the widespread adoption of alloying materials in commercial applications due to their limited lifespan [89].

In order to prevent the detrimental effects of lithiation/sodiation-induced volume changes and avoid pulverization, researchers have employed various nano- and micro-scale structures and morphologies to enable reversible (de)lithiation/(de)sodiation in alloying anode materials. These approaches, which utilize both pure alloying elements and composite materials, primarily focus on increasing the surface-to-volume ratio (SVR) of the alloying anode's morphology. Increasing the SVR reduces concentration and stress-strain gradients from lithiation/sodiation significantly by decreasing the required lengths for ion diffusion on the overall lithiation/sodiation behavior. Furthermore, an increase in SVR results in a higher rate of lithiation/sodiation and an increase in the maximum (dis)charging power available in the anode [90, 91, 92].

One of the most common and well-studied approaches toward increasing the SVR is to create nano-structured morphologies. The introduction of nano-wires in 2008 is considered an important milestone, which effectively accommodated volume expansion during the Li-Si alloying process [93]. Since then, there's been a surge in the exploration of various nano-dimensional structures, including nano-dots [94], nano-pores [95], and 2D nano-sheets [96]. These materials have the potential to mitigate SEI destruction and over-consumption of

electrolytes and subsequently improve cyclic stability. Additionally, due to optimal contact between active material and electrolytes, the high SVR of these materials promotes a better kinetics diffusion and enhances the rate performance [96, 52, 97, 98]. Yet, it is noteworthy that the initial Coulombic efficiency (ICE) is not satisfactory due to an irreversible capacity loss during the first cycle caused by the large contact area between electrolytes and nano-structured materials [78]. Moreover, the low tap density of nano-structures might compromise the battery's volumetric energy density [70]. It is also noteworthy that well-designed nano-materials require complicated crafting and intricate production methods, incurring high manufacturing costs [99, 100].

When comparing micro-sized materials to their nano-sized counterparts, the former exhibits greater potential for practical applications in several aspects, including areal mass loading, volumetric energy density, Coulombic efficiency, fabrication process, and cost [69, 101, 102, 60, 103]. The advantages of micro-sized materials include higher tap density, resulting in higher mass loadings and subsequently boosting the volumetric capacity and energy storage. This characteristic is especially beneficial for compact and portable energy storage solutions [72]. Additionally, the low specific surface area of micro-sized materials reduces the contact area with electrolytes, leading to a mitigated capacity decay in the first cycle and enhanced ICE [70, 69, 102, 60]. Furthermore, the ease of fabrication and resulting cost advantages make micro-sized materials attractive for practical applications [74]. Considering these strengths, micro-sized alloy anodes with substantial specific capacity, low reaction potential, and impressive tap density emerge as promising contenders for the large-scale production of high-energy battery systems, barring the aforementioned challenges of volumetric changes and protection of the SEI layer to ensure optimal electrochemical performance.

In the realm of material science, it has been observed that the formation of the M_xA_y alloy phase leads to a significant volume expansion. During the process of sodiation, the high-capacity P_{red} anode undergoes a volume change of 499% [59]. At the same time, the Sn anode

experiences a volume expansion of $\approx 260\%$ and $\approx 430\%$ during the phase transformation from Sn to $Li_{4.4}Sn$ and $Na_{15}Sn_4$, respectively. Unfortunately, such a notable volume change often results in the pulverization of the active materials, and maintaining an intact SEI layer becomes a significant challenge due to the massive expansion of alloy anodes [78, 103, 77, 79].

During the interaction of the alloy anode with the electrolyte, the protective layer (SEI) forms on the anode's surface; when the SEI layer is ruptured due to excessive strain, the electrolyte will further interact with the now unprotected anode surface, intensifying the electrolyte's depletion [79]. This freshly developed SEI layer can segregate active components, leading to the disruption of solid electrical connections [103, 76]. It is crucial to note that these reactions occur in every battery cycle, triggering recurrent breakdowns and persistent SEI layer formation alongside severe electrode pulverization. Consequently, the SEI layer becomes irregular and thick, with extreme consumption of electrolytes and excessive use of cathode charges, leading to decreased reversible capacity. Additionally, the SEI formed on micro-sized alloy particles experiences significant stress, complicating the preservation of its stability. Hence, establishing a premium-quality SEI layer is fundamental for ensuring optimal electrochemical performance.

Structure, composition, and electrolyte engineering are efficient ways to mitigate the huge volume change for micro-size alloy anode materials. Various factors, such as electrolytes, binders, and morphologies, influence the performance of micro-sized alloy anodes. In this comparative review, we will focus on the recent developments in micro-sized alloy anodes, particularly emphasizing the role of electrolyte, binder, structure, and composition in volume expansion mitigation and performance enhancement. The review will provide an in-depth analysis of recent advancements in each segment and highlight the challenges and opportunities for maximizing the performance of high-energy Li and Na-ion batteries.

2.1 Electrolytes

The electrolyte is an essential and critical component of the battery system [104]. The term electrolyte refers to an ion-conducting solution that consists of a solvent and a salt [105]. Electrolytes in batteries serve as conductive mediums, enabling the shuttling of ions between the cathode and anode during discharging and charging cycles. This transfer is crucial for the battery's overall function and performance. Due to an energy mismatch between the red/ox potential of the electrolyte and the electrode materials, a spontaneous film or layer is generated on the anode surface. It is called the Solid Electrolyte Interphase (SEI) [69, 106]. In Aprotic electrolytes, the formation of an SEI is inevitable for many electrodes, including graphite, Sn, Si, (etc.) Once formed, this layer should protect from undesirable side reactions with the anode and prevent over and continuous consumption of the electrolyte by blocking the electron transfer from the anode to the electrolyte. However, it should allow rapid cation movement to enhance the reaction kinetics [107, 108].

Alloy anodes suffer from repetitive contraction and swelling, rendering the SEI vulnerable. Due to the large volume change, an ideal SEI should have superior mechanical stability, maintaining its integrity without breaking and exposing fresh anode surface to the electrolyte. Thus, electrolyte engineering is an essential approach to designing a flexible and well-suitable SEI for micro-size alloy anode material.

The SEI layer is mainly due to the reduction of both salts and solvents in liquid electrolytes. Electrolyte salts consist of anions and cations. The types of rechargeable batteries determine the cation, such as Li^+, Na^+, Zn^{2+}, Ca^{2+}, and Al^{3+}. Anions such as sulfonyl imide (bis(fluoro-sulfonyl)imide (FSI^-), bis(trifluoro methane sulfonyl)imide ($TFSI^-$)), hexafluorophosphate (PF_6^-), and others are also commonly used [109, 110, 111, 112, 113]. The SEI on anodes is formed from inorganic elements like fluorides and oxides, which result from anion breakdown, and organic compounds like Fluoroethylene Carbonate (FEC) [56]. The anions play a significant role in determining the various characteristics of the SEI and its

reductive kinetics. To build an optimal SEI layer, molecular orbital energy evaluations have been employed to forecast the reductive stability of anions like PF_6^-, FSI^-, and $TFSI^-$. Insights from these evaluations show that PF_6^- possesses notable reductive stability yet is thermodynamically unsuitable for Li metal anodes. Nonetheless, a robust SEI layer formed by pre-reduced salts counteracts salt decomposition. The distinct properties of various salts highlight the significance of selecting an appropriate salt to optimize the SEI and enhance the overall battery performance [109, 114, 115].

Organic solvents that are frequently utilized include esters and ethers. Up to this point, a significant amount of research has been conducted on ethers, carbonate esters, and phosphates, examining their potential role in designing an optimized SEI for micro-sized alloy anodes. Various aspects of these solvents, including their linear formula, molecular weight, and melting points, have been scrutinized. For instance, carbonate esters can be categorized into two types: cyclic carbonate esters, which include compounds like ethylene carbonate (EC) and propylene carbonate (PC), and linear carbonate esters, such as ethyl methyl carbonate (EMC), diethyl carbonate (DEC), and dimethyl carbonate (DMC) [116, 117].

Carbonate-based electrolytes (CBE) have been preferred in commercial Li-ion batteries due to their improved oxidative stability and higher flash points [112, 118]. Nonetheless, used in micro-sized alloy anodes presents certain challenges. One such challenge is the formation of a rigid, thick, and subpar SEI, undermining the stability of the anode. This phenomenon is mainly due to the fragile mechanical interactions between the inorganic particles and the polymer matrix. Gao et al. [119] highlighted that the SEI produced in CBE showcased a minimal maximum elastic deformation energy. Additionally, Zhang et al. [70] observed that SEI layers developed in $NaPF_6 - PC$ with $5wt\%$ FEC were not compact, possibly due to the high solubility of certain SEI components, such as sodium oxides and carbonates, in PC-based electrolytes.

In SIBs' electrolytes, employing a mixture of a couple of Na-salts, which are then dissolved in a combination of two or more solvents, is common practice. However, it is worth noting that

single solvent formulations are a rarity, with the exception of PC [120]. The reason behind this trend lies in the complex and often conflicting demands placed on battery electrolytes, which are challenging to fulfill using a single molecular composition. Therefore, using a combination of solvents and salts has become a primary motivator in developing electrolytes for SIBs. According to recent reports, the EC:DEC combination is the most frequently employed, followed by EC:PC and PC. Concerning the selection of salt, the literature suggests that $NaClO_4$ is the most effective option, followed by $NaPF_6$, $NaCF_3SO_3$, and $NaTFSI$ [121, 122].

Ethers are an organic compound composed of ether groups, symbolized as R-O-R', where both R and R' can be either aryl or alkyl groups. There are two main subcategories within the ether solvent: cyclic ethers include 1,3-dioxolane (DOL), tetrahydrofuran (THF), and 2-methyl tetrahydrofuran (2-MeTHF), and linear ethers include compounds like dimethoxyethane (DME or G1), diglyme (G2), tetraglyme (G4), and ethylene glycol diethyl ether (EGDEE) [112, 123, 124, 125].

Electrolytes based on ether exhibit superior reduction stability on the anode side, fostering the development of a thinner SEI compatible with a range of anodes. Within the family of ether solvents, glyme (Gn, $CH_3O(CH_2CH_2O)\ CH_3$) is a widely used solvent. As the carbon chain length of glyme increases, its viscosity rises, leading to a corresponding decline in ionic conductivity. Early studies of glyme-based electrolytes were conducted by Zhang et al. [70]. They investigated the use of these electrolytes to stabilize micro-sized alloy anodes without the need for intricate electrode designs. Their findings illuminated the consistent cycling of micro-sized Sn in SIBs employing G1-G4 electrolytes in the presence of 1 M $NaPF_6$. For alloy anodes, diglyme, with its longer carbon chain than DME, provides a balance between oxidation stability and viscosity, positioning it as a prime candidate for full-cell applications. As shown in **figure 2.1**, Zhang and his team explored the effects of 1 M $NaPF_6$ in diglyme and $PC + 5\%$ FEC on the SEI layer's quality and the cycling stability of micro-size Sn anodes in SIBs. Post 100 cycles, the anode in a 1 M $NaPF_6$-diglyme electrolyte showcased superior

performance, retaining its structural robustness more effectively than its counterparts. This can be attributed, in large part, to the formation of a highly compact protective film on the surface of the micro-size anode when submerged in 1 M $NaPF_6$-diglyme.

In a comprehensive study led by Huang et al.[69], the team sought to understand the variations in the microstructure, mechanical attributes, and chemical compositions of SEI layers on micro-size Sn anodes in two distinct electrolytes: 1 M $NaBF_4$-diglyme and $NaBF_4$-EC/DMC. Their investigative tools encompassed cryo-TEM, AFM, XPS, and DFT calculations; through cryo-TEM assessments of micro-size anodes post-three cycles, it was deduced that the $NaBF_4$-EC/DMC electrolytes were instrumental in forming substantial SEI layers characterized by polycrystalline domains of Na_2CO_3 and potential NaF inclusions. On the other hand, SEI layers from $NaBF_4$-diglyme were noticeably thinner and marked by a blend of amorphous Na_2CO_3/NaF particles interspersed within a polymer-like matrix. This distinctive configuration facilitated enhanced sodium ion movement, boosted its ionic conductivity, and augmented the mechanical resilience of the SEI. Delving deeper with AFM examinations, the researchers discovered that the SEI originating from $NaBF_4$-diglyme showcased superior rigidity (*about* $355MPa$) and elasticity (*roughly* 79%), which elucidated the heightened electrochemical efficacy observed in diglyme electrolytes. This investigation successfully revealed the structural and mechanical foundations that render SEI layers in glyme-based electrolytes stable **[Figure 2.2]**.

The advantages of ether electrolytes can be effectively implemented in the alloy anodes of LIBs. By forming an SEI layer with high interfacial energy (E_{int}) to the micro-sized Si anode surface, the adhesion of the SEI layer to the anode surface is reduced. This helps accommodate the anode's volume change during the charge and discharge cycles. With its high E_{int}, LiF is a favorable SEI layer component [126]. Ethers are characterized by their low thermodynamic reduction potentials, typically ranging from $\approx 0.0 - 0.3V$. This trait amplifies the decomposition of fluorinated salts. Nevertheless, the solubility of $LiPF_6$ in linear ethers, such as DME and diglyme, is not optimal, which has curtailed their prevalent

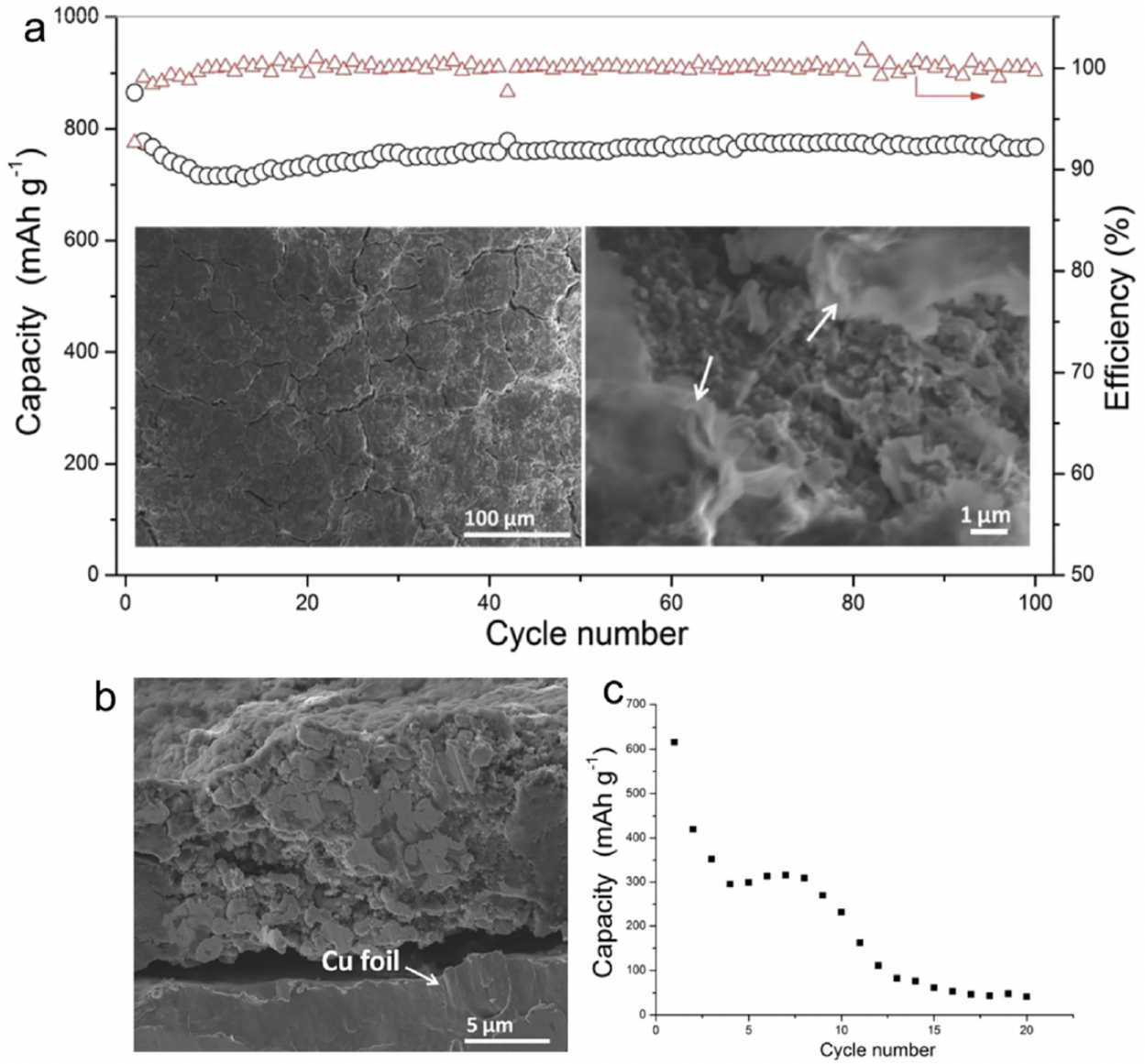

Figure 2.1: (a) Cycling performance of Sn electrode in 1 M $NaPF_6$/DGME electrolyte at 250 $mA.g^{-1}$ (red triangles : efficiency).The morphology of the electrodes after 100 cycles is shown in the insets of (a), and the arrows indicate SEI films. (b) Cross-section image of Sn electrode after cycling in DGME electrolyte. (c) Electrochemical performance of Sn electrode in 1M $NaPF_6/PC$ electrolyte with 5% FEC additives. cycling stability under 100 $mA.g^{-1}$. (Zhang et al. [70])

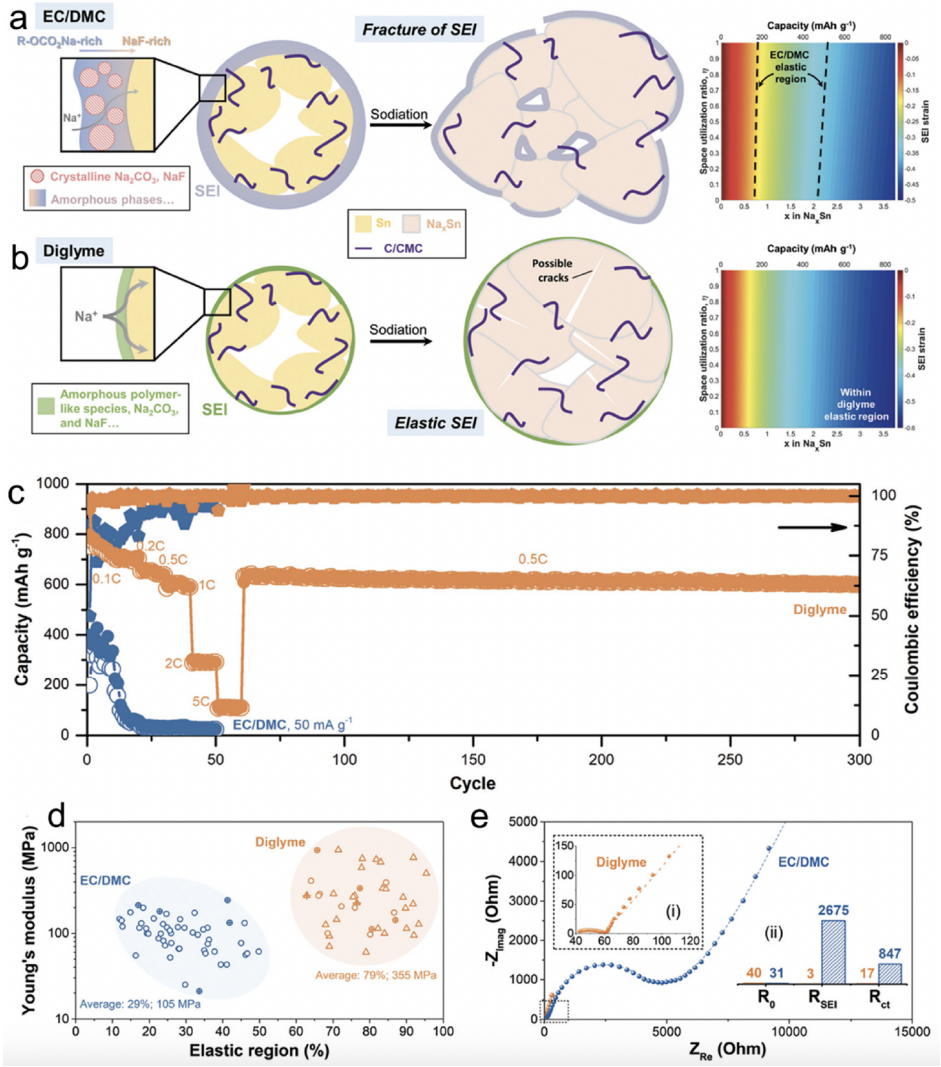

Figure 2.2: Schematics illustrating the chemical compositions, structures and mechanical response to the volume expansion of SEIs derived from (a) $NaBF_4$/EC/DMC and (b) $NaBF_4$/diglyme. The strains imposed on the SEI as a function of x in Na_xSn and space utilization ratio in comparison to the relative elastic region of SEIs are also included. (c) the cyclic stability of Sn micro-particle electrodes in 1 M $NaBF_4$/diglyme (i: 85 $mA.g^{-1}$, c orange: rate test) and 1 M $NaBF_4$/EC/DMC (ii: 20 $mA.g^{-1}$, c blue: 50 $mA.g^{-1}$) electrolytes using the configuration of a Na/Sn half-cell. (d) Distributions of Young's modulus and relative elastic regions of the SEIs with 430 curves for each. The responses with and without fracture/yielding behaviors are plotted by circle and triangle scatters, respectively. The results from electrodeposited Sn without binders and carbons are marked by an additional "+". (e) Three-electrode EIS result of the cycled electrodes with (i) an enlarged Nyquist plot in diglyme and (ii) the fitted impedance as the insets. (Huang et al.[69]).

application in LIBs. Cyclic ethers are generally not employed in LIBs due to their pronounced chemical reactivity. Among the possible cyclic ethers, THF and 2-MeTHF are preferable as they contain fewer ether oxygens, which shield them from such reactions [34, 127].

Chen et al. [126] conducted a screening of salts and solvents for micro-sized alloy anodes in LIBs. The focal point of their research was to discern the reduction potential of the salt and gauge the solvation capabilities of the solvent. In their innovative approach, they formulated a 2 M $LiPF_6$ solution using a combination of THF and 2-MeTHF for different micro-sized anodes (Si, Al, Bi), each exceeding 10 μm in size. Through their experimentation, they discovered that the 2 M $LiPF_6$-THF/2-MeTHF electrolyte facilitated the formation of an SEI layer that was not only thin and homogeneous but also enriched with LiF. This SEI layer, abundant in LiF, exhibited a high E_{int} when interfacing with the alloy anode. This characteristic acted as a buffer, accommodating the plastic deformation occurring in the lithiated alloy (Li_xSi) throughout the alloying and dealloying phases. Consequently, micro-sized anodes were able to achieve stable capacities, with initial CEs of higher than 90% **[Figure 2.3]**. Additionally, Zhang et al. [127] employed 2 M $LiPF_6$ in 2-MeTHF and a blend of 2 M $LiPF_6$ in THF/2-MeTHF as electrolytes. Their aim was to fortify and stabilize the SEI layer on the micro-sized Sn anode for LIBs. The SEI formed on the anode through the 2-MeTHF-based electrolytes was distinguished by its compact and thin structure, which was notably enriched with LiF. This structural characteristic plays a pivotal role in considerably boosting the cycle longevity of the anode.

Solvents that are phosphorus-based, including phosphates, phosphazenes, and phosphonates, are becoming increasingly popular due to their potential to decrease flammability and enhance anodic stability when used with high-voltage cathodes. Traditional carbonate-based electrolytes are prone to flammability and can result in fire accidents [128, 129]. Organic phosphates, like trimethyl phosphate and hexamethylphosphoramide, are valued for their non-flammable properties, as phosphorus can serve as a trapping agent for hydrogen radicals [130]. However, linear organic phosphates are ineffective at producing a suitable SEI on the

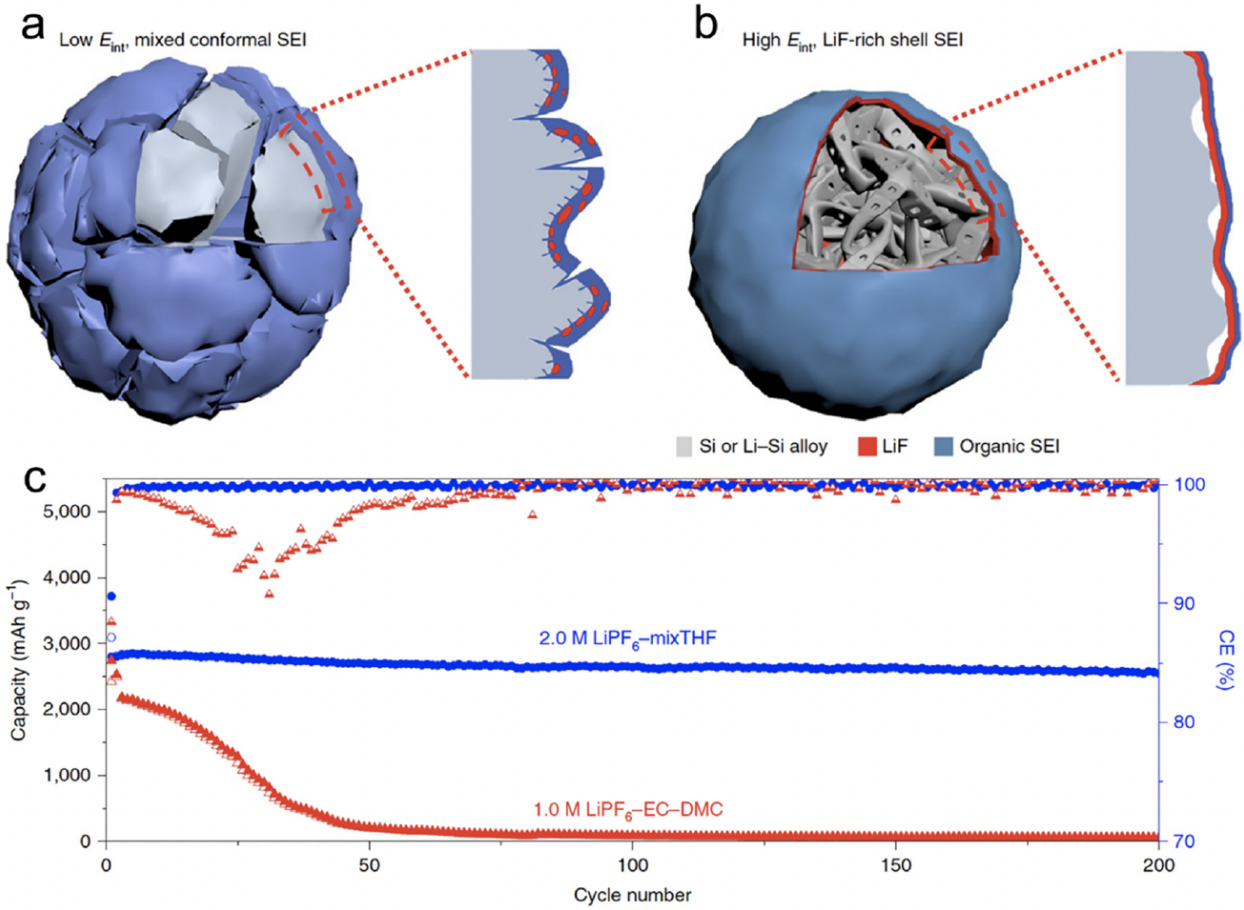

Figure 2.3: Schematic of the cycled alloy anode with an organic, low E_{int} and non-uniform (a) and an inorganic, high E_{int} and uniform (b) Li alloy–SEI interphase. (c) Cycling stability and CEs of SiMPs cycled in 2.0 M $LiPF_6$–mixTHF and 1.0 M $LiPF_6$–EC–DMC electrolytes; the rate is C/5. (Chen et al. [126]).

anode, leading to inferior battery performance when used with graphite or Si-based anodes, and are, therefore, rarely included unless used in high concentrations [131]. Recently, a novel fluorinated cyclic phosphate solvent molecule known as TFEP, has been introduced. This molecule is characterized by its inherent non-flammability and exceptional capability to form SEI on graphite anodes. The SEI, produced by this cyclic phosphate-derived electrolyte, is enriched with polyphosphoesters. These polyphosphoesters are a type of highly flexible elastomer. Alongside other inorganic components, this elastomeric inclusion in the SEI is anticipated to adeptly manage the huge volume change exhibited by Si electrodes [132].

In their research, Yang et al. [133] have proposed a method for designing a cyclic phosphate (TFEP)/hydrofluoroether (HFE)-based electrolyte that is not flammable **[Figure 2.4]**. The goal is to enhance the robustness and elasticity of the solid electrolyte interphase (SEI) on Si-based anodes. The design strategy is based on the ability of TFEP to create polymeric components and HFE to increase the association between Li^+ and FSI^- ions, leading to the formation of additional inorganic components derived from the FSI^- anion. This results in a composite SEI that is highly elastic and robust, consisting mainly of LiF, Li_2O, Li_xPO_y, sulfur compounds, and polyphosphoesters. As a result, the micro-sized Si particles can undergo elastic deformation while maintaining their structural integrity during the charge/discharge process. Phosphates, despite possessing several benefits, are not compatible with most electrode materials. This is due in part to the low reductive stability of phosphates, which leads to the difficulty of creating a stable SEI on the anode surface, as cited in various sources [112, 121]. Nevertheless, the use of phosphates as co-solvents or additives can be effective in preventing reductive decomposition and enhancing electrolyte non-flammability. Consequently, organic phosphorus-based solvents are commonly employed as non-flammable co-solvent additives [134]. Additionally, a compact and stable SEI layer on micro-sized alloy anodes using phosphate-based electrolytes can be achieved through the concepts of high concentration and localized high concentration [60, 112, 135].

In recent decades, the popularity of highly concentrated electrolytes has grown significantly.

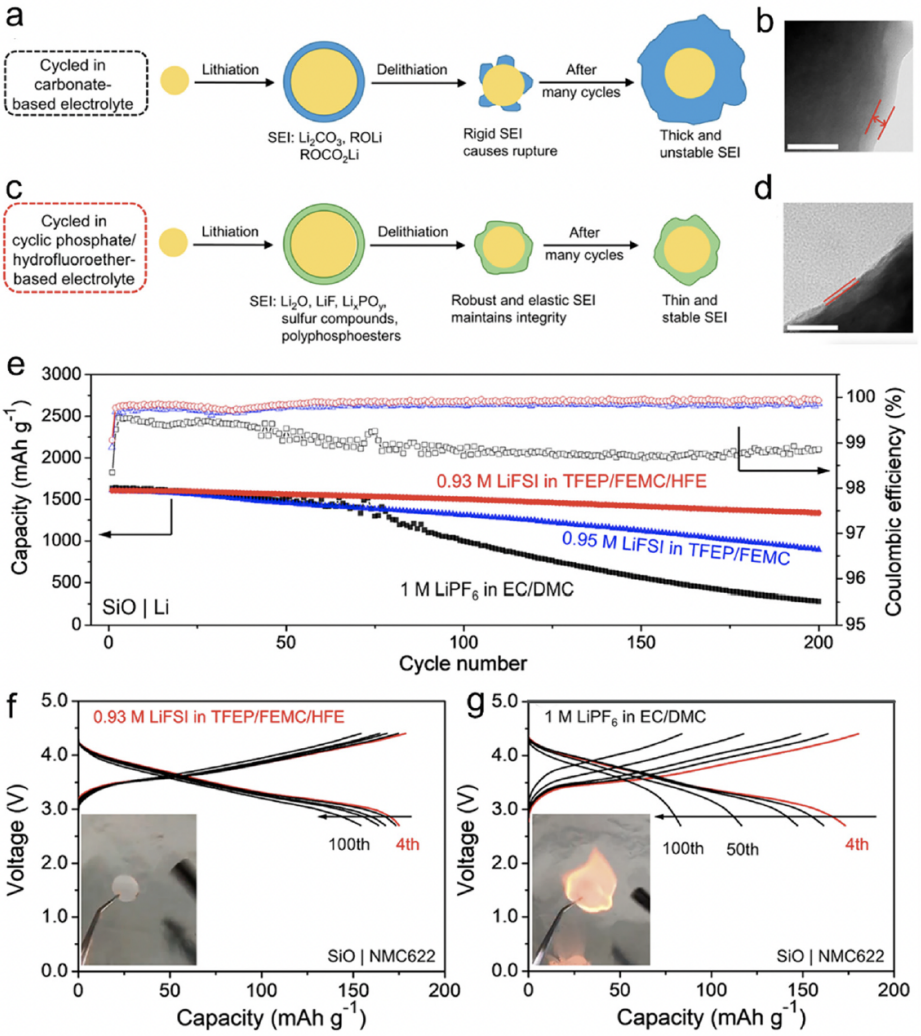

Figure 2.4: Schematic illustrations of SEIs on an SiO particle derived from (a) 1 M $LiPF_6$ in EC/DMC and (c) 0.93 M LiFSI in TFEP/FEMC/HFE. In the conventional EC based electrolyte, an SEI mainly consisting of Li_2CO_3, $ROCO_2Li$, *and* $ROLi$ forms at the first lithiation, which is too rigid to tolerate the volumetric stress during delithiation. On the other hand, the SEI generated by the cyclic phosphate/hydrofluoroether-based electrolyte is mainly composed of Li_2O, LiF, Li_xPO_y, sulfur compounds, and polyphosphoesters, which is highly elastic and robust and can sustain the volume changes of SiO upon cycling. TEM images of the SiO electrodes after cycling in (b) 1 M $LiPF_6$ in EC/DMC and (d) 0.93 M LiFSI in TFEP/FEMC/HFE for 100 cycles. The distance between two lines represents the thickness of the SEI, which clearly shows that the SEI formed in 0.93 M LiFSI in TFEP/FEMC/HFE is much thinner than that in 1 M $LiPF_6$ in EC/DMC electrolyte. The white scale bar represents 50 nm. (e) Cycling performance of the SiO|Li half-cells using 0.93 M LiFSI in TFEP/FEMC/HFE, 0.95 M LiFSI in TFEP/FEMC, and 1 M $LiPF_6$ in EC/DMC at 0.2 C after three formation cycles at 0.05 C. Selected charge-discharge curves for the full cells at 0.4 C with (f) 0.93 M LiFSI in TFEP/FEMC/HFE and (g) 1 M $LiPF_6$ in EC/DMC. The capacity is based on the weight of the NMC622 active material. The insets show the flammability test results. (Yang et al. [133]).

As opposed to conventional electrolytes, where the concentration is only $1M$, these highly concentrated electrolytes have a significantly reduced number of free solvent molecules. This leads to forming a unique 3D solution structure and improves stability by minimizing the interplay between unbound solvent molecules and anode materials [135, 136]. Additionally, increasing the salt concentration of ether-based electrolytes greatly enhances their anodic stability. Moreover, highly concentrated electrolytes promote the creation of a salt-derived SEI layer. This, in turn, beneficially influences the interfacial chemical dynamics of anode surfaces, making them more suitable for high-voltage battery configurations [112].

Despite the significant advantages of highly concentrated electrolytes, their practical application is made challenging by their high viscosity, poor wettability, and high cost. Fortunately, there is an alternative in the form of localized high-concentration electrolytes (LHCE), which can enhance the benefits and alleviate the drawbacks of concentrated electrolytes. Typically, some diluents with appropriate quantities are added to the highly concentrated electrolytes. This addition aims to diminish viscosity and enhance ionic conductivity. At the same time, it ensures the retention of the inherent benefits of concentrated electrolytes, like superior oxidative stability and a structured solvation framework. As a practical example, Jia et al. [135] introduced a fluorinated $bis(2,2,2-trifluoroethyl)$ ether (BTFE) as a diluent into 1.2 $M\ LiFSI\ TEP/FEC$ ($TEP/FEC/BTFE:\ 1.2/0.13/4$), resulting in an LHCE for porous micro-sized Si anode. This electrolyte promoted the creation of locally highly coordinated $Li^+ - TEP$ solvates and an SEI layer rich in LiF, derived from FSI^-. As a direct outcome, when tested in a Si/graphite||NMC333 full cell configuration using the 1.2 $M\ LiFSI - TEP/FEC/BTFE$ electrolyte, there was a noticeable enhancement in electrochemical performance in comparison to the 1 $M\ LiPF_6 - EC/EMC - FEC$ solution **[Figure 2.5]**.

Film-forming electrolyte additives are also a main constituent of electrolyte engineering. Efforts to tailor and tune the SEI will not be successful without suitable and well-optimized additives. Their role can be summarized in 3 key points: first, stabilizing the anode structure:

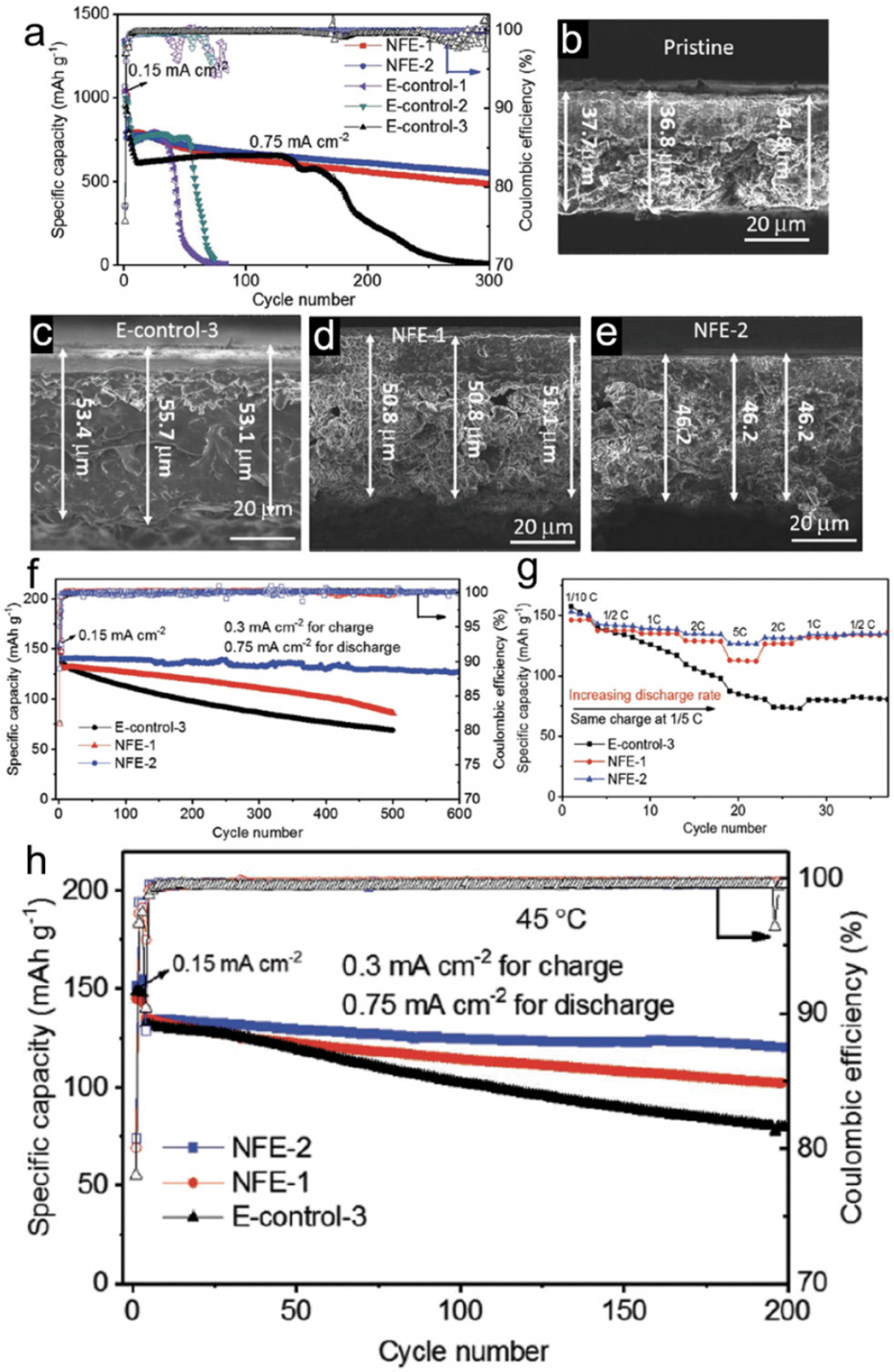

Figure 2.5: Electrochemical behavior of Li||Si/Gr half cells in different electrolytes. a) Long-term cycling performance and Coulombic efficiency of Li||Si/ Gr half cells in different electrolytes. b) SEM image of a pristine Si/Gr electrode. SEM images of fully lithiated electrodes after 1 cycle in c) E-control-3, d) NFE-1, and e) NFE-2. Electrochemical behavior of Si/Gr||NMC333 full cells in different electrolytes. f) Long-term cycling performance of Si/Gr||NMC333 full cells with different electrolytes at $25°C$. g) Rate capability of the Si/Gr||NMC333 cells in different electrolytes at $25°C$. h) Long-term cycling performance of Si/Gr||NMC333 cells cycled at $45°C$ in different electrolytes. (Jia et al. [135]).

a stable SEI layer formed by the additives should act as a buffer against the volume changes during cycling, thus maintaining structural integrity. Second, enhancing ionic conductivity: the right SEI composition facilitated by additives is key for efficient ion transport. Finally, suppressing side reactions: additives form a selective SEI layer that prevents undesirable side reactions that lead to capacity fading. There is no clear demarcation between an additive and a solvent/salt, so an arbitrary threshold of 10 vol% is adopted, below which the new components are considered as additives [29]. Various additives have been investigated, with the most prevalent ones being salt-type additives, fluorine-containing species, and derivatives of unsaturated carbonates [122, 137, 138, 139, 140, 141].

Additives based on salt compounds, including lithium bis(oxalato)borate (LiBOB), lithium nitrate ($LiNO_3$), sodium carbonate (Na_2CO_3), and sodium fluoride (NaF), play a crucial role in augmenting the ionic conductivity and thermal stability of batteries. These additives are key in forming a robust SEI and regulating the anode and electrolyte interactions. The strategic application of these salt-type additives leads to enhanced performance and safety of the battery, especially under extreme operational conditions [104, 111, 142, 143]. Ma et al. [144] employed readily soluble SEI species, Na_2CO_3 and NaF salts, as additives to saturate the electrolytes. The introduction of NaF salt additive in 1 M $NaPF_6 - PC$ significantly hindered the dissolution of the SEI and increased NaF concentration within the SEI layer, promoting the formation of a more inorganic and stable SEI layer.

Additives featuring unsaturated C–C bonds in carbonate derivatives are also gaining much attention lately [112, 145]. A prominent example of such additives is vinyl ethylene carbonate (VC), which has become an essential component in the battery electrolyte industry. The effectiveness of VC lies in its ability to undergo polymerization reactions on the electrode surface, leading to the formation of protective poly(VC) layers. Dahbi et al. [62] demonstrated the distinct capabilities of VC additives in a 1 M $NaPF_6 - EC/DEC$ solution. They found that VC not only contributes to the stability of the SEI but also safeguards the electrolyte against further decomposition through a unique passivation process. The VC-derived SEI

was formed based on a polymerization reaction and consists of a mix of inorganic and organic compounds. This dual composition is key to enhancing battery performance and longevity.

Fluorine-containing (F-containing) species are highly regarded in electrolyte engineering due to their ability to form fluorinated species or polymers, such as LiF, NaF, and KF. These fluorinated components are instrumental in building a robust and optimized SEI layer, essential for minimizing potential side reactions in the battery system. Additionally, the intrinsic characteristics of F-containing species, notably their high electron-withdrawing capacity, can significantly enhance the oxidation stability of electrolytes, especially at higher voltages. This property is particularly valuable for maintaining electrolyte integrity under elevated voltage conditions [137, 146, 147, 148]. FEC, in particular, has achieved commercial success as an electrolyte additive. Its effectiveness lies in its ability to reduce undesirable interactions between the electrolytes and electrodes, especially in micro-sized alloy anodes. Moreover, FEC plays a critical role in promoting the formation of a stable, F-rich SEI layer, contributing significantly to the overall performance and longevity of battery systems [127, 147, 149].

Electrolyte additives are crucial for enhancing the performance of micro-size alloy anodes in advanced battery systems. Their ability to stabilize, improve conductivity, and suppress unwanted reactions opens new avenues for high-efficiency, durable batteries. Ongoing research focusing on electrode material compatibility, cost-efficiency, and environmental impact is vital for harnessing the full potential of these energy storage technologies.

For high-capacity ion batteries, a robust chemical reaction accompanies their operation, producing a significant amount of heat that can potentially expedite thermal runaway [150]. This presents a safety hazard, given the flammable nature of the liquid electrolyte used. Traditional LIBs face a bottleneck in their operating voltage at $4.5V$ due to the decomposition of the electrolyte at higher voltages [151]. However, developing high-voltage batteries with wider electrochemical stability windows is crucial for future technological advancements. To address these issues, solid-state ion batteries (SSBs) employing solid-state electrolytes (SSEs)

with superior chemical stability, mechanical strength, and flame retardation hold significant promise. SSEs can prevent liquid leakage, mitigate the risk of fire due to high temperatures, and withstand higher temperatures than conventional electrolytes.

Additionally, higher temperatures can enhance SSE conductivity within a certain temperature range instead of posing a danger. Furthermore, it possesses an ultra-high mechanical strength that can effectively inhibit the growth of lithium dendrites. This enhances the safety of the entire battery system [152, 153]. Implementing solid-state electrolytes (SSE) in the battery design offers several advantages over traditional liquid-based systems. By eliminating the need for liquid substances and porous separators and replacing them with compact solid electrolytes, the battery design becomes less complex and more cost-effective. This shift also results in a reduction in the number of current collectors required for the cell stack. The use of SSBs results in significant increases in both volumetric and gravimetric energy densities. Furthermore, the manufacturing process of SSBs can be streamlined, with conventional procedures such as electrolyte wetting, formation, and aging being reduced or even eliminated, thereby reducing the time and cost associated with production [154].

In the course of developing solid electrolytes that exhibit superior electrochemical performance and stability, one encounters numerous challenges. The primary obstacles involve ensuring that the electrolyte possesses sufficient ion-transport capacity, which encompasses both ionic conductivity and ion transference number. Additionally, the electrolyte must exhibit satisfactory chemical/electrochemical stability and interfacial fusion ability.

H.S. Tan et al. [155] tapped into the interface stabilizing attributes of sulfide solid-state electrolytes to stabilize a non-carbon micro-size Si anode with an impressively high loading of 99.9 $wt.$ %. Compared to liquid electrolytes, sulfide solid-state electrolytes permit a 2D plane of interfacial contact between themselves and the porous micro-size Si anode, which can be preserved even after the material undergoes large-volume expansion. Furthermore, the absence of carbon in the micro-size anode curtails any pronounced decomposition of the SSE, leading to a marked surge in CE. The immediate ionic and electronic linkage between Li-Si

and micro-size Si paves the way for the Li-Si alloy phase to permeate the entire micro-size Si anode. The study underscored that sulfide SSE counteracts persistent interfacial expansion and the irreversible loss of lithium, culminating in a consistently stable SEI layer upon repeated cycling. Consequently, the carbon-free μSi||SSE||NCM811 full cell demonstrates remarkable reversibility even under severe temperature conditions, ranging from $-20°C$ to $80°C$, which indicates promising advancements in the field **[Figure 2.6]**.

Undeniably, the electrolyte stands out as a paramount component in battery systems. Its constituents, including anions, cations, solvents, additives, and even the concentration, exert intricate and profoundly impactful effects on the micro-structures, composition, and durability, as well as the mechanical and ionic transport characteristics of the SEI layer. To date, a myriad of strategies centered around electrolyte engineering have been put forth to craft a thin yet robust, high-quality SEI. These strategies encompass shifts from carbonate-based solvents to ether derivatives, judicious selection of salts, and modulation of concentration levels, ranging from conventional ($1M$) to elevated ($\geq\ 3M$) or even localized high concentrations and solid-state electrolytes. Despite these advances, the underlying mechanism remains elusive due to the lack of in-situ characterization tools to track micro-sized alloy anode's local structure and morphological changes during charge/discharge. For example, in-situ TEM, widely used to investigate the volume changes of nano-structured anodes, is not an ideal tool for characterizing micro-sized anodes due to resolution limitations. More importantly, how the larger volume change of micro-sized anode affects the resulting SEI and the consequent charge/discharge kinetics and reversibility are still open questions.

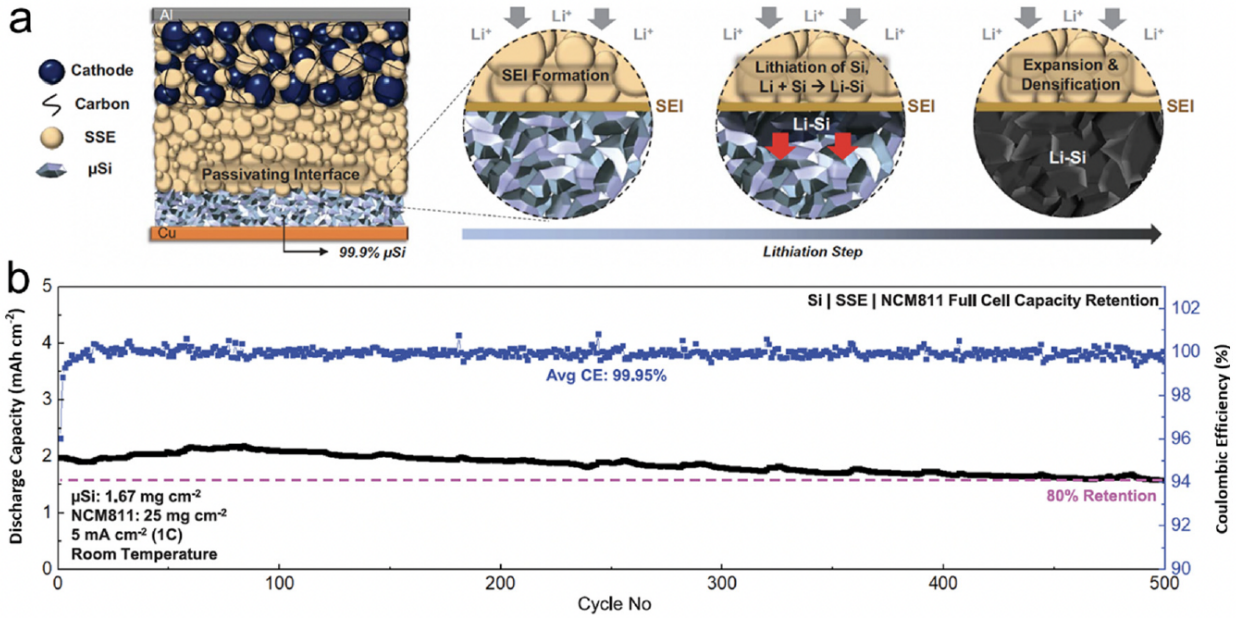

Figure 2.6: (a) Schematic of 99.9 wt % μSi electrode in an ASSB full cell. During lithiation, a passivating SEI is formed between the μSi and the SSE, followed by lithiation of μSi particles near the interface. The highly reactive Li-Si then reacts with Si particles within its vicinity. The reaction propagates throughout the electrode, forming a densified Li-Si layer. (b) Cycle life at room temperature. All cells were tested under similar charge and discharge conditions between 2.0 and 4.3 V. The first cycle voltage profile of each respective cell is plotted in black.(H.S. Tan et al. [155]).

2.2 Binders

In electrochemistry, the binder stands as a pivotal element within the electrode, acting as the unifying agent for active materials, conductive substances, and current collectors. Its importance cannot be overstated, as it is responsible for facilitating tight electrical connectivity among these components. Additionally, the binder adeptly handles volume expansion, ensures the structural coherence of alloy anode materials, and plays a key role in stabilizing the SEI throughout the cyclical operations [156]. According to research, binders can be classified into three categories based on their contact with anode materials: inert adhesion, hydrogen bonding, and covalent cross-linking.

Inert adhesion denotes a scenario where no chemical bond forms between the binder and the active material. Instead, the cohesive integrity of the entire electrode is preserved mechanically, primarily through the van der Waals force. Widely used binders in this context encompass poly(tetrafluoroethylene) (PTFE) and poly(vinylidene difluoride) (PVDF). Research has highlighted that microparticles tend to undergo pulverization due to volume alterations. Consequently, given their subpar mechanical attributes and weak bonding to micro-sized alloy anodes that experience substantial volume expansion, these binders might not be apt choices. In general, inert binders remain passive and do not engage in the SEI formation process [157].

Integrating hydrogen bonding in the adhesion process between the binder and alloy anode has proven superior compared to alternative techniques. Given the dominance of hydroxyl groups on alloy anode surfaces, binders like carboxymethyl cellulose (CMC), poly(acrylic acid) (PAA), and sodium alginate (SA), which are abundant in carboxylic acid groups, can innately form hydrogen bonds with the alloy anode surface. This naturally induced bonding mechanism promotes a more robust linkage between the binder and active materials. Simultaneously, it limits the exposure of the active material's surface area to electrolytes, setting the stage for the development of a resilient and optimized SEI.

The covalent bonding between the binder and anode is established through a chemical reaction between the binder's functional groups and the oxide layers present on anode alloys. This robust bond plays a pivotal role in preserving the electrode's structural integrity, minimizing the degradation of the electrical network throughout the cycling process. The outcome is impressive CE and consistent cycling performance. In contrast to passive binders, those containing functional groups significantly impact the formation of SEI and its spatial distribution and chemical composition. For example, binders like poly(vinyl alcohol) (PVA) [158], polyrotaxane-polyacrylic acid (PR-PAA) [159], and citric acid (CA) [160] have been shown to facilitate the creation of a stable and thin SEI on the surface of alloy anodes.

Binders that exhibit a diverse range of attributes, including pronounced elasticity, dual ionic and electronic conductivity, inherent self-healing mechanisms, and robust adhesive prowess, are highly favored among alloy anode users.

To enhance the self-healing properties of polymeric binders, Wang et al. [161] conducted research to develop a binder with a low glass transition temperature (T_g). The authors reported the formation of a self-healing polymer (SHP) with a low T_g value below $0°C$, which was achieved by controlling the reaction time. When the micro-size Si was expanded, the polymer layer experienced fracturing. Still, the viscous flow of SHP helped in the closure of the cracks through self-healing hydrogen bonding between the urea groups. This highly efficient self-healing property enabled the long-term cyclability of Si micro-particle (SIMP) anodes. In comparison with PVDF SiMP (14%), CMC-SiMP (27%), and Alg-SiMP (47%) after 20 cycles, the SiMP anode with 50 wt % Si delivered 2094 $mAhg^{-1}$ with a high retention of 80% at a current density of 400 mAg^{-1} after 90 cycles. The chemical structure and schematic representation of the self-healing working principle, as well as SEM images, are shown in **Figure 2.7**.

Choi et al. [159] have presented a novel strategy for retaining conductive pathways to whole micro-size Si particles while cycling, accomplished by a highly elastic binder layer that surrounds Si microparticles and prevents the pulverization of Si particles. In order

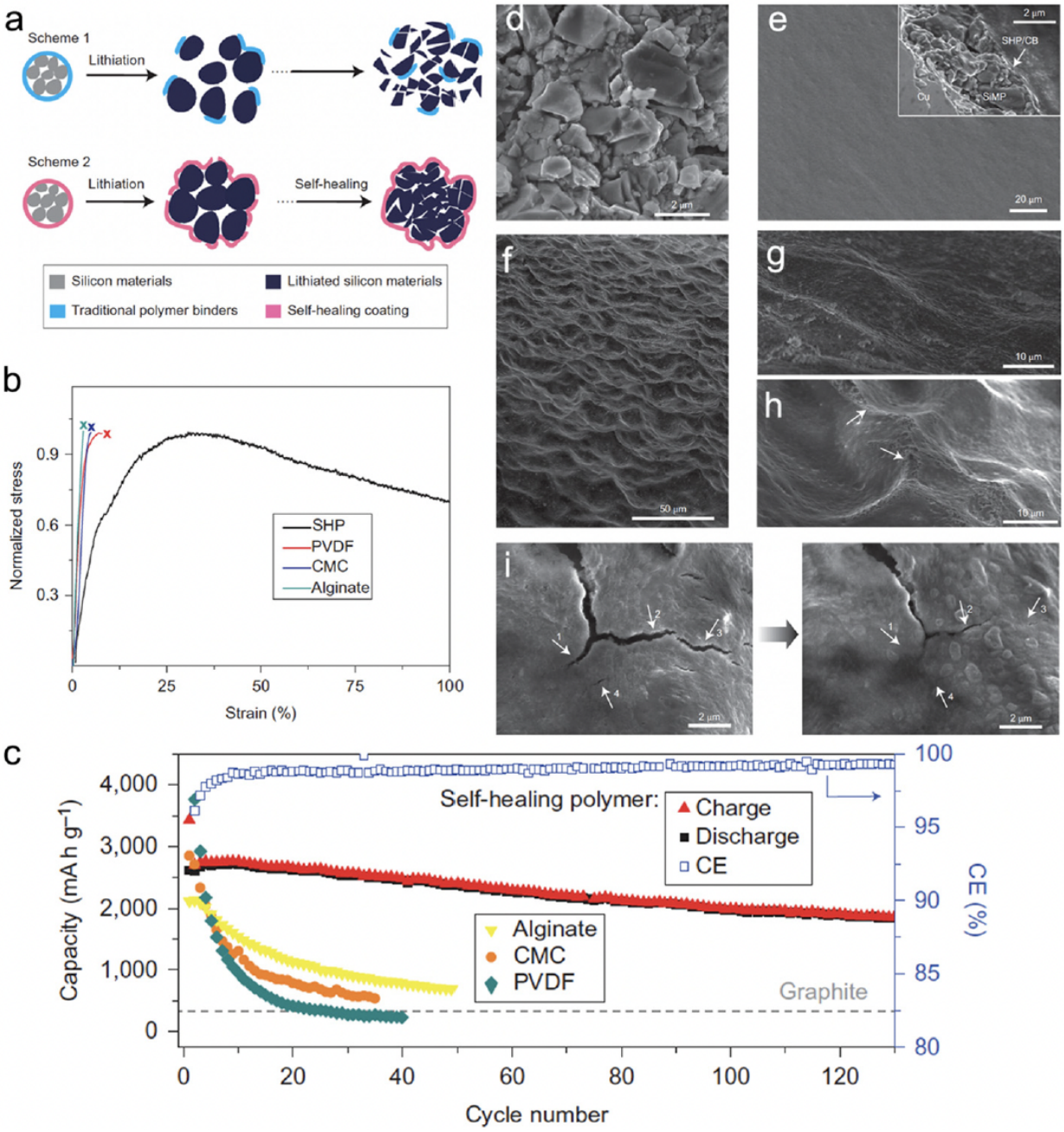

Figure 2.7: A) Schematic illustration of the design and behavior of silicon anode with conventional polymer binder and self-healing polymer (SHP) binder. B) Tensile tests of the SHP and other conventional polymer binders. C) Cyling performance of SiMP electrodes with different polymer binder at C/10 with a potential window of 0.01–1 V versus Li/Li^+. D) SEM image of bare SiMPs E) Surface morphology of the bare Simps electrode before cycling. Inset: cross-sectional SEM image of the electrode. F) low and G) high magnification SEM images of the bare SiMPs electrode after 20 cycles at a rate of C/10. H) Some scare-like structures (arrows) can be found on the electrode after cycling process, which appear to be cracks that subsequently healef. I) Left: cracks in the polymer layer in the lithiated state; Right: after 5h the smaller cracks were healed, uneducated by the arrows on the images. (Wang et al. [161]).

to withstand the mechanical stress caused by Si expansion, the binder must be capable of enduring this continuous stress. They were inspired by the working principle behind moving pulleys, which distribute and equalize localized forces to significantly reduce the tension in the rope. To achieve this principle on a molecular level, they constructed a molecular pulley binder (PR–PAA) by covalently attaching PAA to the ring components of polyrotaxane (PR), as shown in **Figure 2.8**. The stress applied to the polymer is significantly reduced by ring sliding, consistent with the principle of moving pulleys, rendering PR-PAA highly elastic. These unique properties arise from the topological crosslinking between PAA and PR through the ring molecules, which are neither fixed nor dissociated. To examine the mechanical properties of PR–PAA, tensile tests were conducted. During repeated stretch-recovery cycles, the PR-PAA exhibited high elasticity, with a percentage of 390%. Additionally, it displayed less strain hysteresis, indicating its superior performance. The PR-PAA binder was explicitly designed to prevent the disintegration of pulverized Si particles. The effective stabilization of the SEI layer curtailed its recurrent growth, leading to an improved CE and consistent cycling performance at capacities typical of commercial standards. With the employment of the highly elastic PR-PAA binder, the micro-size Si anode showcased a mere 12.1 μm alteration in thickness following ten cycles. In comparison, an anode employing the standard PAA binder underwent a thickness modification of 22.8 μm. This comparison underscores the superior efficacy of high-elasticity binders relative to their traditional PAA counterparts.

In electrochemistry, the stabilizing electrode and SEI layer are crucial for the performance of energy storage devices. The stabilizing electrode ensures the stability of the electrode-electrolyte interface by impeding the dissolution of active material during the charge-discharge process. On the other hand, the SEI layer acts as a protective layer that forms on the electrode's surface and mitigates the electrolyte's reactivity with the electrode material. Both the stabilizing electrode and SEI layer are critical components that are fundamental to the overall performance and longevity of energy storage devices. This discussion elucidates the significant role that binders can play in enhancing the electrochemical effectiveness of ion

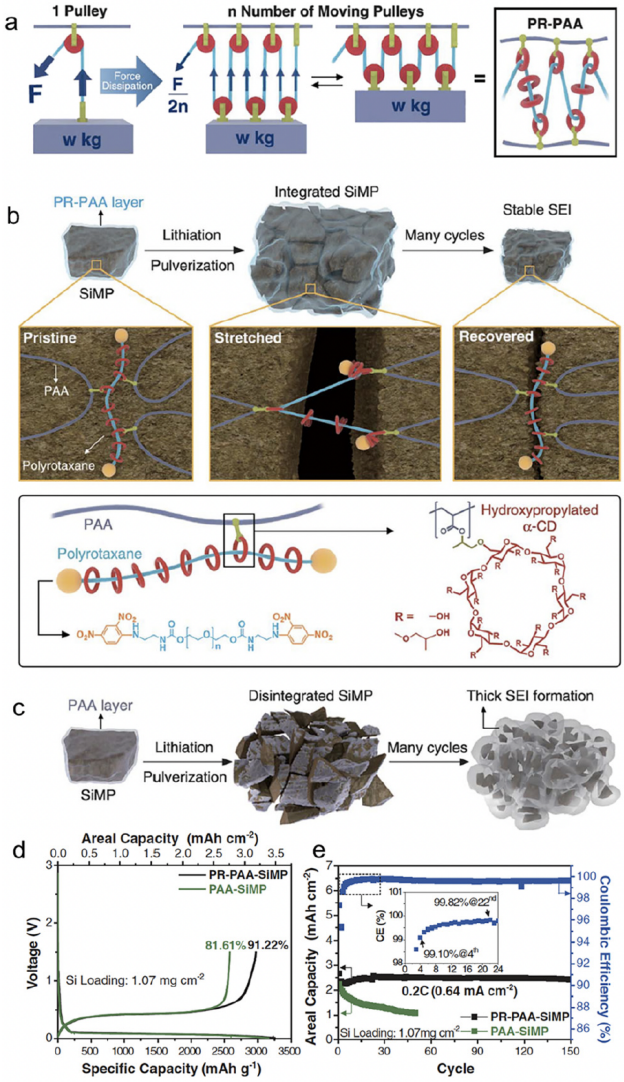

Figure 2.8: A) Proposed stress dissipation mechanism of PR-PAA binder for SiMP anodes. (B) Graphical representation of the operation of PR-PAA binder to dissipate the stress during repeated volume changes of SiMPs, together with chemical structures of polyrotaxane and PAA. (C) Schematic illustration of the pulverization of the PAA-SiMP electrode during cycling and its consequent SEI layer growth. Electrochemical performances of SiMP electrodes incorporating PR-PAA and PAA as binders. (D) The initial charge-discharge profiles of the PR-PAA–SiMP and PAA-SiMP electrodes when measured at 0.033 C (100 mAg^{-1}). (E) Discharging capacity retentions of both electrodes when measured at 0.2 C (600 mAg^{-1}), along with the Coulombic efficiencies of the PR-PAA–SiMP electrode. (Inset) Magnified view of the Coulombic efficiencies in the first 24 cycles. Si loading, 1.07 $mg.cm^{-2}$. (Choi et al. [159]).

batteries. It is important to note that a trade-off always exists when selecting a binder and additive, as it can either lead to higher capacities with poor retention or lower capacities with higher retention. As such, discovering new and improved binders and additives is a promising and captivating field for new energy sector researchers.

Additionally, exploring the possible combinations of binders with various electrolytes presents a hot spot for introducing innovative chemistries and augmenting the electrochemical performance of LIB/SIB. Numerous studies have been conducted to investigate multiple polymers, focusing on their chemical bonds, mechanical properties, supramolecular interactions, and electrochemical properties. However, these studies are sporadic and often specific to a particular case, making it challenging to establish a comprehensive design principle for polymeric binders for micro-size alloy anodes. Binder research must delve into in-situ analyses to enhance our comprehension of the dynamic physicochemical processes involved in electrode components. By employing such studies, researchers can gain a more nuanced understanding of these processes, much like the approach taken in organic reaction mechanisms. Aiming to establish an in-depth mechanistic understanding of these dynamic processes is therefore imperative.

2.3 Morphology and structure

Architectural engineering stands as a powerful method for meticulously adjusting the physicochemical attributes of electrodes, consequently boosting their electrochemical prowess. Techniques like particle size reduction, interfacial property modification, and lattice chemistry tuning can finetune ionic and electronic conductivities, reaction energy barriers, and the electrochemical responses of electrode materials. The incorporation of intricate structures proves advantageous in modulating stress generation, distribution, and the mechanical characteristics of electrode films, resulting in unmatched structural integrity. Given this context, employing structural methodologies becomes especially pertinent for alloying anodes. These anodes undergo more pronounced volume expansion compared to insertion or conversion materials. There has been a fervent dedication to developing a wide range of material and electrode structures to counteract volume expansion challenges. This dedication has yielded notable improvements in amplifying the electrochemical performance of alloying material in both LIBs and SIBs. Theoretically, volume expansion challenges can be approached in a dual-faceted manner: one, by averting material or electrode fragmentation, and two, by preserving unbroken electrical connections amidst the fragmented sections.

To facilitate reversible (de)lithiation/ (de)sodiation in alloying anode materials, researchers have implemented various nano- and microscale structures and morphologies [90, 91, 92, 162, 26]. These methods, which may involve pure alloying elements or composite materials, typically aim to augment the surface-to-volume ratio (SVR) of the anode's morphology. By amplifying the SVR, the slope of concentration and stress-strain gradients during lithiation can be substantially reduced due to the decreased required lengths and the decreased influence of solid-state lithium/sodium diffusion on the overall process. Additionally, increasing SVR concurrently enhances the rate of lithiation/sodiation and the maximum (dis)charging power available in the anode.

While these procedures are implemented for specific alloying materials, they can be

extrapolated to other alloying materials, given their comparable characteristics.

In order to fully utilize the potential capacity of pure alloying anode materials, which tend to crack and break apart during lithiation, innovative methods must be employed to accommodate their large volume changes. One such method is the creation of composite materials, which can significantly decrease overall volume changes, minimize stress gradients, and enhance performance characteristics such as power and capacity. Composite materials provide an array of fabrication options and performance capabilities, as they allow for the selection of multiple elements and materials in a single anode. An active alloying material can be combined with one or more matrix materials in an ideal composite to manage the volume change and prevent plastic deformation and fracturing. This strategy is particularly attractive for alloying anodes, as it provides a broader range of options for fabrication techniques and available properties [163, 164, 165]. For an ideal matrix material, both electrical and ionic conductivity are necessary to enhance lithiation uniformity and optimize the maximum power capabilities. Additionally, the material must possess a superior yield or fracture strength and low stiffness to accommodate the volume expansion caused by lithiation/sodiation to the fullest extent possible. Various materials and combinations can meet these requirements, and these composites can generally be categorized into two groups: active-inactive and active-active composites. Active-active composites refer to composite materials in which all or the majority of the phases present in the anode participate in (de)lithiation/(de)sodiation during cycling and contribute to the overall capacity of the anode. Unlike active-inactive composites, active-active composites do not suffer the same decreases in gravimetric or volumetric capacity as the volume of inactive phases has been reduced or eliminated. It is noteworthy that all materials undergo (de)lithiation/(de)sodiation during cycling, but ideally, these processes do not happen in the same voltage window [166].

In the academic literature, an alternative methodology for fabricating active-active composites has been explored [167, 168, 169]. This approach involves adding an alloying component, for example, silicon, with graphene, a material that does not undergo notable volume fluc-

tuations during (de)lithiation. Graphene possesses remarkable electrical conductivity and mechanical characteristics that aid in the uniform and regulated performance of the composite.

The process of lithiation of alloying anode elements, such as silicon, has been a focus of research due to its high lithiation capacity. This capacity is estimated at approximately 740 $mAh.g^{-1}$, making it a promising candidate for developing high-capacity, high-power, and durable batteries. To address the issue of volume changes during (de)lithiation, graphene has been utilized to create a stable SEI between silicon and the electrolyte. This SEI stabilizes the battery's capacity by preventing the continual re-formation of the SEI during the volume changes. Additionally, the use of graphene or other lithiating and conductive agents has shown potential in developing high-performance composite anode designs [170, 171].

Incorporating both approaches, architectural and material composites, is a logical way for a rational electrode material design. Li et al. [172] unveiled a technique to envelop Si microparticles, ranging from 1–3 μm, with meticulously fabricated cages composed of multiple graphene layers. This graphene enclosure serves as a robust yet flexible shield during intensive galvanostatic cycling. Such a design permits the micro-particles to swell and break apart within the confines of the cage, all while ensuring electrical connectivity at both the individual particle and overarching electrode scales. Additionally, the chemically passive nature of the graphene cage fosters a stable SEI. This stability curtails the non-recoverable consumption of Li-ions, leading to a swift augmentation in CE during the initial cycles. Electrochemical data from the half-cell reveals an estimable reversible capacity of $3,300\ mAh.g^{-1}$ when subjected to a current density of C/20 (with 1C equating to 4.2 Ag^{-1}). This impressive capacity signals that the active materials maintain robust electrical connections and actively participate in both the charge and discharge processes. Notably, this achievement is accomplished devoid of any conductive additives, underscoring the good electrical conductivity intrinsic to the graphene cage. When subjected to rigorous full-cell electrochemical testing, where stable cycling demands are elevated, the graphene-encaged Si microparticles consistently perform, showcasing stable cycling over 100 cycles with a retention of 90% of its capacity **[Figure**

2.9].

One of the main challenges in designing high-capacity anode material is to combine CE, cycling stability, and volume change. Xu et al. [173] prepared nano/micro-structured Si/C composites. Their strategy focused on minimizing the specific surface area while boosting the tap density of Si/C composite by controlling the average size of micro-particles. With a judicious selection of particle size, a minimized specific surface area, and a refined structure, they managed to achieve an outstanding initial CE of 91.2%. Further testifying to their design's efficacy, these nano/micro-structured Si/C anodes showcased remarkable cycling stability, retaining a significant 96.5% of their capacity post 100 cycles, all while being subjected to a current density of 0.2 Ag^{-1} **[Figure 2.10]**.

Micro-sized 2D layered and 3D porous structural electrodes, such as 3D macro-porous Si [174], meso-porous Si [175], nano-porous Si [176], and layered porous Si@CNT [177], have been widely documented. These configurations, endowed with appropriate void or pore spaces, exhibit enhanced capabilities to manage volume fluctuations. Such designs effectively limit the damage to or growth of the SEI layer. Furthermore, they amplify the electrochemical reaction kinetics during the alloying and dealloying phases, all the while upholding a substantial tap density. Additionally, these structures offer the advantage of reducing the contact surface with the electrolytes, further optimizing performance.

Nano-structured silicon in various architectural designs has demonstrated promising results in battery performance, although its implementation in industrial production poses a significant challenge. This is due to the current limitation in the ratio of silicon in graphite as an anode, which currently stands at less than 5 $wt\%$. Lv et al. [178] have presented a scalable approach to the synthesis of a large silicon cage composite, with a size measured in micrometers, which is composed of an ultrathin (<5 nm) mesoporous polypyrrole (PPy) skin and a silicon skeleton using a straightforward wet-chemical technique. They sourced the industrial-grade AlSi alloy as the precursor. The hollow skeleton framework offers generous room to manage the notable volume shifts during cycling. Simultaneously, the conductive

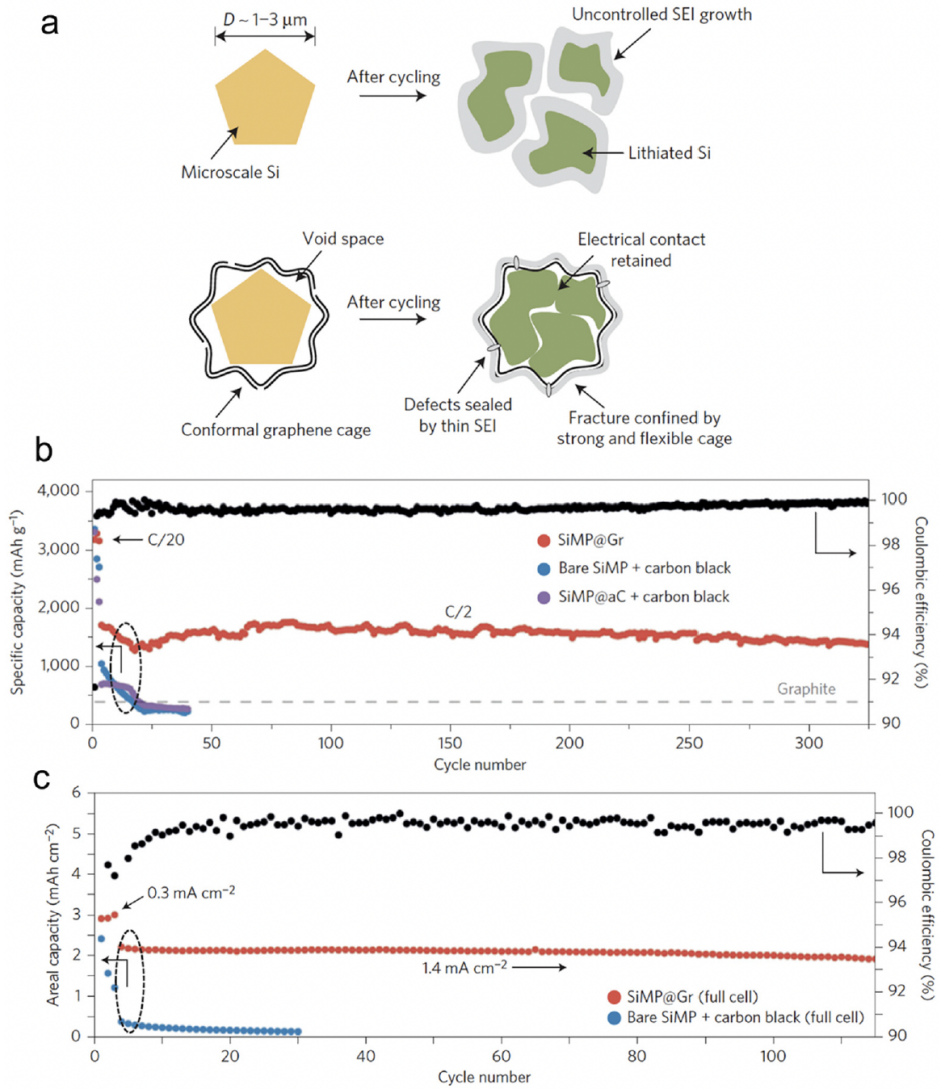

Figure 2.9: (a) Morphology and structural evolution of Si microparticles without and with graphene cage encapsulation during cycling; (b) cycling performance of bare SiMP with conductive carbon additive, amorphous-carbon-coated SiMP with conductive carbon additive, and SiMP@Gr with no conductive additives (the mass loading was 0.8 $mg.cm^{-2}$); (c) cycling performance of bare SiMP with conductive carbon additive and SiMP@Gr (2.0 mg) with no conductive additives when paired with a traditional lithium cobalt oxide cathode. (Li et al. [172]).

Table 1. Comparison of the properties of Si/C composites.

Samples	Average diameter [μm]	SSA [$m^2 g^{-1}$]	Tap density [$g cm^{-3}$]	Initial CE [%]
Si/C-2	6.69	40.8	0.65	80.3
Si/C-3	8.47	98.2	0.53	76.9
Si/C-4	9.42	22.8	0.72	86.9
Si/C-1	15.3	10.5	0.81	91.2

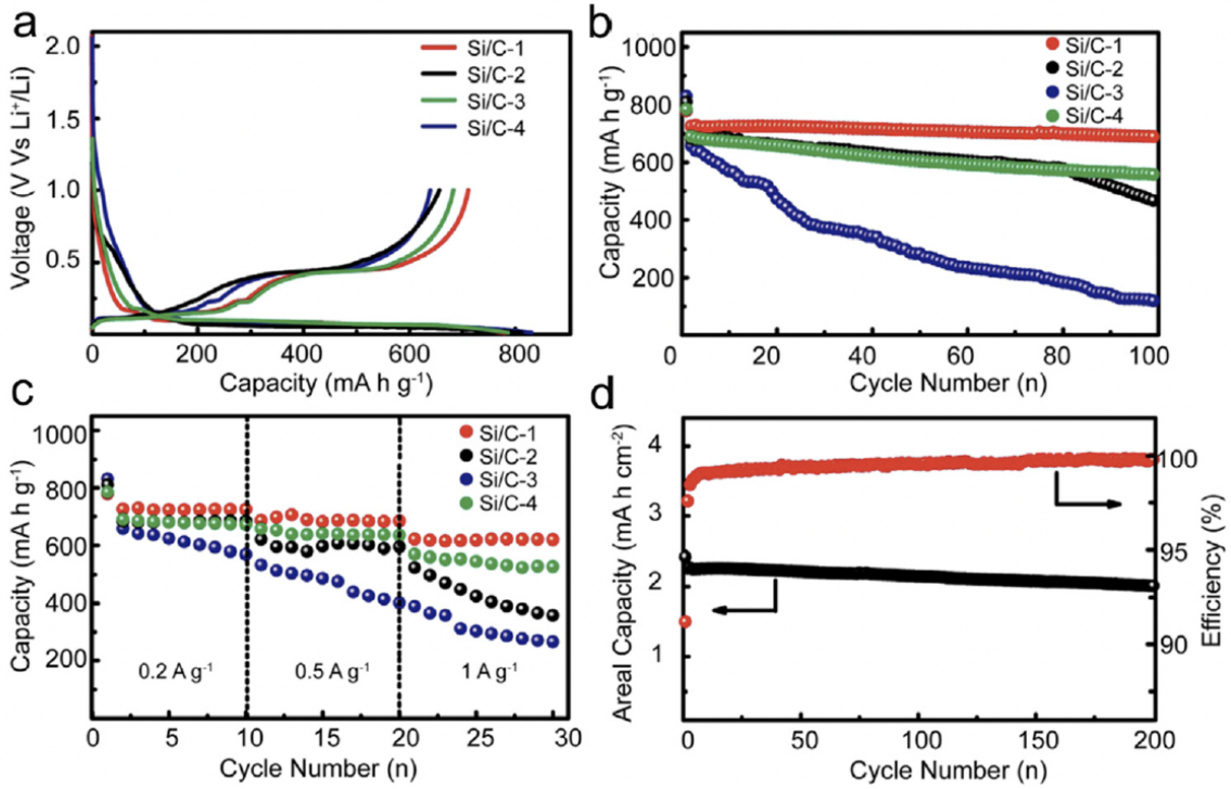

Figure 2.10: (a) The first charge and discharge profiles. (b) The cycling stability of different Si/C anodes. (c) Rate capability of different Si/C anodes. (d) High areal mass loading test and Coulombic efficiency of the Si/C-1 anode. (Xu et al. [173]).

polymer acts both as a safeguard and a fast channel for Li^+/e^- movement. Batteries equipped with these micro-sized silicon cages showcased impressive capacity retention across prolonged cycling at elevated charge/discharge rates and high material loadings. At a 0.2 C rate, the battery delivered a specific capacity close to 1660 $mAh.g^{-1}$. Furthermore, its CE hovered around an impressive 99.8% even after 500 cycles at a material loading of 3 $mg.cm^{-2}$. When further charged at 1 C, a remarkable capacity of 1149 $mAh.g^{-1}$ was preserved even after 500 cycles despite the high loading of silicon. This outcome affirms the battery's potential to power large electrical devices, such as electric vehicles, owing to its high energy density **[Figure 2.11]**.

The transport properties of (Li/Na-ions) within a battery are significantly impacted by morphology and structure. These properties subsequently determine the battery's charge/discharge rates and overall power delivery. One of the essential aspects dictating the charge/discharge rate of LIB/SIB is the combination of the ion diffusion coefficient and diffusion length. Zhao et al. [179] have shed light on how, in an amorphous Si/C multilayer electrode, the silicon-carbon (Si-C) junctions play a pivotal role in facilitating the movement of Li-ions. This facilitation occurs in both directions - perpendicular and parallel to the Si-C interfaces, especially after the electrode undergoes cracking. To realize high-performing LIB anodes, Zhao's group introduced a design strategy characterized by a micro-size hierarchical multilayer block. This approach emphasizes the precise stacking thickness of amorphous Si and carbon. Consequently, the Si/C film anode is formed through the alternating layering of amorphous Si and carbon, with optimal thickness and volume proportion. This layering leads to consistent cracking patterns and the stable formation of the SEI. Impressively, this electrode design reached a significant specific capacity of 2729 $mAh.g^{-1}$. Even after 200 cycles, it retained a capacity that was equivalent to 102.1% of its initial lithiation capacity and 101.8% of its theoretical specific capacity. The strategy hinges on exploiting the stress induced by volume alterations to segment the multilayer Si/C into micro-sized, multilayered hierarchical blocks. Such an approach notably amplifies the electrochemical performance,

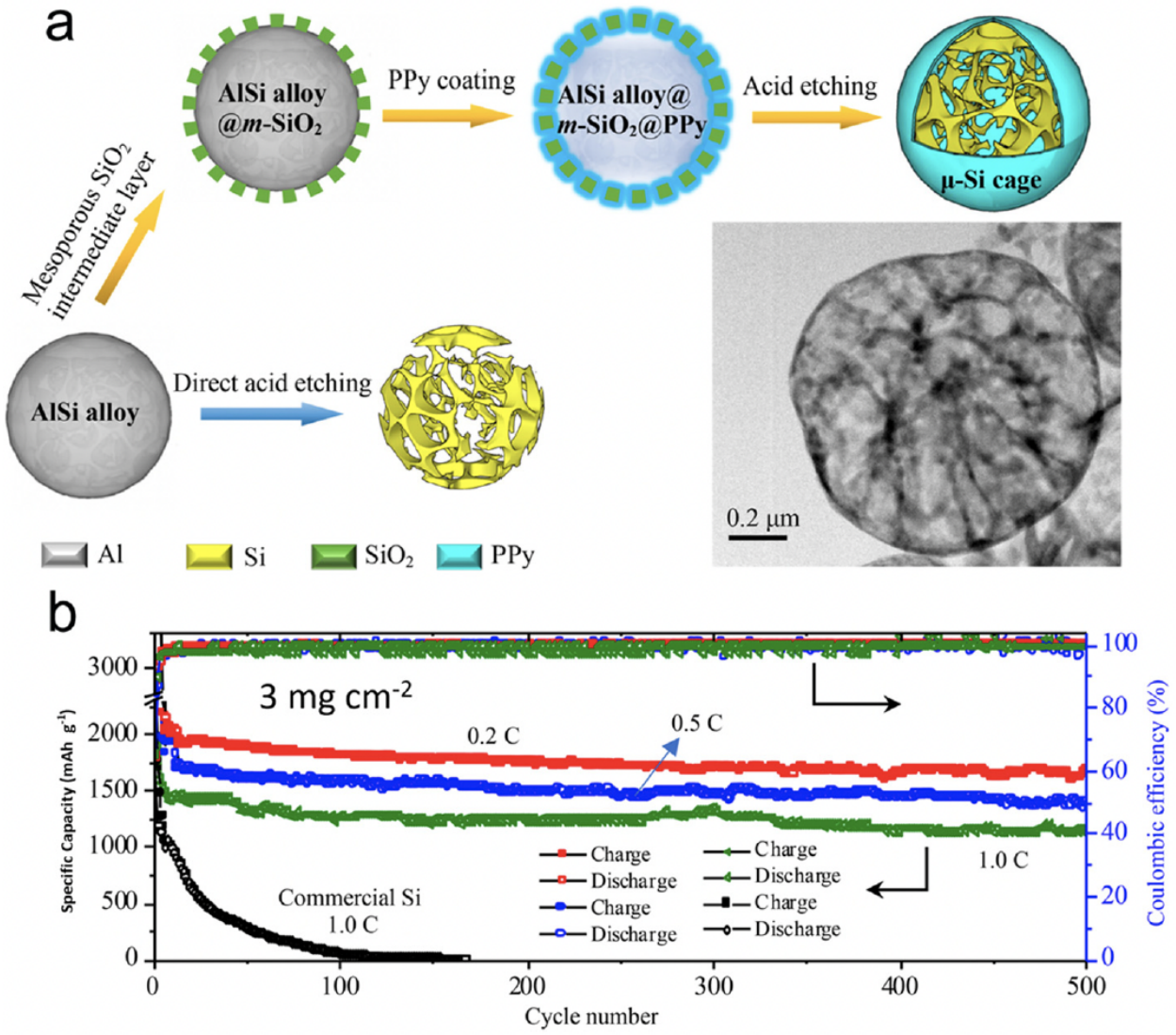

Figure 2.11: A) Scalable synthesis of the μ-Si cage using AlSi microspheres as precursor by a chemical method. Synthetic illustration and TEM morphology (inset) of the μ-Si cage. B) Cycling performance of the battery with a μ-Si cage as anode with loadings of 3 $mg.cm^{-2}$. (Lv et al. [178]).

drawing significant advantages from the Si-C interfaces. While traditionally, the focus has been on confining volume alterations using an inert buffer coating, this research suggests another avenue. It underscores that maintaining impeccable contact between the buffer layer and the active material is crucial. By doing so, it's possible to fully harness the performance of the active material, particularly by amplifying Li-ion diffusion kinetics via these heterointerfaces **[Figure 2.12]**.

Employing a structure that incorporates both primary and secondary particles offers insightful benefits, particularly in managing the mechanical strain resulting from the significant volume changes of high-capacity alloy anodes during continuous cycling. A recent study led by Liu et al. [58] showcased the development of a hierarchical micro/nano-structured Sb-doped P_{red}/KB-MWCNTs anode tailored for SIBs. Both theoretical analyses and practical experiments harmoniously indicated that this Sb-doped P_{red}/KB-MWCNTs anode adeptly managed mechanical stresses and effectively hindered unwanted decomposition of the electrolytes. Notably, the Sb-doped P_{red}/KB-MWCNTs anodes, when placed in traditional carbonate (1 M $NaPF_6$-PC with 2% FEC) and localized high concentration (1.2 M NaFSIDME/BTFE) electrolytes, exhibited similar ICE and cycling stability. This finding underscores the pivotal role played by the anode's structural configuration. Moreover, when juxtaposed with P_{red}/C30, X-ray photoelectron spectroscopy (XPS) analyses revealed that the Sb-doped P_{red}/KB-MWCNTs, regardless of the electrolyte type, could foster the formation of a thin, robust, and fluorine-rich SEI layer by controlling the electrolyte decomposition **[Figure 2.13]**.

The use of porous micro-scale materials, specifically those composed of nano-blocks and nano-pores, has garnered significant interest in recent times [180]. Their popularity can be attributed to several reasons:

1. **Volume Accommodation:** Alloys designed with adjustable pore sizes and porosities can adeptly handle volume changes during the lithiation/sodiation process. This capability minimizes particle-level volume expansion, which in turn restricts electrode swelling and the subsequent detachment of active elements from the current collector.

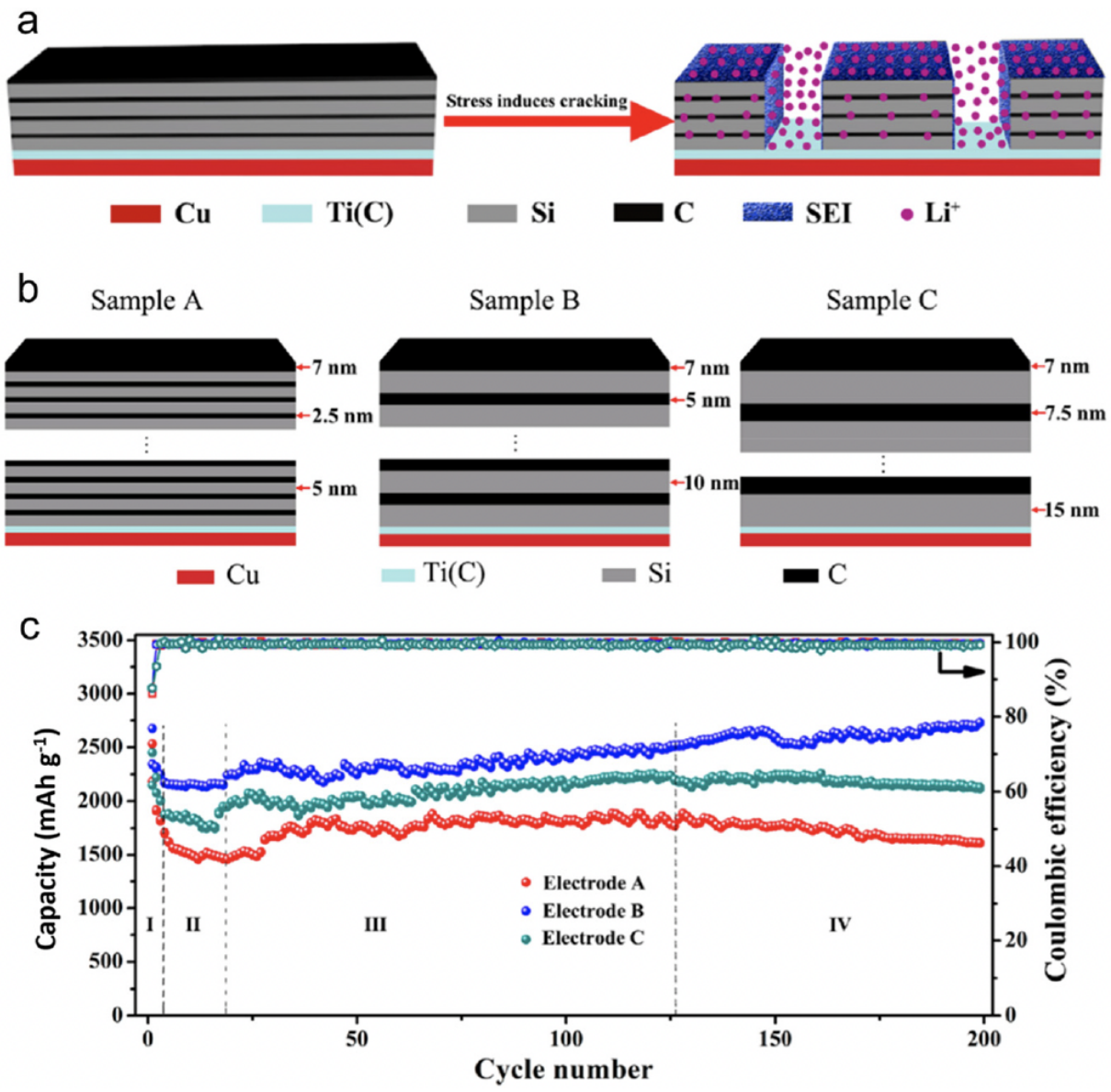

Figure 2.12: A) Schematic illustration of Si/C multilayer blocks formed by stress. B) Schematic illustration of Si/C multilayer films structure. C) Cycling performance of electrodes A, B, and C at a current density of 300 $mA.g^{-1}$. (Zhao et al. [179]).

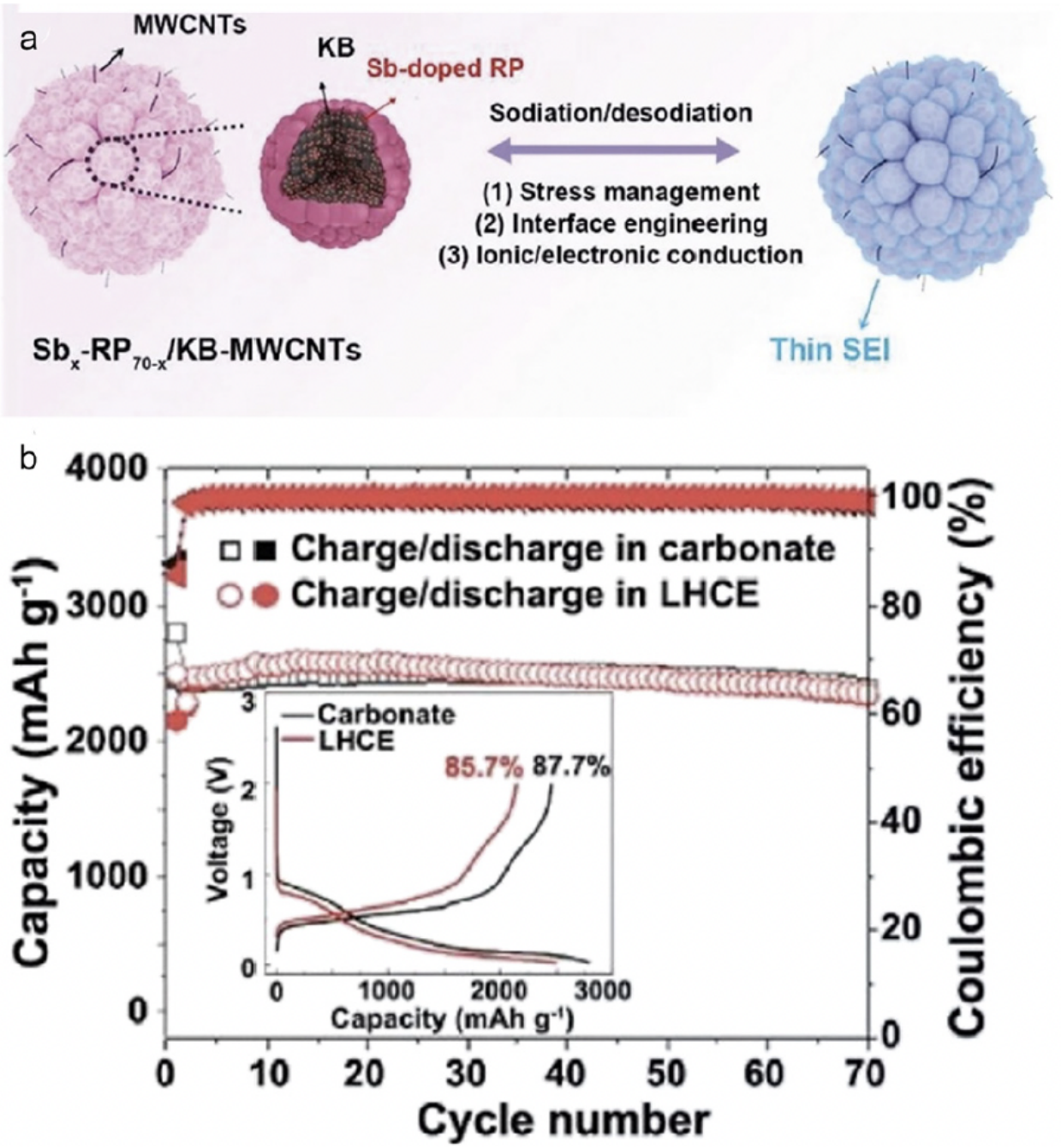

Figure 2.13: a) Schematic illustration and b) cycling performance in carbonate and ether-based electrolytes of hierarchical micro/nanostructured $Sb_x - RP_{70-x}$/KB-MWCNTs. (Liu et al. [58]).

2. **Enhanced Kinetics:** The porous nature of these materials promotes deeper infiltration of the electrolyte, trims down the distance required for ion/electron transfer, and reduces internal impedance. Collectively, these factors lead to improved kinetic performance of the materials.

3. **High Tap Density and Specific BET Surface Area:** These materials exhibit a notable tap density and a reduced specific BET surface area. Such attributes culminate in elevated ICE, mass loading, and energy density. Moreover, their 3D design facilitates electrolyte permeation, endowing the materials with exceptional mass transfer capabilities. This makes them particularly apt for applications even when there's a high mass loading of active components.

4. **Increased Active Sites:** The intricate network of interconnected pores within these materials provides additional active sites for reactions, which amplifies their capacity.

In essence, when considering the performance metrics, porous micro-scale alloys encompassing nano-particles distinctly outshine their counterparts that are solely nano- or micro-scale in design, especially in the context of Lithium-Ion Batteries (LIBs) and Sodium-Ion Batteries (SIBs) [48].

Electrode materials can benefit from the formation of pores, which can improve their electrochemical properties. Nevertheless, the straightforward synthesis of porous structures, particularly in materials like Sn, presents substantial obstacles. This is largely due to Sn's inherent low melting point combined with the inevitable electrochemical agglomeration it undergoes. Song et al. [181] tackled this challenge by fabricating 3D continuous micro-scale Sn with a porous structure from immiscible Al-Sn alloys. Impressively, the resultant micro-porous Sn anode showcased a high initial capacity, measuring 818 $mAh.g^{-1}$, and a commendable CE of 99%. Additionally, the structural integrity of the porous Sn was retained post the inaugural cycle, indicating its potential suitability as an anode in LIBs. Nevertheless, the

as-dealloyed porous Sn still falls short in terms of ductility and strength, leading to a short cycle life. In other words, the porous Sn structures produced through dealloying are unable to sufficiently buffer the strain during lithiation/delithiation for extended cycle life **[Figure 2.14]**.

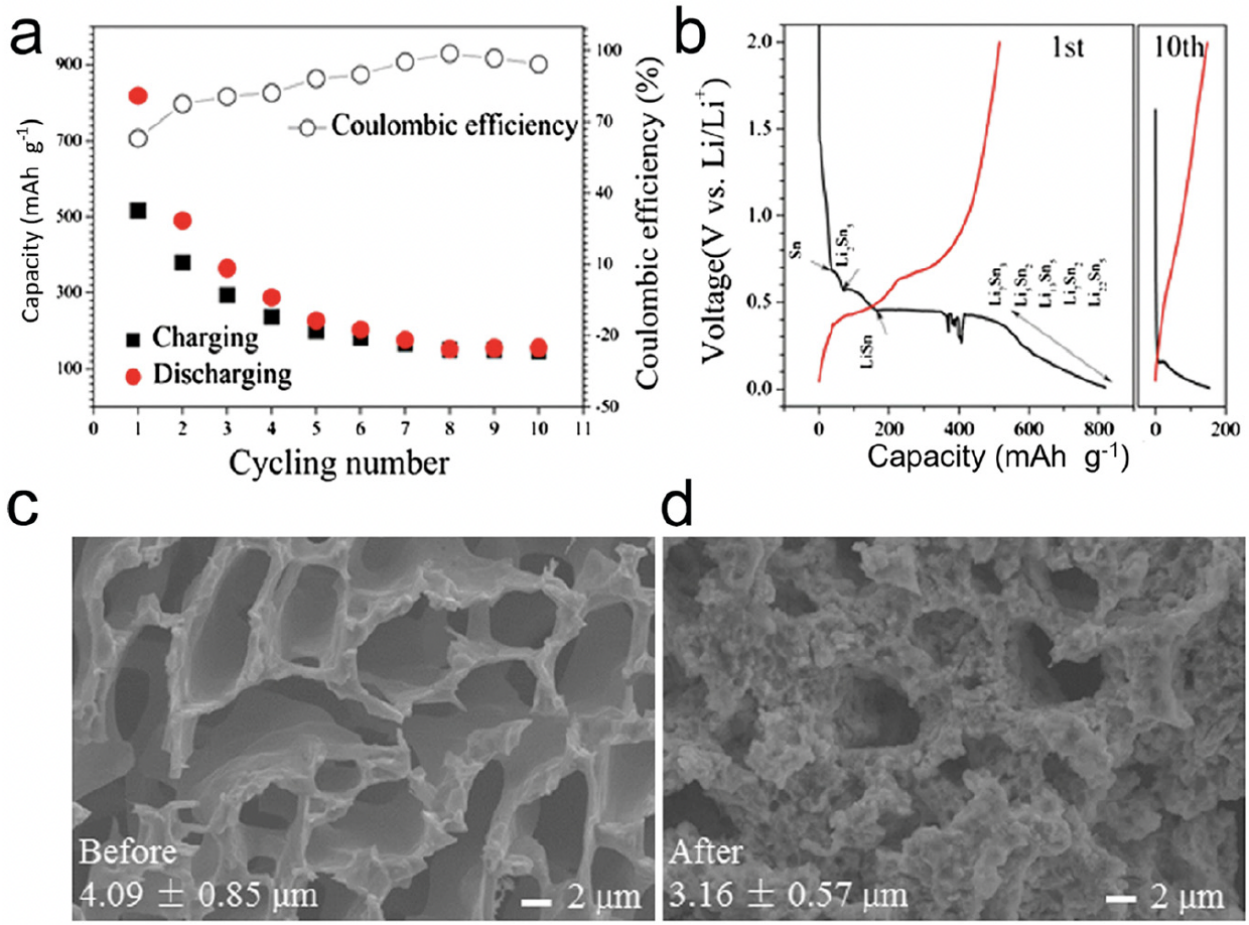

Figure 2.14: (a) Cycling performance and (b) charge/discharge curve of the porous Sn dealloyed from $Al_{80}Sn_{20}$; SEM images of the porous Sn structure before (c) and after (d) the lithiation/delithiation process. (Song et al. [181]).

2.4 Conclusion and outlook

In summary, we have reviewed recent progress on the development of micro-sized alloy anode for alkali-ion batteries through the engineering of electrolytes, binders, and electrode architecture.

The quest for effective and economically viable synthesis techniques for electrode materials continues to be at the forefront of contemporary research in battery technology. A plethora of alloying anodes have showcased impressive cycling stabilities when tested in half cells. However, a select few have managed to achieve the remarkable Coulombic Efficiency (CE) that is indispensable for their integration into full cells.

An inherent challenge lies in their specific capacity. While these anodes possess a commendable specific capacity, their constrained areal capacity might pose a hindrance, especially when one envisages aligning it with the potentially elevated areal capacities of future cathodes.

The creation of micro-scale active materials that combine a high tap density with exceptional performance in LIBs and SIBs presents its own set of challenges. Beyond the technical aspects of material development, there's a broader perspective to consider. For these alloying-type materials to transition from the laboratory to commercial applications, certain prerequisites need to be met.

The continuous quest for higher energy density, improved safety, and cost-effectiveness drives innovations in LIB technology. In this regard, micro/nanostructured alloy anodes represent a significant leap forward. These anodes offer substantial improvements over conventional graphite anodes, particularly in energy density, cycling stability, and life span, which are crucial for applications ranging from consumer electronics to electric vehicles. Silicon, tin, and their carbon composites exhibit dramatically higher specific capacities than traditional anodes. This translates into batteries that can store more energy without a proportional increase in size or weight, a critical factor for industrial applications where space

and weight efficiency are paramount. While the raw material costs for these alloys might be higher, the enhanced energy density means that a smaller amount of active material is required for the same energy output, potentially lowering the overall material cost per kWh of capacity.

The production of micro/nanostructured alloy anodes has become increasingly viable with advancements in battery manufacturing technology. Techniques like electrospinning, chemical vapor deposition, sol–gel processes, and high-energy ball milling enable precise control over the structure of the anode material, leading to better performance and consistency. Importantly, these techniques are scalable and can be integrated into existing battery production lines. This integration is crucial for industrial-scale production, allowing battery manufacturers to adopt these advanced materials without requiring extensive overhauls of current manufacturing facilities. For industrial applications, the longevity and reliability of energy storage systems are as important as their initial costs. These anode materials offer improved cycling stability and are less prone to capacity fade over time than traditional anodes. This longer lifespan of the batteries translates into reduced operational costs as the need for frequent replacements diminishes. Additionally, the enhanced cycle life of these batteries means less downtime and maintenance, which is vital for industrial operations where continuous power is essential. Moreover, the increased energy density of these anodes can lead to smaller and lighter batteries, which is advantageous in terms of material use and logistics, further driving down costs.

Adopting these alloy anodes can also contribute to broader economic and environmental sustainability goals. By improving the efficiency and life span of batteries, these anodes can facilitate a more robust adoption of renewable energy sources in industrial settings, promoting a shift towards greener energy practices. Furthermore, the enhanced battery performance can lead to reductions in waste and a decrease in the environmental footprint of industrial operations, aligning with global efforts toward sustainability.

It's essential to adopt synthesis procedures that are not only efficient but also straight-

forward. The choice of chemicals used should lean towards those that are cost-effective and environmentally benign. Additionally, the synthesis methods should be capable of producing these materials at a scale and yield that aligns with commercial production demands. In essence, the pathway to commercializing these promising materials entails a balanced amalgamation of performance metrics, sustainable practices, and economic viability.

Chapter 3

Research Objectives

In light of the identified research gap from the preceding literature review, the dissertation proposes the following objectives to address the central question of how to mitigate volume change during cycling, thereby ensuring structural stability, enhanced performance, and safety for alloy anodes in alkali-ion battery systems: **[Figure 3.1]**

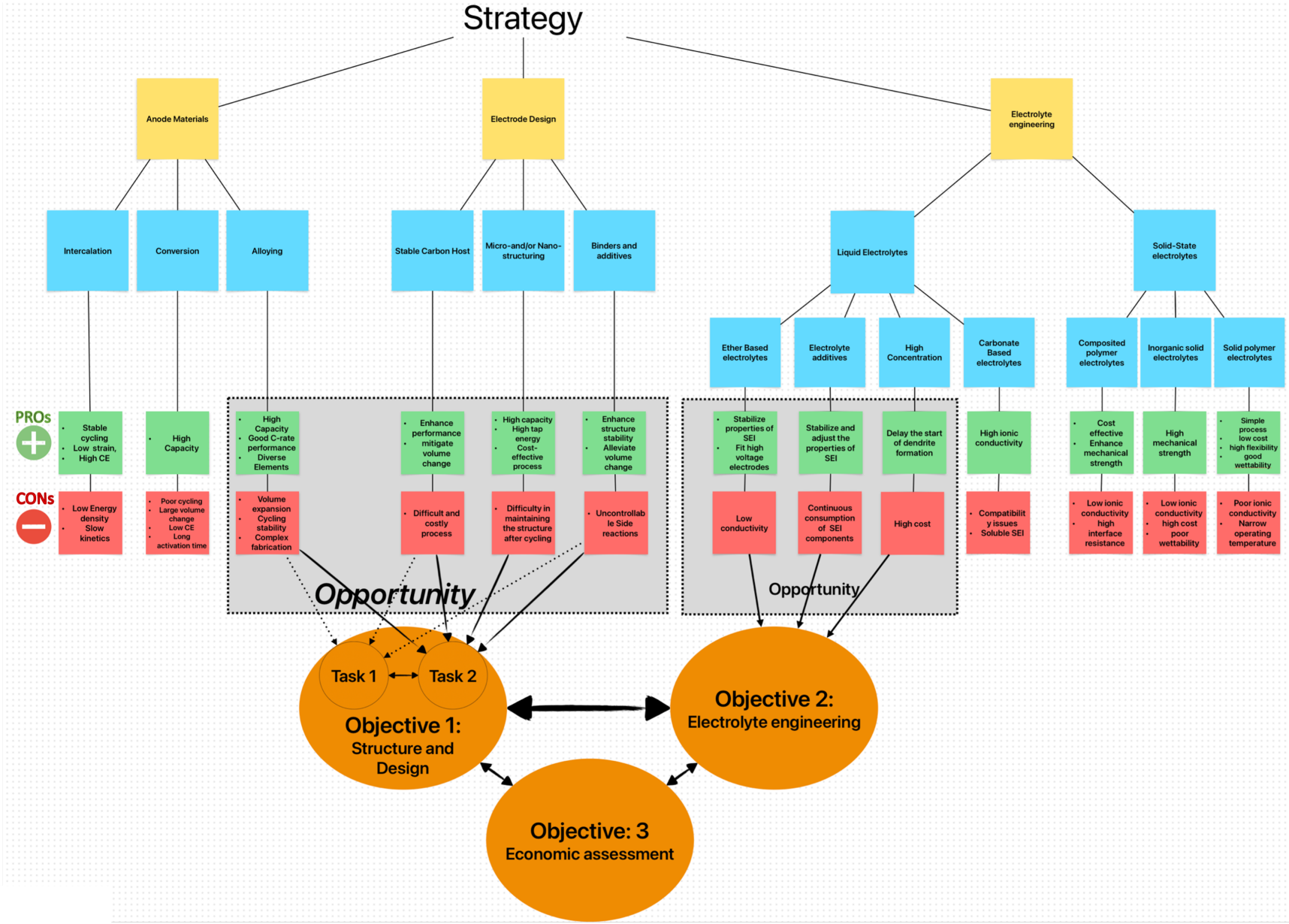

Figure 3.1: Thesis strategy.

3.1 Objective 1:

Investigation and Characterization of Micro-Sized Anode Materials in High-Energy Alkali-Ion Batteries:

Task 1: Tailoring the structures and compositions of alloy anode materials for high-energy and long-life alkali-ion batteries.

Discussion:

As mentioned in the 3^{rd} section of the 1^{st} chapter, this research focuses on using different structures and compositions of alloy anode materials to take advantage of key parameters of battery systems as shown in figure 1.6.

The susceptibility of alloy anodes to interfacial instabilities is a critical impediment to their long-term electrochemical viability. These instabilities, often resulting from irreversible electrochemical reactions with the battery's electrolyte, induce significant volumetric expansion. Such expansion not only risks the structural integrity of the anode material but can also lead to the severance of electrical connectivity. The subsequent capacity decay is a major concern for the retention of high-energy storage capacities in alkali-ion batteries.

Addressing this challenge, the first objective of this thesis is to elucidate the role of carbon integration in supporting the structural resilience of alloy anodes. The incorporation of carbon is hypothesized to act as a mechanical buffer, mitigating the effects of volumetric expansion and thereby preventing the complete pulverization of the anode material. In cases where fragmentation occurs, the presence of a carbon matrix is anticipated to confine these fragments, preserving their functionality by maintaining electrical contact within the anode structure.

The strategic mix of alloying materials with carbon derivatives—ranging from carbon nanotubes to amorphous carbon structures—presents a promising avenue to enhance the electrochemical performance of these anodes. This synergistic approach is expected to yield

a composite wherein the morphology and structural configuration are optimized to distribute mechanical stress more evenly. Such optimization is essential in impeding the anisotropic expansion of the inner alloy materials, which is a key factor in sustaining the anode's structural integrity under the rigors of cyclic expansion and contraction.

The comprehensive studies undertaken in cases 1, 2, and 3 underscore the significance of carbon's role not only as a structural support but also as a facilitator of improved electrical conductivity. This dual functionality of carbon within the composite anodes is theorized to be instrumental in preserving the electrochemical integrity and enhancing the performance of high-energy alkali-ion batteries. Through a combination of experimental and analytical techniques, this thesis aims to provide a deeper understanding of the interaction between carbon materials and alloy anodes, with the ultimate goal of advancing the design and development of robust, high-capacity battery systems.

Task 2: In-situ Characterization of alloy anode composite materials for high-energy alkali-ion batteries:

Discussion:

The pursuit of advanced anode materials for alkali-ion batteries has directed attention toward nano/micro-sized alloy materials such as Phosphorous, Silicon, Tin, and their carbon composite, which are expected to revolutionize the landscape of energy storage. The synthesis of these composite materials via a facile High-Energy Ball Milling (HEBM) technique has yielded alloys with properties that align well with the rigorous demands of next-generation battery technologies.

Striving to thoroughly understand and refine these anode materials, this dissertation employs a combination of in situ, ex-situ, and in-operando characterization techniques. These investigative methods are crucial for real-time probing of the electrochemical processes and morphological changes during battery operation, providing a window into the active interactions within the battery cell.

By leveraging these techniques, the research aims to elucidate the complex mechanisms that govern the performance of alloy anodes, including their phase transformations, interaction with electrolytes, and electrical conductivity pathways. The insights collected from these studies are expected to apprise strategies for enhancing the cycling stability, energy density, and overall efficiency of alkali-ion batteries.

This thesis not only contributes to the fundamental understanding of alloy anode materials but also establishes a methodological framework for the development and optimization of high-performance anode materials. The findings have the potential to significantly impact the design of high-energy Alkali-ion battery systems, paving the way for the creation of more robust, durable, and safer energy storage solutions.

3.2 Objective 2:

Exploring the role of a well-designed electrolyte and stable SEI on the performance and the stability of micro-size anode materials for high-energy alkali ion batteries.

Discussion:

The interface between the anode material and the electrolyte, the solid electrolyte interphase (SEI), plays a pivotal role in the overall performance of alkali-ion batteries. This layer, which forms during the initial charging cycles, is critical in dictating the reversible capacity, initial Coulombic efficiency (ICE), rate performance, and intrinsic safety of the battery. A well-designed SEI can enhance ion transport while minimizing electron leakage, thereby preventing detrimental side reactions that can compromise the anode's structural integrity and electrochemical performance.

Recent advancements in interphase engineering have demonstrated that the chemical composition of the electrolyte can induce a stable SEI, particularly on micro-sized anode particles, which typically suffer from severe volume changes during operation. A stable SEI can ensure sustained electrical contact between the active material and the current collector, mitigating capacity loss that often results from the continuous exposure of fresh active material due to anode expansion.

In alignment with these insights, the third objective of this research is to analyze different electrolyte systems and their respective SEI formation processes, with a particular focus on micro-sized Sn anodes. Case study 4 provides a comparative analysis, revealing the complex interplay between the electrolyte chemistry and the anode material. This involves an intricate examination of the morphological evolutions, shifts in oxidation states, and alterations in the local bond structures during the sodiation/desodiation processes.

The study goes beyond mere observation, aiming to unravel the fundamental mechanisms

that govern the SEI's composition and distribution. Such an understanding is indispensable for the rational design of advanced anode materials and electrolyte formulations for SIBs. By identifying the key parameters that lead to a robust and stable SEI, this objective seeks to contribute significantly to the field of energy storage, particularly in the optimization of high-capacity, safe, and reliable alkali-ion batteries.

3.3 Objective 3:

Conducting a comprehensive analysis of Alkali-Ion Battery manufacturing and recycling, with an economic assessment utilizing micro-size alloy anode material.

Task 1: Investigate the Contemporary Manufacturing and Recycling Processes of Lithium-Ion Batteries (LIBs) and Sodium-Ion Batteries (SIBs)

Discussion:

This task involves a thorough exploration of the latest advancements and methodologies in the manufacturing and recycling of both Lithium-Ion and Sodium-Ion Batteries. The focus will be on identifying and understanding the most current technologies and processes used in the industry, including any recent innovations or improvements that enhance efficiency, sustainability, or cost-effectiveness.

Task 2: Comprehensive Economic Analysis of Micro-Sized Alloy Anode Materials in High-Energy Alkali-Ion Batteries Using BATPAC Software and DOE Statistical Analysis

Discussion:

This task's aim is to perform a detailed economic assessment of alkali-ion batteries with micro-sized alloy anode materials by applying advanced cost analysis techniques for a holistic economic impact evaluation. The task will encompass a multi-faceted cost-benefit analysis aimed at determining the financial feasibility and potential economic benefits of utilizing micro-sized alloy anodes in battery production. This will involve considering key factors such as material costs, production expenses, and market value. To strengthen this analysis, the BATPAC software, developed under the auspices of the Argonne National Laboratory, serves

as the primary tool for generating detailed cost estimates of batteries incorporating alloy anodes. This model facilitates the input of various parameters related to battery composition and manufacturing processes, enabling a dynamic projection of total costs. Subsequently, a rigorous statistical examination, utilizing Design of Experiments (DOE), fractional factorial design, and Analysis of Variance (ANOVA), will be conducted. These statistical methods are chosen for their efficacy in identifying significant factors that influence cost outcomes and in quantifying the extent of these impacts. Moreover, the DOE approach will facilitate the exploration of interactions between variables, thereby offering insights into the complex dynamics at play in battery production economics. This methodological approach enables not only a thorough assessment of operational factors but also facilitates a comparative analysis of alternative materials and processes, thus delivering a comprehensive economic evaluation of the manufacturing techniques for high-energy alkali-ion batteries.

By pursuing these objectives, the dissertation will contribute to closing the research gap in the field of high-energy alkali-ion batteries. It will provide a comprehensive understanding of how micro-size alloy anode materials can be engineered to mitigate the challenges of volume expansion associated with alloy anodes.

Chapter 4

Research

4.1 Case I: Highly Reversible Sodiation / Desodiation from a Carbon-Sandwiched SnS2 Nanosheet Anode for Sodium-Ion-Batteries.

This work has been published[1].

4.1.1 Introduction

The scarcity of fossil fuels and the consequent greenhouse gas emissions have catalyzed the exploration of sustainable and eco-friendly energy alternatives. Nevertheless, the energy output from these renewable sources is contingent upon geographical and climatic conditions. Thus, a reliable, large-scale energy storage system becomes imperative [182, 183]. Established technologies such as lithium-ion batteries (LIBs) have been triumphant in portable electronics but fall short for large-scale energy storage due to the limited and unevenly distributed lithium reserves. Alternatively, sodium-ion batteries (SIBs) are gaining traction owing to their cost-effectiveness and adaptability to varied climatic conditions. Yet, the substantial

[1] doi: 10.1021/acs.nanolett.0c00964

ionic radius of sodium, in contrast to lithium, poses challenges in procuring apt electrode materials that ensure swift and consistent rates of sodiation and desodiation [22, 184, 33]. For instance, graphite, a standard anode material for LIBs, exhibits a suboptimal capacity for sodium storage. Conversely, tin disulfide (SnS_2), distinguished by its conversion and alloying reaction, stands out amongst several transition metal chalcogenides. Its layered configuration, characterized by significant interlayer spacing and feeble van der Waals forces, augments sodium ion diffusion. However, its efficiency decreases during cycling due to volumetric alterations from conversion and alloying, compounded by its inherent low electrical conductance [185, 186]. To counteract these limitations, carbon is often integrated to modulate the volume change and improve the electrode's conductivity. Heteroatom doping into carbon can further amplify its affinity to active materials, fortifying the architecture and facilitating electron and ion transfer [187, 188, 189].

Understanding the interaction between SnS_2 and sodium ions, encompassing intercalation, conversion, and alloying reaction stages, is paramount for battery performance enhancement. Certain ambiguous aspects, such as the reversibility of reactions and nano-structure modifications, remain subjects of debate. Recent progress in-operando synchrotron X-ray methodologies offers real-time insights into electrode transformations. Specifically, synchrotron X-ray absorption near edge spectra (XANES) discloses the average chemical milieu of electrode elements, pivotal for red-ox reactions. In contrast, small-angle X-ray scattering (SAXS) elucidates structural evolutions across the electrode, vital for grasping the conversion and alloying reactions which induce significant volume changes and subsequent capacity decline. A thorough analysis of the SnS_2 anode's reaction mechanism for SIBs can guide electrode optimization [190, 191, 192, 193, 194, 195, 196, 197, 198, 199].

In our study, we employ a previously established methacrylated gelatin (GelMA) hydrogel coating technique to cultivate SnS_2 nanosheets on nitrogen and sulfur co-doped carbon nanotubes (NS-CNTs) [200, 201]. Herein, GelMA is instrumental in preserving structural integrity by directing SnS_2 growth and simultaneously inducing heteroatom doping of the CNT. The

resultant SnS_2/NS-CNT electrode, characterized by a layered configuration, showcases a notable sodium storage capacity. Synchrotron XANES investigations indicate sequential and reversible intercalation, conversion, and alloying reactions during sodiation/desodiation, which is essential for maintaining capacity. However, SAXS observations reveal an irreversible nano-structural transformation, leading to SnS_2 nano-sheet deterioration and the emergence of new SnS_2 nano-particles, as corroborated by ex-situ transmission electron microscopy (TEM). Thus, the carbon-layered SnS_2 electrode emerges as a potential anode for SIBs due to its reversible reaction mechanism. Given the structural alterations during the initial cycle, enhancing the bond between the active ingredient and carbon emerges as a viable approach for carbon support design. The layered configuration realized in this study underscores its potential to guarantee structural stability.

4.1.2 Result and Discussion

Figure 4.1a illustrates the fabrication process of the carbon-sandwiched SnS_2/NS-CNT anode. A thin layer of GelMA hydrogel is first coated on the CNT surface by UV-initiated polymerization using photoinitiator 2-hydroxy-2-methlpropiophenone adsorbed on CNT through π-π stacking [200, 201]. Then, the Sn precursor ($SnCl_2 \cdot 2H_2O$) is infiltrated in GelMA, followed by the annealing at $550°C$ to sulfurize the precursor and convert GelMA into amorphous carbon. To ensure the full sulfurization, excessive S powder is used. The morphology and crystal structure of the final product are first checked by highresolution TEM (HRTEM). As shown in Figure 4.1b and Figure A.1, a dense distribution of few-layer SnS_2 nano-sheets on the surface of CNTs is observed, with a thin carbon layer covering SnS_2, forming a carbon/SnS_2/CNT sandwich structure (Figure A.2). The thickness of SnS_2 layers deposited on CNT is estimated to be less than 20 nm (Figure 4.1e and Figure A.2), in contrast to the bulk SnS_2 detached from the CNT with the diameter close to 1 μm obtained through the method without the hydrogel coating [202]. In the highly magnified TEM images (Figure 4.1c), two types of lattice fringes correspond to the (002) plane of the CNT and the

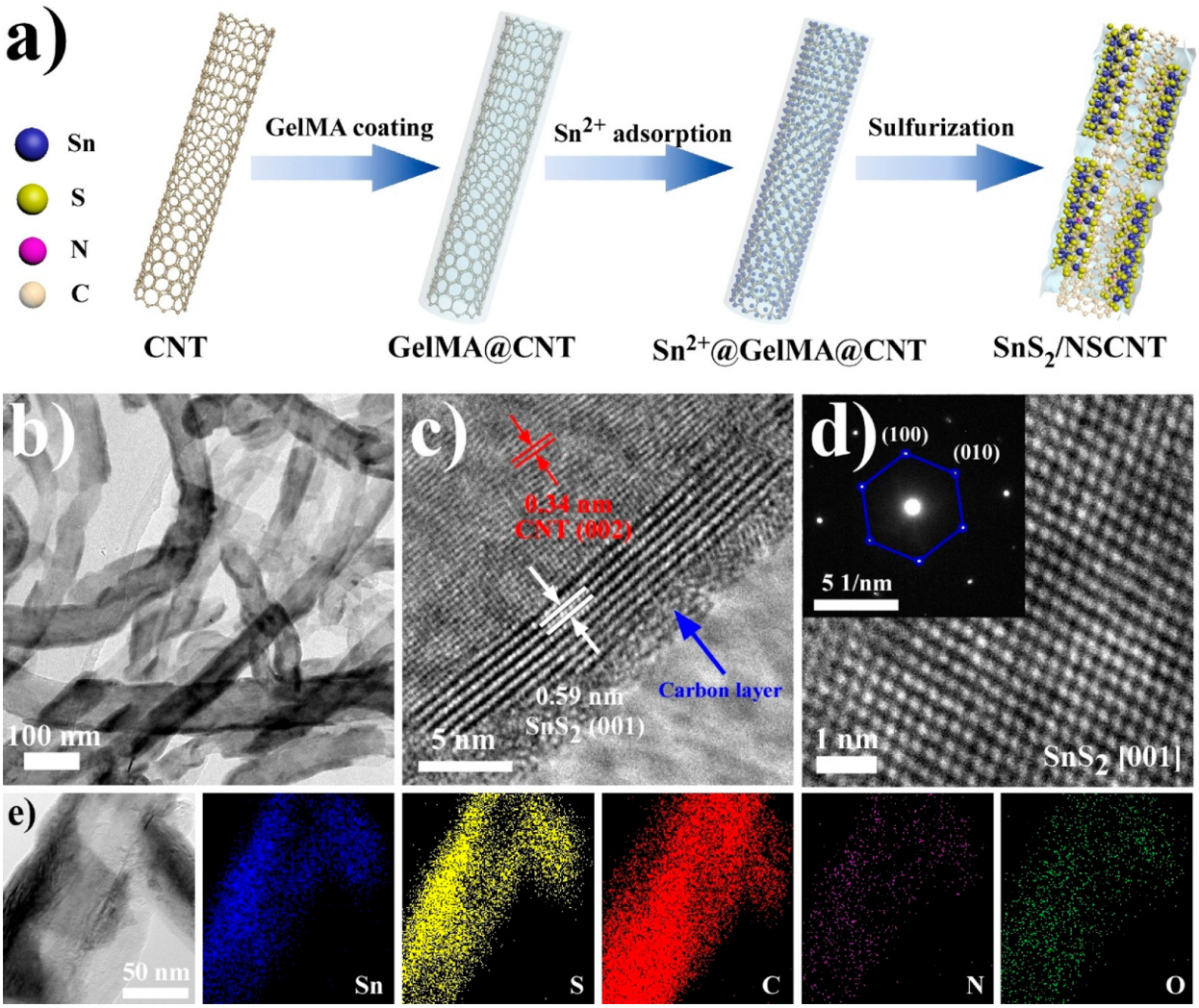

Figure 4.1: Schematics and HRTEM characterization. (a) Fabrication processes of the SnS_2/NS-CNT electrode. Low- (b) and high-magnification (c) HRTEM images of SnS_2 nanoflakes grown on NS-CNTs. (d) HRTEM image illustrating the top view of the SnS_2 (001) crystal plane. The inset is the SAED pattern of SnS_2. (e) HRTEM image of the SnS_2/NS-CNT with elemental mapping of Sn, S, C, N, and O, respectively.

(001) plane of SnS_2 with the interlayer distance of 0.34 and 0.59 nm, respectively. Figure 4.1d is the top view of the SnS_2 (001) crystal plane, showing the hexagonal crystal structure, consistent with the selected area diffraction (SAED) pattern in the inset of Figure 4.1d. Furthermore, energy-dispersive X-ray spectroscopy (EDX) is carried out based on the TEM image in Figure 4.1e, revealing the presence of Sn, S, carbon (C), N, and oxygen (O) elements, confirming the confinement of SnS_2 within carbon support. The high overlapping of C and N signals indicates the successful doping of N into the CNT, which is discussed later in the X-ray photoelectron spectroscopy (XPS) analysis.

The crystal structure is further confirmed with X-raydiffraction (XRD) and Raman spectra. As shown in **Figure 4.2a**, three distinct peaks located at 15.0°, 28.2°, and 32.1° are observed, corresponding to (001), (100), and (101) crystal planes of SnS_2 (JCPDS 23-0677), respectively. A broad peak at around 26° is from the (002) plane of the CNT support. In the Raman spectra (Figure 4.2b), the peaks at around 208 *and* $316cm^{-1}$ are identified as the characteristic E_g and A_{1g} phonon modes of SnS_2, respectively. Given the fact that the intensity of E_g decreases as a function of thickness due to the reduction number of the in-plane scattering center [203, 204], the extremely weak E_g band attests the few-layer nature of the obtained SnS_2 nano-sheets on CNTs, consistent with TEM results.

To investigate the chemical composition and valence state, the XPS spectrum is obtained and displayed in Figure 4.2c, presenting the signal from Sn, S, C, N, and O. The high resolution spectra for N 1s, Sn 3d, and S 2p ae presented in Figure 4.2d-f, respectively. In Figure 4.2e, the peak at 486.7 eV is assigned to $Sn\ 3d_{5/2}$, corresponding to the single +4 oxidation state of Sn in our sample, which can confirm the high phase purity of SnS_2 and exclude other tin sulfides ($SnS\ and\ Sn_2S_3$) [205, 206]. As for S 2p (Figure 4.2f), four strong peaks are observed, with 161.6 eV and 162.9 eV coming from $S\ 2p_{3/2}$ and $S\ 2p_{1/2}$ in SnS_2, respectively, confirming the -2 oxidation state of S, while peaks at 164.0 ev and 165.1 eV are due to thiophene-type S doping into CNTs [207]. This result indicates that S doping occurs, along with the sulfurization of Sn precursor at high temperature. The high-resolution scan

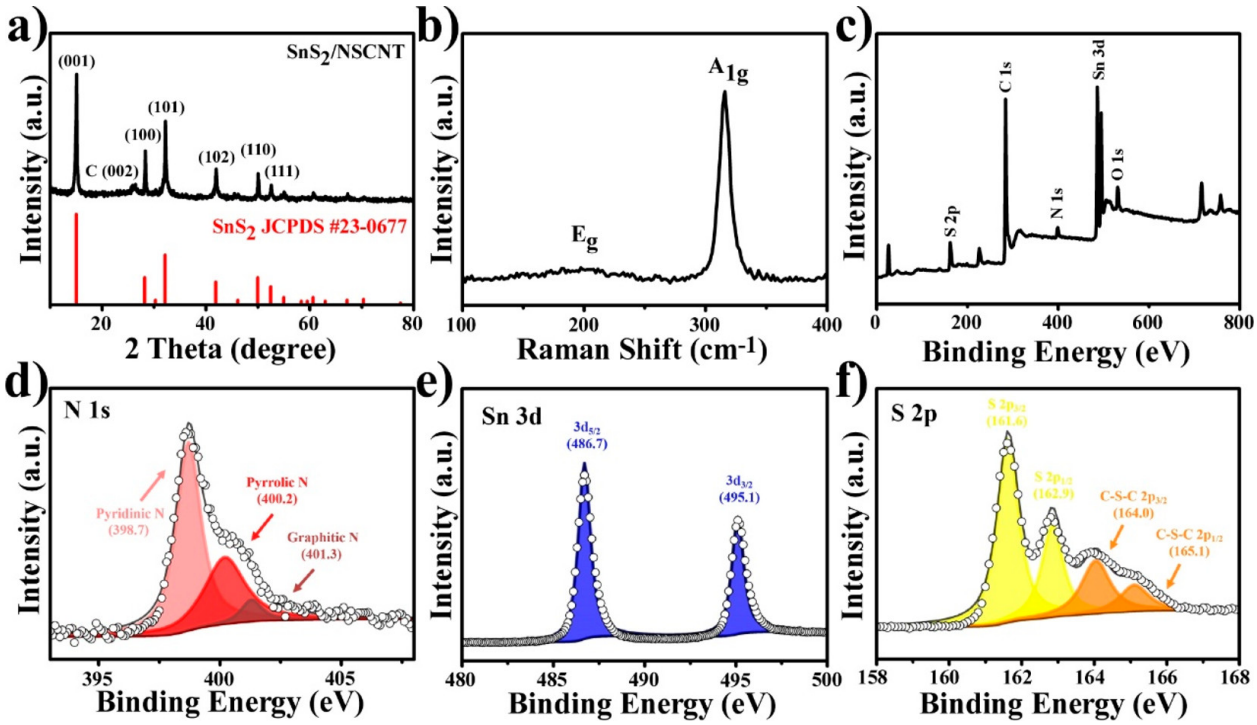

Figure 4.2: Crystal structure and elemental analysis. (a) XRD patterns of SnS_2/NS-CNTs (black) compared with the standard data (red). (b) Raman spectrum of SnS_2/NS-CNTs ranging from 100 *to* 400 cm^{-1}. (c) Full XPS spectra of SnS_2/NS-CNTs. High-resolution scans of N 1s (d), Sn 3d (e), and S 2p (f).

of N 1s (Figure 4.2d) obtains the peaks at 398.7 eV, 400.2 eV, and 401.3 eV, respectively, corresponding to pyridinic N (60.1%), pyrrolic N (34.1%), and graphitic N (5.8%) doping, suggesting that the CNT is doped by N from the amino groups in GelMA [208]. The weight percentage of SnS_2 in SnS_2/NS-CNT is estimated to be 64% (Figure A.3) based on the thermo-gravimetric analysis (TGA).

Then, the electrochemical performance of the obtained SnS_2/NS-CNT anode for SIBs is evaluated. As shown in **Figure 4.3a**, at the current density of 50 $mA.g^{-1}$, the SnS_2/NS-CNT electrode delivers the initial discharge and charge capacities of 1131 $mAh.g^{-1}$ and 611 $mAh.g^{-1}$, respectively, corresponding to a Coulombic efficiency (CE) of 54% but becomes stable with the CE back to 96% after 10 cycles and retains a discharge capacity of 471 $mAh.g-1$ with a capacity retention of 86% after 60 cycles (compared to the 10th cycle). Similarly, the stability is also confirmed at a higher current density (200 $mA.g^{-1}$, Figure 4.3b), with a

discharge capacity of 417 $mAh.g^{-1}$ achieved after 80 cycles along with a CE of around 98% and a high capacity retention of 85%(compared to the 10th cycle). Furthermore, the sodium storage properties of the SnS_2/NS-CNT electrode are investigated under various discharge/charge rates from 0.1 to 5 C ($1C = 500\ mA.g^{-1}$, Figure 4.3c). As the rate increases, it can deliver the average discharge capacities of 738, 613, 538, 463, 411, 382, 360, *and* 344 $mAh.g^{-1}$ at 0.1, 0.2, 0.4, 1, 2, 3, 4, and 5 C, respectively. When the current density is set back to 0.1 C, the capacity is maintained at around 700 $mAh.g^{-1}$, confirming the structure stability even under the fast discharge and charge process. Noticeably, insignificant capacity decay is observed as the rate increases from 3 to 5 C. Here, the high reversible capacity of SnS_2/NS-CNTs benefits from the unique carbon/SnS_2/CNT sandwich structure, where the carbon converted from GelMA works as the protection layer, along with the extra stability from the N, S dual-doped CNT, which increases the affinity between SnS_2 and the CNT. This design can help to prevent the active materials from detaching and dissolving and thus ensure the stability of the whole structure.

To elucidate the storage mechanism, we first analyze the reaction sequence. Figure 4.3d shows the galvanostatic discharge/charge curves for the 1st, 2nd, and 60th cycle at the current density of 50 $mA.g^{-1}$. During the first cycle, two plateaus at around $1.7V$ and $0.7V$ are observed for the discharge, and one plateau at around $1.2V$ is observed for the charge (Figure 4.3e) while the second discharge/charge curves demonstrate plateaus similar to that of the 60th cycle with one at $0.7V$ and the other at $1.2V$ for the discharge and charge, respectively, revealing the similar reaction mechanism after the initial cycle. To further identify voltage for the red-ox reaction, we plot the differential capacity versus voltage as shown in Figure 4.3e,f. In the first discharging process, a sharp peak at $1.66V$ and a broad peak at $1.1V$ arise from the intercalation of Na^+ into the interlayer spacing of SnS_2 with the formation of the Na_xSnS_2 compound as illustrated in **reaction 4.1** [209]. In contrast, the strongest peak at around $0.65V$ is related to the conversion reaction 4.2 where Na_xSnS_2 is converted to Na_2S and metallic Sn along with the formation of a solid electrolyte interface (SEI). The

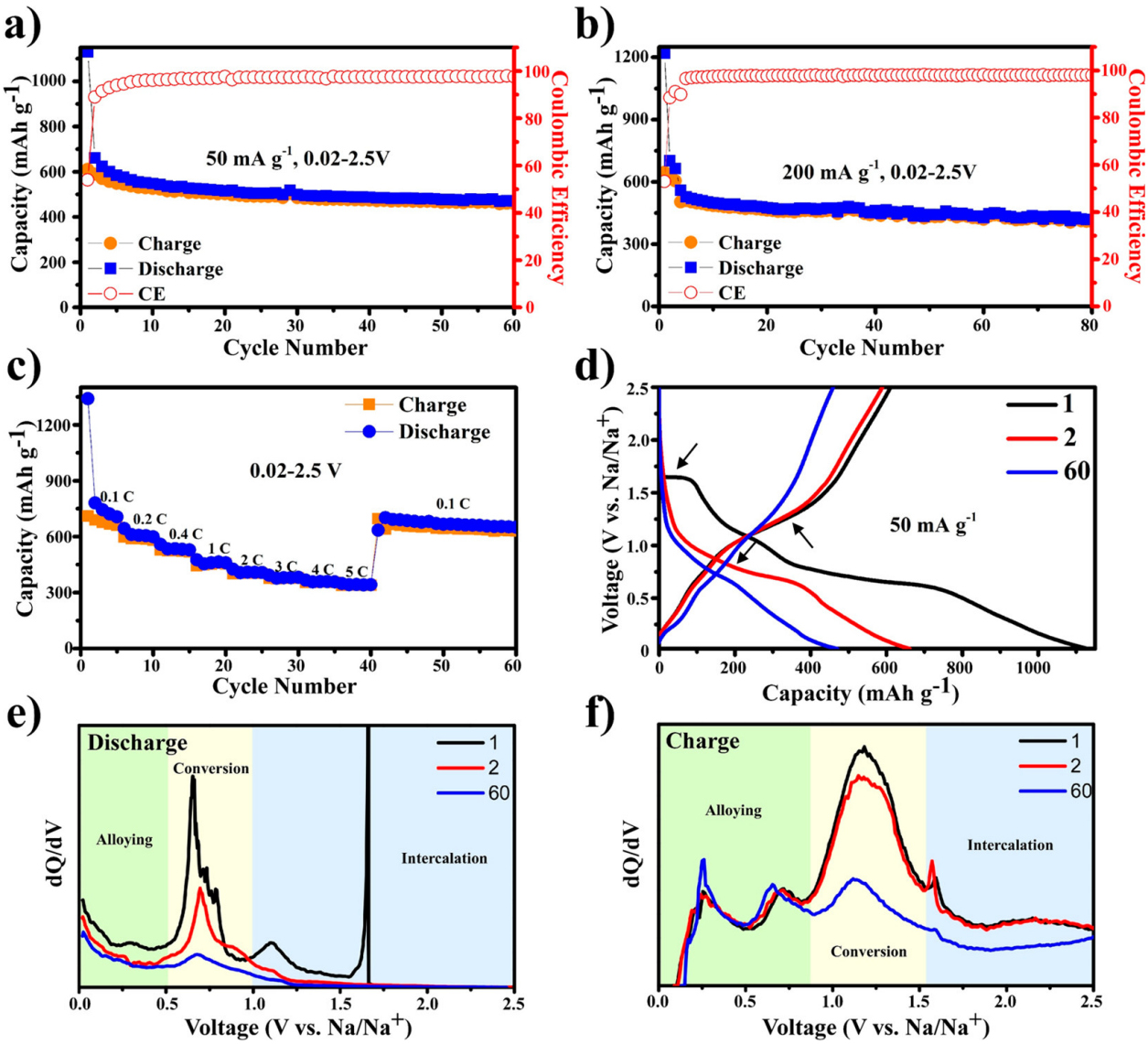

Figure 4.3: Electrochemical performance of the SnS_2/NS-CNT anode for SIBs. Cycling performance at the current densities of $50mA.g^{-1}$ (a) and $200mA.g^{-1}$ (b), respectively. (c) Rate performance at different current densities ($1C = 500mA.g^{-1}$). (d) Discharge and charge curves at a current density of $200mA.g^{-1}$. Differential discharge (e) and charge (f) capacity curves.

following peaks beyond $0.5V$ are attributed to the alloying process between Sn and Na^+ [210]. In the subsequent discharge, the typical peaks corresponding to reactions 1-3 can still be observed, including the peaks at around $1.12V$ (intercalation) and $0.69V$ (conversion) and a series of peaks between 0 and $0.5V$ (alloying). As for the charge process, almost all peak positions are similar over different cycles with the first two peaks at 0.3 and 0.7 V related to the desodiation of Na-Sn alloy, the peak at $1.2V$ manifesting the oxidation of Sn metal into Na_xSnS_2, and the peak at around 1.6 associated with the desodiation from Na_xSnS_2 back to SnS_2 [188, 211].

$$xNa^+ \ + \ SnS_2 \ + \ ce^- \ \rightarrow \ Na_xSnS_2 \tag{4.1}$$

$$Na_xSnS_2 \ + \ (4-x)Na^+ \ + \ (4-x)e^- \ \rightarrow \ Sn \ + \ 2Na_2S \tag{4.2}$$

$$Sn \ + \ 3.75Na^+ \ + \ 3.75e^- \ \rightarrow \ Na_{3.75}Sn \tag{4.3}$$

Subsequently, typical Sn K-edge synchrotron XANES of our electrode are collected at different potentials during the first cycle to confirm the sequence and reversibility of the above reactions. Figure 4.4a is the 2D contour plot constructed by the spectra at the pristine state, $1V$ (discharge), $0.02V$ (discharge), $1V$ (charge), and $2.5V$ (charge). We observe that the reaction between Na^+ and our electrode is almost completely reversible, showing a symmetry with the discharge and charge region. More detailed information is displayed in Figure 4.4b with the inset showing the enlarged version. Compared to the pristine spectra, a slight edge shift to high energy is observed when the cell was discharged from $2.5V$ to $1V$, suggesting that the intercalation of Na^+ would modify the electronic structure of SnS_2. When further discharging to $0.7V$, the edge shift to the low energy region is caused by the conversion reaction 4.2, in which Sn(IV) in SnS_2 is reduced to metallic Sn(0) [196, 212]. The following shift to high energy is probably due to the electron transfer during the alloying reaction 4.3 between Sn and Na [213]. In the subsequent desodiation, the edge shifts back the position of pristine SnS_2, indicating the reversibility of red-ox reactions between SnS_2 and Na^+, which

is critical for maintaining the capacity at a high level of the conversion-type electrode.

Structure evolution during the initial cycle is also investigated through in-operando synchrotron SAXS. Figure 4.4c displays the selected SAXS spectra at different discharge/charge states. Generally, two scattering features show up located at the low q region ($0 - 0.07$ Å^{-1}) and high q region ($0.07 - 0.4$ Å^{-1}), respectively. Then, by fitting the scattering intensity difference between the initial state and fully discharge state, we are able to estimate the particle size evolution quantitatively [198]. The results indicate that the population decreasing for 25 ± 20 nm in diameter, at the low q region, is concurrent with the increasing of population for 1.5 ± 0.2 nm in diameter, at the high q region. Besides, to better visualize the scattering intensity change at different times, 2D contour plots at both the low and high q region are generated as shown in the insets of Figure 4.4c. We found that, in the low q region, the intensity decreases gradually from the initial state to the fully discharged state and increases slightly along the charge process, revealing that the nano-structure change corresponding to this length scale is not fully reversible. By contrast, the scattering intensity in the high q region increases first during the sodiation and then remains the same until the full desodiation. Based on the XANES and SAXS analysis, we conclude that, after the initial sodiation process, SnS_2 nano-sheets grown on CNTs would collapse and lead to the particle size decreasing as made evident by the intensity decreasing in the low q region while the formation of Na-Sn alloyed particles would cause the intensity enhancement at the high q region (Figure 4.4d). At the end of charge process, the original SnS_2 nano-sheets would be replaced by the regenerated SnS_2 particles, rendering the reversible redox reaction between SnS_2 and Na^+ and the irreversible morphology evolution of SnS_2. To confirm this, ex-situ HRTEM is applied to collect the crystal structure and morphology information on the SnS_2/NSCNT electrode during the first cycle. As shown in Figure 4.4e, after the initial discharge, SnS_2/NS-CNT exhibits low crystallinity with small Na-Sn alloying particles embedded in the matrix. New SnS_2 particles form during the complete desodiation process (Figure 4.4f), made evident by the lattice fringe displaying an interlayer distance of 0.214 nm, corresponding to the (102) facet of SnS_2,

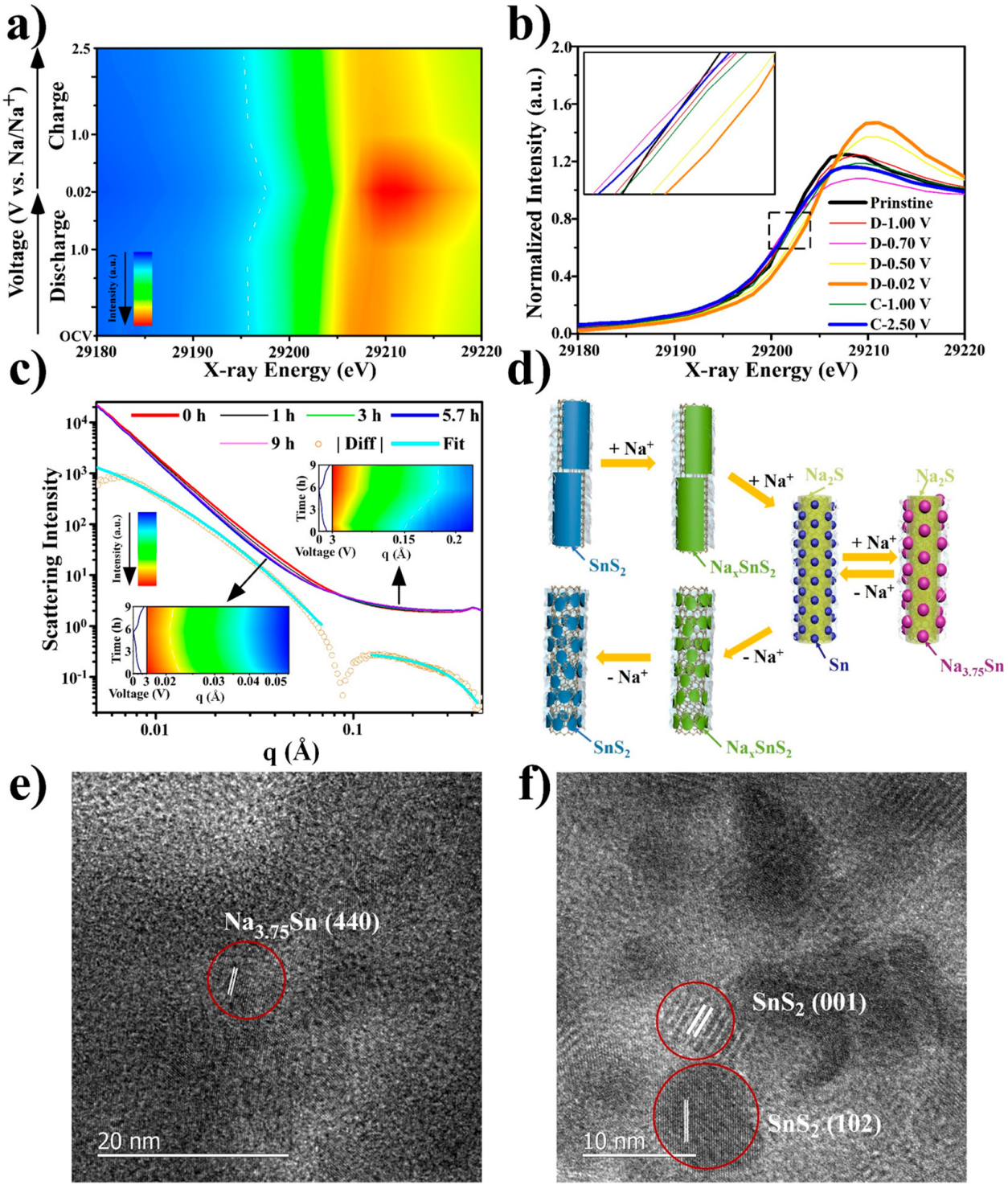

Figure 4.4: Synchrotron X-ray characterization and HRTEM analysis during the initial cycle. 2D contour plot (a) and typical Sn K-edge XANES (b) at different potentials. The inset in panel b is its enlarged version with X-ray energy ranging from 29199eV to 29204eV. (c) Selected SAXS spectra at different times. Insets are the 2D contour plot of the SAXS data in the low ($0.017 - 0.055$ Å) and high ($0.1 - 0.22$ Å) q region, respectively. (d) Reaction pathway of the SnS_2/NS-CNT electrode. High-magnification HRTEM images of the electrode after the initial discharge (e) and charge (f).

consistent with previous XANES and SAXS analysis. Given this serious morphology change, the layered structure of pristine SnS_2 is not the key point for maintaining the stability. Here, the sandwiched structure remains sandwiched between amorphous carbon and the CNT even though the SnS_2 nano-sheets pulverized into smaller nano-particles. It can help to confine the regenerated SnS_2 nano-particles, alleviating the morphology change and maintaining the structure stability of the overall electrode. Without the carbon layer protection, this irreversible structure change would lead to the decay of sodium storage properties. The future design of the carbon coating for the SnS_2-based electrode should reinforce the "protection" role of the carbon coating in stabilizing the structure of SnS_2. The space confinement from the carbon coating is highly required to allow the pulverization of SnS_2 to happen within the carbon support, forming a mechanically stable structure. Besides, increasing the affinity of carbon to SnS_2 and the intermediates formed during the red-ox reactions can further prevent them from detaching and maintaining the highly reversible sodiation/desodiation of SnS_2.

4.1.3 Conclusion

We demonstrate the confined growth of dense and uniform few-layer SnS_2 nano-sheets between N and S doped CNTs (NS-CNTs) and an amorphous carbon using GelMA embedding methods, forming the carbon/SnS_2/NS-CNT sandwich structure. Benefiting from this structure and the dual-doping in the carbon support, the resulting SnS_2/NSCNT electrode exhibits excellent electrochemical properties when used as the anode for SIBs. Subsequently, the intrinsic reaction mechanism is investigated by synchrotron XANES, in operando SAXS techniques, and ex-situ TEM. We found that the intercalation, conversion, and alloying reactions are highly reversible, while the nano-structure evolution after the initial cycle is not reversible. This work confirms the high potential of the SnS_2-based anode for SIBs from its highly reversible capacity and excellent rate capability and points out the significance of the rational design of carbon support for conversion-type SIB anodes.

4.2 Case II: A Practical Phosphorus-based Anode Material for High-Energy Lithium-Ion Batteries.

This work has been published[2].

4.2.1 Introduction

The escalating energy needs of handheld devices and electric vehicles have catalyzed the advancement of high-capacity lithium-ion batteries (LIBs). A strategic approach to augment the energy density of LIBs is the employment of high-capacity anode materials. Presently, graphite stands as the premier anode material, yet its theoretical specific capacity, capped at $372 mAh.g^{-1}$, falls short in fulfilling the rising demands for enhanced energy and power density, even though these anodes are renowned for their enduring cycle stability and elevated initial coulombic efficiency (ICE) [214].

Silicon, with its remarkable theoretical gravimetric capacity of approximately 4200 $mAh.g^{-1}$ [215], has emerged as a potential alternative. Nevertheless, silicon undergoes substantial volume expansion (exceeding 300%) during the lithiation process, resulting in notable capacity deterioration. This is attributed to the fragmentation and subsequent electrical isolation of silicon particles throughout the cycling phase [216]. Moreover, the $c - Li_{15}Si_4$ phase, which emerges during deep lithiation, interacts adversely with non-aqueous electrolytes, potentially leading to electrolyte depletion and further capacity decline [217]. Nano-scale silicon materials, such as nano-wires [93] and porous silicon [175], and their integration with carbon matrices like graphene [218] and graphite [219] have been explored to mitigate these challenges. Yet, the inherent low tap density of nano-scale silicon compromises the volumetric energy density. Furthermore, both nano-scale silicon and silicon/carbon composites have been observed to exhibit suboptimal ICE, a crucial metric for their real-world application [220].

[2]doi: 10.1016/j.nanoen.2020.104849

Studies revealed that the excellent cyclic performance of silicon anodes is predominantly evaluated in half-cells, which utilize surplus lithium as a reference. In practical LIBs, the lithium consumed by silicon, sourced from the limited cathode reserve, degrades both the cathode and the silicon anode, culminating in capacity fade [221]. Consequently, the quest for an anode material that combines optimal ICE, significant capacity, and durability for high-capacity LIBs remains exigent.

In addition to graphite and silicon, phosphorus allotropes, notably black phosphorus (BP) and red phosphorus (RP), have garnered interest as potential anodes for diverse ion batteries [222, 223, 224]. They exhibit a moderate working potential of $0.9V$ and $0.45V$ during charge and discharge cycles. Owing to their ability to form a reversible alloy with lithium, resulting in Li_3P, both BP and RP possess a commendable theoretical specific capacity of 2596 $mAh.g^{-1}$. However, this is accompanied by a pronounced volume change during lithiation [225, 226]. Insights derived from addressing volume changes in silicon anodes have empowered researchers to develop innovative phosphorus anode materials with consistent cyclic performance. Despite these advancements, none of the existing phosphorus anode compositions, including those combined with graphene [227, 228, 229, 230, 231], carbon nano-tubes [232, 233, 234], and other forms, have managed to surpass an ICE of 90% [235].

Herein, we present an effective anode material tailored for high-energy LIBs, conceptualized as a composite of black phosphorus integrated with Ketjenblack-MWCNTs (BPC), containing $70wt.\%$ BP. This composite was synthesized via a scalable high-energy ball milling technique. In-operando high-energy X-ray diffraction (HEXRD) during the charge/discharge processes revealed that the BPC anode undergoes a remarkably reversible phase transition during the lithiation/de-lithiation cycles. In-situ single-particle experiments, utilizing focused ion beam scanning electron microscopy (FIB-SEM), affirmed the efficient accommodation of volume changes in the BPC anode throughout the cycling phases. Consequently, the BPC anode exhibited an impressive ICE of approximately 91% and an exceptional specific capacity of 2512.4 $mAh.g^{-1}$, complemented by outstanding cyclic stability ($>$ 2000 $mAh.g^{-1}$

@100th cycle) and rate capacity(1600 $mAh.g^{-1}$ @ 6.24 $A.g^{-1}$). Additionally, we assessed the electrochemical attributes of a complete cell comprising the BPC anode and a standard $LiNi_{0.6}Co_{0.2}Mn_{0.2O2}$ (NCM622) cathode, underscoring the practical viability of the BPC anode in real-world LIB configurations.

4.2.2 Experimental Section

1. **Materials synthesis:**

   Synthesis of the BPC composite for use as the anode of sodium-ion batteries was previously reported in [224]. Red phosphorus/Ketjenblack-MWCNTs composite with 70% RP loading was synthesized in the present work using a similar procedure but replacing BP with RP.

2. **Electrochemical measurement:**

   The electrodes were prepared by spreading a mixture of 70 $wt.\%$ active material, 20 $wt.\%$ carbon black, and 10 $wt.\%$ carboxymethyl cellulose sodium salt (2 $wt.\%$) onto a copper foil current collector. The as-prepared electrode was dried at $80°C$ in a vacuum oven for 24 h. The loading of active P in the electrode was controlled at about $1.0 - 1.5\ mg.cm^{-2}$. The electrochemical performance of the P-based electrodes was characterized by assembling them into coin cells (type CR2032) in an argon-filled glove box under conditions such that the moisture and oxygen contents were both below 1.0 ppm. The anode was separated from the lithium counter-electrode by a separator (Celgard 2325). The electrolytes were carbonated electrolytes (GEN II), which are composed of $LiPF_6$ (1.2M) dissolved in ethylene carbonate and ethyl methyl carbonate ($3:7 vol.\%$), with 10 $wt.\%$ fluoroethylene carbonate as additive. The cells were charged and discharged in a MACCOR system with a voltage range of $0.02 - 2.0\ V$ (vs. Li/Li^+). Cyclic voltammograms were recorded on a Solartron Analytical 1470 System between 0.01 V and 2.0 V (vs. Li/Li^+) at 0.1 $mV.s^{-1}$. Electrochemical impedance spectroscopy

of the Li/BPC coin cells before and after cycling was performed with a Solartron Analytical 1470 System in a frequency range of $100kHzto0.1Hz$.

3. **Full-cell investigation:**

   To investigate the potential of BPC in a Li metal-free battery, we carried out a full-cell test by coupling a BPC anode and NCM622 cathode. The NCM622 cathode was provided by an industry partner. The NCM622 electrodes were prepared by spreading a mixture of 90 $wt.\%$ active material, 5 $wt.\%$ C45, and 5 $wt.\%$ PVDF (8 $wt.\%$ in NMP) onto an aluminum foil current collector. The as-prepared electrodes were then dried at $100°C$ in a vacuum oven for 12 h. The loading density of NCM622 in the electrodes was controlled at 9 $mg.cm^{-2}$. The BPC/NCM622 full cell was then tested within $1.3-4.2\ V$ with a negative/positive ratio of around 1.1/1. In a typical cell, the active mass of the NCM622 cathode is 14.08 mg, and that of the BPC anode is set at 1.16 mg. The specific capacities and current densities for the BPC/NCM622 full cell were calculated on the basis of the active mass of the NCM622 cathode.

4. **In-situ synchrotron HEXRD:**

   The in-situ synchrotron HEXRD measurement was carried out at Beamline 11-ID-D of the Advanced Photon Source at Argonne National Laboratory. The X-ray wavelength was 0.799898 Å. In situ synchrotron HEXRD patterns were collected with custom-designed coin cells cycled with a MACCOR cycler at $C/10$ ($1\ C = \ 2600\ mA.g^{-1}$) between 0.02 V and 2.0 V. During the charging and discharging, the XRD patterns were collected for 1 min at 10-min intervals, using a Perkin-Elmer 2D X-ray detector. 2D images were converted into a 1D plot of 2ϑ versus intensity by using the FIT2D program calibrated against a CeO_2 standard.

5. **In-situ single-particle charge/discharge inside a scanning electron microscope:**

The setup of the in-situ experiments with a single BPC particle during charge/discharge can be found in our previous work [236]. Typically, to build a single-particle battery cell, a BPC particle attached to a tungsten probe by ion-beam carbon deposition served as the positive electrode. Lithium metal was placed on top of the scanning electron microscope stub to serve as the negative electrode. One drop of ionic liquid electrolyte (ILE) was placed on top of the Li metal. The single-particle battery cycling was controlled by a Keithley 6430 sub-femtoamp remote SourceMeter from Tektronix. The particle was immersed in the ILE drop during cycling and lifted out for imaging in different states of charge and discharge. The ILE was made by dissolving the Li salt, lithium bis (trifluoromethylsul-fonyl) imide (LiTFSI), in a solvent of 1-butyl-1-methylpyrrolidinium bis (trifluoromethylsulfonyl) imide ($P_{14}TFSI$). The particle was immersed in the ILE drop during cycling and lifted out for imaging at different states of charge and discharge. The voltage window was between 0.02 V and 2.0 V. To visualize the micro-structural change of the particle, the imaging area was polished by a focused ion beam to remove the ILE from the surface.

4.2.3 Result and Discussion

The structure of the BPC composites has been characterized in our previous group work [224]; they are composed of micrometer-sized secondary particles consisting of nano-meter-sized ($5- \ to \ 10-nm$) primary particles. Such hierarchical micro/nano-structures could not only increase the tap density of the material, but also could well accommodate the volume changes during charge/discharge. When the BPC composite was used as the anode in sodium-ion batteries, it demonstrated excellent sodium storage performance in terms of specific capacity and cycle stability [224]. In the present work, we further evaluate its feasibility as the anode for practical high-energy LIBs.

Cyclic voltammetry (CV) was used to understand the BPC anode's lithiation/delithiation behavior during charge/discharge. **Figure 4.5** shows the first four cycles of CV profiles of the

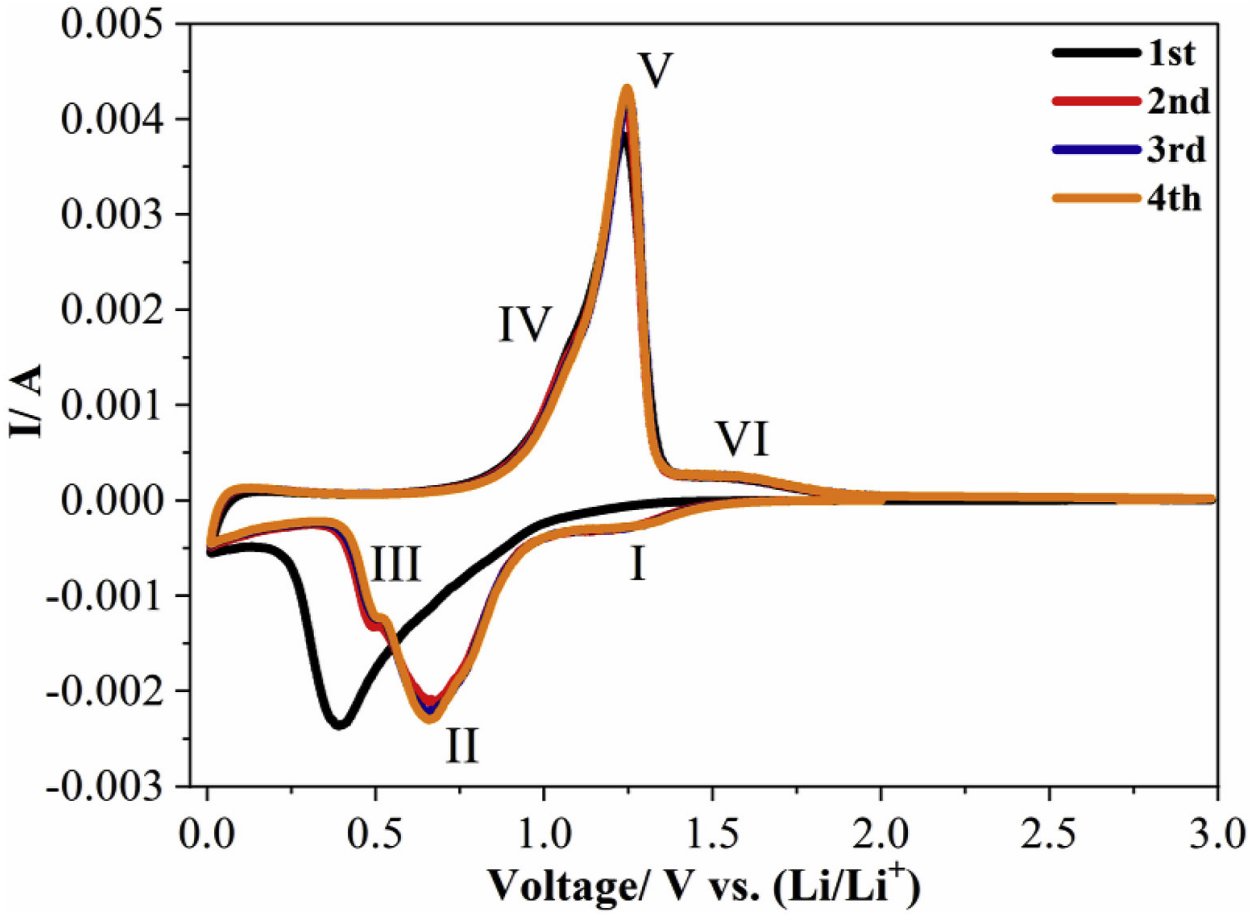

Figure 4.5: The first four cyclic voltammograms of the BPC anode at a scan rate of 0.1 $mV.s^{-1}$.

BPC anode at a scan rate of 0.1 $mV.s^{-1}$. In the first cathodic scan, there was a large reduction peak starting at 1.0 V and centered at 0.4 V, which corresponds to the stepwise lithiation of phosphorus. This peak shifted to a more positive potential and was split into three distinct peaks at 1.26 V, 0.66 V, and 0.5 V in the subsequent cycles; this behavior can be attributed to the formation of different Li_xP phases ($x = 1 - 3$) [229]. Such peak shift during CV test was also reported in other P-based anode materials for LIBs and sodium-ion batteries [224, 229, 234, 237]. This is because CV is potential sweep rate (i.e., $mV.s^{-1}$) controlled, rather than constant current controlled. This forced change in the potential, is independent on the state of charge of the electrode, can increase the current beyond the kinetic limit of the cell, resulting in some capacity from being accessed and hence the activation process observed in the CV. During the anodic scan, there was a strong peak centered at 1.24 V with two weak peaks at 1.07 V and 1.57 V, corresponding to the de-lithiation of the Li_xP phase [229]. Moreover, it can be clearly seen that the CV curves after the first cycle were highly overlapped, indicating that the BPC has excellent lithiation/delithiation reversibility.

To confirm the highly reversible lithiation/de-lithiation of the BPC anode, we further conducted in operando HEXRD using custom-designed coin cells to track the phase transformation of the BPC anode during charge/discharge at 0.1 C ($1C = 2600\ mA.g^{-1}$). As shown in **Figure 4.6a**, the charge/discharge curve of the in situ coin cell can deliver a high and reversible capacity of 2500 $mAh.g^{-1}$, indicating that the lithiation/delithiation process in the BPC anode was not affected by using such a cell design. The HEXRD pattern of the pristine BPC anode (Figure 4.6b) exhibited only two weak and broad peaks at around 11°, confirming the amorphous structure of the BPC anode caused by the breakdown of particle size after high-energy ball milling. During lithiation, the BPC anode remained amorphous in structure until the cell was discharged to 0.48 V. Multiple peaks centered at around 10°, 11.3°, 17.5°, 20.2°, 25° *and* 27° can be clearly seen, and are very likely to be due to the formation of crystalline Li_xP ($x = 1 - 3$). When the cell was further discharged to 0.02 V, the intensities of these peaks increased as a result of the continuous lithiation between Li and

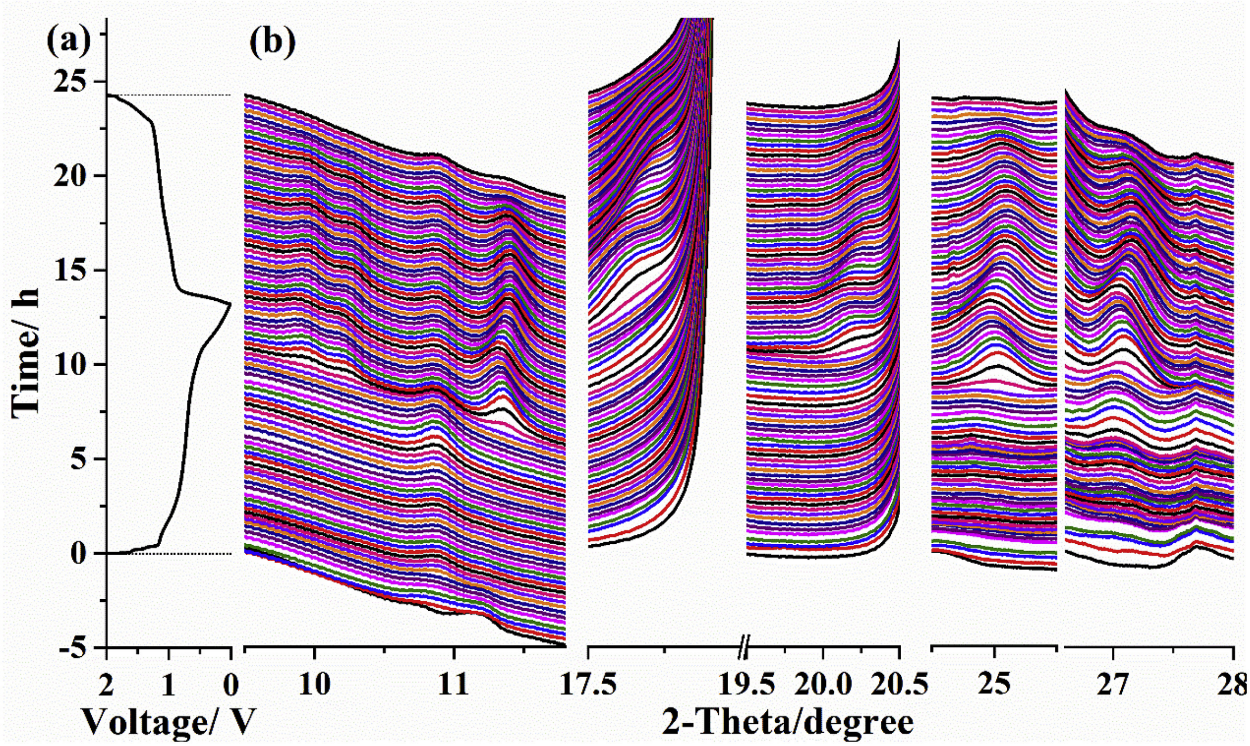

Figure 4.6: (a) The voltage profile of the BPC anode at 0.1 C and (b) the corresponding HEXRD patterns during charge/discharge.

the BPC. Upon de-lithiation, these peaks gradually disappeared as a result of the de-alloying of the Li_xP phase. At the end of the charge process, the BPC anode has completely returned to an amorphous structure, strongly confirming that the lithiation/de-lithiation of the BPC anode is highly reversible.

The HEXRD results serve as a good proof of the excellent structural stability of the BPC anode during charge/discharge. To confirm this stability, we further conducted in-situ FIB-SEM to directly visualize the morphological changes of single BPC particles during charge/discharge. This setup has been successfully used in our previous work to examine the structural changes in single-particle anode materials, e.g., Sn [236] and Ge [238], during charge/discharge. A single BPC particle was charged/discharged at 0.2 C (100 pA) for the first cycle, 0.6 C (300 pA) for the second cycle, and then 1.2 C (600 pA) for the third to ninth cycles. Figure 4.7a shows the voltage profile of a single BPC particle charge/discharge at 0.2 C, which exhibited similar charge/discharge capacity to the coin-cell result. Thus,

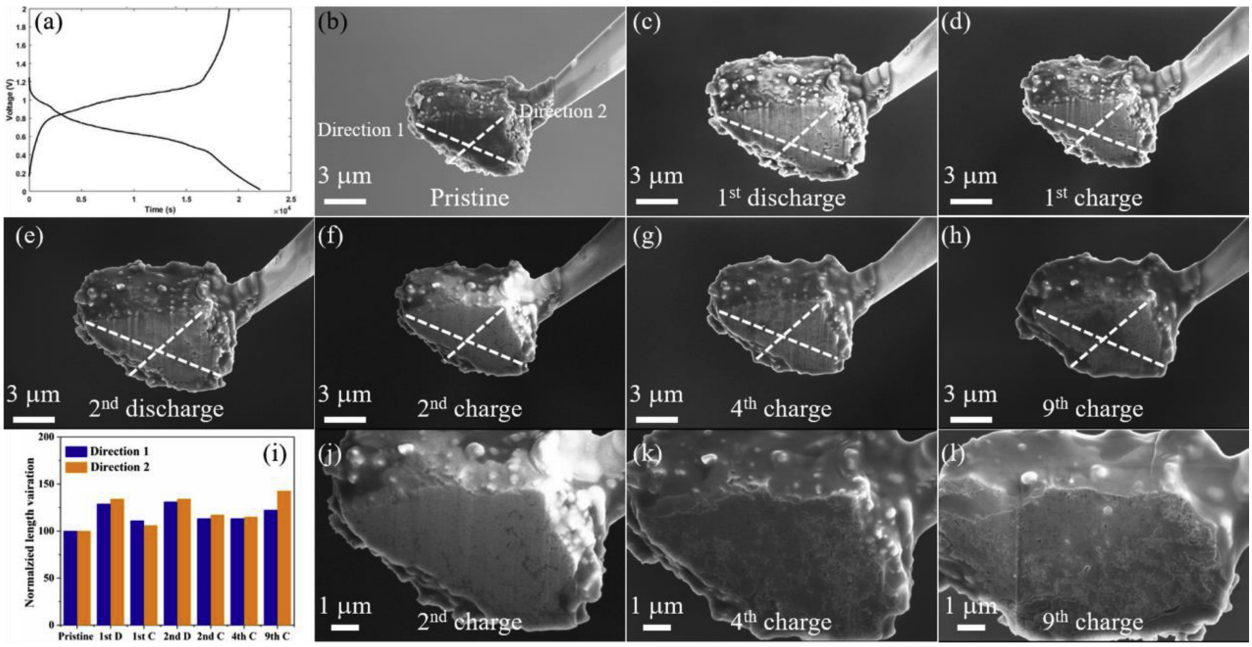

Figure 4.7: (a) The initial lithiation/delithiation curves and (b–h) the corresponding in-situ SEM images of a single BPC particle. (i) Normalized length variation of the BPC particle in different stages of charge/discharge and cycles. We defined the length as 100% in two directions in the pristine state. (j–l) Cross-sectional SEM image of the BPC particle at different cycles.

the morphological changes measured by using this approach can reflect the practical volume changes during lithiation/delithiation of the BPC anode. Figures 4.7b–h show SEM images of the BPC anode at different stages of charge/discharge and different cycles. As shown, the BPC particle expanded during discharge and contracted during charge. However, no obvious particle pulverization can be observed during successive cycling (total of 9 cycles) and even at high rates (up to 1.2 C). Figure 4.7j gives an estimation of the length variation of the BPC particles in two directions. It can be seen that although the BPC anode cannot completely return to the length of the pristine state, the length values are relatively stable during cycling, indicating that the volume changes of the BPC anode have been well accommodated. A close examination of the cross-section of the BPC particle depicted in Figures 4.7j–l clearly shows that the hierarchical micro/nanostructures of the BPC anode are well maintained during charge/discharge.

Thus, the in situ HEXRD and in situ FIB-SEM experiments have clearly confirmed that the BPC anode demonstrates excellent mechanical and structural stability during

lithiation/delithiation, which could thus effectively suppress the parasitic reactions with the electrolytes during long-term and high-temperature cycling and thus lead to superior lithium storage performance. The electrochemical performance of the BPC anodes was evaluated by assembling them into Li/BPC half- cells and charging/discharging within the range of $0.02 - 2.0\ V$. Figure 4.8a shows the first, second, and 100th charge/discharge voltage profiles of the BPC anode during cycling at 0.2 C. As shown, unlike the first charge/discharge curve of other P-based anode materials that usually exhibit a slope plateau above 1.0 V because of solid-electrolyte interphase (SEI) formation during discharge [233, 234, 231, 237], the BPC anode showed only negligible capacity when the cell was discharged from open-circuit voltage to 1.0 V. This finding indicates that the irreversible decomposition of the electrolytes to form SEI has been significantly suppressed with the BPC anode. Below 1.0 V, the BPC anode exhibited a long discharge plateau at 0.75 V, which is related to the lithiation of the BPC anode. The initial discharge specific capacity is measured to be 2775.2 $mAh.g^{-1}$, which is only slightly higher than the theoretical capacity of P anode. This strongly confirms the suppressed decomposition of electrolytes in our BPC anode during charge/discharge. During charging, the BPC anode displayed a long charge plateau of 1.1 V and delivered a reversible capacity as high as 2512.4 $mAh.g^{-1}$, leading to a high utilization of 96.8%. This behavior also resulted in a high ICE of 91%, which has surpassed many reported results, as shown in Figure 4.8b. Such a significant improvement in the ICE of the BPC anode is mainly attributed to its unique structural design, which can well accommodate the huge volume changes during lithiation/delithiation and remarkably reduce the irreversible electrolyte decomposition. Note that we believe the initial irreversible capacity loss (10%) of the BPC anode should come mainly from the irreversible insertion of Li+ into the Ketjenblack/MWCNTs matrix. As shown in Figure 4.8c, the pure Ketjenblack/MWCNTs matrix suffers from a large irreversible capacity loss during the first cycle. Thus, decreasing the amount of Ketjenblack/MWCNTs in the BPC composite may further improve the ICE. However, there is obviously a trade-off between cycle stability and ICE. In our work, the optimal loading of BP in the BPC composite

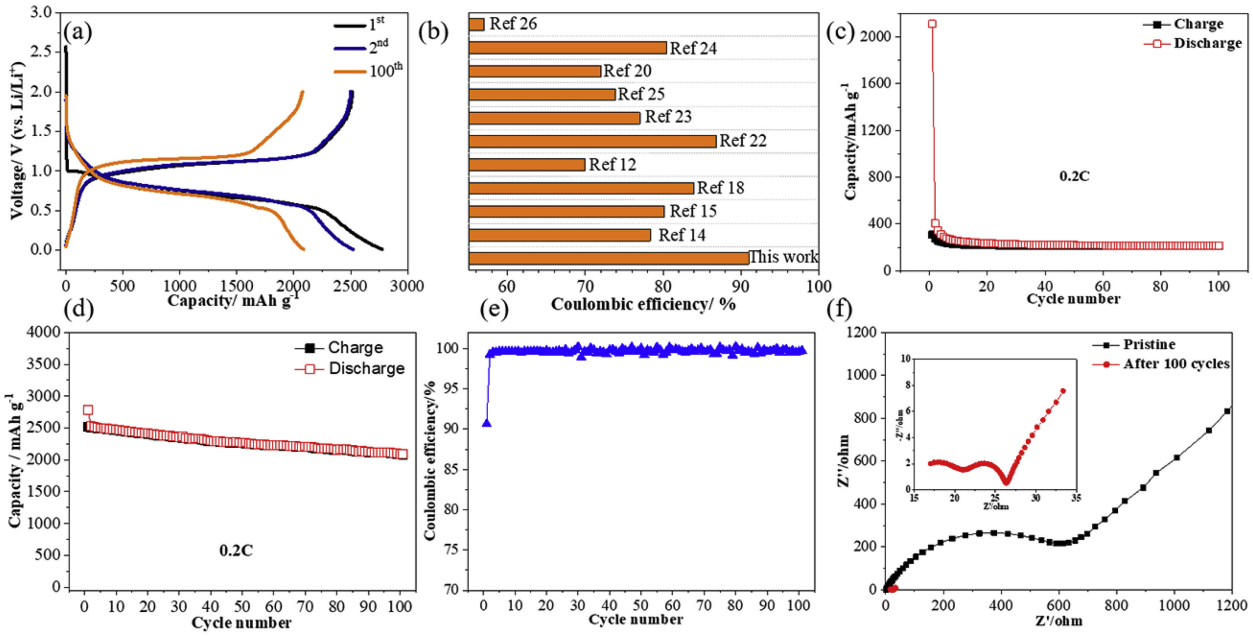

Figure 4.8: (a) Charge/discharge profiles of the BPC anode at 0.2 C. (b) Comparison of the initial coulombic efficiency of the BPC anode with other reported P-based anodes. Cycle performance of (c) the Ketjenblack/MWCNTs electrode and (d) the BPC anode at 0.2 C. (e) Coulombic efficiency of the BPC anode during cycling at 0.2 C. (f) Electrochemical impedance spectroscopy of the Li/BPC anode before and after 100 cycles of charge/discharge at 0.2 C.

is limited to $70wt.\%$. Figure 4.8d shows the cycle performance of the BPC anode at 0.2 C; the BPC anode was able to maintain a high reversible capacity of $>$ 2000 $mAh.g^{-1}$ after 100 cycles, indicating excellent cycle stability. Given the high loading of BP ($70wt.\%$) in the BPC composite, the overall capacity of the composite is higher than 1400 $mAh.g^{-1}$ composite. The tap density of the BPC composite was measured to be 0.8 $cc\ g^{-1}$, resulting in a high volumetric specific capacity of $>$ 1120 $mAh\ cc^{-1}$ composite. The coulombic efficiency of the BPC anode increases to almost 100% after the first cycle, showing high lithiation/de-lithiation reversibility (Figure 4.8e). To better understand the reason for the improved cycle stability of the BPC anode, we conducted electrochemical impedance spectroscopy, as shown in Figure 4.8f. After 100 cycles of charge/discharge, the surface-film thickness and charge-transfer resistance of the cell were both very small, indicating that there is no significant decomposition of the electrolytes to form thicker and thicker SEI, and the electrical contact between the BPC and the current collector was also well maintained [239].

Besides high ICE and stable cycle life, the fast-charging capability of the anode materials is also critical in practical applications. Graphite, owing to its low working potential, is not suitable as the anode of fast-charging LIBs. $Li_4Ti_5O_{12}$ can enable ultrafast charging ($> 10C$), but significantly reduces the energy density of the cell because of its high working potential ($1.5\ V\ vs.\ Li/Li^+$). Si and P are thus more promising anode choices for fast charging, because of their high specific capacity and moderate working voltage, which can reduce the electrode thickness and the charge carrier transport distance as well as avoid Li dendrite formation [240]. Therefore, we further evaluated the cycle stability of the BPC anode under high-rate cycling. As shown in Figure 4.9a, the BP anode was charged/discharged at 1 C, which can still deliver a high initial reversible capacity of 1968.1 $mAh.g^{-1}$ and maintain 1593.2 $mAh.g^{-1}$ after 100 cycles, corresponding to a high capacity retention of 81%. The rate capability of the BPC anode was further evaluated by changing the charge/discharge rate from 0.08 C to 2.4 C, as shown in Figure 4.9b; the corresponding voltage profiles are shown in Figure 4.9c. It can be seen that the BPC anode demonstrates excellent rate capability, which showed a specific capacity of 2596, 2511, 2394, 2240, 2178, 2049, 1927 *and* 1637 $mAh.g^{-1}$ at the rate of 0.08 C, 0.16 C, 0.32 C, 0.64 C, 0.8 C, 1.2 C, 1.6 C and 2.4 C, respectively. The result indicated that the lithiation/delithiation of the BPC anode is reversible even under fast charging/discharging. The high ICE, excellent cycle and rate capability, and high P loading of the BPC anode make it a clear improvement over other P-based anode materials reported recently. The rate capability of the BPC anode is compared to the previously reported data from P-based anodes for LIBs in Figure 4.9d. It is obvious that the BPC anode surpasses many other reported P-based anode materials with similar electrode composition; most of them suffer from significant capacity degradation, with capacities below 1300 $mAh.g^{-1}$at a current density of 4 $A.g^{-1}$, while the BPC anode could still deliver a capacity of over 1600 $mAh.g^{-1}$ at6.25 $A.g^{-1}$.

To further demonstrate the potential practical applications of the BPC anode, full- cell LIBs using the BPC anode and the NCM622 cathode were fabricated. The structure and

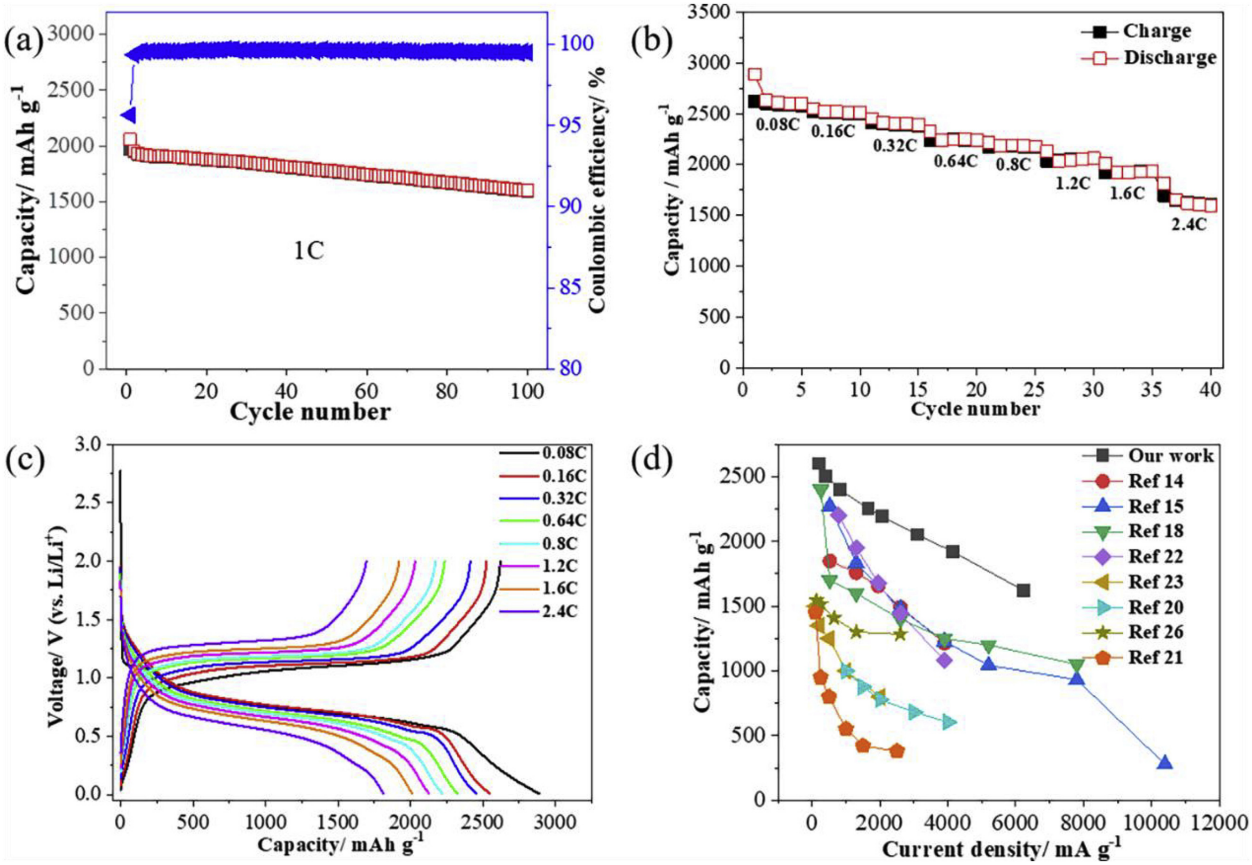

Figure 4.9: (a) Cycle performance of the BPC anode at 1 C. (b) Rate capability and (c) voltage profiles of the BPC anode at different charge/discharge rates. (d) Comparison of the rate capability of the BPC anode with other reported P-based anodes.

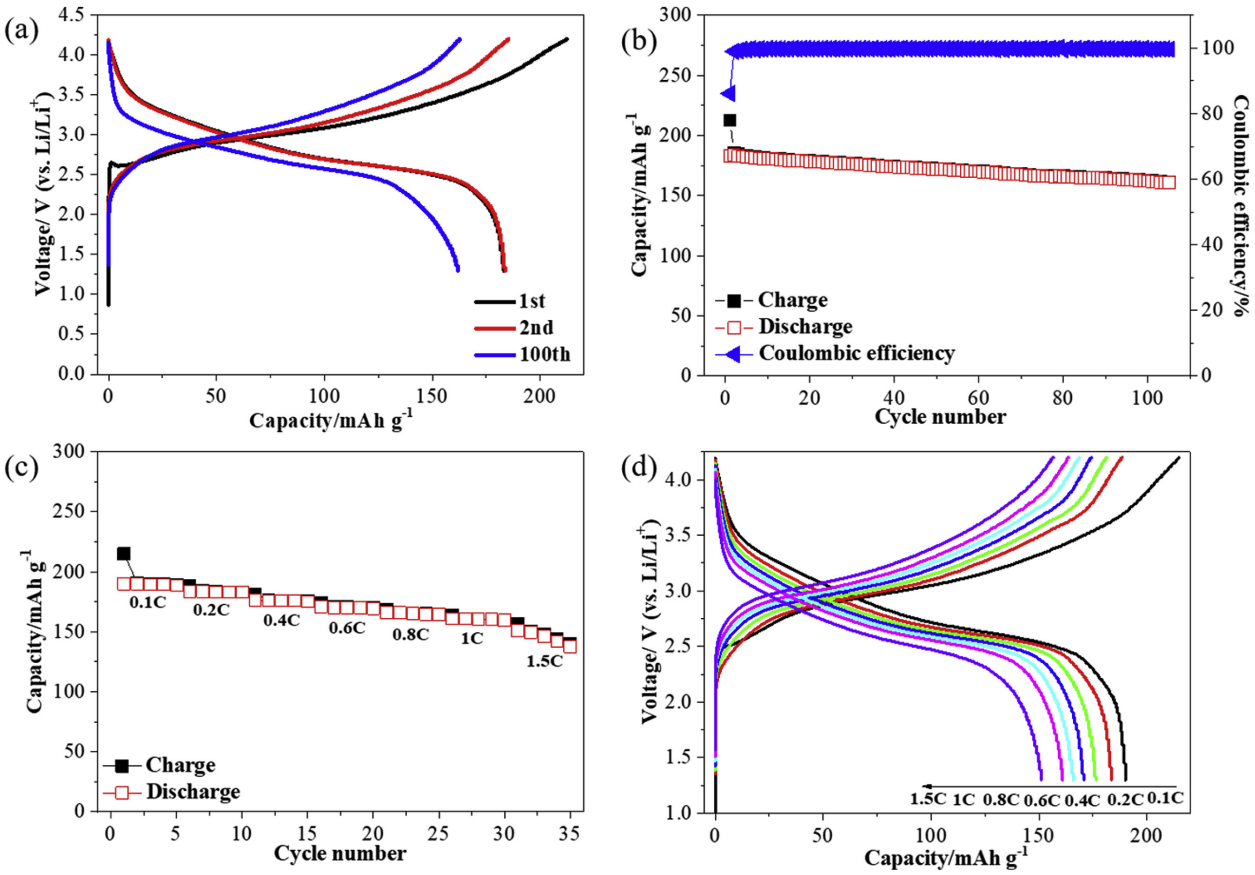

Figure 4.10: (a) Representative charge/discharge curves, (b) cycle performance at 36 $mA.g^{-1}$, and (c, d) rate performance of the $BPC/LiNi_{0.6}Co_{0.2}Mn_{0.2}O_2$ full cell.

electrochemical properties of the NCM622 cathode were described in our previous work [241]. In the present work, the negative/positive ratio is controlled at 1.1. As shown in Figure 4.10a, the BPC/NCM622 full cell demonstrated a high specific charge and discharge capacity of 212.5 *and* 183.1 $mAh.g^{-1}$, respectively, leading to a high ICE of 86%. Because of the high ICE of the BPC anode, no pre-lithiation is needed to mitigate the irreversible capacity loss. As a result, the BPC/NCM622 full cell demonstrated excellent cycle stability at a current density of 36 $mA.g^{-1}$, maintaining 88% of the initial discharge capacity after 100 cycles (Figure 4.10b). Moreover, the BPC/NCM622 full cell has an excellent rate capability, as shown in Figures 4.10c and d. When compared with other anode materials such as graphite and SiO anode, the estimated energy density of NCM622/BPC cell is higher than NCM622/Graphite cell and comparable with NCM622/SiO cell (see Table B.1).

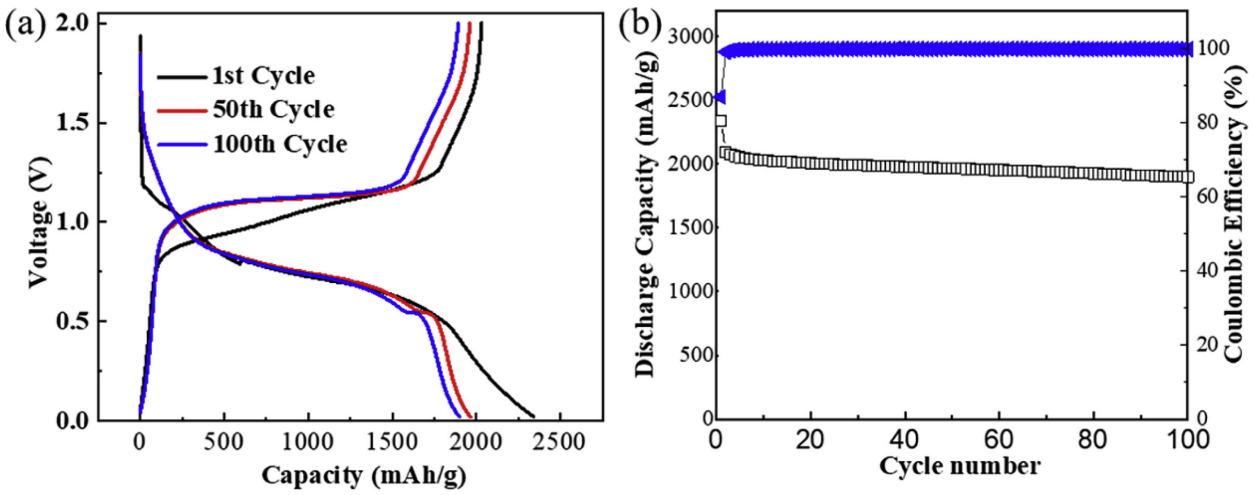

Figure 4.11: (a) Charge/discharge profiles and (b) cycle performance of the RPC anode at 0.2 C.

Note that the cost of BP is a concern in the practical application of the BPC anode. Thus, we have also fabricated a low-cost red phosphorus/Ketjenblack-MWCNTs (RPC) composite using the same process. As shown in Figure 4.11a and b, despite slightly lower specific capacity than the BPC due to lower electronic conductivity of RP as compared to BP, the RPC anode still demonstrated a high specific capacity of 2000 $mAh.g^{-1}$, stable cycle life, and a high ICE of 87%. Thus, we believe a concept using BP- RP/Ketjenblack-MWCNTs composite would be a practical choice in terms of cost, ICE, specific capacity, cycle life, and rate capability.

4.2.4 Conclusions

In summary, we have fabricated a practical P-based anode material with high initial coulombic efficiency, high reversible capacity, and excellent cycle and rate capability for high-energy lithium-ion batteries through a scalable high-energy ball milling approach. The excellent electrochemical performance can be attributed to the well-accommodated volume changes, suppressed irreversible electrolyte decomposition, and highly reversible phase changes achieved by using the hierarchical micro/nanostructure design concept. This work paves the way to improving the alloying anode materials for high-energy lithium-ion batteries.

4.3 Case III: Tuning Working Potential of Silicon Phosphorus Anode via Microstructures Control for High Energy Lithium Ion Batteries

This work has been published[3].

4.3.1 Introduction

Since their introduction in 1990, lithium-ion batteries (LIBs) have become integral to various energy storage applications, attributed to their exemplary electrochemical capabilities and minimal maintenance requirements [242]. With the surge in the electric vehicle sector, there's an imperative demand for batteries with augmented energy/power densities to facilitate extended driving ranges and expedited charging time [243].

Enhancing the energy density of LIBs can be achieved by incorporating high-capacity anode materials. Graphite, the contemporary gold standard for anode materials, offers a theoretical specific capacity of merely 372 $mAh.g^{-1}$, which restricts the energy density potential of LIBs, even with its commendable long-term stability and initial coulombic efficiency (ICE) [244]. Furthermore, graphite's low operating potential (0.1 V $vs.$ Li/Li^{+}) [245] hampers rapid charging capabilities, instigating lithium dendrite growth. Additionally, graphite faces supply chain challenges, particularly in Europe and the US, due to surging demand. Another commercial anode, lithium-titanate, facilitates swift charging but compromises on energy density due to its elevated working potential (1.6V $vs.$ Li/Li^{+}) [246], And a $Li_{3+x}V_2O_5$ anode capable of ultrafast charging with an average working potential of 0.6 V ($vs.$ Li/Li^{+}), however, it exhibits a modest specific capacity of $<$ 300 $mAh.g^{-1}$ [247].

Potential alternatives encompass several alloying-type anodes for LIBs, including silicon, phosphorus, tin, and antimony [248]. Silicon, with its substantial theoretical specific capacity

[3]doi: 10.1007/s10008-022-05192-0

(4200 $mAh.g^{-1}$) and an optimal potential (0.5 V $vs.$ Li/Li^+), is perceived as a promising anode contender [215]. Nevertheless, its significant volume expansion during lithiation/delithiation cycles ($> 300\%$) results in particle pulverization, culminating in swift capacity deterioration. Moreover, many documented Si and Si/C composite anodes grapple with subpar ICE ($< 80\%$), attributed to unavoidable solid-electrolyte interphase (SEI) formation and lithium-ion entrapment [249, 250], constraining their practical implementation.

Phosphorus, with a notable theoretical specific capacity of $2600mAh.g^{-1}$ [222], is another material of interest. Analogous to Si, P encounters substantial volume expansion during charge/discharge cycles, leading to significant capacity decay [225, 251]. Notably, phosphorus-based anodes, like the black phosphorus and Ketjenblack composite reported in case 2., exhibit impressive ICE of 91% and a substantial specific capacity of 2512.4 $mAh.g^{-1}$, alongside superior cyclic stability and rate capability [244]. Yet, phosphorus's elevated working potential (1.2 $V(charge)$/0.7 V $(discharge)$ $vs.$ Li/Li^+) compromises practical energy density [244, 250]. Thus, the quest remains for anode materials that with optimized specific capacity, ICE, and a pragmatic working potential ($0.3 - 0.5$ V $vs.$ Li/Li^+) to strike a balance between energy density, power density, and safety.

Merging silicon and phosphorus has been hypothesized to address the individual challenges they present as exclusive electrode materials [252, 253, 254, 255, 256, 257, 258, 259, 260]. Yet, most Si-P anodes documented to date exhibit issues like inadequate cycling stability [253, 259, 260], suboptimal ICE [256, 258], inappropriate working potential [252, 254, 257], or a combination thereof. For instance, Kwon et al. showcased a SiP_2/carbon anode sustaining a steady capacity of 1000 $mAh.g^{-1}$ across 100 cycles within $0.25 - 2$ V [252], but much of the capacity is realized at an average discharge working potential of 0.8 V $(vs.$ $Li/Li^+)$. Yang et al., by controlling size and crystallinity, introduced a SiP anode delivering $1000mAh.g^{-1}$ across 200 cycles with the majority of capacity at an average discharge working potential of < 0.6 V, albeit with a considerably low ICE of 61% [258]. These performance limitations are intrinsically tied to the inappropriate structural design.

In our study, through high-energy ball milling, we fine-tuned the working potential and specific capacity of two composite anodes integrating silicon and black phosphorus with Ketjenblack-MWCNTs, either derived from micrometer-sized silicon (mSPC) or nanometer-sized silicon (nSPC). The mSPC anode manifested a reversible capacity of 1800 $mAh.g^{-1}$ over 100 cycles at $0.2C$ ($1C = 3400\ mA.g^{-1}$) with a respectable average discharge working potential of $0.3V$ ($vs.\ Li/Li^{+}$), complemented by a superior rate capability. In situ FIB-SEM analysis elucidated the effective mitigation of volume changes during charge/discharge cycles, underscoring its exceptional cyclic stability. In contrast, the nSPC demonstrated diminished specific capacity and heightened charge/discharge working potentials, adversely impacting practical energy density. Our findings underscore the significance of meticulous microstructure/composition optimization in binary anodes for elevating the energy density of LIBs by balancing specific capacity and working potential

4.3.2 Results and Discussion

The scanning electron microscopy (SEM) images in Figure C.1 show that the particle size of micro-Si and nano-Si used in this work are around 10-50 μm and 50 nm, respectively. The microstructures of mSPC and nSPC composites, bulk BP, micro- and nano-Si were characterized by Raman spectra. As shown in Figure 4.12a, micro-Si presents characteristic Raman peaks of crystalline Si at 517 cm^{-1} as well as two weak and broad peaks at 300 cm^{-1} (longitudinal acoustic mode of amorphous Si) and 950 cm^{-1} (the second order vibration mode of the Si-Si bond) [261], while these peaks in the nano-Si become much broader due to the much smaller particle size.

BP shows sharp peaks at 362.5 cm^{-1}, 439.8 cm^{-1}, *and* 467.1 cm^{-1}, which are assigned to the vibrations of the crystalline lattice and match the Raman shifts attributed to the A_g^1, B_g^2, *and* A_g^2 phonon modes [262]. After ball-milling, a weak and broad peak appears instead in the nSPC, indicating that the particle size of silicon and phosphorus have been significantly reduced, while the remaining small peaks at 510 cm^{-1} in the mSPC composite

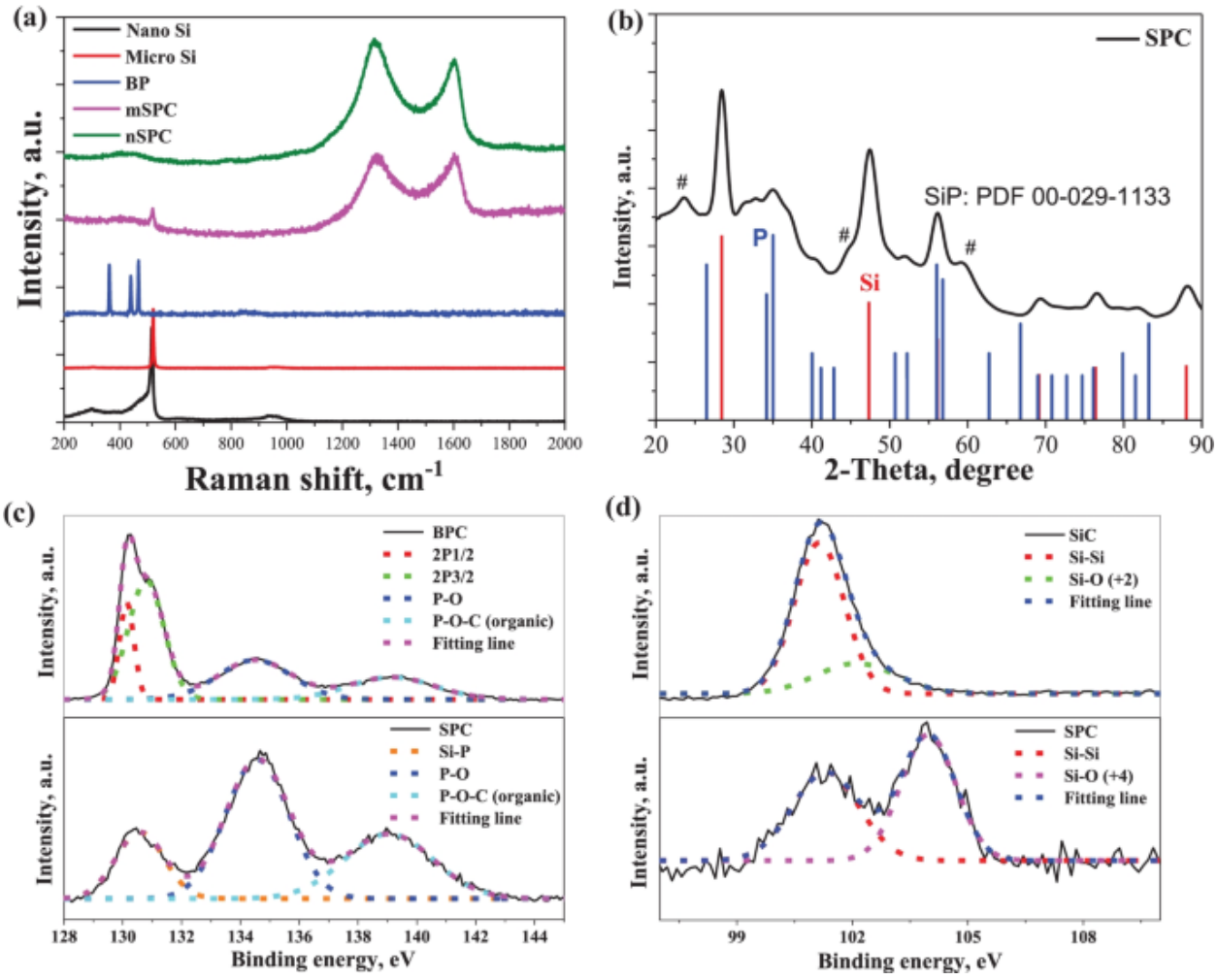

Figure 4.12: (a) Raman Spectra of mSPC, nSPC, BP, micro-Si, and nano-Si; (b) synchrotron XRD pattern of mSPC composite in comparison with standard Si and P; (c) P 2p and (d) Si 2p X-ray photoelectron spectra of BPC, SiC, and mSPC composite

indicates that the particle size of Si after ball milling is slightly larger than that in the nSPC. The Raman spectra of mSPC and nSPC both shows large broad peaks at 1323 *and* 1604 cm^{-1}, which can be assigned to the D and G bands of the carbon matrix (Ketjenblack/MWCNTs) in the composite, respectively [263]. The D-band is related to structural defects or disorder of carbon, while the G-band can be correlated with the stretching vibration mode of crystalline graphite. The intensity ratio of ID/IG in the mSPC and nSPC are calculated to be 1.0 and 1.13, respectively, suggesting that KB and MWCNTs in the nSPC become more disordered after ball-milling in comparison with that in the mSPC. The crystal structures of the mSPC were further characterized by synchrotron X-ray diffraction (XRD). As shown in Figure 4.12b, the mSPC exhibits characteristic but much broader XRD peaks of standard Si and BP, confirming the significantly reduced particle size of micro-Si and micro-BP after ball-milling. In addition, some peaks (marked by#) belong to SiP (PDF no. 00-029-1133) can be observed, indicating the formation of SiP after ball-milling. To obtain the chemical bond information of mSPC, X-ray photoelectron spectroscopy (XPS) was conducted. Figure 4.12c show the recorded P 2p XPS spectrum of mSPC in comparison with that of BPC. The result clearly shows that a new peak at 130.5 eV that can be assigned to Si-P bond appeared [264]. which is different from P 2p3/2 (130.1 eV) and P 2p1/2 (130.8 eV) doublet of the elemental P. Figure 4.12d compares the Si 2p XPS spectra of SiC and mSPC, which shows that the intensity ratio of Si-O (+4)/Si-O (+2) is significantly increased in the mSPC, which is similar to that of P-doped Si [261]. The results illustrate that the electron concentration of mSPC is higher than that of SiC, indicating the existence of electrically active BP in the mSPC.

To further investigate and characterize the micro-structures of mSPC and nSPC composite, SEM and high-resolution Transmission Electron Microscopy (TEM) were conducted. As shown in Figure C.2, both mSPC and nSPC exhibit a hierarchical micro/nan-ostructure, which is composed by micrometer-sized aggregates further comprising of nano-meter-sized primary nano-particles. It is well-known that such structural feature can help to accommodate the volume change of alloying type anodes during charge/discharge. The SEM EDX mapping of

nSPC in Figure C.3 shows that Si, P and C are uniformly distributed in the micrometer-sized aggregates. The high-angle annular dark-field scanning transmission electron microscopy (HAADF-STEM) image and the corresponding EDX mapping of mSPC (Figure 4.13a-c) also confirmed the homogeneous distribution of Si, P and C after ball milling. The high-resolution TEM image in Figure 4.13d depicts that nano-crystalline Si and P particles with a particle size of around 5-10 nm are formed, which are different from the micrometer-sized Si and bulk BP before ball milling. As shown in Figure 4.13e, some particles with a relatively larger particle size ($20 - 30\ nm$) can be observed as well, which exhibit a measured d-spacing of $0.279\ nm$, consisting with that of (132) crystal plane of SiP. This result is in accordance with that of XRD. Due to its secondary particles feature, the selected area electron diffraction (SAED) of mSPC presents a typical feature of polycrystalline materials (Figure 4.13f).

The electrochemical performance of mSPC anode was evaluated by charge/discharging them in half-cells with lithium metal as reference and counter electrode. The electrolytes used in this work contain 10 $wt.\%$ FEC as additive, which can prevent electrode materials from continuous electrolytes decomposition by forming a homogeneous and relatively thinner surface layer [224]. The specific capacity and charge/discharge rates were based on the mass of Si-P in the composite. Figure 4.14a shows the voltage profiles of mSPC anode during cycling at 0.2 C ($1C = \ 3400\ mA.g^{-1}$). The electrochemical reaction process of the mSPC anode during charge/discharge is shown more clearly in the differential capacity curve (Figure C.4). As shown, it possesses the characteristic charge/discharge features of P ($0.75 - 1.0\ V$), Si ($0.2 - 0.5\ V$), and carbon ($0.01 - 0.2\ V$) in sequence. The initial discharge and charge capacity were measured to be 2147.3 *and* 1801.6 $mAh.g^{-1}$, respectively, leading to an ICE of 84%. As evidenced by the reduction of lithiation peak at $0.01 - 0.2\ V$ in the 2nd cycle (Figure C.4), the initial irreversible capacity loss of the mSPC is mainly resulting from the trapping of lithium-ions in the Ketjenblack-MWCNTs matrix at low working potential given their considerably high amount (30%) in the mSPC composite. Meanwhile, the majority ($70 - 80\%$) of the discharge specific capacity is contributed by

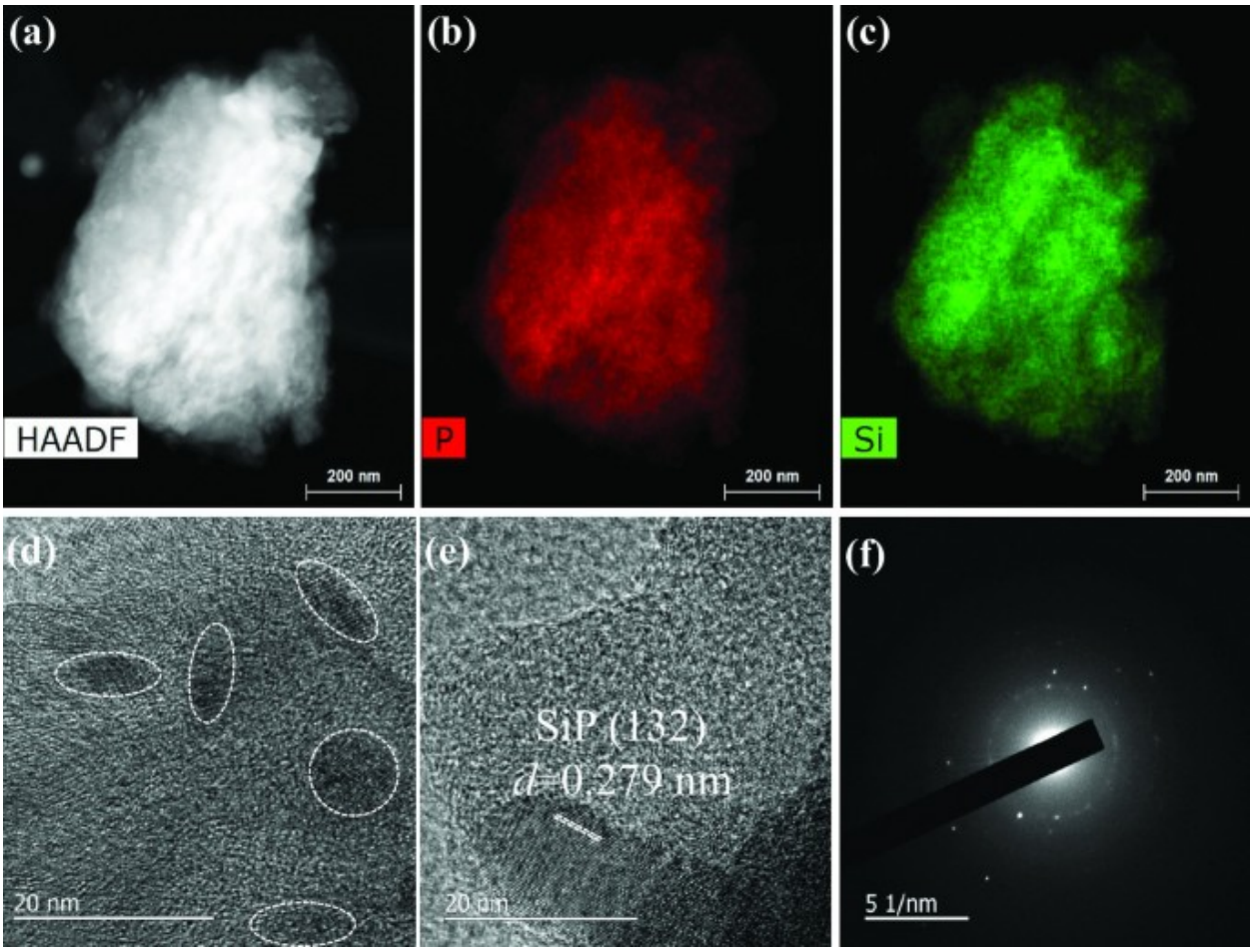

Figure 4.13: (a) HAADF-STEM image and (b), (c) the corresponding elemental mapping of mSPC composite. (d), (e) High-resolution TEM images and (f) SAED pattern of mSPC composite

the working potential of $< \ 0.5 \ V$. The corresponding cycling performance is shown in Figure 4.14b. The mSPC anode demonstrates a reversible capacity of 1646.0 $mAh.g^{-1}$ after 120 cycles at 0.2 C, accounting for a capacity retention as high as 91.4%. The coulombic efficiency after the 1st cycle reaches close to 100%, indicating highly reversible lithiation/de-lithiation process during repeated charge/discharge of mSPC. These should be attributed to its hierarchical micro/nano-structure, which not only shorten the diffusion path of electrons and lithium ions, but also accommodate the volume changes to ensure excellent cycling stability. The rate capability of the mSPC anode was further evaluated by changing the charge/discharge rates from $0.1C \ to \ 4.5 \ C$ ($1C \ = \ 3400 \ mA.g^{-1}$). As shown in Figure 4.14c and d, the mSPC anode demonstrates excellent rate capability, which showed an average reversible capacity of $2131, \ 1926, \ 1712, \ 1515, \ 1488, \ 1416, 1351, \ and \ 1216 \ mAh.g^{-1}$ at the rates of 0.1 C, 0.2 C, 0.4 C, 0.8 C, 1 C, 1.5 C, 2 C and 3 C, respectively. Even under an extremely high rate of 4.5 C (13 minutes charge/discharge), a high reversible capacity of 1000 $mAh.g^{-1}$ can be still attained, demonstrating superior rate performance. When further reducing the charge/discharge rate back to 0.1 C, almost 100% of the capacity could be recovered, indicating the good structural stability during fast charging. Compared to that ($0.7 \ V \ vs. \ Li/Li^+$) of black phosphorus/Ketjenblack anode [244], the decreased working potential of Si-P anode represents higher energy density, despite slightly lower specific capacity ($P: \ 2500 \ mAh.g^{-1} \ vs. \ SiP: \ 2100 \ mAh.g^{-1}$). Noted that the capacity increase during charge/discharge at increased C-rates is not uncommon during testing of battery materials, which is due to the required electrochemical activation process to form a stable ionic and electronic diffusion pathways. In addition, mSPC anode outperformed many of the reported Si-P anodes (Table C.1) and other anodes (Table C.2) in terms of ICE, specific capacity, cycling stability, and rate capability.

To examine the microstructure/composition effect on the working potential and specific capacity of Si-P anode, the electrochemical performance of the nSPC anode was further evaluated for comparison. Figure 4.15a depicts the voltage-normalized capacity curves of

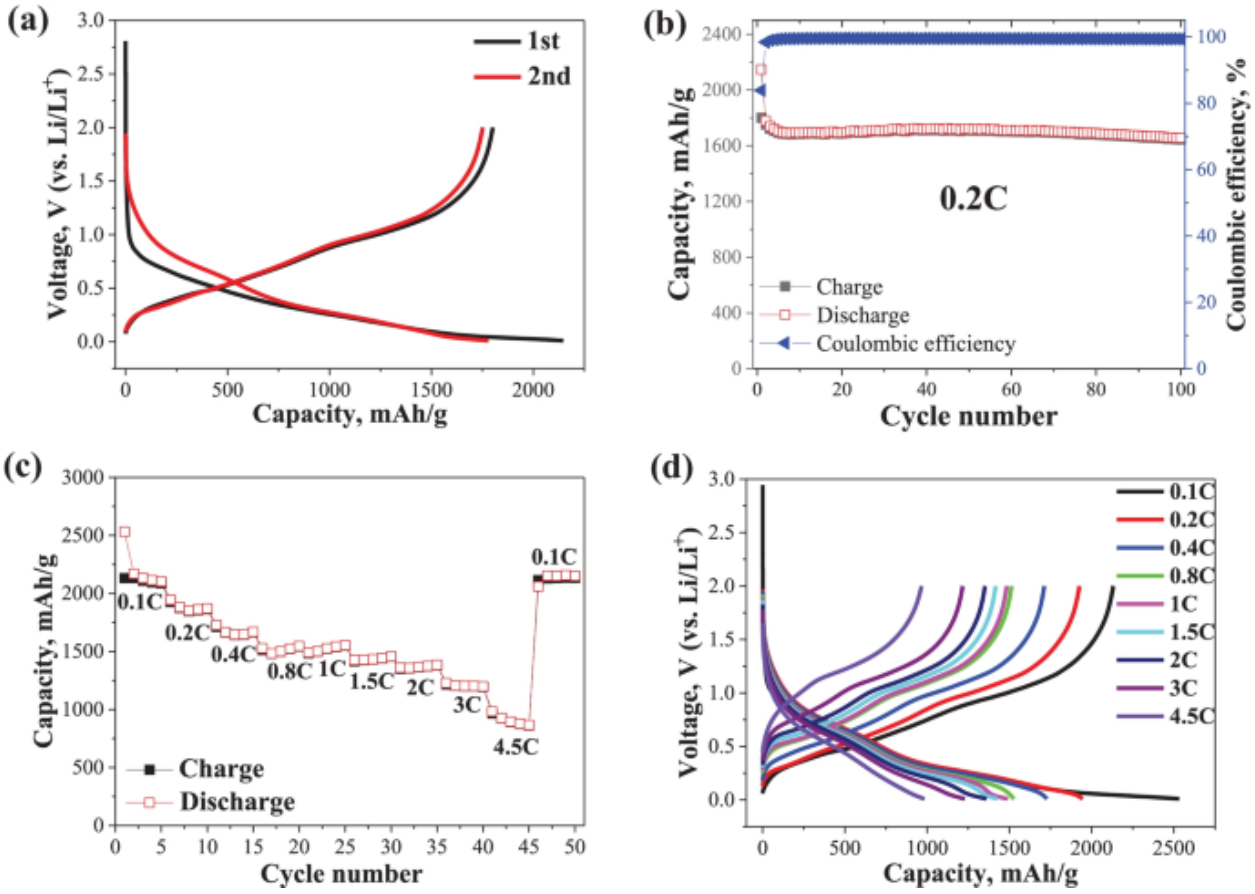

Figure 4.14: (a) Voltage profiles and (b) cycling performance of mSPC anode within 0.02–2.0 V at a charge/discharge rate of 0.2 C. (c) Rate capability and d the corresponding voltage profiles of the mSPC anode

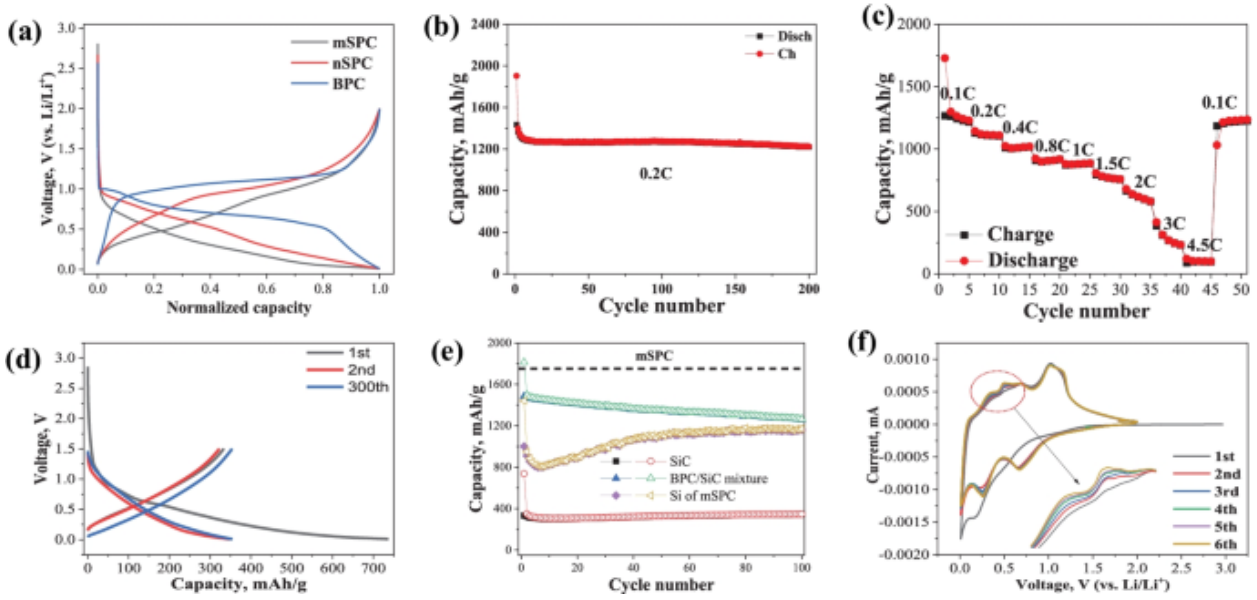

Figure 4.15: (a) Normalized voltage profile comparison of mSPC, nSPC, and BPC anode. (b) Cycling performance of nSPC anode at 0.2 C within 0.02–2.0 V; (c) rate performance of nSPC anode; (d) voltage profile and (e) cycling performance of SiC anode at 0.2 C; (f) cyclic voltammogram of mSPC anode at a scan rate of 0.1 $mV.s^{-1}$. The hollow and solid symbols in (e) represent discharge and charge capacity, respectively

mSPC, nSPC and BPC anode at 0.2 C. As shown, the BPC anode exhibits the highest $charge$ $(1.2\ V)/discharge$ $(0.75\ V)$ average working potential, while the mSPC anode presents the lowest $charge(0.75\ V)/discharge$ $(0.3\ V)$ average working potential. Surprisingly, the nSPC anode that is prepared by using nanometer-sized Si exhibits both higher charge $(1.0V)$ and discharge $(0.5V)$ average working potential than mSPC. Meanwhile, the nSPC anode delivers a lower reversible capacity of 1200 $mAh.g^{-1}$ at 0.2 C despite the excellent cycling stability for 200 cycles (Figure 4.15b). These two features have resulted in a lower energy density of nSPC anode than mSPC anode. Moreover, as shown in Figure 4.15c, the rate capability of nSPC anode is dramatically reduced compared to the mSPC anode. At the same charge/discharge rate of 4.5 C, the reversible capacity of the nSPC anode has dropped to 100 $mAh.g^{-1}$, which is only 1/10 of that of the mSPC anode. These results have indicated the importance of the microstructure/composition control in tuning the working potential, specific capacity, and rate capability of anode materials.

To further clarify the interaction between silicon and phosphorus, SiC composite without

phosphorus was synthesized by using micrometer-sized silicon and Ketjenblack-MWCNTs. As shown in Figure 4.15d, the as-prepared SiC anode delivers a stable but very low specific capacity of 350 $mAh.g^{-1}$ for 300 cycles at 0.2 C. If the mSPC is a physical mixture of SiC and BPC, the specific capacity of mSPC could be estimated based on their weight ratio of 0.332:0.368. As shown in Figure 4.15e, based on the specific capacity of SiC and BPC [244], the calculated specific capacity of SiC/BPC mixture are much lower than the measured capacity of mSPC. In another word, the practical capacity contribution of Si in the mSPC composite should be much higher than that of SiC, which gradually increased to around 1200 $mAh.g^{-1}$ after cycling. This is consistent with the cyclic voltammogram result of the mSPC anode. As shown in Figure 4.15f, the capacity contribution related to the (de) lithiation of phosphorus remain constant during continuous scan, while the intensity of red-ox peaks of Si is gradually enhanced upon cycling. The results indicate that the introduction of phosphorus itself not only contributed to the capacity, but also significantly boost the electrochemical utilization of Si in the mSPC anode during cycling. This might be due to the high electronic conductivity of black phosphorus, which can facilitate the electron transport of mSPC anode during charge/discharge. Previous study by Domi et al. has indicated that it is more difficult to insert Li into P-doped Si than in pure Si and led to lower specific capacity [265], which might be due to the much larger particle size of Si ($>$ 100 μm and 7-10 μm) in their work than ours ($<$ 100 nm).

Particle expansion/shrinkage is one of the critical barriers for the long-cycling of alloying-type anodes. In order to directly probe the volume changes of mSPC anode, we have used our custom-made in situ FIB-SEM to monitor its structural changes during charge/discharge at different current densities. Figure 4.16a shows the schematic image of our set up, in which the battery particle is attached to a W-probe and then is charged/discharged in ionic liquid electrolytes using a SourceMeter. Figure 4.16b shows the voltage-profiles of the mSPC particle during charge/discharge at 300 pA (C/10) within $0.02 - 2.0\ V$ for one cycle, later at 600 pA for another cycle, and eventually at 1500 pA for three cycles to compare the morphology

changes under fast charging. As shown, the charge/discharge profiles of single mSPC particle inside SEM is similar to that of coin cells, which can represent the volume changes of the particles in the electrode during charge/discharge. The particle was taken out at different charge/discharge states for FIB-SEM characterization. Figure 4.16c (i) and the zoomed-in view show the SEM images of mSPC particle before charge/discharge, which presents a secondary particle structure with a particle size of 10 μm, similar to that observed in the Figure C.2. After the first lithiation, as shown in Figure 4.16c (ii), we can see the particle was significantly expanded in comparison with the pristine one (marked by the dot red frame), which is due to the intake of lithium ions to form lithiated Si-P. When lithium was extracted during the charge process Figure 4.16c (iii), the particle was shrinking, which exhibited a slightly larger size than pristine mSPC particle before charge/discharge. Nevertheless, no obvious cracks were generated throughout the entire secondary particle. Even when further increasing the current density to 600 pA (Figure 4.16c(iV)) and 1500 pA (Figure 4.16c (V)), the mSPC still demonstrates good structural stability. This is in contrast with our previous results on micrometer-sized Sn [236], and Ge anode [266], which exhibited severe particle cracking and generation of nano-pores. These results clearly confirm the SPC anode demonstrates excellent mechanical and structural stability during lithiation/de-lithiation, which can benefit its long-term cycling stability and fast charging capability.

4.3.3 Conclusion

In summary, two types of silicon-phosphorus anode with similar hierarchical morphologies but different micro-structures were synthesized through high-energy ball-milling process, which exhibit significantly electrochemical behavior. The optimal mSPC anode that is prepared by using micrometer-sized Si as starting material could deliver a high specific capacity of $>$ 2000 $mAh.g^{-1}$ *at* 0.1 C at an average discharge working potential of 0.3 V versus lithium together with superior cycling stability and rate capability. While the nSPC that uses nanometer-sized Si as starting material demonstrates lower specific capacity and higher

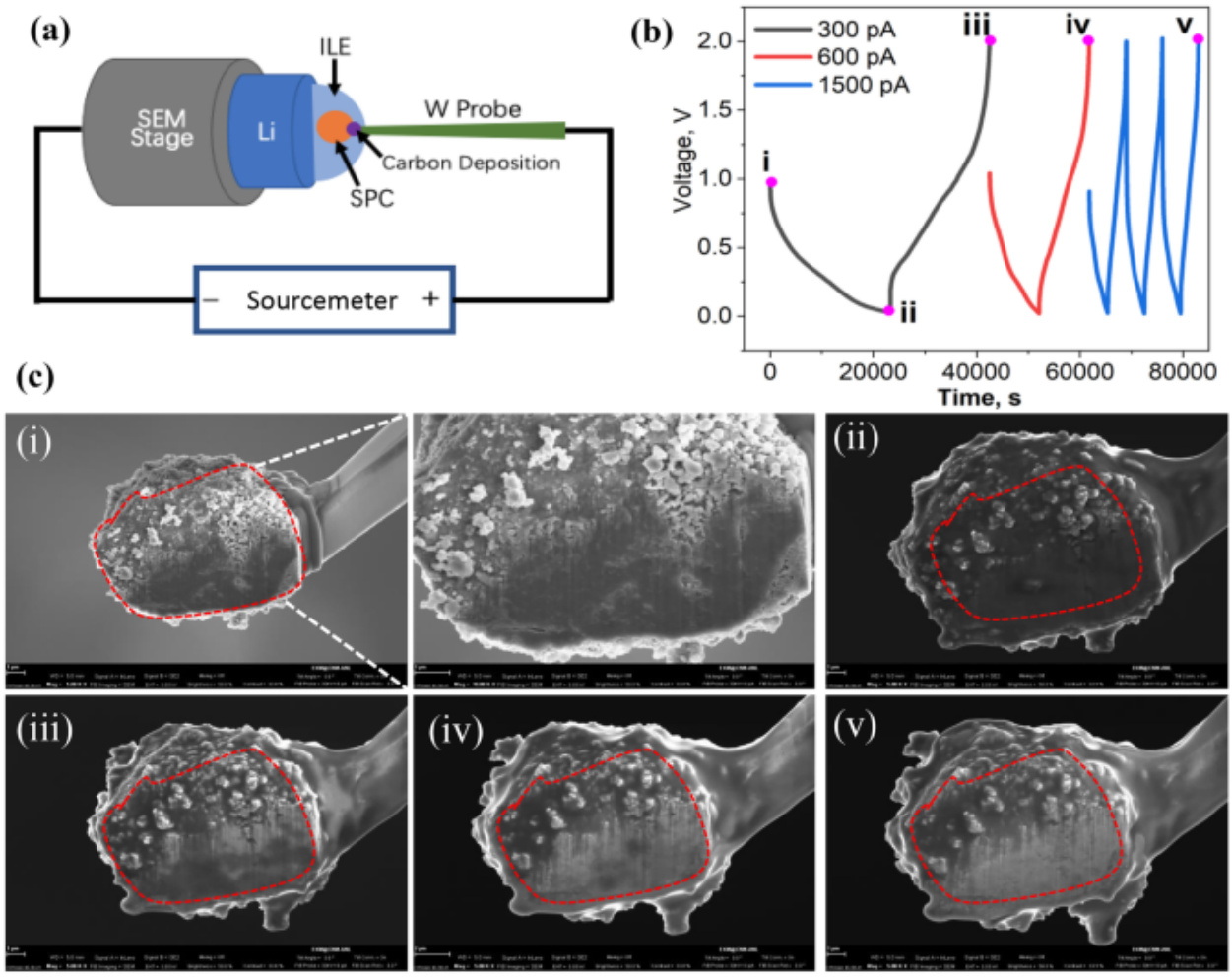

Figure 4.16: (a) Scheme for in situ FIB-SEM set up; (b) corresponding charge/discharge curves; (c) the corresponding in situ SEM images of a single mSPC particle. i, Pristine; ii, 1st discharge; iii, 1st charge; iv, 2nd charge; v, 5th charge

charge/discharge working potential than the mSPC, leading to dramatically reduced cell energy density. The results indicate that it is of critical importance to carefully control the micro-structures and compositions of binary anodes to tailor their specific capacity and working potential, and thus boost the energy density. Moreover, hierarchical micro/nano-structure is a good approach to mitigate the volume changes of alloying- type anodes for long-term cycling stability.

4.4 Case IV: In-Situ Microscopy and Spectroscopy Characterization of Microsized Sn Anode for Sodium Ion Batteries.

This work has been published[4].

4.4.1 Introduction

The depletion of fossil fuels, coupled with escalating greenhouse gas emissions and growing global awareness of the climate emergency, is driving advancements in diverse energy storage systems. Among these, lithium-ion batteries have emerged as the leading and most mature technology, proving to be pivotal for portable electronics and electric vehicles [81]. However, concerns regarding the limited and geographically disparate availability of lithium have cast shadows over the sustainability of the raw material supply chain in catering to the burgeoning energy demands [182, 183, 33]. Over recent decades, sodium-ion batteries (SIBs) have been at the forefront of research, largely due to the affordability and abundant nature of sodium [190]. Marking a significant milestone, 2021 saw the introduction of the first-generation commercial SIBs, equipped with a Prussian blue cathode and hard carbon anode, with an energy density of approximately 160 $Wh.kg^{-1}$ [267]. While the hard carbon anode is a staple in the industry, it is not without its limitations, particularly its constrained specific capacity and the risk of sodium dendrite formation during rapid charging [268, 269]. To enhance the energy density and bolster the safety credentials of SIBs, there's an imperative need to innovate and develop high-capacity anode materials with optimal working potential.

Alloy-based anodes, including elements like Sn [270], Sb [149], and P [224], have garnered substantial interest in recent times. Notably, Sn, which is recognized for its eco-friendliness, and a theoretical capacity of 847 $mAh.g^{-1}$, derived from its full sodiation product, $Na_{15}Sn_4$

[4]doi: 10.1016/j.nanoen.2023.108753

[22]. Additionally, Sn operates at an average potential range of $0.2 - 0.3V$ against sodium, striking a balance between energy density and safety considerations. Nevertheless, Sn is not without its challenges. During the sodiation and de-sodiation processes, Sn undergoes a substantial volume change, approximately 420%, which results in electrode pulverization, particle cracking, and consequently, a loss of both electrical and ionic connectivity. This leads to a pronounced decline in capacity over successive cycles [271, 272, 161]. To counter these setbacks, the industry turned to nano-structured alloys, known for their fracture resistance [273, 274, 275, 94]. Yet, these materials present their own set of challenges. Their inherently low density translates to decreased volumetric energy density in batteries. Additionally, these nanosized materials often come with high production costs, complexities in synthesis, and challenges in scalability. Another significant concern is their expansive surface area, which tends to cause excessive electrolyte decomposition and fosters the growth of a thick solid-electrolyte interphase (SEI).

Recently, micro-sized materials have emerged as a compelling alternative that could potentially address the challenges faced by their nano counterparts. Several innovations have been brought to the fore to enhance the longevity of micro-sized Sn anodes. These include self-healing chemistry [276, 277], phase structure control [278], the incorporation of bimetallic alloys [279], and voltage regulation techniques [280]. Furthermore, accurate electrolyte engineering to influence the formation and properties of the solid-electrolyte interphase (SEI) has demonstrated favorable outcomes in stabilizing micro-sized Sn anodes [69, 70, 127, 281].

However, even with these advancements, a comprehensive understanding of the intricate underlying mechanisms remains obscured. This is largely attributed to the lack of in-situ tools capable of effectively monitoring the nuanced structural and morphological transformations of micro-sized Sn anodes during their charge/discharge cycles. For instance, while in-situ Transmission Electron Microscopy (TEM) has been a popular choice for studying volumetric alterations in nanostructured anodes, it falls short when applied to micro-sized materials due

to its inherent resolution constraints [282, 283]. A pressing question that remains unanswered is the impact of the pronounced volume changes in micro-sized Sn anodes on the subsequent formation of the SEI and how this, in turn, influences the kinetics and reversibility of the sodiation and de-sodiation processes.

In this study, we undertake a detailed analysis of micro-sized Sn anodes for sodium-ion batteries, focusing on their behavior during charge/discharge processes in both ether-based and carbonate-based electrolyte systems. Employing a custom-built in situ scanning electron microscopy (SEM), in conjunction with in-situ synchrotron X-ray absorption spectroscopy (XAS) and X-ray photoelectron spectroscopy (XPS), we meticulously probed the morphological evolutions, shifts in oxidation states, and alterations in local bond structures. Furthermore, we delved into the composition and distribution of the solid-electrolyte interphase (SEI) on the micro-sized Sn anode throughout the sodiation and de-sodiation phases.

Despite the large mechanical cracking of micro-sized Sn anode, ether electrolytes can enable the formation of inorganic species-dominated SEI with improved mechanical strength for cracked particles. It can, therefore, ensure the intimate ion and electron transport, thus promoting the sodiation/de-sodiation kinetics and reversibility. Our results highlight the importance of interface engineering to circumvent the electro-chemo-mechanical breakdown of micro-sized anode materials towards higher energy density and longer cycle life.

4.4.2 Experimental Section

1. **Electrode and electrolytes:** Microsized Sn powder (Sigma-Aldrich, 99% trace metals basis) was used directly without further treatment. To fabricate Sn laminate, the Sn powder was then mixed with conductive carbon (C45) and Poly (acrylic acid) (LiPAA) (9.8 $wt\%$ aqueous solution) binder [284] with a weight ratio of 7:2:1. The mixed slurry was applied to the copper current collector, then dried in a vacuum oven at $80°C\ for\ 24\ h$ to remove moisture before battery assembly. The Sn electrodes were punched out with a diameter of 9/16 inch. The loading of active Sn in the electrode was

controlled at about $1.5 - 2.0\ mg.cm^{-2}$. The ether-based electrolyte used in this work is composed of 1 $M\ NaCF_3SO_3$ in Tetraglyme, while the carbonate based electrolyte is 1 $M\ NaPF_6$ in Propylene Carbonate (PC) solvent with FEC (5 $wt\%$).

2. **Structure characterization and Electrochemical tests:** The tap density of micro-sized Sn powder is measured by Autotap of Quantachrome Instruments. The morphology of Sn powder was observed using a field emission Scanning Electron Microscope (SEM) (HITACHI S-4700- II). The as-prepared electrodes were characterized by assembling them into coin cells (type CR2032) inside an Argon-filled glovebox with the level of moisture and oxygen both below 0.5 ppm. A glass fiber (GF/D, Whatman) was used as the separator. Metallic sodium was used as a counter electrode with adding 50 μL of either ether-based or carbonate-based electrolyte. The galvanostatic charge/discharge was tested on a LAND battery testing system with a voltage range of $0.02 - 2.0V$ ($vs.\ Na/Na^+$). X-ray photoelectron spectroscopy (XPS) was carried out on a PHI 5000 VersaProbe II spectrometer. C-C peak at 284.8 eV was used as the reference peak for calibration. The discharged (0.02 V) electrodes used for XPS tests were washed with dimethyl carbonate (DMC), then transferred to the XPS chamber. Depth profiling was collected with controlled Ar^+ sputtering time.

3. **In Situ X-ray Absorption Near Edge Spectroscopy:** The in-situ Sn K-edge X-ray absorption spectroscopy during charge/discharge of microsized Sn electrode in two electrolytes was carried out in transmission mode at Beamline 20-BM-B of the APS. The incident beam was monochromatized by using a Si(111) fixed-exit, double-crystal monochromator. During the in situ experiment, a MACCOR cycler was used to charge/discharge the cell using a constant current density of 90 $mA.g^{-1}$ $within$ $0.02 - 2.0V$ ($vs.\ Na/Na^+$).

4. **In situ SEM during charge/discharge:** The setup of the in situ SEM for a single Sn particle during charge/discharge can be found in the previous work [236, 238, 244,

58, 285]. Typically, to build a single- particle battery cell, a microsized Sn particle was attached to a tungsten probe by ion beam carbon deposition as the positive electrode. Sodium metal was placed on top of the SEM stub as the negative electrode. One drop of ionic liquid electrolyte (ILE) consisting of 10 $wt.\%$ NaTFSI and 90 $wt.\%$ 1-butyl-1-methylpyrrolidinium bis(trifluoromethylsulfonyl) imide ($P_{14}TFSI$) was placed on top of the sodium metal. The single-particle battery cycling was controlled by a Keithley 6430 sub-femtoamp remote SourceMeter from Tektronix with a constant current of 150 pA. The particle was immersed in the ILE drop during cycling and lifted out for imaging at different states of charge and discharge.

4.4.3 Results and Discussions

The morphologies of micro-sized Sn used in this work were examined by SEM. As shown in Figure 4.17A and B, it exhibits micro-sized spherical particles with a majority of particle size of around 1-2 μm. Compared to the conventional nano-sized Sn particles, the micro-sized Sn particles can increase the volumetric energy density due to its high tap density of 3.18 g/cc, which however suffer from large volume change during sodiation/de-sodiation, and thus significantly challenges the cycling stability.

To investigate the morphological changes of micro-sized Sn particles during charge/discharge, we have used the home-built in-situ focused-ion-beam (FIB) SEM (see Experimental section for details) to track micro-structure evolution. Figure 4.17C shows the corresponding voltage curve of single micro-sized Sn particle during charge/discharge at 150 pA, which exhibits characteristic electrochemical behavior of conventional Sn anode [69]. The morphologies of the particle were taken at different charge/discharge states (D-H). As shown, before discharge, the particle shows a compact spherical shape with a diameter of around 10 μm. However, particle expansion and severe cracks at both surface and interior of the particle were observed after discharged to 50% depth of discharge (Figure 4.17E) due to intake of sodium to form Na_xSn, and further propagated during discharged to 0.02 V (Figure

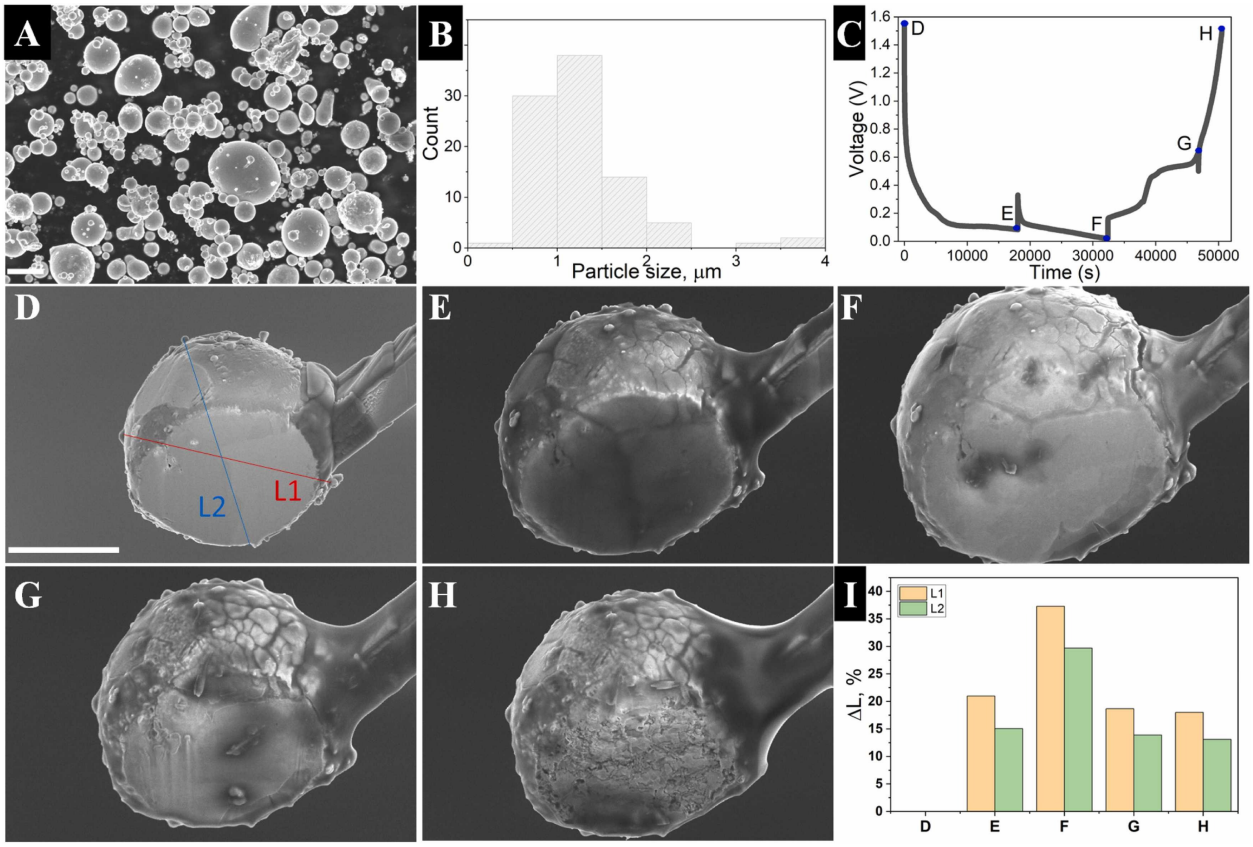

Figure 4.17: (A) SEM images and the corresponding size histogram of microsized Sn powder. (C-H) The initial charge/discharge curve and the corresponding SEM images of single Sn particle during in-situ SEM experiment. (I) Variation percentage of length in L1 and L2 direction (D) at different charge/discharge states. The scale bars in Fig. 1 are 5 μm.

4.17F). Upon charge (Figure 4.17G and H), the particle started to shrink, and formation of nano-particles can be clearly seen. Figure 4.17I shows the length variation of the particle along L1 and L2 direction at different charge/discharge states, which reveals that the particle significantly expanded $(30-40\%)$, and did not return to the original shape, leaving much residual stress inside the particles. To clearly visualize the micro-structures of the particle after charge, we used FIB polishing to obtain the 3D structure throughout the particle. As shown Video 1 Appendix D, the particle became highly porous after only one cycle of charge/discharge, and numerous pores and voids appeared at the surface and outer surface of the particle. This should be due to the better access of electrons and ions at the surface, leading to formation of more pores and voids after lithiation/de-lithiation. We can expect that the micro-sized particle will eventually pulverize into nano-particles during continuous cycling and cause severe capacity loss.

The newly exposed surface and the high surface area of nano-particles will aggravate the parasitic reactions with the electrolytes, and significantly change the composition and micro-structures of SEI, further undermining the mechanical stability and the ion/electron transport at the solid-liquid interface. The formulation of electrolytes (salts, solvents, and additives) would thus play a critical role in the resulted SEI and thus electrochemical performance. Ether-based and carbonate-based electrolytes are the two most common electrolytes for sodium-ion batteries [35]. We therefore have conducted a comparative study on the correlation between SEI and the electrochemical red-ox reaction behavior of micro-sized Sn anode. The electrolytes are 1 M $NaCF_3SO_3$ in tetraglyme (ether-based) and 1 M $NaPF_6$ in PC with $5wt.\%$ FEC additive (carbonate), respectively.

First of all, we used in-depth XPS to examine the derived SEI of micro-sized Sn electrode after discharged to 0.02 V in two electrolytes. As shown in Figure 4.18A and B, before etching, the two electrolytes exhibit similar components in the SEI. There are five deconvoluted C1s peaks that are correlated to different species present in the derived SEI [70, 127, 281], including: (1) 283.0 eV for the sp2 carbon from conductive carbon; (2) 284.7 eV for the C-C

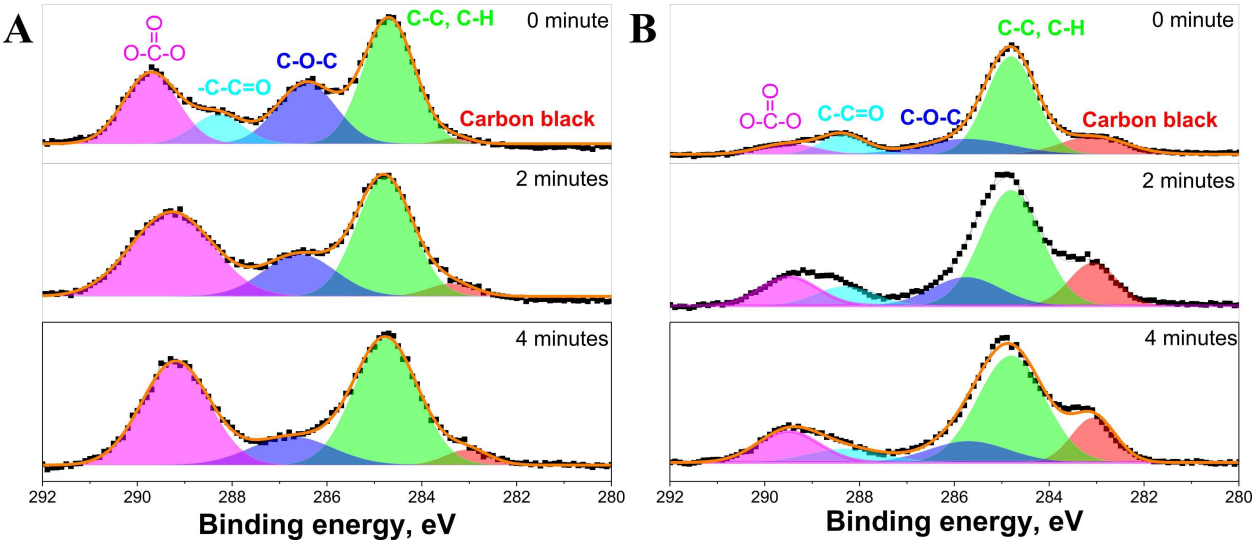

Figure 4.18: Depth profile of C1s XPS spectra of discharged (0.02 V) microsized Sn electrode in (A) ether-based and (B) carbonate-based electrolytes.

or C-H bonds, corresponding to the formation of sodium alkoxides (RCH_2ONa) groups due to the reduction of tetraglyme; (3) 286.5 eV for C-O-C bonds; (4) 288.3 eV for the O=C-C environments, (5) 289.5 eV for the carbonate (Na_2CO_3). Overall, the derived SEI in two electrolytes is composed of both organic (e.g., RCH_2ONa) and inorganic (e.g., Na_2CO_3) species, while the proportions are significantly different, indicating distinct SEI formation process. As shown, in the case of ether-based electrolytes, after etching, the fraction of inorganic Na_2CO_3 gradually increased, while the organic species decreased. The results indicated that the organic species are mainly distributed at the surface, while the inorganic components dominate the inner parts of ether-derived SEI. By sharp contrast, in the case of carbonated electrolytes, the derived SEI is organic species dominated and much thicker, as evidenced by the strong peaks of organic species and slight changes during etching. It has been shown that the ether derived oligomers pose better mechanical flexibility than alkyl carbonate derived from carbonate-based electrolyte [70, 127, 281]. This aspect renders the electrode more tolerant to volume change and can thus lead to improved different electrochemical performance during cycling.

The electrochemical performance of micro-sized Sn anode was evaluated in coin cells

using sodium metal as reference and counter electrode and charged/discharged at a constant current density of 90 $mA.g^{-1}$ *within* $0.02 - 2.0$ V ($vs.$ Na/Na^{+}). Figure 4.19A shows the first two cycles of charge/discharge curves during cycling in the ether-based electrolytes. The initial discharge and charge capacity of micro-sized Sn anode were measured to be 1013.1 $mAh.g^{-1}$ *and* 924.6 $mAh.g^{-1}$, respectively, leading to a high initial coulombic efficiency of 91.3%. The initial sodium inventory loss remains a critical challenge for the practical application of many anode materials [286, 249]. Nevertheless, the ether-derived SEI has enabled a much lower initial irreversible capacity loss compared to the nanostructured Sn anodes [94, 65, 63, 287, 288, 289], highlighting the importance of interface control. The extra discharge capacity in the first cycle is attributed to the decomposition of electrolytes to form solid-electrolyte interphase on micro-sized Sn anode [58]. The results also indicate that the initial coulombic efficiency of alloying-type anode materials is highly determined by the parasitic reactions with the electrolytes. In the case of carbonate electrolytes, a much lower specific capacity (417 $mAh.g^{-1}$) and initial Coulombic efficiency (73%) were attained (Figure 4.19B), which should be directly related to the high thickness and organic-dominated species of the carbonate-derived SEI. The higher fraction of organic species and the larger thickness might significantly slow down the ion/electron transfer at the interface. Meanwhile, it is worth mentioning that 659 $mAh.g^{-1}$ out of 924 $mAhg^{-1}$ (72% of total capacity) is achieved below 0.5 V in the ether-based electrolytes, which is beneficial for improving the energy density of the battery for practical usage, while only 30% of the specific capacity was achieved below 0.5 V in the case of carbonate electrolytes. In both electrolytes, it can be seen that the coulombic efficiency after the 1st cycle remains lower than 100%, which are attributed to the parasitic reactions of cracked particles with the electrolytes. Figure 4.19C compares the initial differential capacity (dQ/dV) curves of micro-sized Sn anode in two electrolytes. The main discharge capacity was contributed by multiple plateaus below 0.25 V, which corresponds to the formation of Na_xSn $(x < 1)$, $NaSn$, Na_9Sn_4 *and* $Na_{15}Sn_4$ phases. During the charge process, four peaks located at 0.15, 0.27, 0.53, 0.65 V are matched with the dealloying

process. By comparing the results in two electrolytes, it can be found that micro-sized Sn anode suffers from larger voltage polarization and thus incomplete sodiation/desodiation. Figure 4.19D shows the corresponding cycling performance of micro-sized Sn anode in two electrolytes. After 20 cycles, micro-sized Sn anode can still maintain a specific capacity of $>$ 400 $mAh.g^{-1}$ in the ether-based electrolytes, while only 60 $mAh.g^{-1}$ in the carbonate-based electrolytes. Such degradation could come from two parts: (1) electronic/ionic isolation of active material due to the pulverization of particles; (2) depletion of electrolytes due to continuous parasitic reactions with the newly exposed surface. Noted that micro-sized Sn particles were directly used without ball milling to reduce the particle size. Thus, the volume change remains a critical challenge for the long-term cycling stability. There might be a critical size effect, which will be further studied in the future to achieve long-term cycling stability. Nevertheless, the significant difference between two electrolytes during the first sodiation/desodiation of micro-sized Sn anode serves as a solid evidence for the correlation between SEI and electrochemical behavior.

To clearly reveal the underlying mechanism, in-situ synchrotron Sn K-edge XAS including X-ray absorption near edge spectroscopy (XANES) and extended X-ray Absorption Fine Structure (EXAFS) during charge/discharge of micro-sized Sn anode in two electrolytes were conducted. In particular, XANES is sensitive to the electronic changes and/or oxidation state of all the atoms of the targeted type in the samples regardless of phase structure and crystallinity, while EXAFS can probe the bond structure and local coordination environment [290]. Figure 4.20A shows the 2D contour plot of in-situ Sn K-edge XANES spectra along with the corresponding charge/discharge curve at 90 $mA.g^{-1}$ in the case of ether-based electrolyte. The color represents the normalized absorption intensity, with red and blue meaning high and low, respectively. The charge/discharge curve of in-situ battery is similar to that of electrochemical evaluation, indicating the observed phenomenon could reflect the underlying electrochemical reactions. As shown, the absorption edge gradually shifted to higher energy during discharge, while reversibly shifted back during the charge process. In general, positive

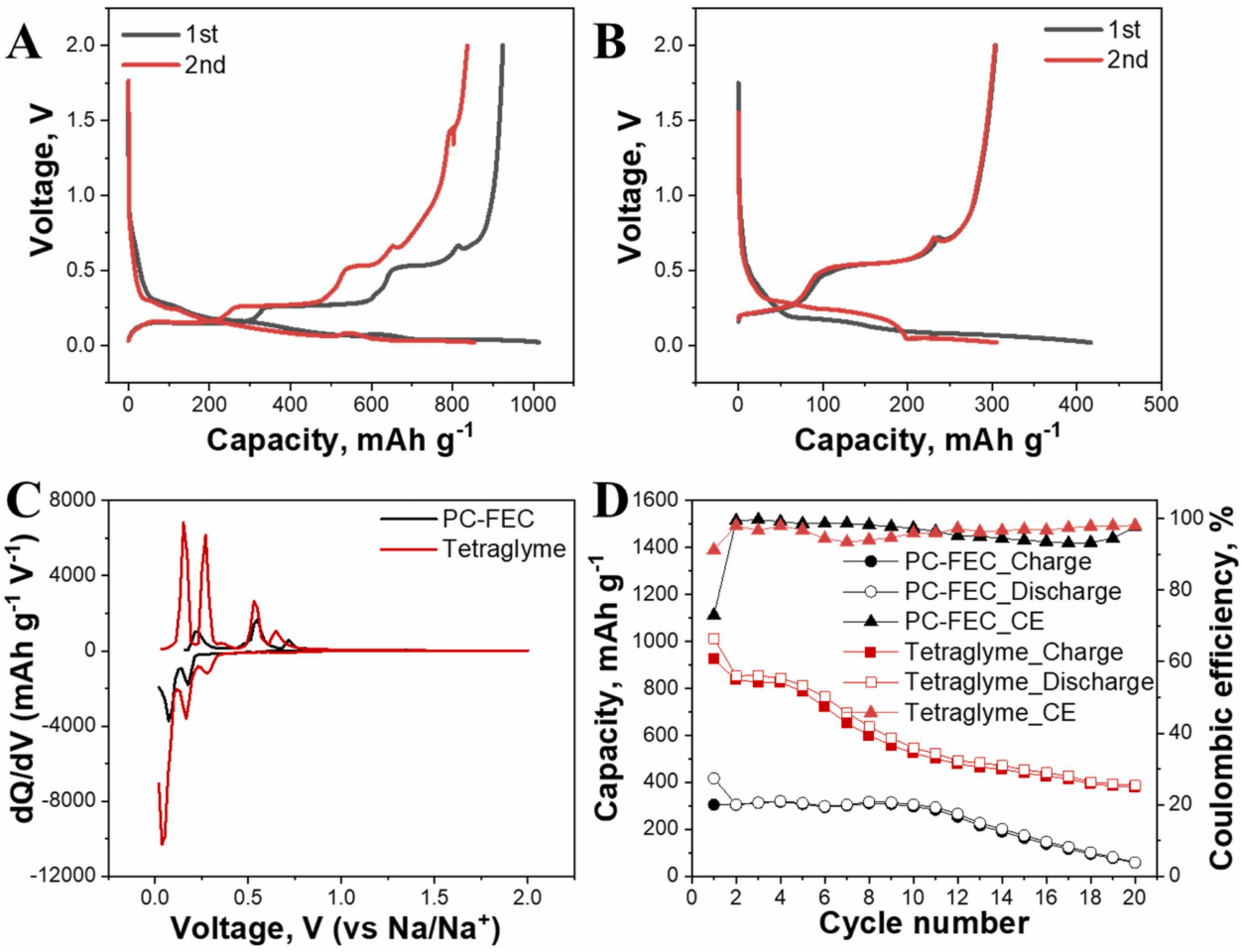

Figure 4.19: Charge/discharge curves of microsized Sn electrode during cycling in (A) ether-based and (B) carbonate-based electrolytes at 90 $mA.g^{-1}$. (C) The corresponding initial dQ/dV curve and (D) cycling performance of micro-sized Sn electrode in two electrolytes.

shift corresponds to the oxidation of the element, vice versa. Nevertheless, the edge shift of Sn might be attributed to the reduced screening effect due to alloying between Na and Sn, similar as the case of S and Se with Li [291]. The representative Sn K-edge XANES spectra of pristine micro-sized Sn electrode, after 1st discharge and 1st charge are shown in Figure 4.20B. The Sn XANES spectrum at the pristine state reassembles that of Sn foil and shifted to higher edge together with decreased white line intensity after 1st discharge, indicating changes in the average local coordination [292]. After the 1st charge, the XANES spectrum can be almost recovered to the pristine state, leading to the high initial coulombic efficiency of micro-sized Sn anode. The process can be seen more clearly on the in situ Sn K-edge XANES spectra at different discharge (Figure 4.20C) and charge states (Figure 4.20D). In brief, micro-sized Sn anode exhibits highly reversible sodiation/desodiation process during the first cycle. By contrast, when charge/discharge in carbonate electrolyte (Figure 4.20E and H), a much distinct edge-shift together with a lower specific capacity were observed, confirming that the reaction between sodium and Sn in the carbonate electrolytes is less complete and reversible.

To further explore the chemical states and coordination environment of the Sn atoms in both electrolytes, in-situ Sn K-edge EXAFS during charge/discharge of micro-sized Sn anode was conducted and analyzed. Figure 4.21A shows the 2D contour plot of in-situ EXAFS spectra along with the corresponding charge/discharge curve at 90 $mA.g^{-1}$ in the case of ether-based electrolyte. As shown, the inflection point in the contour plot is consistent well with the critical point in the fully discharge state. The good symmetry of the data set with reversible intensity reduction/increase during discharge/charge indicates a highly reversible sodiation/desodiation process of micro-sized Sn anode in ether-based electrolytes. The represented Sn K-edge EXAFS spectra at different charge/discharge states are shown in Figure 4.21B-D. The pristine electrode exhibits a characteristic peak of Sn-Sn bond at about 2.77 A, matching well with that of Sn foil [293]. During sodiation, the amplitude of this peak gradually decreased, indicating an amorphization of the crystal structure [292]. At

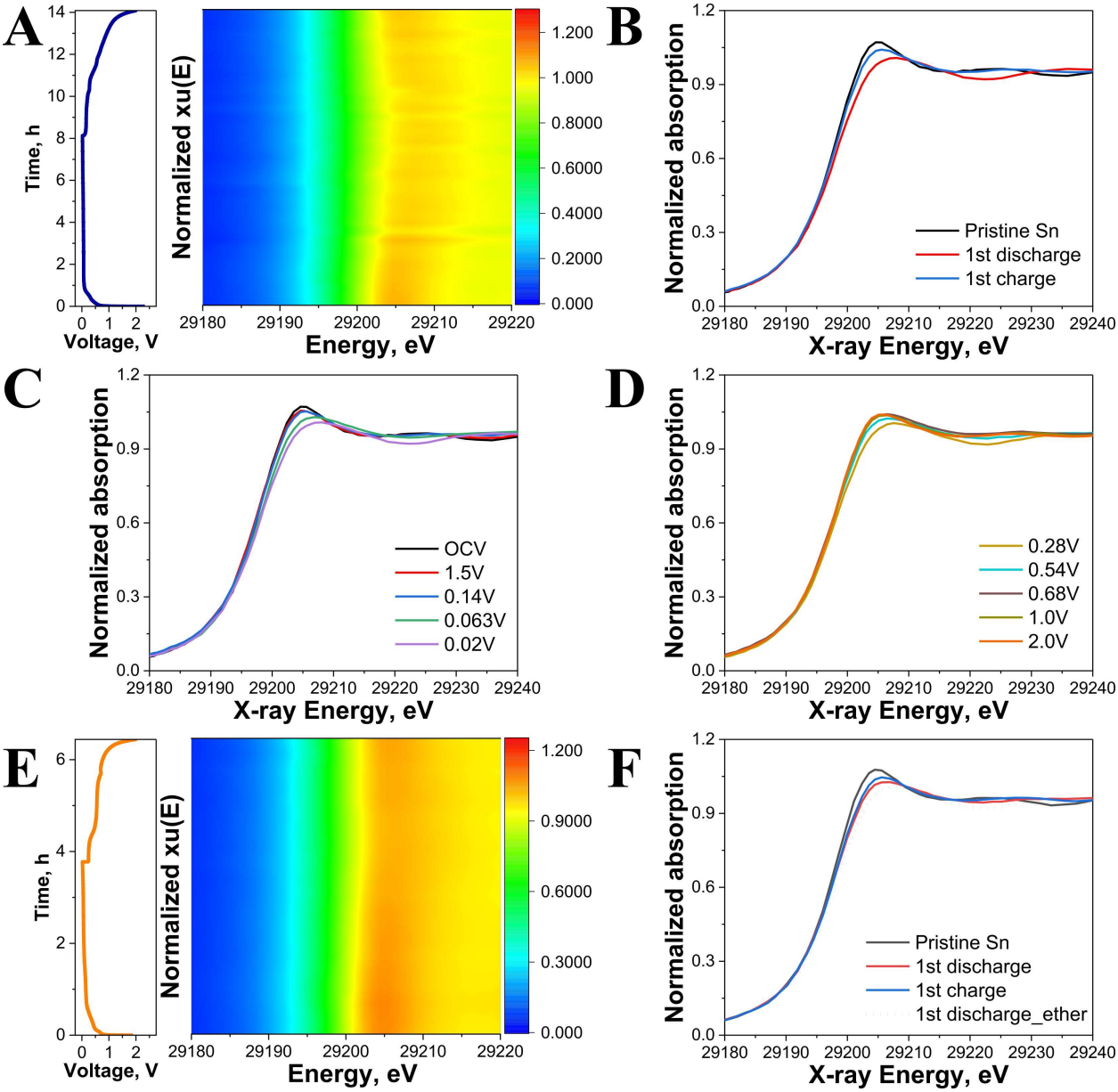

Figure 4.20: (A) 2D contour plot of in situ Sn K-edge XANES data of microsized Sn anode during charge/discharge in ether-based electrolytes. (B) The corresponding Sn K-edge XANES spectra for the pristine electrode, first discharge state and first charge state. Typical Sn K-edge XANES spectra collected at different potential during the first (C) discharge and (D) charge process. (E) 2D contour plot of in situ Sn K-edge XANES data of microsized Sn anode during charge/discharge in carbonate-based electrolytes. (F) The corresponding Sn K-edge XANES spectra for the pristine electrode, first discharge state and first charge state. The color in (A) and (E) represents the normalized absorption intensity.

a discharge voltage of 0.14 V that corresponds to the onset potential of sodiation, the peak broadening was observed, which eventually evolved into two broad peaks with significantly reduced intensity at the end of discharge (0.02 V). This should be due to the alloying process between Na and Sn, which changed the local coordination environment of Sn atoms, a process similar to the lithiation of Sn-based anode [294]. Nevertheless, during the charge process, the characteristic peak of Sn-Sn bond was gradually recovered and almost reassembled the pristine one at the end of charge process. In the case of carbonate-based electrolytes (Figure 4.21E and F), the Sn-Sn bond of pristine Sn electrode undergo a significantly less reduction during discharge, corresponding to the incomplete sodiation of micro-sized Sn anode and the lower specific capacity. The results indicate that the SEI of anode material can greatly regulate the interfacial ion/electron transport, and thus the bulk electrochemical behavior.

4.4.4 Conclusions

In summary, this study spots the light on the importance of a well and suitable design of the solid-electrolyte interphase (SEI) for improving the performance of micro-sized alloying anodes. In-situ microscopy study revealed that micro-sized Sn anode undergoes severe mechanical deformation, leading to generation of nano-particles together with numerous pores and voids at the very beginning of cycling. X-ray photoelectron spectroscopy and in-situ X-ray absorption spectroscopy further demonstrated a strong correlation between SEI and bulk electrochemical behavior. Specifically, compared to carbonate electrolytes, ether-based electrolytes enabled formation of inorganic species dominated SEI with improved mechanical strength and interfacial charge transport, leading to higher initial coulombic efficiency and improved cycling stability. This work paves the way to improving the micro-sized alloying anode materials for rechargeable batteries with high volumetric energy density.

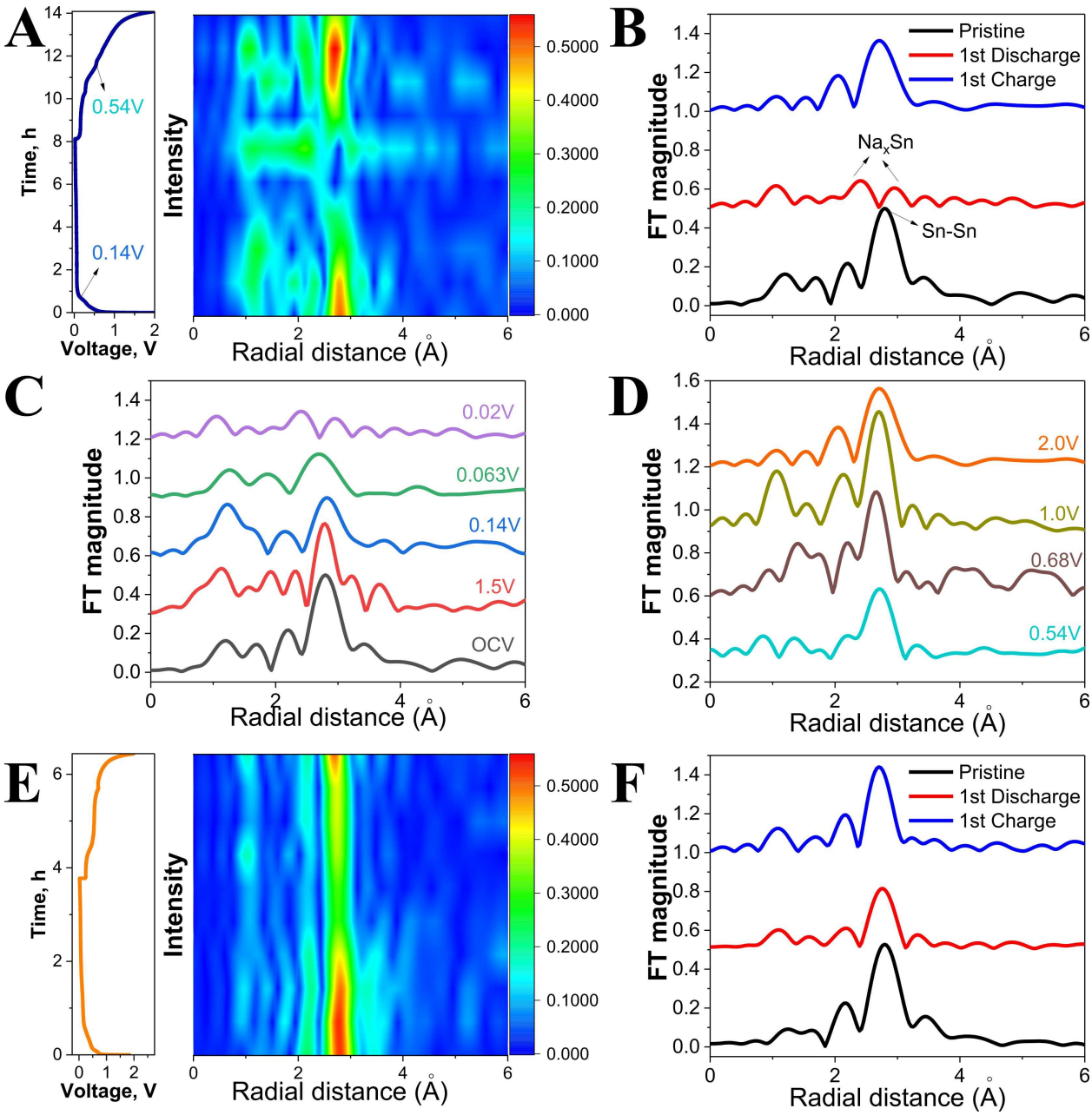

Figure 4.21: A) 2D contour plot of in situ Sn K-edge EXAFS data of microsized Sn anode during charge/discharge in ether-based electrolytes. (B) The corresponding Sn K-edge EXAFS spectra for the pristine electrode, first discharge state and first charge state. Typical Sn K-edge EXAFS spectra collected at different potential during the first (C) discharge and (D) charge process. (E) 2D contour plot of in situ Sn K-edge EXAFS data of microsized Sn anode during charge/discharge in carbonate-based electrolytes. (F) The corresponding Sn K-edge EXAFS spectra for the pristine electrode, first discharge state and first charge state. The color in (A) and (E) represents the normalized absorption intensity.

Chapter 5

Manufacturing-Recycling-Economic assessment

Research has highlighted the detrimental environmental effects of carbon-based energy sources, particularly their role in exhausting fossil fuel reserves and significantly contributing to the elevation of CO_2 levels, a leading factor of global warming. The necessity for a shift towards an economy devoid of fossil fuel dependency is mandatory, aiming to curtail reliance on carbon-intensive energy solutions while enhancing the deployment of renewable energy alternatives. In pursuit of this paradigm shift, international bodies and regulatory authorities have fervently advocated for the adoption of measures aimed at reducing CO_2 emissions. Notable initiatives such as the United Nations' Paris Climate Agreement of 2015, China's ambition for Carbon Neutrality by 2060, and the Climate Act of Sweden in 2017 illustrate the global commitment to this cause. This concerted effort has facilitated advancements in energy storage and conversion technologies, notably through the increased utilization of rechargeable batteries and the push towards electrification to bolster renewable energy infrastructures. LIBs, recognized for their superior energy storage and efficiency, have emerged as pivotal in powering portable electronics and electric vehicles and supporting renewable energy grids [10]. The worldwide demand for batteries has increased steadily, with approximately 960

GWh of batteries being demanded between 2020 and 2021 and around 7-10 million tons of batteries being produced as a result. The battery market is expected to grow exponentially in subsequent years, with projections indicating that it will surpass 3,200 GWh by 2030 (Fig 5.1a) [295, 296]. The reliance on LIBs alone is unsustainable in meeting the burgeoning demand for battery technology, as current projections of consumption suggest that the world's lithium reserves could be exhausted within the next century [297]. The dearth of economically viable lithium reserves has raised the alarm for the security of worldwide energy resources, leading to a pressing need for alternatives and diversifications of battery technologies that rely on more abundant metals. In recent years, researchers have become increasingly interested in metals such as aluminum, calcium, magnesium, potassium, sodium, and zinc for use in ion batteries as the price of lithium continues to soar [22, 298, 299] (Fig 5.1b). Leveraging metal reserves for ion battery production represents a strategic approach to sustaining long-term global energy security.

SIBs have gained prominence as a highly viable alternative to LIBs, primarily because of their analogous cell architecture and operational mechanisms. Additionally, the scalability of SIBs, facilitated by the utilization of pre-existing manufacturing infrastructures established for LIBs, positions them as an advantageous option for deployment in electric vehicles and energy storage systems. This compatibility and the potential for seamless integration into current production lines enhance the appeal of SIBs as a complementary energy storage solution, underscoring their role in advancing the diversification of battery technologies [300, 19]. A pivotal advantage of SIBs is that sodium is a highly abundant element in the Earth's crust, with a concentration of 23,000 ppm (2.3%), making it a cost-effective material for battery production. In contrast, lithium's concentration is much lower at 20 ppm, making it a considerably more expensive option. In 2022, the price of battery-grade lithium carbonate was over 200 times more expensive than sodium carbonate, costing US$78,000 per ton versus US$350 per ton, respectively.

Additionally, SIBs exhibit excellent safety features and can be paired with a diverse

Table 5.1: Projected cumulative world battery material demand to 2025 (1000 tons).

Elements	**Projected Demand**		**USGS reserves**
	If all NMC is low Co (811)	**If all NMC is high Co (111)**	
Li	230	230	16000
Co	790	910	7100
Ni	580	340	74000

range of electrode materials. These electrode systems are generally devoid of Lithium (Li) and Cobalt (Co) and composed of low-cost materials. The use of cobalt was obviously identified as a cause for concern. Based on estimates in cathode demand forecasts (Table 5.1, the world's cumulative demand for batteries alone (excluding other cobalt markets) is projected to consume roughly 10% of the available reserves through 2025 [301]. This significant demand has already had an observable impact on the cost of cobalt, which has skyrocketed to exorbitant heights.

Moreover, concerns regarding child labor in the Democratic Republic of the Congo, where cobalt mining is most prevalent, have prompted battery manufacturers to reformulate cathodes to reduce their dependence on cobalt and increase their reliance on nickel. Currently, cobalt constitutes 90% of the $55 per kilogram cost of high-cobalt cathodes (LCO) but only 30% of the $17 cost of new, lower-cobalt formulations (NMC811). Due to heightened apprehension about cobalt, recycling has emerged as a potentially viable source of materials and has garnered increased attention. On the other hand, sodium ions exhibit a low reactivity with aluminum (Al) metal within the standard operational parameters of SIBs. This characteristic permits the exclusive use of Al as the only metal source needed in SIBs [19, 301, 302].

SIBs have garnered attention for commercialization from several companies, such as Contemporary Amperex Technology (CATL, China), Natron Energy (USA), and Tiamat (France). These batteries exhibit energy densities ranging from 100 $Whkg^{-1}$ to 160 $Whkg^{-1}$, a range that is comparable to $LiFePO_4$ batteries [303]. As such, SIBs are predicted to supplant conventional lead-acid batteries and encroach upon the market share of lithium-ion batteries, especially in applications like low-speed electric vehicles, home energy storage grids,

and systems supporting renewable energy sources. Market analysis forecasts a rapid expansion in the SIB sector over the forthcoming decade. From a baseline demand of approximately 12 GWh in 2023, projections suggest an increase to 500 GWh by 2030 (Fig 5.1c). This surge in demand could result in SIBs capturing over 20% of the total battery market share. This growth is largely attributed to their utilization in large-scale energy storage systems and the electric vehicle industry. With advancements in energy density and the exploration of new commercial uses for SIBs, market analysts predict a potential surge in demand of up to 2 TWh, contingent upon the successful resolution of existing safety concerns. This outlook reflects the significant potential of SIBs to impact the battery market profoundly, driven by their advantages in safety, cost-effectiveness, and energy density [304].

SIBs, much like LIBs, have a significant disadvantage: they possess a relatively short lifespan. Typically, SIBs have an average service life of 2-5 years due to capacity deterioration over time and the eventual obsolescence of the battery devices themselves. The challenge of recycling spent SIBs mirrors that of LIBs; however, it is compounded by the absence of high-value metals such as lithium (Li) and cobalt (Co), which serve as incentives for the recycling and resource recovery processes in LIBs. This lack of valuable materials in SIBs poses a significant economic hurdle to their recycling efforts, raising concerns about the potential for accumulating waste from spent SIBs (Fig 5.1d). To mitigate this risk, it is imperative that advancements in both manufacturing and recycling technologies for SIBs proceed hand in hand with their commercial roll-out, mirroring the developmental trajectory observed with LIBs. Addressing these challenges is crucial for ensuring the long-term viability and environmental sustainability of SIB technology by minimizing waste and promoting the circular use of resources.

Recycling lithium-ion batteries (LIBs) has been a focal point since their commercialization, with significant efforts invested towards developing modern recycling methodologies[305, 306, 307]. More recently, innovative approaches for the manufacture and recycling of valuable materials from advanced batteries and their components, including solid-state batteries [308],

polymer electrolytes [309], and liquid electrolytes [310], have been presented. These techniques are believed to greatly enhance the sustainability of LIBs and other ion battery technologies, paving the way for the SIB industry. Moreover, the experiences and insights gained from LIBs can be effectively utilized to formulate streamlined and effective strategies for SIBs that are tailored to their individual characteristics.

This Chapter focuses on delineating the key phases involved in the manufacturing and recycling of materials and components in LIBs and SIBs and their corresponding implications for the industrial and environmental sectors.

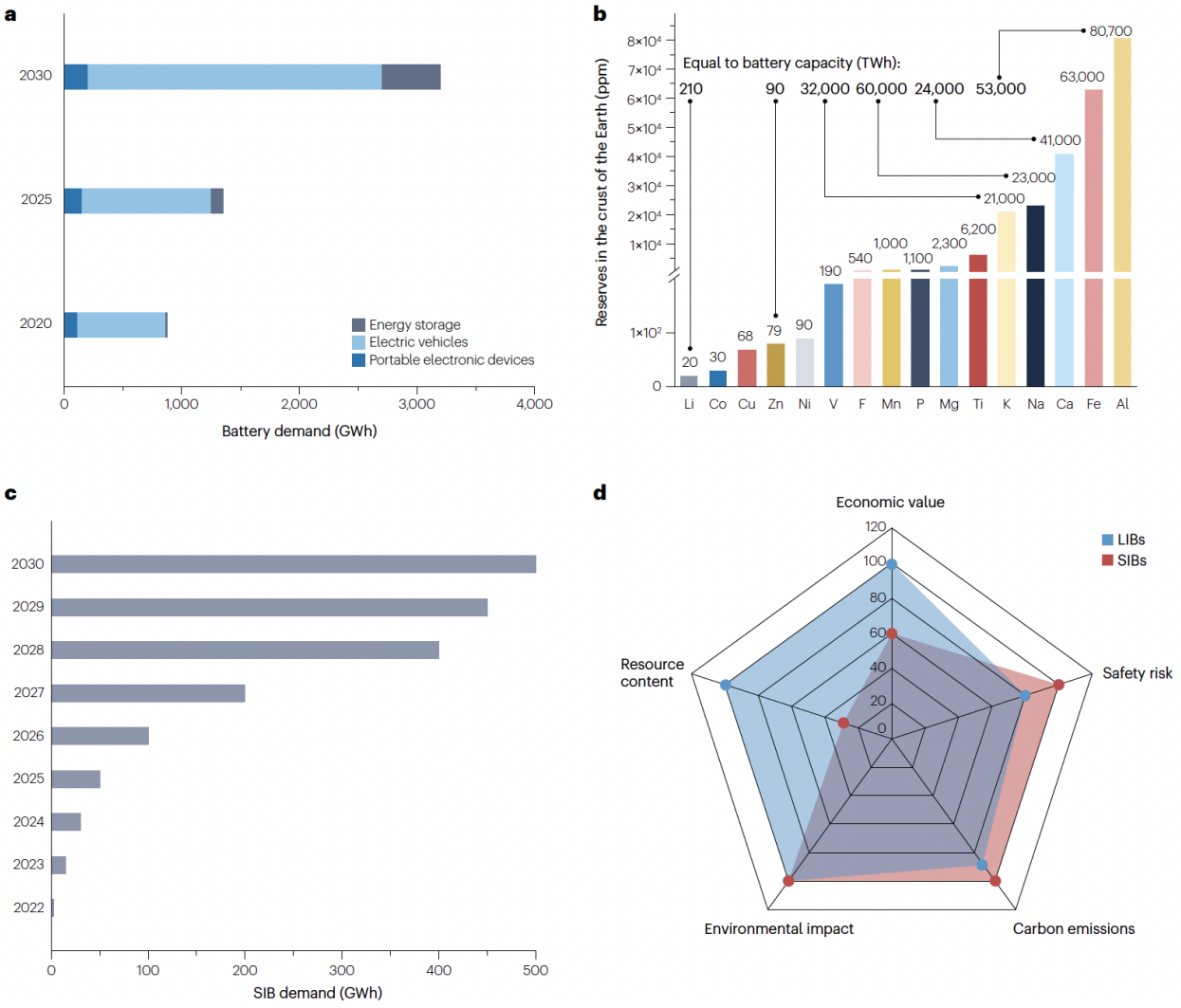

Figure 5.1: a) The projected battery demand (GWh) for energy storage systems, electric vehicles and portable electronic devices from 2020 to 2030. b) The estimated total battery capacity (TWh) available for manufacturing by metal reserves in the crust of the Earth (ppm). c) The predicted demand (GWh) for SIBs from 2020 to 2030. d) A radar chart indicates the resource content, cell economic value, safety risk, carbon emissions and environmental impact for 1kg of spent lithium-ion batteries (LIBs) and sodium-ion batteries (SIBs) (Zhao et al.[296]).

5.1 Manufacturing

Most research related to LIBs has been mainly centered on investigating appropriate active electrode materials and electrolytes that are better suited for high cutoff voltage applications. This investigative focus encompasses the development of cathode materials that are either rich in nickel or devoid of cobalt, alongside anodes made from silicon or lithium metal and their corresponding electrolytes. Although the manufacturing processes represent around 25% of LIBs' overall cost, much progress in this area has yet to be made [311]. The production of LIBs is a complex, multi-stage procedure that encompasses slurry mixing, coating, drying, calendaring, slitting, vacuum drying, and the creation of the jelly roll design through stacking (for pouch cells) or winding (for cylindrical and prismatic cells). This process continues with welding, packaging, electrolyte filling, formation, and aging. Despite the widespread adoption of this manufacturing sequence within the industry, substantial opportunities for enhancement remain. The intricacies of each step offer potential avenues for innovation, aiming to streamline operations, reduce costs, and improve the overall efficiency and quality of the batteries. Addressing these areas of improvement could significantly impact the scalability and sustainability of LIB production, reflecting the ongoing need for technological advancements and process optimizations in the field.

The manufacturing methodology for LIBs was initially developed for batteries intended for consumer electronics. Over time, this foundation has facilitated the transfer of numerous mature technologies to the forefront of contemporary LIB production. Despite the variety in cell designs employed by different LIB manufacturers—including cylindrical (e.g., Panasonic's design for Tesla), pouch (as used by LG Chem, A123 Systems, and SK Innovation), and prismatic formats (e.g., Samsung SDI and CATL)—the underlying production methods across these designs share remarkable similarities. This standardization reflects the industry's ability to adapt and evolve production techniques to meet diverse application requirements while maintaining efficiency and quality.

Figure 5.2 [312] illustrates the current state-of-the-art process for manufacturing batteries, which can be succinctly categorized into three primary phases: electrode preparation, cell assembly, and the activation of battery electrochemistry. Initially, a homogeneous slurry comprising the active material (AM), conductive additive, and binder is synthesized by blending these constituents with an appropriate solvent. Specifically, for the cathode, the binder polyvinylidene fluoride (PVDF) is dissolved in N-methyl-2-pyrrolidone (NMP), while for the anode, styrene-butadiene rubber (SBR) binder is dissolved in a water and carboxymethyl cellulose (CMC) mixture. This slurry is then uniformly applied to both of the surfaces of the current collectors (aluminum foil for the cathode and copper foil for the anode) using a slot die coating method, followed by a drying process to evaporate the solvent. The use of NMP as the solvent for the cathode presents environmental and health challenges due to its toxicity and the strict regulations governing its emissions. Consequently, the drying stage incorporates a solvent recovery mechanism, allowing for the recirculation of NMP in the production process, albeit with a 20% to 30% loss [313]. In contrast, the water-based solvent used for the anode produces benign vapors that can be safely released into the environment without additional processing. The calendaring process that follows serves to refine the physical properties of the electrodes, such as porosity, bonding, density, and conductivity, thereby enhancing the battery's overall performance and longevity.

Upon completing the various processes involved in making electrodes, they are then subject to stamping and slitting to meet the necessary dimensions for cell design. In the next phase, the prepared electrodes undergo a vacuum treatment to remove any residual moisture, a crucial step aimed at minimizing potential side reactions and corrosion within the cell. Following this moisture reduction, the electrodes' moisture content is meticulously measured to ensure optimal conditions. The dry electrodes, alongside the separators, are then transported to a controlled environment known as a dry room, marking the beginning of cell assembly. The internal configuration of the cell is meticulously constructed by alternately layering the electrodes and separators. This assembly process involves the precise alignment and

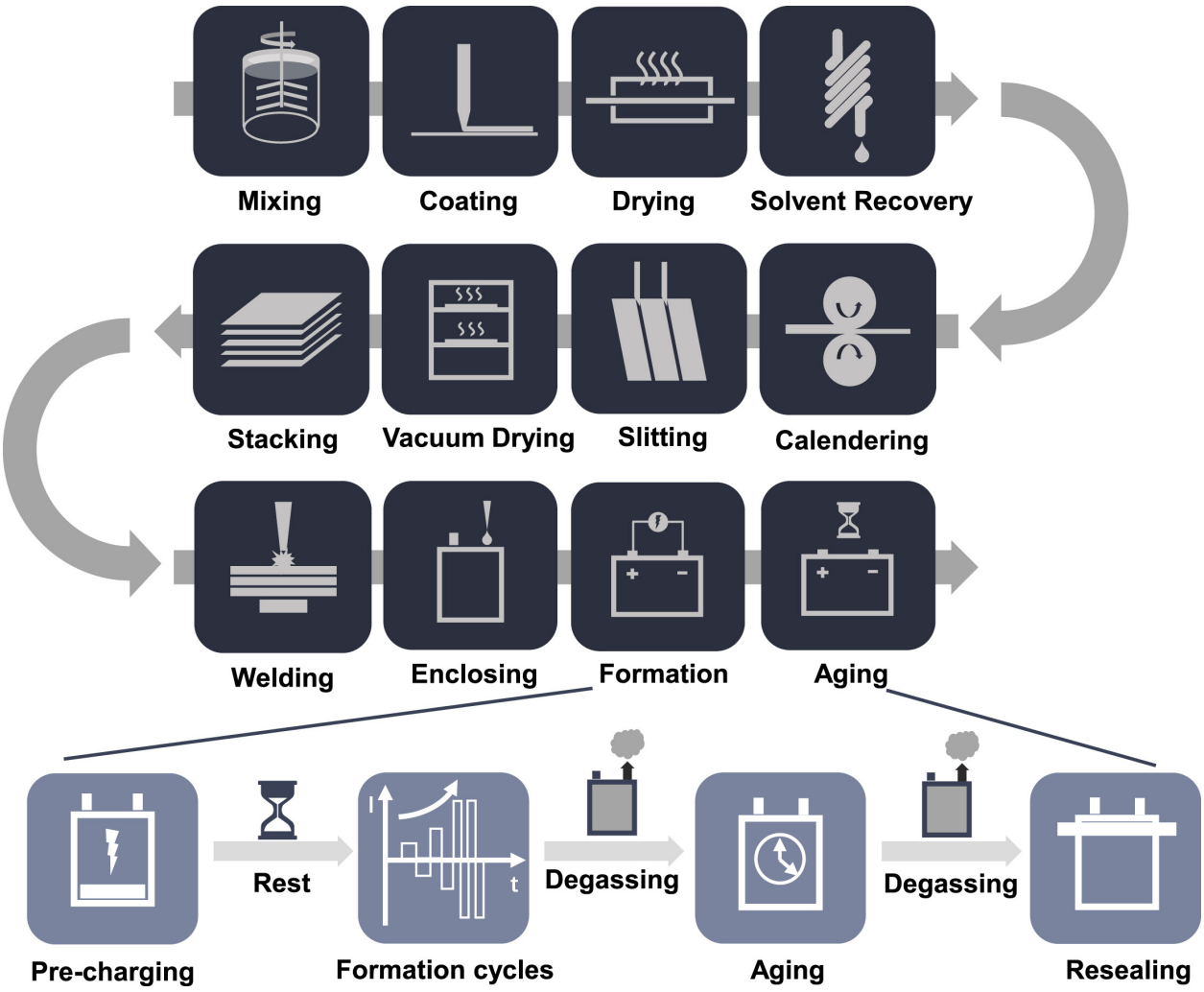

Figure 5.2: Schematic of LIB manufacturing processes (Liu et al. [312]).

stacking of these components, with the cathode and anode being connected to their respective current collectors using aluminum and copper tabs. The connection is typically achieved through ultrasonic welding, a method favored for its reliability and efficiency, although some manufacturers may opt for alternative techniques, such as resistance welding, depending on specific requirements or preferences. Once the electrode-separator stack, or 'cell stack', is complete, it is carefully housed within a casing designed according to the specific application needs of the cells. This is a critical juncture where the cell's final form factor is determined, be it cylindrical, pouch, or prismatic; the electrolyte is then introduced to the enclosure. The cell assembly process culminates with the sealing of the cell, securing the electrolyte within, and marking the completion of the physical construction of the battery.

In order to ensure operational stability, cells intended for use in end-product manufacturing undergo electrochemistry activation procedures. The creation of a stable solid electrolyte interphase (SEI) layer is a critical step in this process, as it is crucial for preventing the irreversible loss of electrolytes and shielding the anode against overpotential scenarios during rapid charging processes. Such conditions could precipitate the formation of lithium dendrites, posing significant safety risks [56]. The formation and aging procedure commences with an initial charge to the cells at a low voltage threshold, approximately 1.5V, to protect the copper current collector from corrosive damage. This is followed by a resting phase to allow for thorough wetting of the electrolyte. Subsequently, the cells undergo a series of charging and discharging cycles starting at a low rate, typically C/20, with the rate incrementally increased to foster the formation of a robust and stable SEI layer atop the anode [154]. A critical safety protocol during this process involves the venting of any gases produced during the formation cycles to mitigate the risk of pressure build-up within the cells. Following the formation cycles, the cells are allocated time on aging shelves, promoting the comprehensive wetting of the electrolyte and stabilization of the SEI layer. An additional degassing step may be conducted before or during this period to further ensure safety. The cells are then sealed, marking the completion of their preparation. The duration of the aging process is

Table 5.2: Cost and throughput of LIB manufacturing processes

Manufacturing Processes	**Cost per year/$***	**Percentage**	**Throughput**
Slurry mixing	7,396,000	7.91%	30min-5h
Coating/drying	13,984,000	14.96%	35-80 m/min
Solvent recovery	4,296,000	4.60%	NA
Calendering	4,849,000	5.19%	60-100 m/min
Slitting	2,891,000	3.09%	80-150 m/min
Vacuum drying	2,990,000	3.20%	12-30 h
Stacking	8,086,000	8.65%	NA
Welding	6,864,000	7.34%	NA
Enclosing	11,636,000	12.45%	Depend on the cell design
Formation/aging	30,482,750	32.61%	Up to 1.5-3 weeks

- **The manufacturing cost includes equipment depreciation, labor cost, and plant floor space cost.*
- *The labor cost was calculated based on the US average factory worker's salary of $15/h.*
- *The floor space cost was calculated based on* $\$3,000/m^2$ *per year (includes rent, utility, and management)*
- *The depreciation cost was calculated by 16.7% of capital investment and 5% of floor space cost.*

contingent upon the specific formation protocol and the temperature conditions under which aging occurs, often spanning several weeks.

In determining the areas of manufacturing that necessitate further research and innovation, it is essential to estimate the cost, throughput, and energy consumption of each step involved. Such an evaluation helps in pinpointing where efforts should be concentrated to address the most significant challenges. According to the BatPac model developed by the Argonne National Laboratory, the manufacturing cost breakdown for a 67 Ah $LiNi_{0.6}Mn_{0.2}-Co_{0.2}O_2$ (NMC622)/graphite cell with a 100,000 EV battery packs/year plant is presented in Table 5.2 and Figure 5.3A [314]. According to this model, the processes of electrode mixing, coating, drying, cell formation, and aging collectively constitute over 48% of the total manufacturing cost. This insight underscores these stages as not only the most expensive but also as the areas

Table 5.3: Energy consumption of LIB manufacturing processes

Manufacturing Processes	Energy Consumption per cell/kWh	percentage
Slurry mixing	0.11	0.83%
Coating	0.18	1.36%
Drying/solvent recovery	6.22	46.84%
Calendering	0.38	2.86%
Slitting	0.71	5.35%
Stacking	0.77	5.8%
Welding	0.25	1.88%
Enclosing	0.69	5.20%
Formation/ aging	0.07	0.53%
Dry room	3.9	29.37%

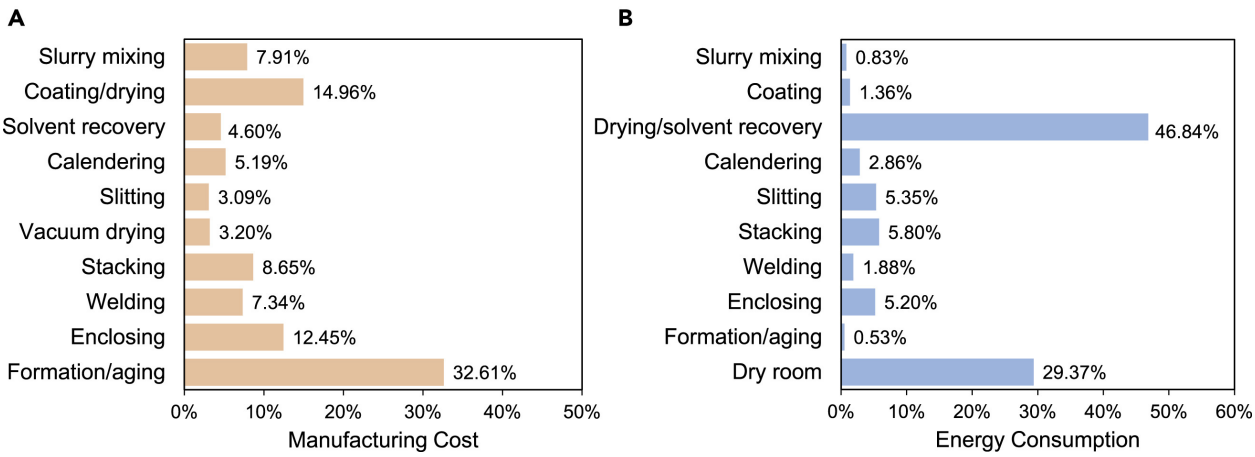

Figure 5.3: Cost and energy consumption breakdown of LIB manufacturing processes:(A) Cost breakdown and (B) energy consumption breakdown (Liu et al. [312]).

demanding substantial capital investment and labor, highlighting them as prime candidates for innovation and optimization. Transferring laboratory novelties to these manufacturing methods could lead to major cost efficiency.

The correlation between throughput and manufacturing cost is indisputable. Enhanced productivity not only saves labor expenses but also reduces expenditures on rented venues. Table 5.2 displays the distribution of production time and indicates the throughput. Roll-to-roll manufacturing techniques, such as coating, calendaring, and slitting, stand out with an impressive throughput exceeding 35 m/min. Conversely, stages like vacuum drying and formation/aging are time-intensive. These stages are characterized by strict moisture control and the need to manage sensitive chemical reactions carefully, resulting in durations that can extend up to three weeks. The lengthy nature of these processes is primarily due to the critical importance of ensuring the chemical stability and integrity of the batteries, which in turn affects their performance and lifespan [315].

Yuan et al. (2017) [316] conducted a study on the energy consumption of a 32-Ah lithium manganese oxide (LMO)/graphite cell production at Johnson Control Inc.'s industrial pilot-scale manufacturing facility. The findings, depicted in Table 5.3 and Figure 5.3B, reveal that the drying and solvent recovery phase stands out as the most energy-intensive segment of the production process, accounting for approximately 47% of the total energy consumption. This high level of energy usage is attributed to the need for prolonged heating to dry the electrode coatings and the subsequent cooling of off-gases during solvent recovery. Another significant area of energy consumption identified in the study is the dry room, which is responsible for 29% of the overall energy usage. The strict control of moisture levels during cell assembly in the dry room necessitates a substantial amount of energy to maintain the required low-humidity environment. These energy-intensive stages not only increase the overall production costs but also contribute to higher greenhouse gas emissions, potentially diminishing the environmental benefits of LIBs. Therefore, reducing the amount of solvent used or eliminating its use should be the primary focus for battery production. Moreover,

innovations aimed at improving the efficiency of maintaining low moisture levels in the dry room could further reduce the energy footprint of LIB production.

Upon examination, it is evident that certain stages of the manufacturing process bear a significant impact on the cost, energy consumption, and throughput involved in fabricating LIBs. Therefore, manufacturing innovation must be implemented to achieve substantial reductions in production cost and energy consumption while simultaneously increasing the overall throughput.

5.2 Recycling

The escalating interest in electric vehicles (EVs) and energy storage systems (ESS) within the United States has significantly amplified the necessity for critical battery components such as cobalt, nickel, and lithium. Regrettably, the domestic reserves of these essential minerals are sparse. An analysis of the reserve estimates by the U.S. Geological Service, juxtaposed with the material requirements for manufacturing EVs equipped with Lithium-ion batteries featuring NMC622 cathodes (as detailed in Table 5.4 [317]), reveals a stark insufficiency in the supply of nickel and cobalt to fulfill the needs of the domestic annual automobile production. This production is estimated at approximately 10 million units, presuming a complete transition to electric vehicles. Additionally, these batteries serve various other applications, creating parallel demands for these resources. While potential exists for increasing domestic supplies, such increments would come at a heightened cost. Consequently, the United States finds itself in a position of substantial dependence on the importation of these critical minerals.

While the United States lithium reserves present a more optimistic outlook, it is essential to note that prior to the emergence of the South American salars, the U.S. was a primary provider of this material. Nevertheless, insufficient investment in mining and conversion over several decades has resulted in a prolonged timeframe before the country can fully capitalize on its existing resources. As a result, recycling has gained importance as a supplementary source, given its potential to alleviate the necessity for new materials.

Table 5.4: Potential for U.S. reserves

Element	**Kg/Car (100 kWh)**	**U.S.A Reserves (kT)**	**World Reserves (kT)**	**Nbre for U.S.A (M)***	**Nbre for World (B)****
Co	15.4	69	8300	4.5	0.54
Ni	46.3	370	>100,000	8.0	2.2
Li	9.4	1000	26,000	107	2.8
*M: Million **B: Billion					

Numerous studies have been conducted to determine critical materials' global and/or regional supply potential by recycling LIBs. However, there appears to be a lack of consensus in the academic community regarding the definition of battery recycling rates and associated concepts. Furthermore, realizing that batteries have a limited lifespan and could become a challenging waste stream is only beginning to dawn on people. A recent study [318] estimated that one million electric vehicles sold in 2017 will produce 250,000 tons of waste once they reach the end of their lives. While there is no overwhelming stockpile of waste just yet, steps must be taken to prevent such a scenario from occurring. The practice of simply stockpiling used batteries until a more definitive recycling or disposal solution is identified poses significant risks. Incidents of fires and explosions at waste storage facilities and during transport have been attributed to the inherent volatility of LIBs. Additionally, there have been reports of fires and explosions at recycling facilities caused by LIBs concealed within pallets, an action often motivated by the desire to evade disposal fees [301]. These concerns spotlight the critical need for the development of sustainable and safe practices for the disposal and recycling of LIBs at the end of their life.

Repurposing used batteries, particularly those from EVs, for a "second life" in less demanding applications presents an intriguing strategy to address sustainability challenges. This approach capitalizes on the residual storage capacity of batteries that may no longer meet the performance standards required for EVs, typically when their capacity falls to around 80% of the original specification. Utilities, businesses, or households could potentially employ these batteries for energy storage, leveraging off-peak generated electricity for use during peak demand times or even to power EV charging stations, thus maximizing the utility of the battery's life cycle. However, the transition of a battery from its primary use in an EV to a secondary application is not straightforward. It necessitates rigorous testing to evaluate remaining capacity and overall health, reconfiguration to suit the new application, and the installation of an appropriate battery management system (BMS) tailored to its new role. These requirements can escalate the costs associated with repurposing, often rendering the

reused battery more expensive than a new one, especially in a market where battery prices are continually decreasing and the lifespan of a repurposed battery remains uncertain. One solution to this issue could involve designing batteries specifically for reuse, such as developing a programmable BMS that allows for easy adaptation of batteries to new applications, as well as designing battery modules that are conducive to recovery and repurposing [319].

As batteries inevitably reach the end of their functional life, it's crucial to recognize that they still house valuable materials that are ripe for recycling. The establishment of a robust recycling infrastructure is vital in preparing for the expected increase in battery disposal. Although several recycling facilities are operational, the majority of LIBs currently being retired are smaller consumer cells, which suffer from low collection rates [320]. Nobel Laureate Akira Yoshino underscored the significance of battery recycling as a critical component of the strategy to meet the surging demand for electric vehicles. Recycling these materials is not just a matter of waste management; it presents a strategic opportunity to diminish the reliance on imported critical materials, thereby contributing to the stabilization of material prices. Furthermore, recycling can significantly reduce the energy consumption and emissions associated with the production of new batteries, offering a pathway to decrease overall battery costs [321].

The topic of recycling has been the subject of frequent and varied discussion in the media and among different interest groups. However, the terminologies used in these discussions are often imprecise. It is necessary first to establish some fundamental concepts to address this issue. To clarify, when a product falls short of performing its intended function satisfactorily, several strategies can be employed to prolong its utility. These strategies encompass repairing or refurbishing the product to its original condition or, alternatively, repurposing it for a task that demands less from its capabilities. Although such measures are beneficial, their applicability is finite, leading to the eventual necessity of recycling the product. Recycling entails the collection and reprocessing of a used product into valuable materials, which then can be utilized in the fabrication of new products or to enhance the quality of existing ones,

distinctly without resorting to incineration for energy recovery. The critical metric for gauging the effectiveness of recycling efforts is the recycling rate. This rate is calculated by dividing the mass of the recycled material by the total mass of the material that has become obsolete or discarded, expressed as a percentage. This rate aims to quantify the proportion of material from a specific category of products manufactured within a certain timeframe and place that is successfully reintegrated into productive use after the product's lifecycle concludes. Yet, accurately assessing this rate for lithium-ion batteries poses a challenge, especially in evaluating the quantity of generated or out-of-service material. It is essential to recognize that not all collected material undergoes processing and recycling, further complicating the calculation of recycling rates [317].

The recycling process of LIBs encompasses a complex procedure that necessitates considerable energy or chemical resources, thereby invoking questions about the genuine environmental benefits of such processes. While numerous life cycle assessment (LCA) studies have meticulously examined the manufacturing and utilization phases of LIBs, the end-of-life (EOL) stage often remains underexplored [322, 323]. It is generally acknowledged that the assembly and usage phases exert the most substantial influence on the battery's life cycle environmental footprint. Nonetheless, an efficient recycling process, by mitigating the need for virgin raw materials, can markedly diminish the overall environmental impact of batteries. Indeed, this diminution might become a pivotal factor in determining the ecological competitiveness of specific battery technologies [324]. However, the LCA studies incorporating recycling phases frequently depend on broad, indeterminate assumptions, such as undifferentiated mixed battery waste streams or generalized recycling methodologies. The scarcity of detailed life cycle inventory (LCI) data sharing poses a significant barrier to refining process models for new or varied cell chemistries. The existing emphasis in publishing such information often lies in gauging the environmental efficiency of recycling methods or in comparing different techniques rather than in the comparison of diverse cell chemistries. As a result, these analyses typically scrutinize only a handful of cell chemistries, thereby constraining

the applicability and relevance of the findings. This limitation becomes particularly flagrant when considering the importance of cell chemistry in selecting the most suitable battery type for specific applications. Thus, the development of a recycling model tailored specifically to LIBs, with the capacity to adapt to emerging or future battery technologies like SIB or KIB, is essential. Such a model would not only facilitate a more precise assessment of various battery types but also enhance our understanding of their respective environmental impacts. This approach would significantly contribute to the strategic selection of battery technologies, ensuring that environmental considerations are duly integrated into the decision-making process for battery recycling and overall lifecycle management [325].

Chen et al.[326] provide a comprehensive portrayal of the recycling methods utilized for lithium-ion batteries (LIBs), as well as ongoing efforts to enhance their efficacy and environmental sustainability. Figure 5.4 depicts a conceptual diagram outlining the three principal recycling processes under scrutiny [319]. Among these, pyrometallurgical recycling, or smelting, emerges as the most extensive process. This method essentially treats used batteries as raw ore, necessitating the replication of all processing steps involved in ore refinement. In the pyrometallurgical approach, batteries undergo minimal pre-conditioning before being fed into a high-temperature furnace (EV batteries might require disassembly into modules). The organic components of the battery combust, generating the heat necessary for the process, while the most valuable metals—cobalt, nickel, and copper—are reduced and extracted as an alloy mixture. This mixture is then further processed to separate and reclaim the individual metals for potential reuse across various products. The economic viability of this method significantly hinges on the recovery of cobalt, the battery's most precious component. However, as the trend moves towards reducing cobalt content in batteries, the profitability of smelting as a recycling technique may diminish. Moreover, this process results in the entrapment of lithium and aluminum within the slag, a byproduct of smelting. While it is technically feasible to extract these materials from the slag, such recovery efforts have not been deemed economically viable thus far.

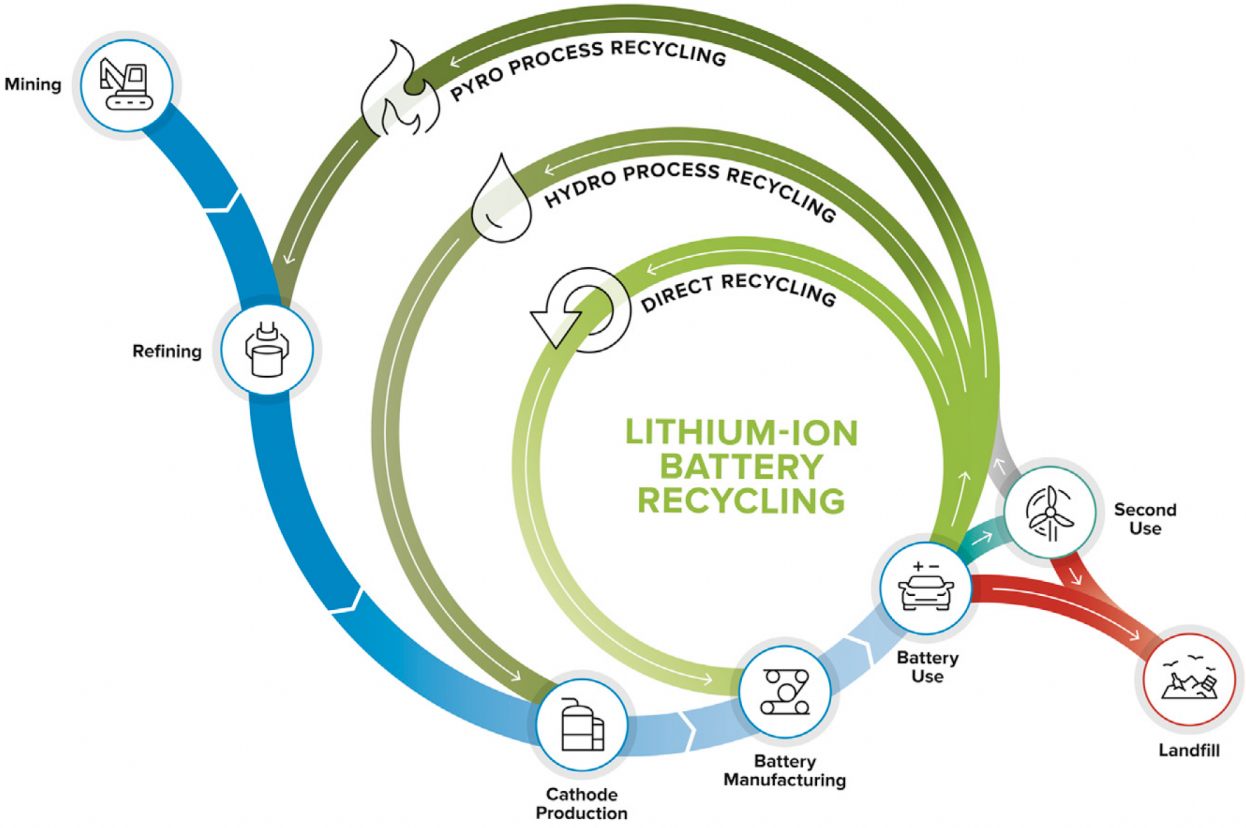

Figure 5.4: Life Cycle of a Lithium-Ion Battery (Gaines et al. [319]).

The middle loop in the diagram, termed hydrometallurgy or leaching, delineates a process distinct from pyrometallurgy by its focus on chemical rather than thermal treatment. This method commences with the shredding of batteries, a step that facilitates the separation and recovery of copper and aluminum metal foils. Subsequently, the active material powders extracted from the batteries are treated with acid, a process that enables the dissolution of metal ions from the cathode structure into solution. Following acid treatment, a combination of precipitation and solvent extraction techniques is employed to isolate the metal ions from the solution. The purified salts obtained through these procedures are then marketable as raw materials for the fabrication of new cathode materials. It is worth noting that this hydrometallurgical process does not facilitate the recovery of the electrolyte or anode carbon, representing a limitation in terms of material recovery efficiency. Despite its commercial application on a significant scale in countries like China and Korea, hydrometallurgy has seen less adoption in the United States, where higher labor and construction costs pose challenges. Moreover, the financial viability of this recycling method is under pressure due to the ongoing reduction in cobalt content in electrode materials, which traditionally has been a key revenue driver in the recycling of lithium-ion batteries [319].

The current stage of the smallest loop, otherwise known as direct recycling, is still undergoing development. Direct recycling aims to extract materials in their most usable form, employing physical processes. This method is distinct in its ability to preserve the complex and valuable crystalline structure of the cathode material, ensuring minimal loss of its inherent value, irrespective of the cobalt content. By focusing on retaining the quality of the extracted materials, direct recycling not only facilitates the reuse of cathode materials without the need for extensive reprocessing but also enables the recovery of additional components such as anode carbon and electrolyte solvents and salts. This comprehensive recovery approach has the potential to open new revenue streams while simultaneously reducing the costs associated with material disposal. Projected to be more economically viable on a smaller scale compared to other recycling methods, direct recycling could incentivize the development of

local recycling facilities. This decentralization offers significant advantages, including reduced transportation costs and emissions, and fosters a more localized recycling ecosystem [326].

Mohr et al. [325] conducted a life cycle assessment for battery recycling using three methods (Pyrometallurgical treatment, hydrometallurgical treatment, and advanced hydrometallurgical treatment) for different LIB systems: NCA, NMC, LFP and SIB. They concluded that recycling is essential in reducing the potential environmental impacts of producing LIB cells. High potential environmental benefits can be achieved through effective and advanced recycling methods. These benefits, however, are largely dependent on the processed cell chemistry. The research demonstrated that closed-loop recycling processes, particularly for NMC and NCA cells, can substantially reduce the resource depletion impact, potentially leading these cells to exhibit a lower net environmental impact when compared to LFP or SIBs. Notably, LFP and SIB cells tend to have a more favorable environmental profile during the production phase, emphasizing the complex interplay between cell chemistry, manufacturing practices, and recycling methodologies. Moreover, the study indicated that the composition, layout, and energy densities of the cells play a pivotal role in determining the effectiveness and benefits of recycling efforts.

The benefits of recycling vary depending on the impact category being considered. For instance, resource exhaustion benefits are much greater than those for greenhouse gas emissions, as recycling can only mitigate impacts from mining and not cell manufacturing, which is the significant contributor to LIB cells' Global Warming Potential (GWP). Nonetheless, recycling may result in GWP benefits that are likely to rise in the future, particularly as the manufacturing process incorporates a greater share of renewable energy or, more generally, less energy-intensive LIB cell production [322, 323].

The recycling of battery cells requires an approach specific to the cells' chemistry due to the significant differences in their compositions. In order to achieve the highest environmental benefit and quality output, recycling processes must be customized to suit the unique characteristics of each cell chemistry. Neglecting to do so can result in recycling

efforts that offset the benefits achieved from the recovered materials and trigger additional harmful impacts, as has been observed with the hydrometallurgical process of LFP and SIB cells [325]. It is crucial to note that the depth of recycling—referring to how extensively materials are recovered and processed—does not necessarily correlate with environmental benefits. As battery technology evolves, with a focus on reducing reliance on costly and scarce metals like cobalt and instead utilizing more abundant and less environmentally taxing materials such as phosphorus or sodium, the strategies for recycling must adapt accordingly. The goal is to recover materials in a manner that minimizes the input of chemicals and energy, thereby enhancing the process's environmental sustainability. A critical step towards achieving this is the accurate identification of cell chemistries, possibly through comprehensive labeling systems. Such identification would allow recyclers to adjust their processes to the specifics of each cell chemistry, thereby enhancing the efficiency and environmental footprint of recycling operations. Among the methods proposed, particularly for cost-effective cells like those made of LFP, is direct recycling. This method aims to preserve the electrode material's crystal structure, offering significant potential benefits in terms of resource efficiency and material recovery [327]. Nonetheless, the method has yet to be commercialized, and concerns about the quality of the reclaimed cathode material persist [328].

The recycling of SIBs faces challenges that are analogous to those encountered by LIB recyclers. However, it is worth noting that SIBs possess a distinct chemical composition, are less valuable than their LIB counterparts, and lack the requisite recycling procedures to optimize economic returns. Zhao et al.[296] outlined four primary impediments to the sustainable expansion of the battery recycling industry, which must immediately be addressed.

1. **High energy consumption and waste generation:** When it comes to recycling, the discharge and recycling strategies used for batteries can significantly impact material and energy consumption, as well as waste generation. The recycling process typically yields batteries with a state of charge of approximately 70%, a potentially hazardous

situation considering their highly reactive components. The lithiated and sodiated carbon materials in charged spent batteries can react exothermically with oxygen and water, creating a fire and explosion risk when disassembled or pulverized. Thus, a crucial consideration is whether spent batteries require discharge and, if so, what the optimal discharge method should be. Traditional brine discharge methods generate significant amounts of wastewater and are subject to restrictive regulations [329], necessitating the development of alternative discharge techniques that can be employed at scale with minimal environmental impact. The current state of industrial recycling processes is constrained by technological limitations, leading them to prioritize extracting high-value elements. As a result, these processes tend to be energy and resource-intensive and lead to the production of significant amounts of wastewater and greenhouse gas emissions (Fig. 5.5a) [296]. Lower-value materials found in spent batteries are often incinerated and consequently released as gas emissions, while cross-contaminated, poor-quality materials are disposed of in landfills in the form of slag, posing considerable environmental threats.

2. **Low recycling and utilization efficiencies:** Inadequate recycling and utilization efficiencies remain a challenge for spent batteries, largely attributed to these energy sources' intricate compositions and structures. Typically, spent batteries consist of a blend of up to ten different materials, resulting in suboptimal recycling and reuse rates. The presence of contaminants in materials remains a persistent challenge in the field of recycling. Extracting elements in their purest forms from various materials has proven to be a tremendous task. Deep-cycled batteries' intricate materials and inner structures can merge, rendering this task more complex. Failure to effectively separate materials results in substandard recycled materials that are only suitable for elemental extraction.

3. **Poor Material Regeneration:** The process of regenerating recycled electrode materials is often hindered by impurities and complex failure mechanisms. Recovering

pure cathode or anode materials poses practical challenges due to the presence of plastics, metals, and their oxides, which are difficult to remove after pulverization. Such impurities can significantly compromise the recovered materials' quality and increase the post-processing complexity [330, 331]. Furthermore, anode materials obtained through current industrial recycling processes cannot be regenerated and do not have practical applications. In contrast, recovered cathode materials are primarily used for leaching valuable elements. The recovered cathode and anode material powders can be unsuitable for regeneration and reuse in new batteries due to several reasons, such as physical parameters (size and density), structural damage, interfacial phase transitions, and active sodium loss. The significance of these factors may vary depending on the chosen recycling method. Currently, cathode and anode materials are primarily restored using simple techniques that involve active element supplementation and thermal treatment. The practical utility of materials repaired in this manner has yet to be thoroughly evaluated.

4. **Poor economic revenue:** The primary obstacle in SIB recycling is the inadequate economic return. This is primarily due to the low fixed value of spent SIB materials [332] (Figure 5.5e). Unlike LIBs, SIBs do not contain valuable materials and elements that would make recycling them financially viable. For instance, lithium carbonate costs must exceed \$22,000 per ton for $LiFePO_4$ battery recycling to be profitable. Due to the absence of expensive metals, recycling SIBs is less profitable and, consequently, less feasible, even if complete material recovery is achieved. The potential revenue from recycling SIBs through material regeneration is $\$7.52 kg^{-1}$ battery. However, this figure decreases significantly due to the devaluation of the SIB cathode material from cross-contamination or the absence of value recovered from electrolyte and anode materials. In mature industrial battery recycling methods, the material regeneration approach for SIBs yields only \$2.36 kg per cell, with an economic input of \$2.10 kg per cell, resulting in a profit of only \$0.26 kg per cell. The theoretical and practical revenues

of elemental extraction are calculated to be $\$2.68 kg^{-1}$ and $\$1.03 kg^{-1}$, respectively [333]. Consequently, the comparatively reduced profitability of SIB recycling may impede their widespread acceptance and subsequent recycling despite their relative technical simplicity when compared to their lithium-ion battery (LIB) counterparts.

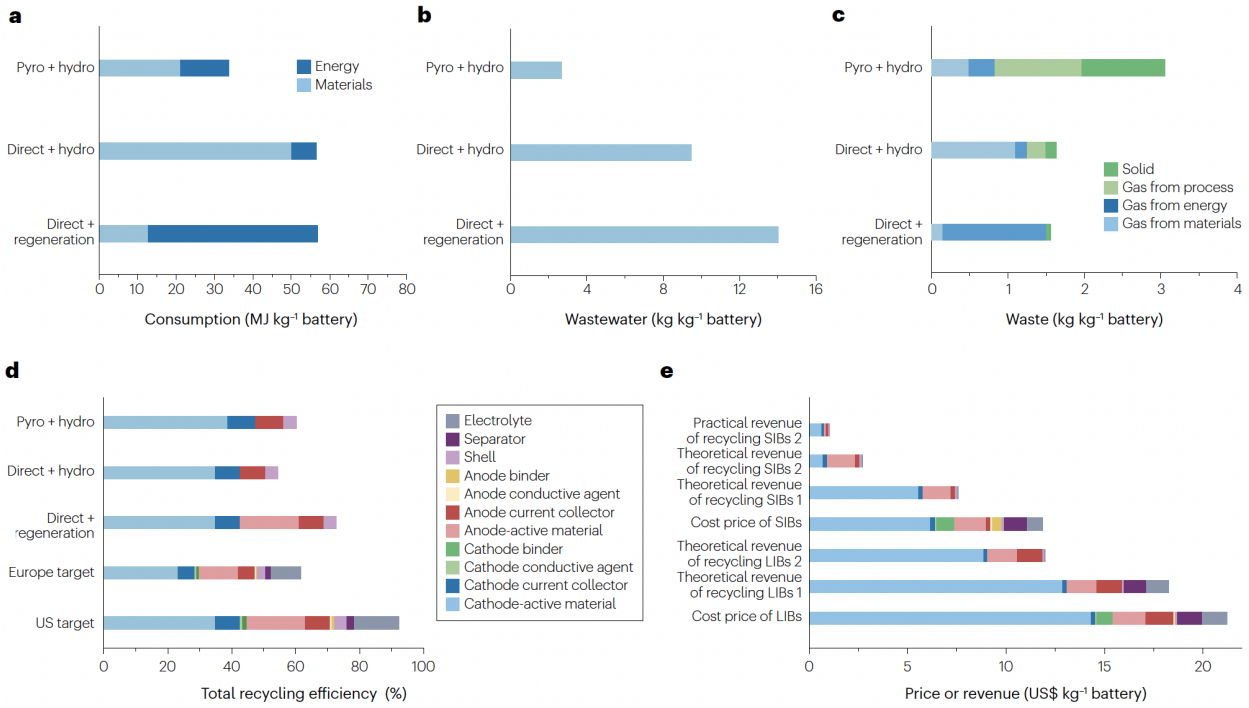

Figure 5.5: a, The projected battery demand (GWh) for energy storage systems, electric vehicles and portable electronic devices from 2020 to 2030. b, The estimated total battery capacity (TWh) available for manufacturing by metal reserves in the crust of the Earth (ppm). c, The predicted demand (GWh) for SIBs from 2020 to 2030. d, A radar chart indicates the resource content, cell economic value, safety risk, carbon emissions and environmental impact for 1kg of spent lithium-ion batteries (LIBs) and sodium-ion batteries (SIBs) (Zhao et al. [296]).

5.3 Economic assessment of alloy anode for LIBs

To comprehensively grasp the integration of alloy anodes into LIB systems, a meticulous economic evaluation rooted in statistical analysis is imperative. The methodology known as Design of Experiments (DoE) has long been esteemed for its efficacy in elucidating the relationship between variables and their outcomes. Despite its longstanding success across various scientific domains and industrial applications, its adoption for scrutinizing LIBs has only recently gained momentum. DoE encompasses a statistical discipline focused on the meticulous planning, collecting, and scrutinization of experimental data, thereby facilitating the derivation of legitimate and unbiased engineering insights. Within this framework, employing a factorial design emerges as an effective strategy for dissecting the main and interaction effects of independent (input) variables on a dependent (output) variable, optimizing the exploratory process through a minimized experimental set. Fundamental to DoE are the principles of randomization, blocking, replication, factorial methodology, and variance analysis. The empirical data derived from diverse factorial combinations undergo statistical evaluation, and the process response obtained for a combination of factor levels is represented by a mathematical function. This approach presupposes the predictability of responses via low-order polynomial functions of the independent variables, culminating in the regression equation. DoE finds application in a breadth of engineering endeavors, notably in comparative studies, screening, modeling, optimization, the crafting of robust designs, and formulation [334, 335, 336, 337]

This study's objective is to elucidate the impact of alloy anodes on the overall costs associated with the battery system, including the pack and cell levels. To generate data for this analysis, "BATPAC v5.0" will be utilized. This model, developed by the Argonne National Laboratory, plays an essential role in designing lithium-ion battery packs tailored for transportation applications.

BatPaC is a publicly accessible model that conducts a bottom-up LIB design and cost

calculation. It customizes the battery configuration based on specified requirements concerning power, energy, and the type of vehicle—ranging from hybrid and plug-in hybrid to fully electric models. The costing process within the model comprehensively encompasses every phase of the lithium-ion battery's manufacturing journey. This model, alongside its documentation, has undergone a rigorous peer review process by a panel of battery specialists convened by the U.S. Environmental Protection Agency.

BatPaC is engineered to accurately estimate the dimensions, mass, and financial outlay for electric vehicle (EV) packs of the near future, premised on the utilization of modules filled with prismatic and stiff pouch cells. Its computations are meticulously tailored to align with the performance criteria, design configurations, and manufacturing inputs specified by the user. These comprehensive input parameters fed into BatPaC are crafted to support a broad examination of factors influencing both the physical size and cost of the battery pack. These factors extend to but are not confined to, the configuration of the pack, the physical and chemical properties of materials, the requisite energy and power densities, the intricacies of the manufacturing process, and the scale of production. To ease the analysis, BatPaC comes pre-loaded with default values reflecting the commercially viable cell chemistries and vehicle categories. Users retain the flexibility to adjust these inputs to reflect their specific conditions and also introduce new sets of default parameters to extend the model's applicability.

BatPaC employs a systematic, iterative process to formulate a cell design that meets all the conditions as specified by the user. This comprehensive design approach encompasses the cell, module, and pack levels, which are instrumental in determining the requisite pack management and thermal management systems. Within the framework of BatPaC version 5.0, it is presumed that all packs will incorporate liquid-cooled thermal management systems. The outcomes derived from the battery management and thermal management designs are pivotal in shaping the ultimate structure of the battery system. This final battery configuration serves as a cornerstone for the manufacturing cost model and the estimation of recyclable materials. The computation of manufacturing costs is predicated on the assumption of

a highly automated production facility anticipated to be operational in the near future. Moreover, the cost analysis for raw materials and purchased components is based on projected near-future prices, taking into account the benefits of economies of scale. This forward-looking approach ensures that the cost estimations remain relevant and closely aligned with future market dynamics and technological advancements [338].

In the context of an EV, the battery pack plays a key role. It comprises a multitude of cells interconnected through series and parallel arrangements to fulfill the requisite pack voltage, energy, and power specifications. The BatPaC model is tasked with calculating the mass, dimensions, and cost of such a battery pack, predicated on the assumption that it consists of modules housing stiff pouch cells. The next level is the module, where several cells are connected, potentially in various series or parallel configurations. Each module is equipped with aluminum heat conductors enveloping the cells, facilitating effective thermal management. Moreover, the module encompasses a management control system, electrical terminals, and a protective enclosure, ensuring both functional and structural integrity. Then, BatPaC assumes that multiple modules are placed within a row rack. These row racks are engineered to provide structural support, which is crucial for maintaining the necessary compression on the modules. Additionally, they are integrated with cooling panels to adeptly manage the thermal output from the cells within the modules. Next, BatPaC assumes the interconnection of all row racks, constituting the complete battery pack. This comprehensive pack incorporates an extensive battery management system alongside advanced thermal management features, including bus bars and terminals for efficient power distribution. The architecture allows for the strategic connection of rows of modules—and the modules within these rows—in series or parallel configurations to achieve the desired pack voltage. Elevating to the battery system level, BatPaC accounts for the mass and cost implications of additional cooling systems external to the pack. These systems are integrated into the vehicle to ensure optimal battery operation, highlighting the model's thorough consideration of the entire battery ecosystem within electrified vehicles [314].

In this study, we leverage a comprehensive 2^5-factorial design to investigate the impact of incorporating an alloy anode composed of a phosphorus/silicone composite, alongside other variables, on the cost of the battery system, the pack, and the cell. Our analysis is predicated on several key assumptions tailored specifically to the battery system. These include a focus solely on EVs, a target for the rated peak power of the pack at 300 kW, a total pack energy capacity of 100 kWh, and an annual production volume of 500,000 packs. It is also assumed that packs are produced at an equivalent rate (GWh/year) to the cells themselves.

To conduct this experiment, five distinct factors or independent variables, each with two levels, were selected: (Figure:5.6).

- A. Yield: It was evaluated at two levels, 90%, and 95%, to understand the influence of manufacturing efficiency on the outcomes.
- B. Charging Speed: To gauge the effect of charging speed on system design and cost, it is categorized into two charging modalities: base/slow (overnight charging) and fast (approximately 60 minutes).
- C. Phosphorus Incorporation: A binary variable (0: absent, 1: present) to ascertain the effect of phosphorus addition to the anode material.
- D. Anode Material: Examined with two types of anode materials: Graphene and Silicone Graphene, to explore their respective impacts on the battery system's performance and cost.
- E. Cathode Material: Differentiated between NMC811 and NMC622 to determine how these cathode materials influence the overall battery pack design and economics.

This factorial design methodology allows for a detailed analysis of not only the individual effects of these variables but also their interaction effects on the targeted outcomes, thereby offering a robust statistical foundation to ascertain the significance of the alloy anode within the broader context of EV battery system development.

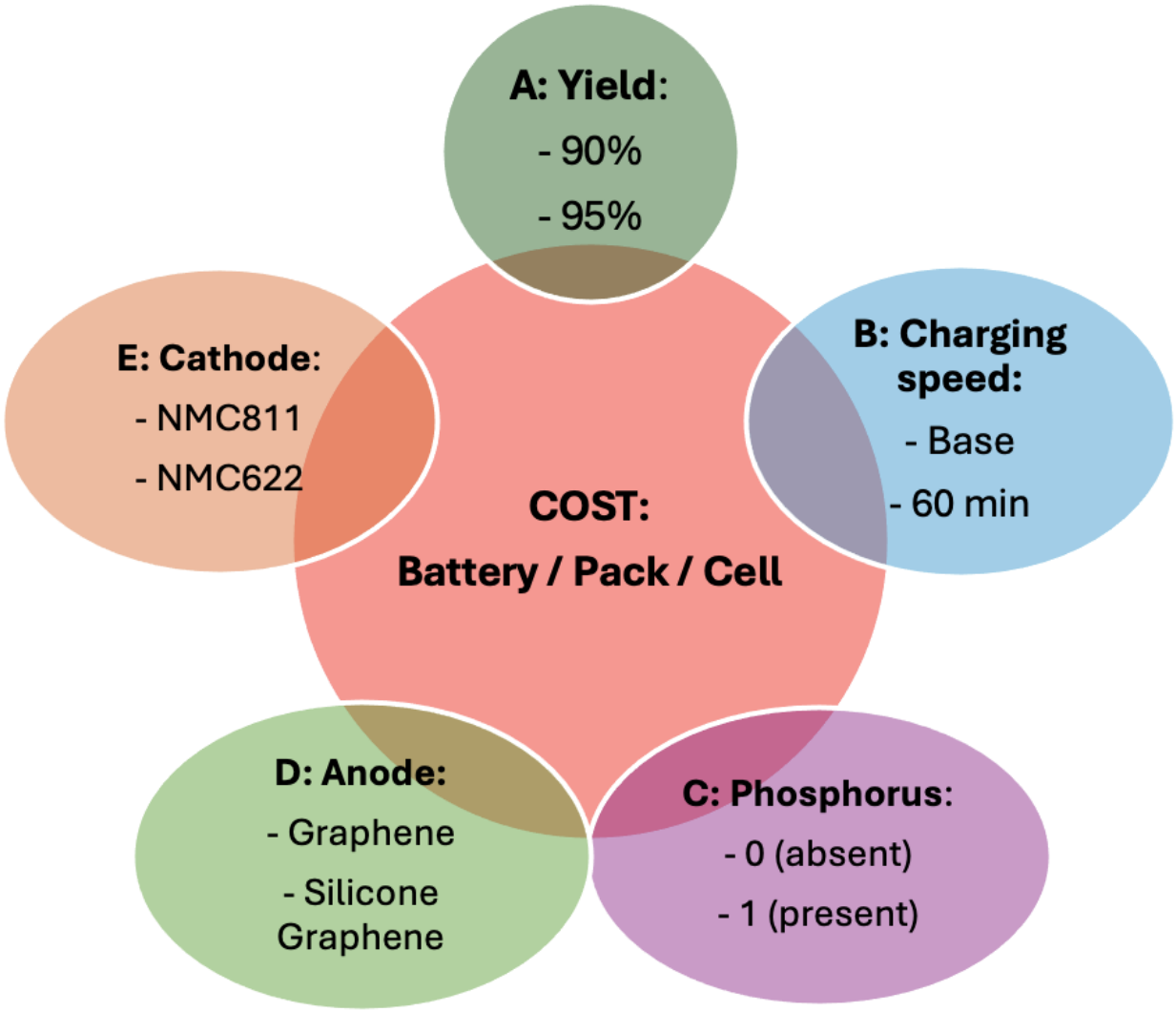

Figure 5.6: The response variables and the five factors and their two levels.

Upon finalizing the inputs, BatPaC proceeds to calculate the associated costs for eight default batteries, each distinguished by its unique pack configurations and cells. These eight batteries yield a diverse range of cost outcomes directly attributable to their respective pack configurations, as detailed in Table E.1 in Appendix E.

From this dataset, three critical metrics are derived to serve as our dependent variables or responses in the study:

- Maximum Cost: This value represents the highest cost among the eight battery configurations. Identifying the maximum cost is essential for understanding the upper-cost threshold within the current design and material parameters.

- Minimum Cost: Conversely, this value signifies the lowest cost observed across the configurations. The minimum cost highlights the most economically viable option under the given conditions, offering insights into cost-saving potentials.

- Average Cost: Calculated as the mean cost across all eight configurations, this metric provides a comprehensive view of the overall cost landscape. The average cost offers a balanced perspective, smoothing out the extremes to present a generalized cost expectation for the battery packs.

These three values collected for the battery, the pack, and the cell collectively offer a multifaceted understanding of the financial implications associated with different battery pack configurations. By analyzing the maximum, minimum, and average costs, we can gain valuable insights into cost drivers, enabling informed decisions to optimize battery design for cost-efficiency and performance within the context of electric vehicle production.

In the execution of the Design of Experiments (DoE), MINITAB software plays a crucial role, particularly in the statistical analysis phase. This process involves a rigorous assessment of regression terms based on a 95% confidence level. The method entails comparing the standardized effects of regression coefficients against a t-distribution to discern their statistical significance. Following this comparison, only the terms that exhibit significant impacts are

retained for inclusion in the regression model. This step ensures that the model is both efficient and reflective of genuinely influential factors.

Subsequently, the Analysis of Variance (ANOVA) technique is employed further to evaluate the statistical robustness of the regression models. ANOVA serves a dual purpose: it verifies the significance of the models themselves and conducts a test for lack of fit. Assessments are conducted at a 95% confidence level, adhering to the stringent criteria for statistical validity. The lack of fit test is particularly important as it measures how well the model, with its selected significant terms, represents the data, excluding random error.

Lastly, the coefficient of determination, denoted as R^2, is utilized to gauge the goodness of fit for each model. The R^2 value is a key metric in regression analysis, indicating the proportion of variance in the dependent variable that is predictable from the independent variables. A higher R^2 value suggests a better fit of the model to the data, implying that the model can explain a larger portion of the variability in the response variable.

In this particular analysis, the focus is on the maximum cost of the battery as the dependent variable or response. The regression model incorporates all factor terms with the exception of the highest 5-way interaction, which is typically disregarded due to its negligible effect on the response. The model demonstrates exceptional adequacy, as evidenced by an adjusted R^2 value of 99.89% and an R^2 value of 100%, indicating near-perfect explanatory power regarding the variability of the maximum cost in relation to the input factors. To identify which design factors significantly influence the maximum cost, the Analysis of Variance (ANOVA) is employed, utilizing the P-value as a criterion for significance. In this context, a design factor is deemed statistically significant if its P-value is less than the alpha threshold of 0.05. According to the ANOVA results for our model, only six terms meet this criterion, corroborating the findings presented in the normal plot of standardized effects and the Pareto charts referenced in figure 5.7. The significant factors identified are the yield, the charging speed, the Phosphorus, the cathode chemistry, and the interaction between

the charging speed and Phosphorus and between the Anode and phosphorus. (see ANOVA results in figure E.1 in Appendix E1)

Following the identification of six significant terms, a refined screening was conducted using a reduced model that encompasses only these impactful factors. This streamlined approach maintains high model adequacy, as evidenced by an adjusted R^2 of 98.40% and an R^2 of 98.76%, indicating a strong correlation between the selected factors and the maximum battery cost (maxB-Cost). The newly derived regression equation for this model is given by:

$$\begin{aligned} maxB - Cost = {} & 11497.4 - 254.1Yield + 171.4FastCharging - 450.0Phosphorus \\ & + 10.6Anode + 87.6CathodeChem + 51.3FastCharging * Phosphorus \\ & + 75.1Phosphorus * Anode \end{aligned} \tag{5.1}$$

This equation provides a quantitative framework for predicting the maximum battery cost based on the significant variables and their interactions.

To further elucidate the influence of these variables on battery cost, main effects plots were utilized. These plots are instrumental in visualizing how varying levels of each factor affect the response variable. According to figure 5.8, factors that exhibit a steep angle in their main effects plot exert the greatest influence on the battery cost, whereas factors whose plot lines run parallel to the mean line are deemed insignificant in this context. Notably, a high yield of 95% and the inclusion of phosphorus in the battery's composition emerged as the levels that positively affect cost reduction, indicating that these factors are pivotal in enhancing the cost-efficiency of the battery system. The inclusion of phosphorus, in particular, is highlighted as a key factor expected to significantly lower the battery system cost.

Extending the analysis to encompass both the maximum pack cost and the maximum cell cost, similar rigorous statistical methodologies were applied. The outcomes underscore the robustness of the models, demonstrating high model adequacy. Specifically, for the pack analysis, both the adjusted R^2 and R^2 stand at an exceptional 99.89% and 100%, respectively.

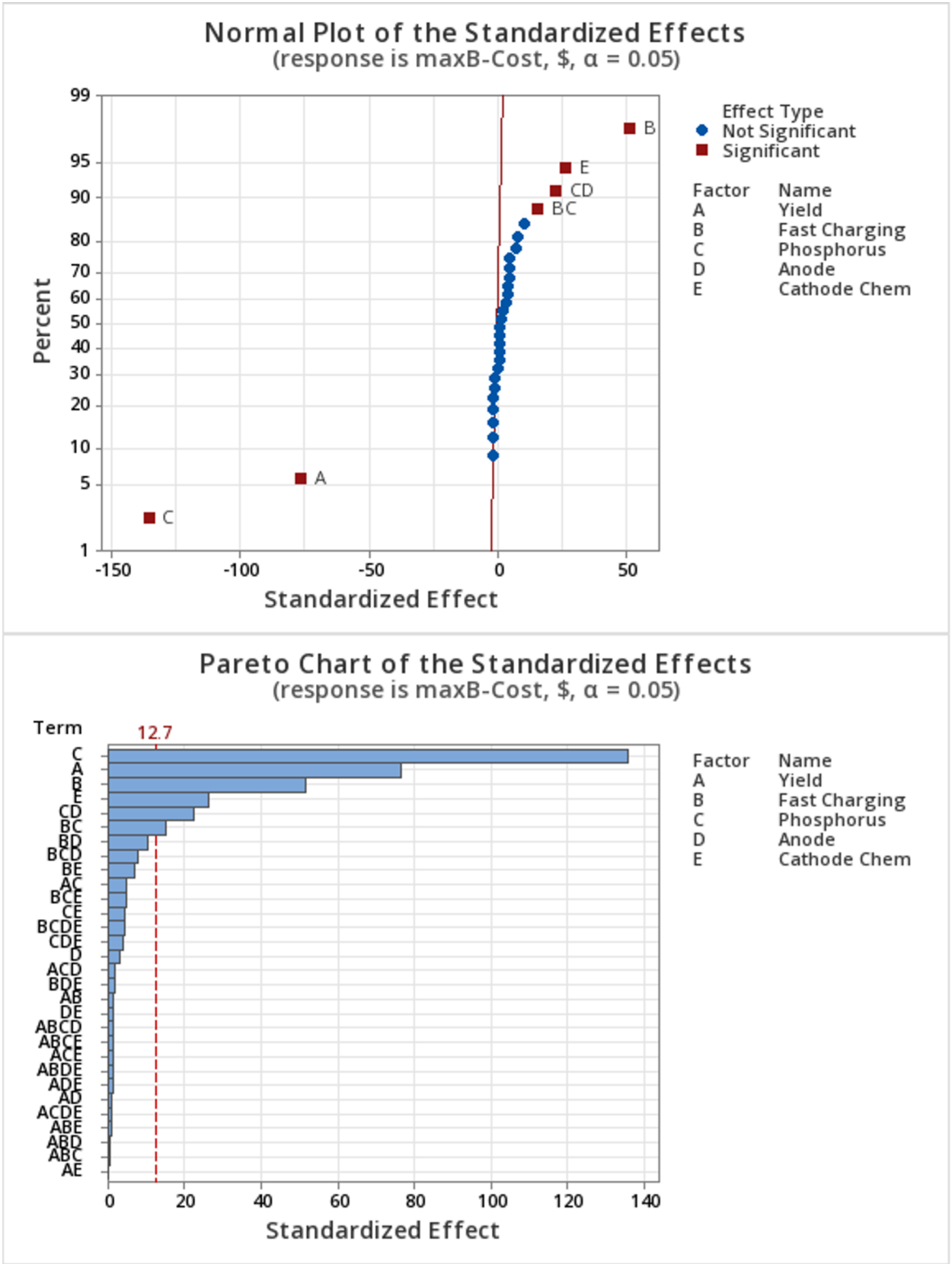

Figure 5.7: Normal plot and Pareto chart for the standardized effects.

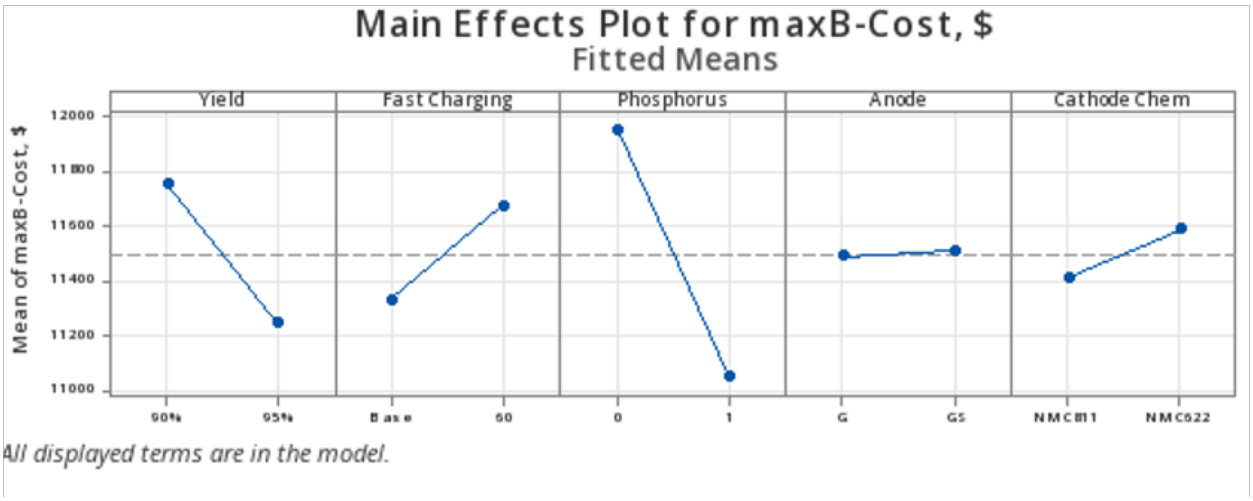

Figure 5.8: Main effect plots for maximum battery cost.

This indicates a near-perfect fit, suggesting that the model can almost entirely explain the variability in pack costs based on the input factors. Regarding the cell, the cost model exhibits an adjusted R^2 of 99.98%, signifying an extremely high level of explanatory power, with an R^2 of 98.27%, reflecting a slightly lower but still very strong predictive capability. Upon reviewing the ANOVA results to discern the significance of various factors within these models, a clear pattern emerges. For the pack cost, the significant factors align closely with those identified in the battery cost analysis. These include the yield, the charging speed, the Phosphorus, the cathode chemistry, and the interaction between the charging speed and Phosphorus and between the Anode and phosphorus. Conversely, the cell cost analysis narrows down the significant factors to yield and phosphorus. This refined focus is evident from the normal plots presented in figure 5.9, which distill the complex interplay of variables down to these two primary factors. Such specificity in the cell analysis underscores the critical roles that manufacturing efficiency (yield) and anode material composition (phosphorus) play in driving cell cost outcomes.

Furthermore, the use of main effect plots serves as a vital tool for analyzing the contributions of different factor levels to the response variables, in this case, the pack and cell costs. These plots provide a visual representation of how each factor influences the cost, either by increasing or decreasing it. Figure 5.10, which encompasses the results for both pack and

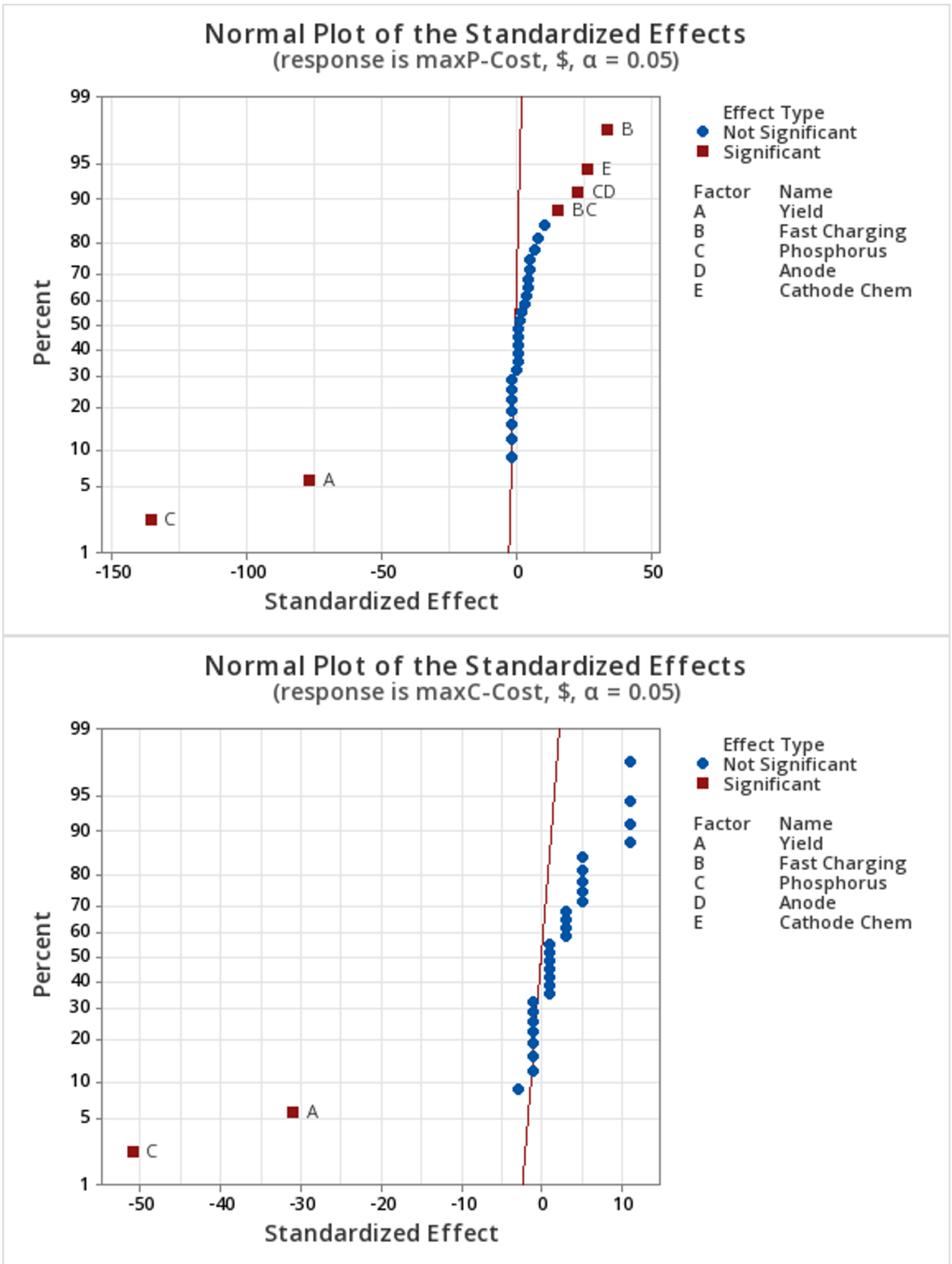

Figure 5.9: Normal plots of the standardized effects of the maximum cost of the pack and the cell.

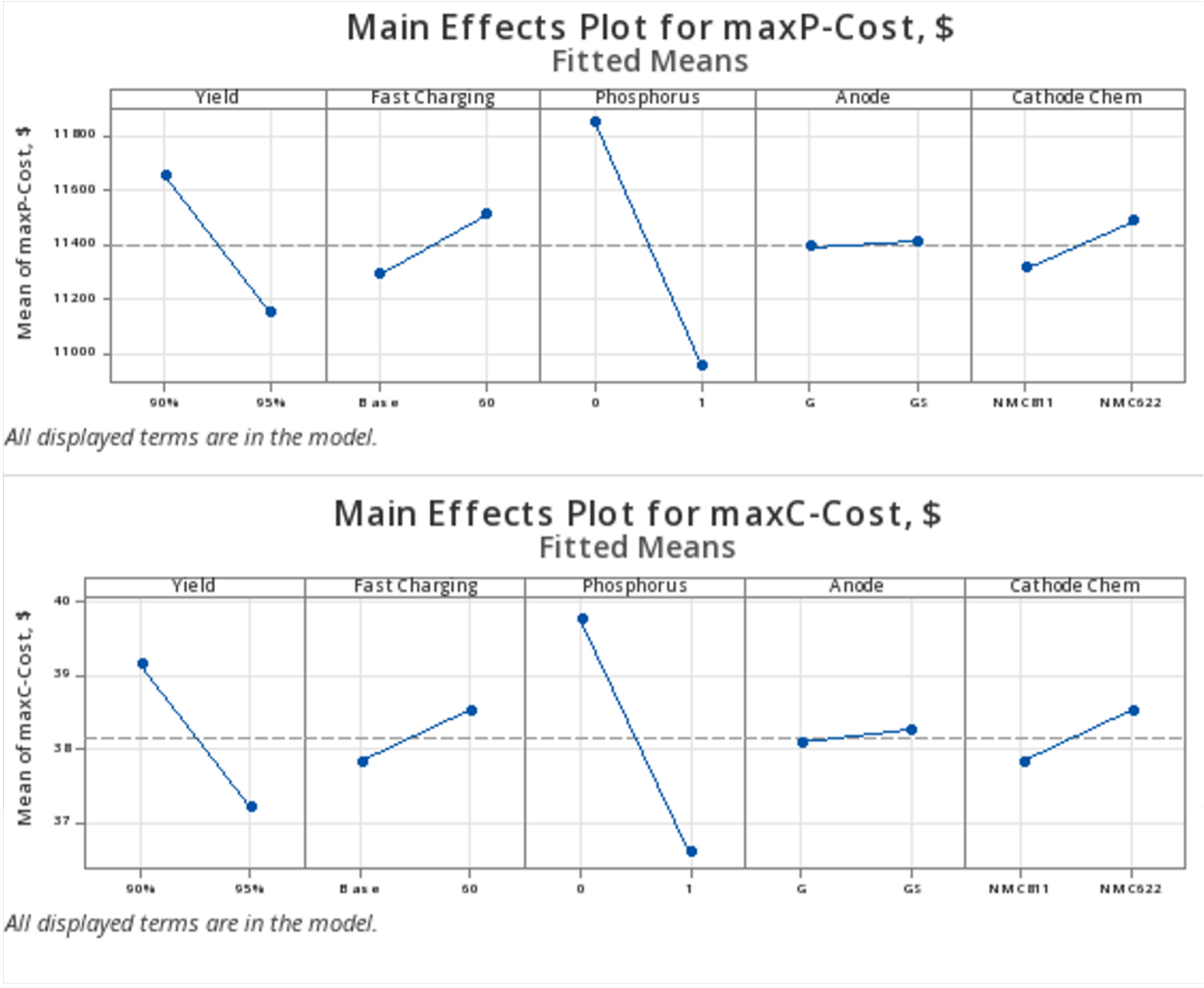

Figure 5.10: Main effects plots for maximum pack and cell costs.

cell costs, corroborates findings from the battery cost analysis, particularly emphasizing the beneficial impact of incorporating phosphorus into the anode composition. The significance of phosphorus as a component in the anode material is highlighted through its positive effect on reducing costs. This observation is consistent across the different analyses for battery, pack, and cell costs, reinforcing the strategic value of using phosphorus in alloy anodes for LIBs. The main effect plots demonstrate that among the tested factors, the inclusion of phosphorus stands out for its cost-reducing potential.

The replication of the initial study, with a focus on the minimum and average costs of the 8 BatPaC default configurations yielding the same conclusions, further underscores

the robustness of the findings. This consistency across different cost metrics (maximum, minimum, and average) highlights the fundamental role that certain factors play in influencing battery system economics within EV applications. (see Appendix E Figures E.2,E.3, and E.4)

Two key observations are to be noted:

- I. The Impact of Phosphorus: The positive influence of incorporating phosphorus into the anode composition remains significant across all cost metrics. This confirms the material's value in reducing production costs, reinforcing the viability of alloy anodes for LIBs.

- II. Significant factors and their interactions: Factors such as yield, charging speed, cathode chemistry, anodes, and their interactions with phosphorus consistently emerge as significant across different cost evaluations. This consistency validates the initial findings and suggests that these factors are integral to cost optimization strategies for LIB systems.

This repeated observation across multiple facets of the battery system cost analysis validates the approach of integrating alloy anodes, specifically those that include phosphorus, into LIBs. The consistent pattern observed in the reduction of costs associated with phosphorus inclusion underscores its efficacy as a material choice, lending credibility to the exploration and adoption of alloy anodes in the pursuit of more cost-effective and efficient LIB solutions. Such findings are instrumental in guiding future research and development efforts in battery technology, particularly in optimizing material compositions for enhanced performance and cost efficiency.

Chapter 6

Conclusion-Future work

6.1 Conclusion

This dissertation has methodically explored the development and structural optimization of alloy anodes for high-energy alkali-ion batteries, with a particular emphasis on lithium-ion (LIB) and sodium-ion (SIB) batteries. Through the integration of novel material design strategies, cutting-edge characterization techniques, and comprehensive electrochemical analyses, this study has shed light on the underlying mechanisms that contribute to the performance improvement of alloy-based anodes. The research underscores the critical role of structural engineering, alloy-carbon composites, and surface modifications in overcoming challenges associated with volume expansion and electrode degradation. These strategies facilitate enhanced electronic/ionic conductivity and stabilize the solid-electrolyte interphase (SEI) layer, thereby markedly augmenting the anodes' cycling stability and rate capability.

- Chapter 1 outlines the substitution of graphite in lithium-ion batteries with alloying anode materials attributed to their superior specific capacity. It addresses the hurdles of volumetric changes and mechanical degradation during cycling, underscoring the imperative for optimized design and a profound comprehension of the alloying mechanism.

- Chapter 2 offers a comprehensive literature review on mitigative approaches for volume expansion in micro-sized alloy anodes. It examines the impact of electrolytes, binders, and architectural configurations on anode efficacy. It concludes that micro-sized alloy anodes offer potential for practical applications in high-energy and long-life alkali-ion batteries, and strategies like electrolyte modulation, binder design, and architecture engineering are crucial for enabling the use of micro-sized alloy anodes.

- Chapter 4 unfolds through four case studies on varied alloy anode materials for lithium-ion and sodium-ion batteries, discussing their reversible reaction mechanisms, structural control, performance optimization, and practical validation using in situ and operando characterization tools (XRD, XANES, EXAF, SAX, FIB-SEM, ...). The first three cases showcase the role of engineered carbon support in electrode structure stability. Cases 2 and 3 propose a P-based and a Si-P Based micro-size composite alloy anodes with high initial coulombic efficiency of 91% and 84% and high specific capacity of $> 2000\, mAh.g^{-1}$ for both, with excellent cycle stability and superior rate capability up to $15A.g^{-1}$. Moreover, the Si-P anode demonstrates an average discharge working potential of 0.3 V versus lithium which is very crucial to enhancing the energy density. Lastly, case 4 emphasizes the importance of interface engineering. Ether-based electrolytes enable the formation of inorganic species-dominated solid-electrolyte interphase (SEI) with improved mechanical strength to mitigate the huge volume expansion of micro-Sn alloy anode, resulting in higher initial coulombic efficiency and improved cycling stability compared to conventional carbonate electrolytes. In situ X-ray absorption spectroscopy, furthermore, revealed a highly reversible sodiation/de-sodiation process of micro-sized Sn anode in ether-based electrolytes, indicating improved performance.

- Chapter 5 evaluates the manufacturing and recycling frameworks for alloy anodes and incorporates an economic analysis of lithium-ion battery alloy anodes, leveraging the BATPAC model and statistical methodologies. Yet, many efforts are still needed in

the recycling sector; SIBs are leveraging the lessons learned from manufacturing LIBs and offering a suitable addition and alternative for the future. DOE analysis was then executed on BATPAC-generated data. A fractional design 2^5 (5 factors with 2 levels) was performed to investigate the impact of incorporating an alloy anode composed of a phosphorus-silicone composite, alongside other variables, on three critical aspects: the cost of the battery system, the configuration of the pack, and the design of the cell. The discernment of these factors, facilitated by statistical analyses, provides a nuanced understanding of cost drivers, enabling targeted strategies for cost reduction and efficiency improvement in EV battery systems. The positive influence of incorporating phosphorus into the anode composition remains significant across all cost metrics. This confirms the material's value in reducing production costs, reinforcing the viability of alloy anodes for lithium-ion batteries (LIBs).

The discoveries accentuate the strategic importance of the incorporation of micro-sized alloy anodes, particularly Silicon and Phosphorus composites, to bolster the battery sector. These advancements not only enrich the theoretical landscape of alloying dynamics in alkali-ion batteries but also herald the advent of superior energy storage systems, pivotal for surmounting global energy predicaments.

6.2 Future work

The encouraging outcomes of this investigation signal multiple pathways for future research. To augment the contributions of this dissertation, subsequent studies should pivot around the ensuing focal points:

- Material Optimization: It is essential to refine the composition and microstructure of alloy anodes to amplify their operational capacities and energy densities. Probing into new materials and alloy combinations may unveil anodes with enhanced performance indices.

- Scalability and Manufacturability: Future endeavors should scale the synthesis processes of the anodes developed herein. Tackling the challenges associated with production scalability, cost-effectiveness, and material availability is crucial for their industrial deployment.

- Advanced Characterization Techniques: The adoption of in situ and operando characterization methodologies will unveil intricate dynamics within the anode materials during battery operation, which is critical for devising strategies to elevate battery performance further.

- Electrolyte and Interface Engineering: Investigating the synergies between alloy anodes and electrolytes could lead to optimized electrolyte solutions and interface engineering methods, enhancing battery durability and performance.

- Full Cell Integration: Advancing beyond the anode materials delineated in this study, it is vital to design and assess full cells that incorporate compatible cathodes and electrolytes to determine the practical applicability of these anodes in LIBs and SIBs.

- Sustainability and Recycling: With the escalating demand for high-energy batteries, the development of sustainable production and recycling methods becomes impera-

tive. Future research should also delve into the lifecycle analysis, recyclability, and environmental footprint of novel anode materials.

Pursuing these directions will enable future research to build on this dissertation's foundational work, advancing toward the realization of more efficient, durable, and eco-friendly alkali-ion batteries to meet the forthcoming energy storage requirements.

Bibliography

[1] M. Stanley Whittingham. "History, Evolution, and Future Status of Energy Storage". In: *Proceedings of the IEEE* 100 (Special Centennial Issue May 2012). Conference Name: Proceedings of the IEEE, pp. 1518–1534. ISSN: 1558-2256. DOI: 10.1109/JPROC.2012.2190170. URL: https://ieeexplore.ieee.org/abstract/document/6184265.

[2] Intergovernmental Panel on Climate Change and Ottmar Edenhofer, eds. *Climate change 2014: mitigation of climate change: Working Group III contribution to the Fifth Assessment Report of the Intergovernmental Panel on Climate Change*. OCLC: ocn892580682. New York, NY: Cambridge University Press, 2014. 1435 pp. ISBN: 978-1-107-05821-7.

[3] P.F. Ribeiro et al. "Energy storage systems for advanced power applications". In: *Proceedings of the IEEE* 89.12 (Dec. 2001). Conference Name: Proceedings of the IEEE, pp. 1744–1756. ISSN: 1558-2256. DOI: 10.1109/5.975900. URL: https://ieeexplore.ieee.org/abstract/document/975900?casa_token=q7EW33rTNkUAAAAA:MNTizaY7dxYFYO9ZxgPMplV0BldyxmKx30Cp9RgCKfqDmIqYP6KohQjEav08ZiEu6MgDfAsl6g.

[4] Rajendra K. Pachauri et al. *Climate change 2014: Synthesis report. Contribution of Working Groups I, II and III to the Fifth Assessment Report of the Intergovernmental Panel on Climate Change*. Geneva, Switzerland: IPCC, Jan. 1, 2015. 151 pp. ISBN: 978-92-9169-143-2. URL: https://epic.awi.de/id/eprint/37530/.

[5] Siraj Sultan et al. "Single Atoms and Clusters Based Nanomaterials for Hydrogen Evolution, Oxygen Evolution Reactions, and Full Water Splitting". In: *Advanced Energy Materials* 9.22 (2019). _eprint: https://onlinelibrary.wiley.com/doi/pdf/10.1002/aenm.201900624, p. 1900624. ISSN: 1614-6840. DOI: 10.1002/aenm.201900624. URL: https://onlinelibrary.wiley.com/doi/abs/10.1002/aenm.201900624.

[6] Jaeki Jeong et al. "Pseudo-halide anion engineering for α-FAPbI3 perovskite solar cells". In: *Nature* 592.7854 (Apr. 2021). Number: 7854 Publisher: Nature Publishing Group, pp. 381–385. ISSN: 1476-4687. DOI: 10.1038/s41586-021-03406-5. URL: https://www.nature.com/articles/s41586-021-03406-5.

[7] BloombergNEF. *Electric Vehicle Outlook 2023*. Executive Summary. BloombergNEF, 2023, p. 22. URL: https://assets.bbhub.io/professional/sites/24/2431510_BNEFElectricVehicleOutlook2023_ExecSummary.pdf.

[8] Bruce Dunn, Haresh Kamath, and Jean-Marie Tarascon. "Electrical Energy Storage for the Grid: A Battery of Choices". In: *Science* 334.6058 (Nov. 18, 2011). Publisher: American Association for the Advancement of Science, pp. 928–935. DOI: 10.1126/science.1212741. URL: https://www.science.org/doi/full/10.1126/science.1212741.

[9] H. Ibrahim, A. Ilinca, and J. Perron. "Energy storage systems—Characteristics and comparisons". In: *Renewable and Sustainable Energy Reviews* 12.5 (June 1, 2008), pp. 1221–1250. ISSN: 1364-0321. DOI: 10.1016/j.rser.2007.01.023. URL: https://www.sciencedirect.com/science/article/pii/S1364032107000238.

[10] M. Armand and J.-M. Tarascon. "Building better batteries". In: *Nature* 451.7179 (Feb. 2008). Number: 7179 Publisher: Nature Publishing Group, pp. 652–657. ISSN: 1476-4687. DOI: 10.1038/451652a. URL: https://www.nature.com/articles/451652a.

[11] Wu Xu et al. "Lithium metal anodes for rechargeable batteries". In: *Energy & Environmental Science* 7.2 (2014). Publisher: Royal Society of Chemistry, pp. 513–537. DOI: 10.1039/C3EE40795K. URL: https://pubs.rsc.org/en/content/articlelanding/2014/ee/c3ee40795k.

[12] Xin-Bing Cheng and Qiang Zhang. "Dendrite-free lithium metal anodes: stable solid electrolyte interphases for high-efficiency batteries". In: *Journal of Materials Chemistry A* 3.14 (Mar. 24, 2015). Publisher: The Royal Society of Chemistry, pp. 7207–7209. ISSN: 2050-7496. DOI: 10.1039/C5TA00689A. URL: https://pubs.rsc.org/en/content/articlelanding/2015/ta/c5ta00689a.

[13] John B. Goodenough and Kyu-Sung Park. "The Li-Ion Rechargeable Battery: A Perspective". In: *Journal of the American Chemical Society* 135.4 (Jan. 30, 2013). Publisher: American Chemical Society, pp. 1167–1176. ISSN: 0002-7863. DOI: 10.1021/ja3091438. URL: https://doi.org/10.1021/ja3091438.

[14] D. Larcher and J.-M. Tarascon. "Towards greener and more sustainable batteries for electrical energy storage". In: *Nature Chemistry* 7.1 (Jan. 2015). Number: 1 Publisher: Nature Publishing Group, pp. 19–29. ISSN: 1755-4349. DOI: 10.1038/nchem.2085. URL: https://www.nature.com/articles/nchem.2085).

[15] Dingchang Lin, Yayuan Liu, and Yi Cui. "Reviving the lithium metal anode for high-energy batteries". In: *Nature Nanotechnology* 12.3 (Mar. 2017). Number: 3 Publisher: Nature Publishing Group, pp. 194–206. ISSN: 1748-3395. DOI: 10.1038/nnano.2017.16. URL: https://www.nature.com/articles/nnano.2017.16.

[16] Hongshuai Hou et al. "Carbon Anode Materials for Advanced Sodium-Ion Batteries". In: *Advanced Energy Materials* 7.24 (2017). _eprint: https://onlinelibrary.wiley.com/doi/pdf/10.1002/aenm.201602898, p. 1602898. ISSN: 1614-6840. DOI: 10.1002/aenm.201602898. URL: https://onlinelibrary.wiley.com/doi/abs/10.1002/aenm.201602898.

[17] Haegyeom Kim et al. "Recent Progress and Perspective in Electrode Materials for K-Ion Batteries". In: *Advanced Energy Materials* 8.9 (2018). _eprint: https://onlinelibrary.wiley.com/doi/pdf/10.1002/aenm.201702384, p. 1702384. ISSN: 1614-6840. DOI: 10.1002/aenm.201702384. URL: https://onlinelibrary.wiley.com/doi/abs/10.1002/aenm.201702384.

[18] Wenli Zhang et al. "Graphitic Nanocarbon with Engineered Defects for High-Performance Potassium-Ion Battery Anodes". In: *Advanced Functional Materials* 29.35 (2019). _eprint: https://onlinelibrary.wiley.com/doi/pdf/10.1002/adfm.201903641, p. 1903641. ISSN: 1616-3028. DOI: 10.1002/adfm.201903641. URL: https://onlinelibrary.wiley.com/doi/abs/10.1002/adfm.201903641.

[19] Christoph Vaalma et al. "A cost and resource analysis of sodium-ion batteries". In: *Nature Reviews Materials* 3.4 (Mar. 13, 2018). Number: 4 Publisher: Nature Publishing Group, pp. 1–11. ISSN: 2058-8437. DOI: 10.1038/natrevmats.2018.13. URL: https://www.nature.com/articles/natrevmats201813.

[20] Alexander Bauer et al. "The Scale-up and Commercialization of Nonaqueous Na-Ion Battery Technologies". In: *Advanced Energy Materials* 8.17 (2018). _eprint: https://onlinelibrary.wiley.com/doi/pdf/10.1002/aenm.201702869, p. 1702869. ISSN: 1614-6840. DOI: 10.1002/aenm.201702869. URL: https://onlinelibrary.wiley.com/doi/abs/10.1002/aenm.201702869.

[21] Damien Saurel et al. "From Charge Storage Mechanism to Performance: A Roadmap toward High Specific Energy Sodium-Ion Batteries through Carbon Anode Optimization". In: *Advanced Energy Materials* 8.17 (2018). _eprint: https://onlinelibrary.wiley.com/doi/pdf/10.1002/aenm.201703268, p. 1703268. ISSN: 1614-6840. DOI: 10.1002/aenm.201703268. URL: https://onlinelibrary.wiley.com/doi/abs/10.1002/aenm.201703268.

[22] Naoaki Yabuuchi et al. "Research Development on Sodium-Ion Batteries". In: *Chemical Reviews* 114.23 (Dec. 10, 2014). Publisher: American Chemical Society, pp. 11636–11682. ISSN: 0009-2665. DOI: 10.1021/cr500192f. URL: https://doi.org/10.1021/cr500192f.

[23] Wenli Zhang et al. "Sodium-ion battery anodes: Status and future trends". In: *EnergyChem* 1.2 (Sept. 2019), p. 100012. ISSN: 25897780. DOI: 10.1016/j.enchem.2019.100012. URL: https://linkinghub.elsevier.com/retrieve/pii/S2589778019300156.

[24] Jason J. Huang et al. "Disorder Dynamics in Battery Nanoparticles During Phase Transitions Revealed by Operando Single-Particle Diffraction". In: *Advanced Energy Materials* 12.12 (2022). _eprint: https://onlinelibrary.wiley.com/doi/pdf/10.1002/aenm.202103521, p. 2103521. ISSN: 1614-6840. DOI: 10.1002/aenm.202103521. URL: https://onlinelibrary.wiley.com/doi/abs/10.1002/aenm.202103521.

[25] M. Stanley Whittingham. "Lithium Batteries and Cathode Materials". In: *Chemical Reviews* 104.10 (Oct. 1, 2004). Publisher: American Chemical Society, pp. 4271–4302. ISSN: 0009-2665. DOI: 10.1021/cr020731c. URL: https://doi.org/10.1021/cr020731c.

[26] Naoki Nitta and Gleb Yushin. "High-Capacity Anode Materials for Lithium-Ion Batteries: Choice of Elements and Structures for Active Particles". In: *Particle & Particle Systems Characterization* 31.3 (2014). _eprint: https://onlinelibrary.wiley.com/doi/pdf/10.1002/ppsc.201300231, pp. 317–336. ISSN: 1521-4117. DOI: 10.1002/ppsc.201300231. URL: https://onlinelibrary.wiley.com/doi/abs/10.1002/ppsc.201300231.

[27] Aditya Narayan Singh et al. "Unleashing the Potential of Sodium-Ion Batteries: Current State and Future Directions for Sustainable Energy Storage". In: *Advanced Functional Materials* 33.46 (Nov. 2023), p. 2304617. ISSN: 1616-301X, 1616-3028. DOI: 10.1002/adfm.202304617. URL: https://onlinelibrary.wiley.com/doi/10.1002/adfm.202304617.

[28] Ling-Fei Zhao et al. "Hard Carbon Anodes: Fundamental Understanding and Commercial Perspectives for Na-Ion Batteries beyond Li-Ion and K-Ion Counterparts". In: *Advanced Energy Materials* 11.1 (2021). _eprint: https://onlinelibrary.wiley.com/doi/pdf/10.1002/aenm.202002704, p. 2002704. ISSN: 1614-6840. DOI: 10.1002/aenm.202002704. URL: https://onlinelibrary.wiley.com/doi/abs/10.1002/aenm.202002704.

[29] Kang Xu. "Nonaqueous Liquid Electrolytes for Lithium-Based Rechargeable Batteries". In: *Chemical Reviews* 104.10 (Oct. 1, 2004). Publisher: American Chemical Society, pp. 4303–4418. ISSN: 0009-2665. DOI: 10.1021/cr030203g. URL: https://doi.org/10.1021/cr030203g.

[30] Noriaki Kamaya et al. "A lithium superionic conductor". In: *Nature Materials* 10.9 (Sept. 2011). Number: 9 Publisher: Nature Publishing Group, pp. 682–686. ISSN: 1476-4660. DOI: 10.1038/nmat3066. URL: https://www.nature.com/articles/nmat3066.

[31] Akitoshi Hayashi et al. "Superionic glass-ceramic electrolytes for room-temperature rechargeable sodium batteries". In: *Nature Communications* 3.1 (May 22, 2012). Number: 1 Publisher: Nature Publishing Group, p. 856. ISSN: 2041-1723. DOI: 10.1038/ncomms1843. URL: https://www.nature.com/articles/ncomms1843.

[32] Qingguang Pan, Decai Gong, and Yongbing Tang. "Recent progress and perspective on electrolytes for sodium/potassium-based devices". In: *Energy Storage Materials* 31 (Oct. 1, 2020), pp. 328–343. ISSN: 2405-8297. DOI: 10.1016/j.ensm.2020.06.025. URL: https://www.sciencedirect.com/science/article/pii/S2405829720302452.

[33] Gui-Liang Xu et al. "Challenges in Developing Electrodes, Electrolytes, and Diagnostics Tools to Understand and Advance Sodium-Ion Batteries". In: *Advanced Energy Materials* 8.14 (2018). _eprint: https://onlinelibrary.wiley.com/doi/pdf/10.1002/aenm.201702403, p. 1702403. ISSN: 1614-6840. DOI: 10.1002/aenm.201702403. URL: https://onlinelibrary.wiley.com/doi/abs/10.1002/aenm.201702403.

[34] Ying Li et al. "Ether-based electrolytes for sodium ion batteries". In: *Chemical Society Reviews* 51.11 (2022). Publisher: Royal Society of Chemistry, pp. 4484–4536. DOI: 10.1039/D1CS00948F. URL: https://pubs.rsc.org/en/content/articlelanding/2022/cs/d1cs00948f.

[35] Haiying Che et al. "Electrolyte design strategies and research progress for room-temperature sodium-ion batteries". In: *Energy & Environmental Science* 10.5 (May 17, 2017). Publisher: The Royal Society of Chemistry, pp. 1075–1101. ISSN: 1754-5706. DOI: 10.1039/C7EE00524E. URL: https://pubs.rsc.org/en/content/articlelanding/2017/ee/c7ee00524e.

[36] A. Ponrouch et al. "Non-aqueous electrolytes for sodium-ion batteries". In: *Journal of Materials Chemistry A* 3.1 (2015). Publisher: Royal Society of Chemistry, pp. 22–42. DOI: 10.1039/C4TA04428B. URL: https://pubs.rsc.org/en/content/articlelanding/2015/ta/c4ta04428b.

[37] K. Vignarooban et al. "Current trends and future challenges of electrolytes for sodium-ion batteries". In: *International Journal of Hydrogen Energy* 41.4 (Jan. 30, 2016), pp. 2829–2846. ISSN: 0360-3199. DOI: 10.1016/j.ijhydene.2015.12.090. URL: https://www.sciencedirect.com/science/article/pii/S0360319915027706.

[38] Shibing Ni et al. "The fine electrochemical performance of porous Cu 3 P/Cu and the high energy density of Cu 3 P as anode for Li-ion batteries". In: *Journal of Materials Chemistry A* 2.48 (2014). Publisher: Royal Society of Chemistry, pp. 20506–20509. DOI: 10.1039/C4TA03871A. URL: https://pubs.rsc.org/en/content/articlelanding/2014/ta/c4ta03871a.

[39] Junhua Zhou et al. "Phosphorus-Based Composites as Anode Materials for Advanced Alkali Metal Ion Batteries". In: *Advanced Functional Materials* 30.49 (2020). _eprint: https://onlinelibrary.wiley.com/doi/pdf/10.1002/adfm.202004648, p. 2004648. ISSN: 1616-3028. DOI: 10.1002/adfm.202004648. URL: https://onlinelibrary.wiley.com/doi/abs/10.1002/adfm.202004648.

[40] Lichuan Wang et al. "Promises and challenges of alloy-type and conversion-type anode materials for sodium–ion batteries". In: *Materials Today Energy* 11 (Mar. 1, 2019), pp. 46–60. ISSN: 2468-6069. DOI: 10.1016/j.mtener.2018.10.017. URL: https://www.sciencedirect.com/science/article/pii/S2468606918302491.

[41] Huang Zhang, Ivana Hasa, and Stefano Passerini. "Beyond Insertion for Na-Ion Batteries: Nanostructured Alloying and Conversion Anode Materials". In: *Advanced Energy Materials* 8.17 (2018). _eprint: https://onlinelibrary.wiley.com/doi/pdf/10.1002/aenm.201702582, p. 1702582. ISSN: 1614-6840. DOI: 10.1002/aenm.201702582. URL: https://onlinelibrary.wiley.com/doi/abs/10.1002/aenm.201702582.

[42] Xiang Li et al. "Electroactive organics as promising anode materials for rechargeable lithium ion and sodium ion batteries". In: *Energy Materials* 2.2 (2022), p. 200014. ISSN: 27705900. DOI: 10.20517/energymater.2022.11. URL: https://energymaterj.com/article/view/4835.

[43] Hui Chang et al. "Recent developments in advanced anode materials for lithium-ion batteries". In: *Energy Materials* 1.1 (2022), p. 100003. ISSN: 27705900. DOI: 10.20517/energymater.2021.02. URL: https://energymaterj.com/article/view/4302.

[44] Liang Cao et al. "Heterointerface Engineering of Hierarchical Bi2S3/MoS2 with Self-Generated Rich Phase Boundaries for Superior Sodium Storage Performance". In: *Advanced Functional Materials* 30.16 (2020). _eprint: https://onlinelibrary.wiley.com/doi/pdf/10.1002/adfm.201910732, p. 1910732. ISSN: 1616-3028. DOI: 10.1002/adfm.201910732. URL: https://onlinelibrary.wiley.com/doi/abs/10.1002/adfm.201910732.

[45] Kongyao Chen et al. "Simple Preparation of Baroque Mn-Based Chalcogenide/Honeycomb-like Carbon Composites for Sodium-Ion Batteries from Renewable Pleurotus Eryngii". In: *Energy & Fuels* 35.7 (Apr. 1, 2021). Publisher: American Chemical Society, pp. 6265–6271. ISSN: 0887-0624. DOI: 10.1021/acs.energyfuels.1c00338. URL: https://doi.org/10.1021/acs.energyfuels.1c00338.

[46] Chao Wu, Shi-Xue Dou, and Yan Yu. "The State and Challenges of Anode Materials Based on Conversion Reactions for Sodium Storage". In: *Small* 14.22 (2018). _eprint: https://onlinelibrary.wiley.com/doi/pdf/10.1002/smll.201703671, p. 1703671. ISSN: 1613-6829. DOI: 10.1002/smll.201703671. URL: https://onlinelibrary.wiley.com/doi/abs/10.1002/smll.201703671.

[47] Yan Lu, Le Yu, and Xiong Wen (David) Lou. "Nanostructured Conversion-type Anode Materials for Advanced Lithium-Ion Batteries". In: *Chem* 4.5 (May 10, 2018), pp. 972–996. ISSN: 2451-9294. DOI: 10.1016/j.chempr.2018.01.003. URL: https://www.sciencedirect.com/science/article/pii/S2451929418300251.

[48] Gaojie Li et al. "Recent advances and perspectives of microsized alloying-type porous anode materials in high-performance Li- and Na-ion batteries". In: *Energy Materials* 2.3 (2022), p. 200020. ISSN: 27705900. DOI: 10.20517/energymater.2022.24. URL: https://energymaterj.com/article/view/4937.

[49] Jiazheng Niu, Zhonghua Zhang, and Doron Aurbach. "Alloy Anode Materials for Rechargeable Mg Ion Batteries". In: *Advanced Energy Materials* 10.23 (2020). _eprint: https://onlinelibrary.wiley.com/doi/pdf/10.1002/aenm.202000697, p. 2000697. ISSN: 1614-6840. DOI: 10.1002/aenm.202000697. URL: https://onlinelibrary.wiley.com/doi/abs/10.1002/aenm.202000697.

[50] Biao Zhang et al. "Recent advances in electrospun carbon nanofibers and their application in electrochemical energy storage". In: *Progress in Materials Science* 76 (Mar. 1, 2016), pp. 319–380. ISSN: 0079-6425. DOI: 10.1016/j.pmatsci.2015.08.002. URL: https://www.sciencedirect.com/science/article/pii/S0079642515000936.

[51] Mengmeng Lao et al. "Alloy-Based Anode Materials toward Advanced Sodium-Ion Batteries". In: *Advanced Materials* 29.48 (2017). _eprint: https://onlinelibrary.wiley.com/doi/pdf/10.1002/adma.201700622, p. 1700622. ISSN: 1521-4095. DOI: 10.1002/adma.201700622. URL: https://onlinelibrary.wiley.com/doi/abs/10.1002/adma.201700622.

[52] Yongling An et al. "Dealloying: An effective method for scalable fabrication of 0D, 1D, 2D, 3D materials and its application in energy storage". In: *Nano Today* 37 (Apr. 1, 2021), p. 101094. ISSN: 1748-0132. DOI: 10.1016/j.nantod.2021.101094. URL: https://www.sciencedirect.com/science/article/pii/S1748013221000190.

[53] Hana Yoo et al. "Helical Silicon/Silicon Oxide Core–Shell Anodes Grown onto the Surface of Bulk Silicon". In: *Nano Letters* 11.10 (Oct. 12, 2011). Publisher: American Chemical Society, pp. 4324–4328. ISSN: 1530-6984. DOI: 10.1021/nl202417c. URL: https://doi.org/10.1021/nl202417c.

[54] Yongling An et al. "One-Step, Vacuum-Assisted Construction of Micrometer-Sized Nanoporous Silicon Confined by Uniform Two-Dimensional N-Doped Carbon toward Advanced Li Ion and MXene-Based Li Metal Batteries". In: *ACS Nano* 16.3 (Mar. 22, 2022). Publisher: American Chemical Society, pp. 4560–4577. ISSN: 1936-0851. DOI: 10.1021/acsnano.1c11098. URL: https://doi.org/10.1021/acsnano.1c11098.

[55] Huajun Tian et al. "High capacity group-IV elements (Si, Ge, Sn) based anodes for lithium-ion batteries". In: *Journal of Materiomics* 1.3 (Sept. 1, 2015), pp. 153–169. ISSN: 2352-8478. DOI: 10.1016/j.jmat.2015.06.002. URL: https://www.sciencedirect.com/science/article/pii/S2352847815000477.

[56] Tao Li et al. "Fluorinated Solid-Electrolyte Interphase in High-Voltage Lithium Metal Batteries". In: *Joule* 3.11 (Nov. 20, 2019), pp. 2647–2661. ISSN: 2542-4351. DOI: 10.1016/j.joule.2019.09.022. URL: https://www.sciencedirect.com/science/article/pii/S2542435119304829.

[57] Shuai Liu et al. "A controlled red phosphorus@Ni–P core@shell nanostructure as an ultralong cycle-life and superior high-rate anode for sodium-ion batteries". In: *Energy & Environmental Science* 10.5 (2017). Publisher: Royal Society of Chemistry, pp. 1222–1233. DOI: 10.1039/C7EE00102A. URL: https://pubs.rsc.org/en/content/articlelanding/2017/ee/c7ee00102a.

[58] Xiang Liu et al. "Stress- and Interface-Compatible Red Phosphorus Anode for High-Energy and Durable Sodium-Ion Batteries". In: *ACS Energy Letters* 6.2 (Feb. 12, 2021). Publisher: American Chemical Society, pp. 547–556. DOI: 10.1021/acsenergylett.0c02650. URL: https://doi.org/10.1021/acsenergylett.0c02650.

[59] Ying Wu et al. "The Promise and Challenge of Phosphorus-Based Composites as Anode Materials for Potassium-Ion Batteries". In: *Advanced Materials* 31.50 (2019). _eprint: https://onlinelibrary.wiley.com/doi/pdf/10.1002/adma.201901414, p. 1901414. ISSN: 1521-4095. DOI: 10.1002/adma.201901414. URL: https://onlinelibrary.wiley.com/doi/abs/10.1002/adma.201901414.

[60] Xiaoqiong Du and Biao Zhang. "Robust Solid Electrolyte Interphases in Localized High Concentration Electrolytes Boosting Black Phosphorus Anode for Potassium-Ion Batteries". In: *ACS Nano* 15.10 (Oct. 26, 2021). Publisher: American Chemical Society, pp. 16851–16860. ISSN: 1936-0851. DOI: 10.1021/acsnano.1c07414. URL: https://doi.org/10.1021/acsnano.1c07414.

[61] Hanwen Liu et al. "Recent Advances on Black Phosphorus for Energy Storage, Catalysis, and Sensor Applications". In: *Advanced Materials* 30.32 (2018). _eprint: https://onlinelibrary.wiley.com/doi/pdf/10.1002/adma.201800295, p. 1800295. ISSN: 1521-4095. DOI: 10.1002/adma.201800295. URL: https://onlinelibrary.wiley.com/doi/abs/10.1002/adma.201800295.

[62] Mouad Dahbi et al. "Black Phosphorus as a High-Capacity, High-Capability Negative Electrode for Sodium-Ion Batteries: Investigation of the Electrode/Electrolyte Interface". In: *Chemistry of Materials* 28.6 (Mar. 22, 2016). Publisher: American Chemical Society, pp. 1625–1635. ISSN: 0897-4756. DOI: 10.1021/acs.chemmater.5b03524. URL: https://doi.org/10.1021/acs.chemmater.5b03524.

[63] Yunhua Xu et al. "Electrochemical Performance of Porous Carbon/Tin Composite Anodes for Sodium-Ion and Lithium-Ion Batteries". In: *Advanced Energy Materials* 3.1 (2013). _eprint: https://onlinelibrary.wiley.com/doi/pdf/10.1002/aenm.201200346, pp. 128–133. ISSN: 1614-6840. DOI: 10.1002/aenm.201200346. URL: https://onlinelibrary.wiley.com/doi/abs/10.1002/aenm.201200346.

[64] Junpeng Xie et al. "Bifunctional Alloy/Solid-Electrolyte Interphase Layer for Enhanced Potassium Metal Batteries Via Prepassivation". In: *ACS Nano* 17.2 (Jan. 24, 2023). Publisher: American Chemical Society, pp. 1511–1521. ISSN: 1936-0851. DOI: 10.1021/acsnano.2c10535. URL: https://doi.org/10.1021/acsnano.2c10535.

[65] Yihang Liu et al. "Tin-Coated Viral Nanoforests as Sodium-Ion Battery Anodes". In: *ACS Nano* 7.4 (Apr. 23, 2013). Publisher: American Chemical Society, pp. 3627–3634. ISSN: 1936-0851. DOI: 10.1021/nn400601y. URL: https://doi.org/10.1021/nn400601y.

[66] Yuan Tian et al. "A general method for constructing robust, flexible and freestanding MXene@metal anodes for high-performance potassium-ion batteries". In: *Journal of Materials Chemistry A* 7.16 (2019). Publisher: Royal Society of Chemistry, pp. 9716–9725. DOI: 10.1039/C9TA02233C. URL: https://pubs.rsc.org/en/content/articlelanding/2019/ta/c9ta02233c.

[67] Zhiming Liu et al. "Sb@C coaxial nanotubes as a superior long-life and high-rate anode for sodium ion batteries". In: *Energy & Environmental Science* 9.7 (2016). Publisher: Royal Society of Chemistry, pp. 2314–2318. DOI: 10.1039/C6EE01501H. URL: https://pubs.rsc.org/en/content/articlelanding/2016/ee/c6ee01501h.

[68] Cheng-Zhi Ke et al. "Boosting lithium storage performance of Si nanoparticles via thin carbon and nitrogen/phosphorus co-doped two-dimensional carbon sheet dual encapsulation". In: *Rare Metals* 40.6 (June 1, 2021), pp. 1347–1356. ISSN: 1867-7185. DOI: 10.1007/s12598-021-01716-1. URL: https://doi.org/10.1007/s12598-021-01716-1.

[69] Jiaqiang Huang et al. "Nanostructures of solid electrolyte interphases and their consequences for microsized Sn anodes in sodium ion batteries". In: *Energy & Environmental Science* 12.5 (May 16, 2019). Publisher: The Royal Society of Chemistry, pp. 1550–1557. ISSN: 1754-5706. DOI: 10.1039/C8EE03632B. URL: https://pubs.rsc.org/en/content/articlelanding/2019/ee/c8ee03632b.

[70] Biao Zhang et al. "Microsized Sn as Advanced Anodes in Glyme-Based Electrolyte for Na-Ion Batteries". In: *Advanced Materials* 28.44 (2016). _eprint: https://onlinelibrary.wiley.com/doi/pdf/10.1002/adma.201603212, pp. 9824–9830. ISSN: 1521-4095. DOI: 10.1002/adma.201603212. URL: https://onlinelibrary.wiley.com/doi/abs/10.1002/adma.201603212.

[71] Junwei Han et al. "Realizing High Volumetric Lithium Storage by Compact and Mechanically Stable Anode Designs". In: *ACS Energy Letters* 5.6 (June 12, 2020). Publisher: American Chemical Society, pp. 1986–1995. DOI: 10.1021/acsenergylett.0c00851. URL: https://doi.org/10.1021/acsenergylett.0c00851.

[72] Rishabh Jain et al. "Nanostructuring versus microstructuring in battery electrodes". In: *Nature Reviews Materials* 7.9 (Sept. 2022). Number: 9 Publisher: Nature Publishing Group, pp. 736–746. ISSN: 2058-8437. DOI: 10.1038/s41578-022-00454-9. URL: https://www.nature.com/articles/s41578-022-00454-9.

[73] Amine Daali et al. "In situ microscopy and spectroscopy characterization of microsized Sn anode for sodium-ion batteries". In: *Nano Energy* 115 (2023), p. 108753. ISSN: 2211-2855. DOI: 10.1016/j.nanoen.2023.108753. URL: https://www.sciencedirect.com/science/article/pii/S2211285523005906.

[74] Yi-Fan Tian et al. "Micrometer-Sized SiMgyOx with Stable Internal Structure Evolution for High-Performance Li-Ion Battery Anodes". In: *Advanced Materials* 34.15 (2022). _eprint: https://onlinelibrary.wiley.com/doi/pdf/10.1002/adma.202200672, p. 2200672. ISSN: 1521-4095. DOI: 10.1002/adma.202200672. URL: https://onlinelibrary.wiley.com/doi/abs/10.1002/adma.202200672.

[75] Dequan Liu et al. "Group IVA Element (Si, Ge, Sn)-Based Alloying/Dealloying Anodes as Negative Electrodes for Full-Cell Lithium-Ion Batteries". In: *Small* 13.45 (2017). _eprint: https://onlinelibrary.wiley.com/doi/pdf/10.1002/smll.201702000, p. 1702000. ISSN: 1613-6829. DOI: 10.1002/smll.201702000. URL: https://onlinelibrary.wiley.com/doi/abs/10.1002/smll.201702000.

[76] Yihang Liu et al. "Red-phosphorus-impregnated carbon nanofibers for sodium-ion batteries and liquefaction of red phosphorus". In: *Nature Communications* 11.1 (May 20, 2020). Number: 1 Publisher: Nature Publishing Group, p. 2520. ISSN: 2041-1723. DOI: 10.1038/s41467-020-16077-z. URL: https://www.nature.com/articles/s41467-020-16077-z.

[77] Hongli Zhu et al. "Tin Anode for Sodium-Ion Batteries Using Natural Wood Fiber as a Mechanical Buffer and Electrolyte Reservoir". In: *Nano Letters* 13.7 (July 10, 2013). Publisher: American Chemical Society, pp. 3093–3100. ISSN: 1530-6984. DOI: 10.1021/nl400998t. URL: https://doi.org/10.1021/nl400998t.

[78] Jiaqiang Huang et al. "Bismuth Microparticles as Advanced Anodes for Potassium-Ion Battery". In: *Advanced Energy Materials* 8.19 (2018). _eprint: https://onlinelibrary.wiley.com/doi/pdf/10.1002/aenm.201703496, p. 1703496. ISSN: 1614-6840. DOI: 10.1002/aenm.201703496. URL: https://onlinelibrary.wiley.com/doi/abs/10.1002/aenm.201703496.

[79] Yue Gao et al. "General Method of Manipulating Formation, Composition, and Morphology of Solid-Electrolyte Interphases for Stable Li-Alloy Anodes". In: *Journal of the American Chemical Society* 139.48 (Dec. 6, 2017). Publisher: American Chemical Society, pp. 17359–17367. ISSN: 0002-7863. DOI: 10.1021/jacs.7b07584. URL: https://doi.org/10.1021/jacs.7b07584.

[80] Martin Winter, Brian Barnett, and Kang Xu. "Before Li Ion Batteries". In: *Chemical Reviews* 118.23 (Dec. 12, 2018). Publisher: American Chemical Society, pp. 11433–11456. ISSN: 0009-2665. DOI: 10.1021/acs.chemrev.8b00422. URL: https://doi.org/10.1021/acs.chemrev.8b00422.

[81] Matthew Li et al. "30 Years of Lithium-Ion Batteries". In: *Advanced Materials* 30.33 (2018). _eprint: https://onlinelibrary.wiley.com/doi/pdf/10.1002/adma.201800561, p. 1800561. ISSN: 1521-4095. DOI: 10.1002/adma.201800561. URL: https://onlinelibrary.wiley.com/doi/abs/10.1002/adma.201800561.

[82] Huiteng Tan et al. "Peering into Alloy Anodes for Sodium-Ion Batteries: Current Trends, Challenges, and Opportunities". In: *Advanced Functional Materials* 29.14 (2019). _eprint: https://onlinelibrary.wiley.com/doi/pdf/10.1002/adfm.201808745, p. 1808745. ISSN: 1616-3028. DOI: 10.1002/adfm.201808745. URL: https://onlinelibrary.wiley.com/doi/abs/10.1002/adfm.201808745.

[83] Suzhe Liang et al. "A Chronicle Review of Nonsilicon (Sn, Sb, Ge)-Based Lithium/Sodium-Ion Battery Alloying Anodes". In: *Small Methods* 4.8 (2020). _eprint: https://onlinelibrary.wiley.com/doi/pdf/10.1002/smtd.202000218, p. 2000218. ISSN: 2366-9608. DOI: 10.1002/smtd.202000218. URL: https://onlinelibrary.wiley.com/doi/abs/10.1002/smtd.202000218.

[84] Vanchiappan Aravindan, Yun-Sung Lee, and Srinivasan Madhavi. "Research Progress on Negative Electrodes for Practical Li-Ion Batteries: Beyond Carbonaceous Anodes". In: *Advanced Energy Materials* 5.13 (2015). _eprint: https://onlinelibrary.wiley.com/doi/pdf/10.1002/aenm.201402225, p. 1402225. ISSN: 1614-6840. DOI: 10.1002/aenm.201402225. URL: https://onlinelibrary.wiley.com/doi/abs/10.1002/aenm.201402225.

[85] Eric J. McShane et al. "Quantification of Inactive Lithium and Solid–Electrolyte Interphase Species on Graphite Electrodes after Fast Charging". In: *ACS Energy Letters* 5.6 (June 12, 2020). Publisher: American Chemical Society, pp. 2045–2051. DOI: 10.1021/acsenergylett.0c00859. URL: https://doi.org/10.1021/acsenergylett.0c00859.

[86] Xianchun Deng, Zhongxue Chen, and Yuliang Cao. "Transition metal oxides based on conversion reaction for sodium-ion battery anodes". In: *Materials Today Chemistry* 9 (Sept. 1, 2018), pp. 114–132. ISSN: 2468-5194. DOI: 10.1016/j.mtchem.2018.06.002. URL: https://www.sciencedirect.com/science/article/pii/S2468519418300569.

[87] Siva P. V. Nadimpalli, Rajasekhar Tripuraneni, and Vijay A. Sethuraman. "Real-Time Stress Measurements in Germanium Thin Film Electrodes during Electrochemical Lithiation/Delithiation Cycling". In: *Journal of The Electrochemical Society* 162.14 (Oct. 28, 2015). Publisher: IOP Publishing, A2840. ISSN: 1945-7111. DOI: 10.1149/2.0941514jes. URL: https://iopscience.iop.org/article/10.1149/2.0941514jes/meta.

[88] Qidi Wang et al. "Advanced Nanostructured Anode Materials for Sodium-Ion Batteries". In: *Small* 13.42 (2017). _eprint: https://onlinelibrary.wiley.com/doi/pdf/10.1002/smll.201701835, p. 1701835. ISSN: 1613-6829. DOI: 10.1002/smll.201701835. URL: https://onlinelibrary.wiley.com/doi/abs/10.1002/smll.201701835.

[89] Songtao Guo et al. "Architectural Engineering Achieves High-Performance Alloying Anodes for Lithium and Sodium Ion Batteries". In: *Small* 17.19 (May 2021), p. 2005248. ISSN: 1613-6810, 1613-6829. DOI: 10.1002/smll.202005248. URL: https://onlinelibrary.wiley.com/doi/10.1002/smll.202005248.

[90] Brian L. Ellis, Philippe Knauth, and Thierry Djenizian. "Three-Dimensional Self-Supported Metal Oxides for Advanced Energy Storage". In: *Advanced Materials* 26.21 (2014). _eprint: https://onlinelibrary.wiley.com/doi/pdf/10.1002/adma.201306126, pp. 3368–3397. ISSN: 1521-4095. DOI: 10.1002/adma.201306126. URL: https://onlinelibrary.wiley.com/doi/abs/10.1002/adma.201306126.

[91] Konstantinos Gerasopoulos et al. "Hierarchical Three-Dimensional Microbattery Electrodes Combining Bottom-Up Self-Assembly and Top-Down Micromachining". In: *ACS Nano* 6.7 (July 24, 2012). Publisher: American Chemical Society, pp. 6422–6432. ISSN: 1936-0851. DOI: 10.1021/nn301981p. URL: https://doi.org/10.1021/nn301981p.

[92] Jeffrey W. Long et al. "Three-Dimensional Battery Architectures". In: *Chemical Reviews* 104.10 (Oct. 1, 2004). Publisher: American Chemical Society, pp. 4463–4492. ISSN: 0009-2665. DOI: 10.1021/cr0207401. URL: https://doi.org/10.1021/cr0207401.

[93] Candace K. Chan et al. "High-performance lithium battery anodes using silicon nanowires". In: *Nature Nanotechnology* 3.1 (Jan. 2008), pp. 31–35. ISSN: 1748-3387, 1748-3395. DOI: 10.1038/nnano.2007.411. URL: https://www.nature.com/articles/nnano.2007.411.

[94] Yongchang Liu et al. "Tin Nanodots Encapsulated in Porous Nitrogen-Doped Carbon Nanofibers as a Free-Standing Anode for Advanced Sodium-Ion Batteries". In: *Advanced Materials* 27.42 (2015). _eprint: https://onlinelibrary.wiley.com/doi/pdf/10.1002/adma.201503015, pp. 6702–6707. ISSN: 1521-4095. DOI: 10.1002/adma.201503015. URL: https://onlinelibrary.wiley.com/doi/abs/10.1002/adma.201503015.

[95] Yongling An et al. "Micron-Sized Nanoporous Antimony with Tunable Porosity for High-Performance Potassium-Ion Batteries". In: *ACS Nano* 12.12 (Dec. 26, 2018). Publisher: American Chemical Society, pp. 12932–12940. ISSN: 1936-0851. DOI: 10.1021/acsnano.8b08740. URL: https://doi.org/10.1021/acsnano.8b08740.

[96] Shuai Liu et al. “Nanoporous Red Phosphorus on Reduced Graphene Oxide as Superior Anode for Sodium-Ion Batteries”. In: *ACS Nano* 12.7 (July 24, 2018). Publisher: American Chemical Society, pp. 7380–7387. ISSN: 1936-0851. DOI: 10.1021/acsnano.8b04075. URL: https://doi.org/10.1021/acsnano.8b04075.

[97] Yongling An et al. “Scalable and Physical Synthesis of 2D Silicon from Bulk Layered Alloy for Lithium-Ion Batteries and Lithium Metal Batteries”. In: *ACS Nano* 13.12 (Dec. 24, 2019). Publisher: American Chemical Society, pp. 13690–13701. ISSN: 1936-0851. DOI: 10.1021/acsnano.9b06653. URL: https://doi.org/10.1021/acsnano.9b06653.

[98] Yongling An et al. “Porosity- and Graphitization-Controlled Fabrication of Nanoporous Silicon@Carbon for Lithium Storage and Its Conjugation with MXene for Lithium-Metal Anode”. In: *Advanced Functional Materials* 30.9 (2020). _eprint: https://onlinelibrary.wiley.com/doi/pdf/10.1002/adfm.201908721, p. 1908721. ISSN: 1616-3028. DOI: 10.1002/adfm.201908721. URL: https://onlinelibrary.wiley.com/doi/abs/10.1002/adfm.201908721.

[99] Naoki Nitta et al. “Li-ion battery materials: present and future”. In: *Materials Today* 18.5 (June 1, 2015), pp. 252–264. ISSN: 1369-7021. DOI: 10.1016/j.mattod.2014.10.040. URL: https://www.sciencedirect.com/science/article/pii/S1369702114004118.

[100] Wei Zhai et al. “Walnut-inspired microsized porous silicon/graphene core–shell composites for high-performance lithium-ion battery anodes”. In: *Nano Research* 10.12 (Dec. 1, 2017), pp. 4274–4283. ISSN: 1998-0000. DOI: 10.1007/s12274-017-1584-5. URL: https://doi.org/10.1007/s12274-017-1584-5.

[101] Jiangyan Wang and Yi Cui. “Electrolytes for microsized silicon”. In: *Nature Energy* 5.5 (May 2020). Number: 5 Publisher: Nature Publishing Group, pp. 361–362. ISSN: 2058-7546. DOI: 10.1038/s41560-020-0608-7. URL: https://www.nature.com/articles/s41560-020-0608-7.

[102] Guanjia Zhu et al. “Microscale Silicon-Based Anodes: Fundamental Understanding and Industrial Prospects for Practical High-Energy Lithium-Ion Batteries”. In: *ACS Nano* 15.10 (Oct. 26, 2021). Publisher: American Chemical Society, pp. 15567–15593. ISSN: 1936-0851. DOI: 10.1021/acsnano.1c05898. URL: https://doi.org/10.1021/acsnano.1c05898.

[103] Xiaoqiong Du, Yao Gao, and Biao Zhang. “Building Elastic Solid Electrolyte Interphases for Stabilizing Microsized Antimony Anodes in Potassium Ion Batteries”. In: *Advanced Functional Materials* 31.26 (2021). _eprint: https://onlinelibrary.wiley.com/doi/pdf/10.1002/adfm.202102562, p. 2102562. ISSN: 1616-3028. DOI: 10.1002/adfm.202102562. URL: https://onlinelibrary.wiley.com/doi/abs/10.1002/adfm.202102562.

[104] Kang Xu. “Electrolytes and Interphases in Li-Ion Batteries and Beyond”. In: *Chemical Reviews* 114.23 (Dec. 10, 2014). Publisher: American Chemical Society, pp. 11503–11618. ISSN: 0009-2665. DOI: 10.1021/cr500003w. URL: https://doi.org/10.1021/cr500003w.

[105] Jürgen O. Besenhard, ed. *Handbook of battery materials*. Weinheim ; New York: Wiley-VCH, 1999. 618 pp. ISBN: 978-3-527-29469-5.

[106] Pekka Peljo and Hubert H. Girault. "Electrochemical potential window of battery electrolytes: the HOMO–LUMO misconception". In: *Energy & Environmental Science* 11.9 (2018). Publisher: Royal Society of Chemistry, pp. 2306–2309. DOI: 10.1039/C8EE01286E. URL: https://pubs.rsc.org/en/content/articlelanding/2018/ee/c8ee01286e.

[107] Byeongyong Lee et al. "Sodium Metal Anodes: Emerging Solutions to Dendrite Growth". In: *Chemical Reviews* 119.8 (Apr. 24, 2019). Publisher: American Chemical Society, pp. 5416–5460. ISSN: 0009-2665. DOI: 10.1021/acs.chemrev.8b00642. URL: https://doi.org/10.1021/acs.chemrev.8b00642.

[108] Alexandra K. Stephan. "Completing the Picture of the Solid Electrolyte Interphase". In: *Joule* 3.8 (Aug. 21, 2019), pp. 1812–1814. ISSN: 2542-4351. DOI: 10.1016/j.joule.2019.08.002. URL: https://www.sciencedirect.com/science/article/pii/S2542435119303770.

[109] Junxiong Wu et al. "Understanding solid electrolyte interphases: Advanced characterization techniques and theoretical simulations". In: *Nano Energy* 89 (Nov. 1, 2021), p. 106489. ISSN: 2211-2855. DOI: 10.1016/j.nanoen.2021.106489. URL: https://www.sciencedirect.com/science/article/pii/S2211285521007424.

[110] Nan Yao et al. "Applying Classical, Ab Initio, and Machine-Learning Molecular Dynamics Simulations to the Liquid Electrolyte for Rechargeable Batteries". In: *Chemical Reviews* 122.12 (June 22, 2022). Publisher: American Chemical Society, pp. 10970–11021. ISSN: 0009-2665. DOI: 10.1021/acs.chemrev.1c00904. URL: https://doi.org/10.1021/acs.chemrev.1c00904.

[111] Mengjie Li et al. "Electrolytes in Organic Batteries". In: *Chemical Reviews* 123.4 (Feb. 22, 2023). Publisher: American Chemical Society, pp. 1712–1773. ISSN: 0009-2665. DOI: 10.1021/acs.chemrev.2c00374. URL: https://doi.org/10.1021/acs.chemrev.2c00374.

[112] Xiulin Fan and Chunsheng Wang. "High-voltage liquid electrolytes for Li batteries: progress and perspectives". In: *Chemical Society Reviews* 50.18 (2021). Publisher: Royal Society of Chemistry, pp. 10486–10566. DOI: 10.1039/D1CS00450F. URL: https://pubs.rsc.org/en/content/articlelanding/2021/cs/d1cs00450f.

[113] Bharathy S. Parimalam and Brett L. Lucht. "Reduction Reactions of Electrolyte Salts for Lithium Ion Batteries: LiPF6, LiBF4, LiDFOB, LiBOB, and LiTFSI". In: *Journal of The Electrochemical Society* 165.2 (Jan. 19, 2018). Publisher: IOP Publishing, A251. ISSN: 1945-7111. DOI: 10.1149/2.0901802jes. URL: https://iopscience.iop.org/article/10.1149/2.0901802jes/meta.

[114] Liang Ma et al. "Re-oxidation reconstruction process of solid electrolyte interphase layer derived from highly active anion for potassium-ion batteries". In: *Nano Energy* 87 (Sept. 1, 2021), p. 106150. ISSN: 2211-2855. DOI: 10.1016/j.nanoen.2021.106150. URL: https://www.sciencedirect.com/science/article/pii/S2211285521004067.

[115] Hao Zheng et al. "Lithium Difluorophosphate-Based Dual-Salt Low Concentration Electrolytes for Lithium Metal Batteries". In: *Advanced Energy Materials* 10.30 (2020). _eprint: https://onlinelibrary.wiley.com/doi/pdf/10.1002/aenm.202001440, p. 2001440. ISSN: 1614-6840. DOI: 10.1002/aenm.202001440. URL: https://onlinelibrary.wiley.com/doi/abs/10.1002/aenm.202001440.

[116] Gebrekidan Gebresilassie Eshetu et al. "Electrolytes and Interphases in Sodium-Based Rechargeable Batteries: Recent Advances and Perspectives". In: *Advanced Energy Materials* 10.20 (2020). _eprint: https://onlinelibrary.wiley.com/doi/pdf/10.1002/aenm.202000093, p. 2000093. ISSN: 1614-6840. DOI: 10.1002/aenm.202000093. URL: https://onlinelibrary.wiley.com/doi/abs/10.1002/aenm.202000093.

[117] Yongling An et al. "Commercial expanded graphite as a low–cost, long-cycling life anode for potassium–ion batteries with conventional carbonate electrolyte". In: *Journal of Power Sources* 378 (Feb. 28, 2018), pp. 66–72. ISSN: 0378-7753. DOI: 10.1016/j.jpowsour.2017.12.033. URL: https://www.sciencedirect.com/science/article/pii/S037877531731635X.

[118] Zhihong Piao et al. "A Review on Regulating Li+ Solvation Structures in Carbonate Electrolytes for Lithium Metal Batteries". In: *Advanced Materials* 35.15 (2023). _eprint: https://onlinelibrary.wiley.com/doi/pdf/10.1002/adma.202206009, p. 2206009. ISSN: 1521-4095. DOI: 10.1002/adma.202206009. URL: https://onlinelibrary.wiley.com/doi/abs/10.1002/adma.202206009.

[119] Yao Gao et al. "Unraveling the mechanical origin of stable solid electrolyte interphase". In: *Joule* 5.7 (July 21, 2021), pp. 1860–1872. ISSN: 2542-4351. DOI: 10.1016/j.joule.2021.05.015. URL: https://www.sciencedirect.com/science/article/pii/S2542435121002506.

[120] Atetegeb Meazah Haregewoin, Aselefech Sorsa Wotango, and Bing-Joe Hwang. "Electrolyte additives for lithium ion battery electrodes: progress and perspectives". In: *Energy & Environmental Science* 9.6 (2016). Publisher: Royal Society of Chemistry, pp. 1955–1988. DOI: 10.1039/C6EE00123H. URL: https://pubs.rsc.org/en/content/articlelanding/2016/ee/c6ee00123h.

[121] Ziqi Zeng et al. "A Safer Sodium-Ion Battery Based on Nonflammable Organic Phosphate Electrolyte". In: *Advanced Science* 3.9 (2016). _eprint: https://onlinelibrary.wiley.com/doi/pdf/10.1002/advs.201600066, p. 1600066. ISSN: 2198-3844. DOI: 10.1002/advs.201600066. URL: https://onlinelibrary.wiley.com/doi/abs/10.1002/advs.201600066.

[122] Yanting Jin et al. "Understanding Fluoroethylene Carbonate and Vinylene Carbonate Based Electrolytes for Si Anodes in Lithium Ion Batteries with NMR Spectroscopy". In: *Journal of the American Chemical Society* 140.31 (Aug. 8, 2018). Publisher: American Chemical Society, pp. 9854–9867. ISSN: 0002-7863. DOI: 10.1021/jacs.8b03408. URL: https://doi.org/10.1021/jacs.8b03408.

[123] Bingsheng Qin et al. "Highly Reversible Sodiation of Tin in Glyme Electrolytes: The Critical Role of the Solid Electrolyte Interphase and Its Formation Mechanism". In: *ACS Applied Materials & Interfaces* 12.3 (Jan. 22, 2020). Publisher: American Chemical Society, pp. 3697–3708. ISSN: 1944-8244. DOI: 10.1021/acsami.9b20616. URL: https://doi.org/10.1021/acsami.9b20616.

[124] Juan Luis Gómez-Cámer et al. "Unravelling the impact of electrolyte nature on Sn 4 P 3 /C negative electrodes for Na-ion batteries". In: *Journal of Materials Chemistry A* 7.31 (2019). Publisher: Royal Society of Chemistry, pp. 18434–18441. DOI: 10.1039/C9TA04288A. URL: https://pubs.rsc.org/en/content/articlelanding/2019/ta/c9ta04288a.

[125] Huaping Wang et al. "Electrolytes Enriched by Crown Ethers for Lithium Metal Batteries". In: *Advanced Functional Materials* 31.2 (2021). _eprint: https://onlinelibrary.wiley.com/doi/pdf/10.1002/adfm.202002578, p. 2002578. ISSN: 1616-3028. DOI: 10.1002/adfm.202002578. URL: https://onlinelibrary.wiley.com/doi/abs/10.1002/adfm.202002578.

[126] Ji Chen et al. "Electrolyte design for LiF-rich solid–electrolyte interfaces to enable high-performance microsized alloy anodes for batteries". In: *Nature Energy* 5.5 (May 2020). Number: 5 Publisher: Nature Publishing Group, pp. 386–397. ISSN: 2058-7546. DOI: 10.1038/s41560-020-0601-1. URL: https://www.nature.com/articles/s41560-020-0601-1.

[127] Nan Zhang et al. "Tuning electrolyte enables microsized Sn as an advanced anode for Li-ion batteries". In: *Journal of Materials Chemistry A* 9.3 (Jan. 26, 2021). Publisher: The Royal Society of Chemistry, pp. 1812–1821. ISSN: 2050-7496. DOI: 10.1039/D0TA10861H. URL: https://pubs.rsc.org/en/content/articlelanding/2021/ta/d0ta10861h.

[128] E. Peter Roth and Christopher J. Orendorff. "How Electrolytes Influence Battery Safety". In: *The Electrochemical Society Interface* 21.2 (Jan. 1, 2012). Publisher: IOP Publishing, p. 45. ISSN: 1944-8783. DOI: 10.1149/2.F04122if. URL: https://iopscience.iop.org/article/10.1149/2.F04122if/meta.

[129] Kaoru Dokko et al. "Solvate Ionic Liquid Electrolyte for Li–S Batteries". In: *Journal of The Electrochemical Society* 160.8 (June 6, 2013). Publisher: IOP Publishing, A1304. ISSN: 1945-7111. DOI: 10.1149/2.111308jes. URL: https://iopscience.iop.org/article/10.1149/2.111308jes/meta.

[130] Suzette Izquierdo-Gonzales, Wentao Li, and Brett L. Lucht. "Hexamethylphosphoramide as a flame retarding additive for lithium-ion battery electrolytes". In: *Journal of Power Sources* 135.1 (Sept. 3, 2004), pp. 291–296. ISSN: 0378-7753. DOI: 10.1016/j.jpowsour.2004.04.011. URL: https://www.sciencedirect.com/science/article/pii/S0378775304005427.

[131] Ziqi Zeng et al. "Safer lithium ion batteries based on nonflammable electrolyte". In: *Journal of Power Sources*. 9th International Conference on Lead-Acid Batteries – LABAT 2014 279 (Apr. 1, 2015), pp. 6–12. ISSN: 0378-7753. DOI: 10.1016/j.jpowsour.

2014.12.150. URL: https://www.sciencedirect.com/science/article/pii/S0378775314021892.

[132] Qifeng Zheng et al. "A cyclic phosphate-based battery electrolyte for high voltage and safe operation". In: *Nature Energy* 5.4 (Apr. 2020). Number: 4 Publisher: Nature Publishing Group, pp. 291–298. ISSN: 2058-7546. DOI: 10.1038/s41560-020-0567-z. URL: https://www.nature.com/articles/s41560-020-0567-z.

[133] Shaoxiong Yang et al. "Rational Electrolyte Design to Form Inorganic–Polymeric Interphase on Silicon-Based Anodes". In: *ACS Energy Letters* 6.5 (May 14, 2021). Publisher: American Chemical Society, pp. 1811–1820. DOI: 10.1021/acsenergylett.1c00514. URL: https://doi.org/10.1021/acsenergylett.1c00514.

[134] Guifang Zeng et al. "Nonflammable Fluorinated Carbonate Electrolyte with High Salt-to-Solvent Ratios Enables Stable Silicon-Based Anode for Next-Generation Lithium-Ion Batteries". In: *ACS Applied Materials & Interfaces* 11.26 (July 3, 2019). Publisher: American Chemical Society, pp. 23229–23235. ISSN: 1944-8244. DOI: 10.1021/acsami.9b05570. URL: https://doi.org/10.1021/acsami.9b05570.

[135] Haiping Jia et al. "High-Performance Silicon Anodes Enabled By Nonflammable Localized High-Concentration Electrolytes". In: *Advanced Energy Materials* 9.31 (2019). _eprint: https://onlinelibrary.wiley.com/doi/pdf/10.1002/aenm.201900784, p. 1900784. ISSN: 1614-6840. DOI: 10.1002/aenm.201900784. URL: https://onlinelibrary.wiley.com/doi/abs/10.1002/aenm.201900784.

[136] Lu Wang et al. "In-situ Nano-Crystallization and Solvation Modulation to Promote Highly Stable Anode Involving Alloy/De-alloy for Potassium Ion Batteries". In: *Angewandte Chemie* 133.28 (2021). _eprint: https://onlinelibrary.wiley.com/doi/pdf/10.1002/ange.202100654, pp. 15509–15517. ISSN: 1521-3757. DOI: 10.1002/ange.202100654. URL: https://onlinelibrary.wiley.com/doi/abs/10.1002/ange.202100654.

[137] Noah M. Johnson et al. "Enabling Silicon Anodes with Novel Isosorbide-Based Electrolytes". In: *ACS Energy Letters* 7.2 (Feb. 11, 2022). Publisher: American Chemical Society, pp. 897–905. DOI: 10.1021/acsenergylett.2c00099. URL: https://doi.org/10.1021/acsenergylett.2c00099.

[138] Liwen Ji et al. "Controlling SEI Formation on SnSb-Porous Carbon Nanofibers for Improved Na Ion Storage". In: *Advanced Materials* 26.18 (2014). _eprint: https://onlinelibrary.wiley.com/doi/pdf/10.1002/adma.201304962, pp. 2901–2908. ISSN: 1521-4095. DOI: 10.1002/adma.201304962. URL: https://onlinelibrary.wiley.com/doi/abs/10.1002/adma.201304962.

[139] Atetegeb Meazah Haregewoin, Aselefech Sorsa Wotango, and Bing-Joe Hwang. "Electrolyte additives for lithium ion battery electrodes: progress and perspectives". In: *Energy & Environmental Science* 9.6 (June 8, 2016). Publisher: The Royal Society of Chemistry, pp. 1955–1988. ISSN: 1754-5706. DOI: 10.1039/C6EE00123H. URL: https://pubs.rsc.org/en/content/articlelanding/2016/ee/c6ee00123h.

[140] Yuan Li et al. "Stable and Safe Lithium Metal Batteries with Ni-Rich Cathodes Enabled by a High Efficiency Flame Retardant Additive". In: *Journal of The Electrochemical Society* 166.13 (Aug. 7, 2019). Publisher: IOP Publishing, A2736. ISSN: 1945-7111. DOI: 10.1149/2.0081913jes. URL: https://iopscience.iop.org/article/10.1149/2.0081913jes/meta.

[141] Manqi Peng et al. "Alloy-Type Anodes for High-Performance Rechargeable Batteries". In: *Angewandte Chemie International Edition* 61.33 (2022). _eprint: https://onlinelibrary.wiley.com/doi/pdf/10.1002/anie.202206770, e202206770. ISSN: 1521-3773. DOI: 10.1002/anie.202206770. URL: https://onlinelibrary.wiley.com/doi/abs/10.1002/anie.202206770.

[142] Qujiang Sun et al. "Interfacial and Interphasial Chemistry of Electrolyte Components to Invoke High-Performance Antimony Anodes and Non-Flammable Lithium-Ion Batteries". In: *Advanced Functional Materials* 33.1 (2023). _eprint: https://onlinelibrary.wiley.com/doi/pdf/10.1002/adfm.202210292, p. 2210292. ISSN: 1616-3028. DOI: 10.1002/adfm.202210292. URL: https://onlinelibrary.wiley.com/doi/abs/10.1002/adfm.202210292.

[143] Guochun Yan et al. "A New Electrolyte Formulation for Securing High Temperature Cycling and Storage Performances of Na-Ion Batteries". In: *Advanced Energy Materials* 9.41 (2019). _eprint: https://onlinelibrary.wiley.com/doi/pdf/10.1002/aenm.201901431, p. 1901431. ISSN: 1614-6840. DOI: 10.1002/aenm.201901431. URL: https://onlinelibrary.wiley.com/doi/abs/10.1002/aenm.201901431.

[144] Le Anh Ma et al. "Strategies for Mitigating Dissolution of Solid Electrolyte Interphases in Sodium-Ion Batteries". In: *Angewandte Chemie International Edition* 60.9 (2021). _eprint: https://onlinelibrary.wiley.com/doi/pdf/10.1002/anie.202013803, pp. 4855–4863. ISSN: 1521-3773. DOI: 10.1002/anie.202013803. URL: https://onlinelibrary.wiley.com/doi/abs/10.1002/anie.202013803.

[145] Zhiwei Li, Ning Fu, and Zhenglong Yang. "Particulate modification of lithium-ion battery anode materials and electrolytes". In: *Particuology* 83 (Dec. 1, 2023), pp. 129–141. ISSN: 1674-2001. DOI: 10.1016/j.partic.2023.02.010. URL: https://www.sciencedirect.com/science/article/pii/S1674200123000500.

[146] Jing Zhang et al. "Engineering Solid Electrolyte Interphase on Red Phosphorus for Long-Term and High-Capacity Sodium Storage". In: *Chemistry of Materials* 32.1 (Jan. 14, 2020). Publisher: American Chemical Society, pp. 448–458. ISSN: 0897-4756. DOI: 10.1021/acs.chemmater.9b04043. URL: https://doi.org/10.1021/acs.chemmater.9b04043.

[147] Xu Bian et al. "Microsized Antimony as a Stable Anode in Fluoroethylene Carbonate Containing Electrolytes for Rechargeable Lithium-/Sodium-Ion Batteries". In: *ACS Applied Materials & Interfaces* 12.3 (Jan. 22, 2020). Publisher: American Chemical Society, pp. 3554–3562. ISSN: 1944-8244. DOI: 10.1021/acsami.9b18006. URL: https://doi.org/10.1021/acsami.9b18006.

[148] Mengyang Xu et al. "NaF-rich solid electrolyte interphase for dendrite-free sodium metal batteries". In: *Energy Storage Materials* 44 (Jan. 1, 2022), pp. 477–486. ISSN: 2405-8297. DOI: 10.1016/j.ensm.2021.10.038. URL: https://www.sciencedirect.com/science/article/pii/S2405829721005018.

[149] Ali Darwiche et al. "Better Cycling Performances of Bulk Sb in Na-Ion Batteries Compared to Li-Ion Systems: An Unexpected Electrochemical Mechanism". In: *Journal of the American Chemical Society* 134.51 (Dec. 26, 2012). Publisher: American Chemical Society, pp. 20805–20811. ISSN: 0002-7863. DOI: 10.1021/ja310347x. URL: https://doi.org/10.1021/ja310347x.

[150] Xuning Feng et al. "Characterization of penetration induced thermal runaway propagation process within a large format lithium ion battery module". In: *Journal of Power Sources* 275 (Feb. 1, 2015), pp. 261–273. ISSN: 0378-7753. DOI: 10.1016/j.jpowsour.2014.11.017. URL: https://www.sciencedirect.com/science/article/pii/S0378775314018436.

[151] Shimou Chen et al. "Progress and future prospects of high-voltage and high-safety electrolytes in advanced lithium batteries: from liquid to solid electrolytes". In: *Journal of Materials Chemistry A* 6.25 (June 26, 2018). Publisher: The Royal Society of Chemistry, pp. 11631–11663. ISSN: 2050-7496. DOI: 10.1039/C8TA03358G. URL: https://pubs.rsc.org/en/content/articlelanding/2018/ta/c8ta03358g.

[152] Zeyu Shen et al. "Design Principles of the Anode–Electrolyte Interface for All Solid-State Lithium Metal Batteries". In: *Small Methods* 4.1 (2020). _eprint: https://onlinelibrary.wiley.com/doi/pdf/10.1002/smtd.201900592, p. 1900592. ISSN: 2366-9608. DOI: 10.1002/smtd.201900592. URL: https://onlinelibrary.wiley.com/doi/abs/10.1002/smtd.201900592.

[153] Li-Ping Wang et al. "Ameliorating the Interfacial Problems of Cathode and Solid-State Electrolytes by Interface Modification of Functional Polymers". In: *Advanced Energy Materials* 8.24 (2018). _eprint: https://onlinelibrary.wiley.com/doi/pdf/10.1002/aenm.201801528, p. 1801528. ISSN: 1614-6840. DOI: 10.1002/aenm.201801528. URL: https://onlinelibrary.wiley.com/doi/abs/10.1002/aenm.201801528.

[154] David L. Wood, Jianlin Li, and Seong Jin An. "Formation Challenges of Lithium-Ion Battery Manufacturing". In: *Joule* 3.12 (Dec. 18, 2019), pp. 2884–2888. ISSN: 2542-4351. DOI: 10.1016/j.joule.2019.11.002. URL: https://www.sciencedirect.com/science/article/pii/S254243511930532X.

[155] Darren H. S. Tan et al. "Carbon-free high-loading silicon anodes enabled by sulfide solid electrolytes". In: *Science* 373.6562 (Sept. 24, 2021). Publisher: American Association for the Advancement of Science, pp. 1494–1499. DOI: 10.1126/science.abg7217. URL: https://www.science.org/doi/full/10.1126/science.abg7217.

[156] Yu-Ming Zhao et al. "Advances of polymer binders for silicon-based anodes in high energy density lithium-ion batteries". In: *InfoMat* 3.5 (2021). _eprint: https://onlinelibrary.wiley.com/doi/pdf/10.1002/inf2.12185, pp. 460–501. ISSN: 2567-

3165. DOI: 10.1002/inf2.12185. URL: https://onlinelibrary.wiley.com/doi/abs/10.1002/inf2.12185.

[157] Lin Han et al. "Undervalued Roles of Binder in Modulating Solid Electrolyte Interphase Formation of Silicon-Based Anode Materials". In: *ACS Applied Materials & Interfaces* 13.38 (Sept. 29, 2021). Publisher: American Chemical Society, pp. 45139–45148. ISSN: 1944-8244. DOI: 10.1021/acsami.1c13971. URL: https://doi.org/10.1021/acsami.1c13971.

[158] Jiangxuan Song et al. "Interpenetrated Gel Polymer Binder for High-Performance Silicon Anodes in Lithium-ion Batteries". In: *Advanced Functional Materials* 24.37 (2014). _eprint: https://onlinelibrary.wiley.com/doi/pdf/10.1002/adfm.201401269, pp. 5904–5910. ISSN: 1616-3028. DOI: 10.1002/adfm.201401269. URL: https://onlinelibrary.wiley.com/doi/abs/10.1002/adfm.201401269.

[159] Sunghun Choi et al. "Highly elastic binders integrating polyrotaxanes for silicon microparticle anodes in lithium ion batteries". In: *Science* 357.6348 (July 21, 2017). Publisher: American Association for the Advancement of Science, pp. 279–283. DOI: 10.1126/science.aal4373. URL: https://www.science.org/doi/full/10.1126/science.aal4373.

[160] Zhen-Ji Han et al. "High-capacity Si–graphite composite electrodes with a self-formed porous structure by a partially neutralized polyacrylate for Li-ion batteries". In: *Energy & Environmental Science* 5.10 (2012). Publisher: Royal Society of Chemistry, pp. 9014–9020. DOI: 10.1039/C2EE22292B. URL: https://pubs.rsc.org/en/content/articlelanding/2012/ee/c2ee22292b.

[161] Chao Wang et al. "Self-healing chemistry enables the stable operation of silicon microparticle anodes for high-energy lithium-ion batteries". In: *Nature Chemistry* 5.12 (Dec. 2013). Number: 12 Publisher: Nature Publishing Group, pp. 1042–1048. ISSN: 1755-4349. DOI: 10.1038/nchem.1802. URL: https://www.nature.com/articles/nchem.1802.

[162] Timothy S. Arthur et al. "Three-dimensional electrodes and battery architectures". In: *MRS Bulletin* 36.7 (July 2011). Publisher: Cambridge University Press, pp. 523–531. ISSN: 1938-1425, 0883-7694. DOI: 10.1557/mrs.2011.156. URL: https://www.cambridge.org/core/journals/mrs-bulletin/article/threedimensional-electrodes-and-battery-architectures/A21C5AF6FD840BDB8808E12F84E856DC.

[163] Rotem Marom et al. "A review of advanced and practical lithium battery materials". In: *Journal of Materials Chemistry* 21.27 (2011). Publisher: Royal Society of Chemistry, pp. 9938–9954. DOI: 10.1039/C0JM04225K. URL: https://pubs.rsc.org/en/content/articlelanding/2011/jm/c0jm04225k.

[164] Bo Liang, Yanping Liu, and Yunhua Xu. "Silicon-based materials as high capacity anodes for next generation lithium ion batteries". In: *Journal of Power Sources* 267 (Dec. 1, 2014), pp. 469–490. ISSN: 0378-7753. DOI: 10.1016/j.jpowsour.2014.05.096. URL: https://www.sciencedirect.com/science/article/pii/S0378775314007897.

[165] Robert A. Huggins. "Lithium alloy negative electrodes". In: *Journal of Power Sources* 81-82 (Sept. 1, 1999), pp. 13–19. ISSN: 0378-7753. DOI: 10.1016/S0378-7753(99)00124-X. URL: https://www.sciencedirect.com/science/article/pii/S037877539900124X.

[166] Wei-Jun Zhang. "Lithium insertion/extraction mechanism in alloy anodes for lithium-ion batteries". In: *Journal of Power Sources* 196.3 (Feb. 1, 2011), pp. 877–885. ISSN: 0378-7753. DOI: 10.1016/j.jpowsour.2010.08.114. URL: https://www.sciencedirect.com/science/article/pii/S0378775310015995.

[167] Minseong Ko et al. "Elastic a-Silicon Nanoparticle Backboned Graphene Hybrid as a Self-Compacting Anode for High-Rate Lithium Ion Batteries". In: *ACS Nano* 8.8 (Aug. 26, 2014). Publisher: American Chemical Society, pp. 8591–8599. ISSN: 1936-0851. DOI: 10.1021/nn503294z. URL: https://doi.org/10.1021/nn503294z.

[168] Jeong K. Lee et al. "Silicon nanoparticles – graphene paper composites for Li ion battery anodes". In: *Chemical Communications* 46.12 (2010). Publisher: Royal Society of Chemistry, pp. 2025–2027. DOI: 10.1039/B919738A. URL: https://pubs.rsc.org/en/content/articlelanding/2010/cc/b919738a.

[169] Zhongxue Chen et al. "In Situ Generation of Few-Layer Graphene Coatings on SnO2-SiC Core-Shell Nanoparticles for High-Performance Lithium-Ion Storage". In: *Advanced Energy Materials* 2.1 (2012). _eprint: https://onlinelibrary.wiley.com/doi/pdf/10.1002/aenm.201100464, pp. 95–102. ISSN: 1614-6840. DOI: 10.1002/aenm.201100464. URL: https://onlinelibrary.wiley.com/doi/abs/10.1002/aenm.201100464.

[170] J. R. Dahn et al. "Mechanisms for Lithium Insertion in Carbonaceous Materials". In: *Science* 270.5236 (Oct. 27, 1995). Publisher: American Association for the Advancement of Science, pp. 590–593. DOI: 10.1126/science.270.5236.590. URL: https://www.science.org/doi/abs/10.1126/science.270.5236.590.

[171] Rahul Mukherjee et al. "Photothermally Reduced Graphene as High-Power Anodes for Lithium-Ion Batteries". In: *ACS Nano* 6.9 (Sept. 25, 2012). Publisher: American Chemical Society, pp. 7867–7878. ISSN: 1936-0851. DOI: 10.1021/nn303145j. URL: https://doi.org/10.1021/nn303145j.

[172] Yuzhang Li et al. "Growth of conformal graphene cages on micrometre-sized silicon particles as stable battery anodes". In: *Nature Energy* 1.2 (Jan. 25, 2016), p. 15029. ISSN: 2058-7546. DOI: 10.1038/nenergy.2015.29. URL: https://www.nature.com/articles/nenergy201529.

[173] Quan Xu et al. "Nano/Micro-Structured Si/C Anodes with High Initial Coulombic Efficiency in Li-Ion Batteries". In: *Chemistry – An Asian Journal* 11.8 (Apr. 20, 2016), pp. 1205–1209. ISSN: 1861-4728, 1861-471X. DOI: 10.1002/asia.201600067. URL: https://onlinelibrary.wiley.com/doi/10.1002/asia.201600067.

[174] Byoung Man Bang et al. “High-Performance Macroporous Bulk Silicon Anodes Synthesized by Template-Free Chemical Etching”. In: *Advanced Energy Materials* 2.7 (2012). _eprint: https://onlinelibrary.wiley.com/doi/pdf/10.1002/aenm.201100765, pp. 878–883. ISSN: 1614-6840. DOI: 10.1002/aenm.201100765. URL: https://onlinelibrary.wiley.com/doi/abs/10.1002/aenm.201100765.

[175] Xiaolin Li et al. “Mesoporous silicon sponge as an anti-pulverization structure for high-performance lithium-ion battery anodes”. In: *Nature Communications* 5.1 (July 8, 2014), p. 4105. ISSN: 2041-1723. DOI: 10.1038/ncomms5105. URL: https://www.nature.com/articles/ncomms5105.

[176] Yongling An et al. “Green, Scalable, and Controllable Fabrication of Nanoporous Silicon from Commercial Alloy Precursors for High-Energy Lithium-Ion Batteries”. In: *ACS Nano* 12.5 (May 22, 2018). Publisher: American Chemical Society, pp. 4993–5002. ISSN: 1936-0851. DOI: 10.1021/acsnano.8b02219. URL: https://doi.org/10.1021/acsnano.8b02219.

[177] Yang Ren et al. “Layered porous silicon encapsulated in carbon nanotube cage as ultra-stable anode for lithium-ion batteries”. In: *Chemical Engineering Journal* 431 (Mar. 1, 2022), p. 133982. ISSN: 1385-8947. DOI: 10.1016/j.cej.2021.133982. URL: https://www.sciencedirect.com/science/article/pii/S1385894721055558.

[178] Yingying Lv et al. “Largely Improved Battery Performance Using a Microsized Silicon Skeleton Caged by Polypyrrole as Anode”. In: *ACS Nano* 13.10 (Oct. 22, 2019), pp. 12032–12041. ISSN: 1936-0851, 1936-086X. DOI: 10.1021/acsnano.9b06301. URL: https://pubs.acs.org/doi/10.1021/acsnano.9b06301.

[179] Yi Zhao et al. “Li-Ions Transport Promoting and Highly Stable Solid–Electrolyte Interface on Si in Multilayer Si/C through Thickness Control”. In: *ACS Nano* 13.5 (May 28, 2019), pp. 5602–5610. ISSN: 1936-0851, 1936-086X. DOI: 10.1021/acsnano.9b00670. URL: https://pubs.acs.org/doi/10.1021/acsnano.9b00670.

[180] Xiaolong Cheng et al. “A Self-Healing Volume Variation Three-Dimensional Continuous Bulk Porous Bismuth for Ultrafast Sodium Storage”. In: *Advanced Functional Materials* 31.22 (2021). _eprint: https://onlinelibrary.wiley.com/doi/pdf/10.1002/adfm.202011264, p. 2011264. ISSN: 1616-3028. DOI: 10.1002/adfm.202011264. URL: https://onlinelibrary.wiley.com/doi/abs/10.1002/adfm.202011264.

[181] Tingting Song, Ming Yan, and Ma Qian. “A dealloying approach to synthesizing micro-sized porous tin (Sn) from immiscible alloy systems for potential lithium-ion battery anode applications”. In: *Journal of Porous Materials* 22.3 (June 2015), pp. 713–719. ISSN: 1380-2224, 1573-4854. DOI: 10.1007/s10934-015-9944-6. URL: http://link.springer.com/10.1007/s10934-015-9944-6.

[182] Michael D. Slater et al. “Sodium-Ion Batteries”. In: *Advanced Functional Materials* 23.8 (2013). _eprint: https://onlinelibrary.wiley.com/doi/pdf/10.1002/adfm.201200691, pp. 947–958. ISSN: 1616-3028. DOI: 10.1002/adfm.201200691. URL: https://onlinelibrary.wiley.com/doi/abs/10.1002/adfm.201200691.

[183] Tiefeng Liu et al. "Exploring competitive features of stationary sodium ion batteries for electrochemical energy storage". In: *Energy & Environmental Science* 12.5 (May 16, 2019). Publisher: The Royal Society of Chemistry, pp. 1512–1533. ISSN: 1754-5706. DOI: 10.1039/C8EE03727B. URL: https://pubs.rsc.org/en/content/articlelanding/2019/ee/c8ee03727b.

[184] Jang-Yeon Hwang, Seung-Taek Myung, and Yang-Kook Sun. "Sodium-ion batteries: present and future". In: *Chemical Society Reviews* 46.12 (2017). Publisher: Royal Society of Chemistry, pp. 3529–3614. DOI: 10.1039/C6CS00776G. URL: https://pubs.rsc.org/en/content/articlelanding/2017/cs/c6cs00776g.

[185] Z. Hu et al. "Advances and Challenges in Metal Sulfides/selenides for Next-generation Rechargeable Sodium-ion Batteries". In: *Adv. Mater.* 29 (2017), p. 1700606.

[186] Y. Xiao, S. H. Lee, and Y. K. Sun. "The Application of Metal Sulfides in Sodium Ion Batteries". In: *Adv. Energy Mater.* 7 (2017), p. 1601329.

[187] Y. Liu et al. "Flexible Paper-like Free-standing Electrodes by Anchoring Ultrafine SnS2 Nanocrystals on Graphene Nanoribbons for High-performance Sodium Ion Batteries". In: *ACS Appl. Mater. Interfaces* 9 (2017), p. 15484.

[188] Y. Liu et al. "Confining SnS2 Ultrathin Nanosheets in Hollow Carbon Nanostructures for Efficient Capacitive Sodium Storage". In: *Joule* 2 (2018), p. 725.

[189] X. Xiong et al. "SnS Nanoparticles Electrostatically Anchored on Three-dimensional N-doped Graphene as An Active and Durable Anode for Sodium-ion Batteries". In: *Energy Environ. Sci.* 10 (2017), p. 1757.

[190] S. Hwang et al. "Multistep Lithiation of Tin Sulfide: An Investigation Using in Situ Electron Microscopy". In: *ACS Nano* 12 (2018), p. 3638.

[191] P. Gao et al. "In Situ Atomic-scale Observation of Reversible Sodium Ions Migration in Layered Metal Dichalcogenide SnS2 Nanostructures". In: *Nano Energy* 32 (2017), p. 302.

[192] D.-H. Lee and C.-M. Park. "Tin Selenides with Layered Crystal Structures for Li-ion Batteries: Interesting Phase Change Mechanisms and Outstanding Electrochemical Behaviors". In: *ACS Appl. Mater. Interfaces* 9 (2017), p. 15439.

[193] L. Zhang et al. "Electrochemical Reaction Mechanism of the MoS2 Electrode in A Lithium-ion Cell Revealed by in Situ and Operando X-ray Absorption Spectroscopy". In: *Nano Lett.* 18 (2018), p. 1466.

[194] X. Wang et al. "In Situ Electron Microscopy Investigation of Sodiation of Titanium Disulfide Nanoflakes". In: *ACS Nano* 13 (2019), p. 9421.

[195] X. Xu et al. "Progressively Exposing Active Facets of 2D Nanosheets toward Enhanced Pseudocapacitive Response and High-Rate Sodium Storage". In: *Adv. Mater.* 31 (2019), p. 1900526.

[196] G.-L. Xu et al. "Insights into the Distinct Lithiation/sodiation of Porous Cobalt Oxide by in Operando Synchrotron X-ray Techniques and Ab Initio Molecular Dynamics Simulations". In: *Nano Lett.* 17 (2017), p. 953.

[197] M. Zhuang et al. "Sub-5 nm Edge-rich 1T'-ReSe2 as Bifunctional Materials for Hydrogen Evolution and Sodium-ion Storage". In: *Nano Energy* 58 (2019), p. 660.

[198] Y. Ren and X. Zuo. "Synchrotron X-Ray and Neutron Diffraction, Total Scattering, and Small-Angle Scattering Techniques for Rechargeable Battery Research". In: *Small Methods* 2 (2018), p. 1800064.

[199] K. M. Wiaderek et al. "Mesoscale Effects in Electrochemical Conversion: Coupling of Chemistry to Atomic-and Nanoscale Structure in Iron-based Electrodes". In: *J. Am. Chem. Soc.* 136 (2014), p. 6211.

[200] M. Zhuang et al. "Polymer-embedded Fabrication of Co2P Nanoparticles Encapsulated in N, P-doped Graphene for Hydrogen Generation". In: *Nano Lett.* 16 (2016), p. 4691.

[201] M. Zhuang et al. "Methacrylated Gelatin-embedded Fabrication of 3D Graphene-supported Co3O4 Nanoparticles for Water Splitting". In: *Nanoscale* 11 (2019), p. 6866.

[202] D. Guan et al. "Carbon Nanotube-assisted Growth of Single-/multi-layer SnS2 and SnO2 Nanoflakes for High-performance Lithium Storage". In: *RSC Adv.* 5 (2015), p. 58514.

[203] J.-H. Ahn et al. "Deterministic Two-dimensional Polymorphism Growth of Hexagonal n-type SnS2 and Orthorhombic p-type SnS Crystals". In: *Nano Lett.* 15 (2015), p. 3703.

[204] G. Ye et al. "Synthesis of Large-scale Atomic-layer SnS2 through Chemical Vapor Deposition". In: *Nano Res.* 10 (2017), p. 2386.

[205] T. J. Whittles et al. "Band Alignments, Valence Bands, and Core Levels in the Tin Sulfides SnS, SnS2, and Sn2S3: Experiment and Theory". In: *Chem. Mater.* 28 (2016), p. 3718.

[206] L. S. Price et al. "Atmospheric Pressure Chemical Vapor Deposition of Tin Sulfides (SnS, Sn2S3, and SnS2) on Glass". In: *Chem. Mater.* 11 (1999), p. 1792.

[207] A. M. El-Sawy et al. "Controlling the Active Sites of Sulfur-doped Carbon nanotube–Graphene Nanolobes for Highly Efficient Oxygen Evolution and Reduction Catalysis". In: *Adv. Energy Mater.* 6 (2016), p. 1501966.

[208] M. Zhuang et al. "Engineering Sub-100 nm Mo(1–x)WxSe2 Crystals for Efficient Hydrogen Evolution Catalysis". In: *J. Mater. Chem. A* 6 (2018), p. 2900.

[209] L. Fan et al. "Promising Dual-doped Graphene Aerogel/SnS2 Nanocrystal Building High Performance Sodium Ion Batteries". In: *ACS Appl. Mater. Interfaces* 10 (2018), p. 2637.

[210] Z. Ren et al. "Rational Design of Layered SnS2 on Ultralight Graphene Fiber Fabrics as Binder-Free Anodes for Enhanced Practical Capacity of Sodium-Ion Batteries". In: *Nano-Micro Lett.* 11 (2019), p. 66.

[211] J. Wang et al. "Solid-state Fabrication of SnS2/C Nanospheres for High-performance Sodium Ion Battery Anode". In: *ACS Appl. Mater. Interfaces* 7 (2015), p. 11476.

[212] D. Wang et al. "Hierarchical Nanostructured Core–shell Sn@C Nanoparticles Embedded in Graphene Nanosheets: Spectroscopic View and their Application in Lithium Ion Batteries". In: *Phys. Chem. Chem. Phys.* 15 (2013), p. 3535.

[213] S. Mukerjee and J. McBreen. "An in Situ X-Ray Absorption Spectroscopy Investigation of the Effect of Sn Additions to Carbon-Supported Pt Electrocatalysts: Part I". In: *J. Electrochem. Soc.* 146 (1999), p. 600.

[214] E. Peled et al. "Improved Graphite Anode for Lithium-Ion Batteries Chemically: Bonded Solid Electrolyte Interface and Nanochannel Formation". In: *Journal of The Electrochemical Society* 143.1 (Jan. 1, 1996), pp. L4–L7. ISSN: 0013-4651, 1945-7111. DOI: 10.1149/1.1836372. URL: https://iopscience.iop.org/article/10.1149/1.1836372.

[215] D. Lin et al. "A high tap density secondary silicon particle anode fabricated by scalable mechanical pressing for lithium-ion batteries". In: *Energy Environ Sci* 8 (2015). DOI: 10.1039/C5EE01363A. URL: https://doi.org/10.1039/C5EE01363A.

[216] Chong-Min Wang et al. "In Situ TEM Investigation of Congruent Phase Transition and Structural Evolution of Nanostructured Silicon/Carbon Anode for Lithium Ion Batteries". In: *Nano Letters* 12.3 (Mar. 14, 2012), pp. 1624–1632. ISSN: 1530-6984, 1530-6992. DOI: 10.1021/nl204559u. URL: https://pubs.acs.org/doi/10.1021/nl204559u.

[217] Han Gao et al. "Parasitic Reactions in Nanosized Silicon Anodes for Lithium-Ion Batteries". In: *Nano Letters* 17.3 (Mar. 8, 2017), pp. 1512–1519. ISSN: 1530-6984, 1530-6992. DOI: 10.1021/acs.nanolett.6b04551. URL: https://pubs.acs.org/doi/10.1021/acs.nanolett.6b04551.

[218] Jian-Guo Ren et al. "Silicon-Graphene Composite Anodes for High-Energy Lithium Batteries". In: *Energy Technology* 1.1 (Jan. 2013), pp. 77–84. ISSN: 21944288. DOI: 10.1002/ente.200038. URL: http://doi.wiley.com/10.1002/ente.200038.

[219] B. Fuchsbichler et al. "High capacity graphite–silicon composite anode material for lithium-ion batteries". In: *Journal of Power Sources* 196.5 (Mar. 2011), pp. 2889–2892. ISSN: 03787753. DOI: 10.1016/j.jpowsour.2010.10.081. URL: https://linkinghub.elsevier.com/retrieve/pii/S0378775310018811.

[220] Yang Jin et al. "Self-healing SEI enables full-cell cycling of a silicon-majority anode with a coulombic efficiency exceeding 99.9%". In: *Energy & Environmental Science* 10.2 (2017), pp. 580–592. ISSN: 1754-5692, 1754-5706. DOI: 10.1039/C6EE02685K. URL: http://xlink.rsc.org/?DOI=C6EE02685K.

[221] Fangzhou Zhang et al. "Boosting the initial coulombic efficiency in silicon anodes through interfacial incorporation of metal nanocrystals". In: *Journal of Materials Chemistry A* 7.29 (2019), pp. 17426–17434. ISSN: 2050-7488, 2050-7496. DOI: 10.1039/C9TA05340A. URL: http://xlink.rsc.org/?DOI=C9TA05340A.

[222] H. Jin et al. "Black phosphorus composites with engineered interfaces for high-rate high-capacity lithium storage". In: *Science* 370 (2020). DOI: 10.1126/science.aav5842. URL: https://doi.org/10.1126/science.aav5842.

[223] Li Wang et al. "Nano-Structured Phosphorus Composite as High-Capacity Anode Materials for Lithium Batteries". In: *Angewandte Chemie International Edition* 51.36 (Sept. 3, 2012), pp. 9034–9037. ISSN: 1433-7851, 1521-3773. DOI: 10.1002/anie.201204591. URL: https://onlinelibrary.wiley.com/doi/10.1002/anie.201204591.

[224] Gui-Liang Xu et al. "Nanostructured Black Phosphorus/Ketjenblack–Multiwalled Carbon Nanotubes Composite as High Performance Anode Material for Sodium-Ion Batteries". In: *Nano Letters* 16.6 (June 8, 2016). Publisher: American Chemical Society, pp. 3955–3965. ISSN: 1530-6984. DOI: 10.1021/acs.nanolett.6b01777. URL: https://doi.org/10.1021/acs.nanolett.6b01777 (visited on 01/20/2024).

[225] W. Lei et al. "Improvement of cycling phosphorus-based anode with LiF-rich solid electrolyte interphase for reversible lithium storage". In: *ACS Appl Energy Mater* 2 (2019). DOI: 10.1021/acsaem.9b00025. URL: https://doi.org/10.1021/acsaem.9b00025.

[226] Jianbin Zhou et al. "Wet-Chemical Synthesis of Hollow Red-Phosphorus Nanospheres with Porous Shells as Anodes for High-Performance Lithium-Ion and Sodium-Ion Batteries". In: *Advanced Materials* 29.29 (Aug. 2017), p. 1700214. ISSN: 0935-9648, 1521-4095. DOI: 10.1002/adma.201700214. URL: https://onlinelibrary.wiley.com/doi/10.1002/adma.201700214.

[227] Yijun Yang et al. "In Situ Electrochemistry of Rechargeable Battery Materials: Status Report and Perspectives". In: *Advanced Materials* 29.31 (Aug. 2017), p. 1606922. ISSN: 0935-9648, 1521-4095. DOI: 10.1002/adma.201606922. URL: https://onlinelibrary.wiley.com/doi/10.1002/adma.201606922.

[228] Xingxing Jiao et al. "Crumpled Nitrogen-Doped Graphene-Wrapped Phosphorus Composite as a Promising Anode for Lithium-Ion Batteries". In: *ACS Applied Materials & Interfaces* 11.34 (Aug. 28, 2019), pp. 30858–30864. ISSN: 1944-8244, 1944-8252. DOI: 10.1021/acsami.9b08915. URL: https://pubs.acs.org/doi/10.1021/acsami.9b08915.

[229] Zhaoxin Yu et al. "Phosphorus-Graphene Nanosheet Hybrids as Lithium-Ion Anode with Exceptional High-Temperature Cycling Stability". In: *Advanced Science* 2.1 (Feb. 2015), p. 1400020. ISSN: 2198-3844, 2198-3844. DOI: 10.1002/advs.201400020. URL: https://onlinelibrary.wiley.com/doi/10.1002/advs.201400020.

[230] Zishuang Yue et al. "Utilizing a graphene matrix to overcome the intrinsic limitations of red phosphorus as an anode material in lithium-ion batteries". In: *Carbon* 127 (Feb. 2018), pp. 588–595. ISSN: 00086223. DOI: 10.1016/j.carbon.2017.11.043. URL: https://linkinghub.elsevier.com/retrieve/pii/S0008622317311570.

[231] Yongming Sun et al. "Design of Red Phosphorus Nanostructured Electrode for Fast-Charging Lithium-Ion Batteries with High Energy Density". In: *Joule* 3.4 (Apr. 2019), pp. 1080–1093. ISSN: 25424351. DOI: 10.1016/j.joule.2019.01.017. URL: https://linkinghub.elsevier.com/retrieve/pii/S2542435119300467.

[232] Yupu Zhang et al. "3D Chemical Cross-Linking Structure of Black Phosphorus@CNTs Hybrid as a Promising Anode Material for Lithium Ion Batteries". In: *Advanced Functional Materials* 30.12 (Mar. 2020), p. 1909372. ISSN: 1616-301X, 1616-3028. DOI: 10.1002/adfm.201909372. URL: https://onlinelibrary.wiley.com/doi/10.1002/adfm.201909372.

[233] Xingxing Jiao et al. "Amorphous phosphorus-carbon nanotube hybrid anode with ultralong cycle life and high-rate capability for lithium-ion batteries". In: *Carbon* 148 (July 2019), pp. 518–524. ISSN: 00086223. DOI: 10.1016/j.carbon.2019.03.053. URL: https://linkinghub.elsevier.com/retrieve/pii/S0008622319302775.

[234] Tao Yuan et al. "3D red phosphorus/sheared CNT sponge for high performance lithium-ion battery anodes". In: *Energy Storage Materials* 13 (July 2018), pp. 267–273. ISSN: 24058297. DOI: 10.1016/j.ensm.2018.01.014. URL: https://linkinghub.elsevier.com/retrieve/pii/S2405829717305743.

[235] Huan Liu et al. "Fluffy carbon-coated red phosphorus as a highly stable and high-rate anode for lithium-ion batteries". In: *Journal of Materials Chemistry A* 7.18 (2019), pp. 11205–11213. ISSN: 2050-7488, 2050-7496. DOI: 10.1039/C9TA02030F. URL: http://xlink.rsc.org/?DOI=C9TA02030F.

[236] Xinwei Zhou et al. "In Situ Focused Ion Beam Scanning Electron Microscope Study of Microstructural Evolution of Single Tin Particle Anode for Li-Ion Batteries". In: *ACS Applied Materials & Interfaces* 11.2 (Jan. 16, 2019). Publisher: American Chemical Society, pp. 1733–1738. ISSN: 1944-8244. DOI: 10.1021/acsami.8b13981. URL: https://doi.org/10.1021/acsami.8b13981.

[237] Wei-Chung Chang, Kuan-Wei Tseng, and Hsing-Yu Tuan. "Solution Synthesis of Iodine-Doped Red Phosphorus Nanoparticles for Lithium-Ion Battery Anodes". In: *Nano Letters* 17.2 (Feb. 8, 2017), pp. 1240–1247. ISSN: 1530-6984, 1530-6992. DOI: 10.1021/acs.nanolett.6b05081. URL: https://pubs.acs.org/doi/10.1021/acs.nanolett.6b05081.

[238] Bing-Qing Xiong et al. "Boosting Superior Lithium Storage Performance of Alloy-Based Anode Materials via Ultraconformal Sb Coating–Derived Favorable Solid-Electrolyte Interphase". In: *Advanced Energy Materials* 10.4 (2020). _eprint: https://onlinelibrary.wiley.com/doi/pdf/10.1002/aenm.201903186, p. 1903186. ISSN: 1614-6840. DOI: 10.1002/aenm.201903186. URL: https://onlinelibrary.wiley.com/doi/abs/10.1002/aenm.201903186.

[239] Jiangxuan Song et al. "Chemically Bonded Phosphorus/Graphene Hybrid as a High Performance Anode for Sodium-Ion Batteries". In: *Nano Letters* 14.11 (Nov. 12, 2014), pp. 6329–6335. ISSN: 1530-6984, 1530-6992. DOI: 10.1021/nl502759z. URL: https://pubs.acs.org/doi/10.1021/nl502759z.

[240] Yayuan Liu, Yangying Zhu, and Yi Cui. "Challenges and opportunities towards fast-charging battery materials". In: *Nature Energy* 4.7 (June 3, 2019), pp. 540–550. ISSN: 2058-7546. DOI: 10.1038/s41560-019-0405-3. URL: https://www.nature.com/articles/s41560-019-0405-3.

[241] Xiaoqiao Zeng et al. "Kinetic Study of Parasitic Reactions in Lithium-Ion Batteries: A Case Study on LiNi $_{0.6}$ Mn $_{0.2}$ Co $_{0.2}$ O $_{2}$". In: *ACS Applied Materials & Interfaces* 8.5 (Feb. 10, 2016), pp. 3446–3451. ISSN: 1944-8244, 1944-8252. DOI: 10.1021/acsami.5b11800. URL: https://pubs.acs.org/doi/10.1021/acsami.5b11800.

[242] X. Zeng et al. "Commercialization of lithium battery technologies for electric vehicles". In: *Adv Energy Mater* 9 (2019). DOI: 10.1002/aenm.201900161. URL: https://doi.org/10.1002/aenm.201900161.

[243] A. P. Yuda et al. "Advances of the top-down synthesis approach for high-performance silicon anodes in Li-ion batteries". In: *J Mater Chem A* 9 (2021). DOI: 10.1039/D1TA02711E. URL: https://doi.org/10.1039/D1TA02711E.

[244] Rachid Amine et al. "A practical phosphorus-based anode material for high-energy lithium-ion batteries". In: *Nano Energy* 74 (Aug. 1, 2020), p. 104849. ISSN: 2211-2855. DOI: 10.1016/j.nanoen.2020.104849. URL: https://www.sciencedirect.com/science/article/pii/S2211285520304067.

[245] W. Cai et al. "A review on energy chemistry of fast-charging anodes". In: *Chem Soc Rev* 49 (2020). DOI: 10.1039/C9CS00728H. URL: https://doi.org/10.1039/C9CS00728H.

[246] H. -. C. Chiu et al. "Capacity fade mechanism of Li4Ti5O12 nanosheet anode". In: *Adv Energy Mater* 7 (2017). DOI: 10.1002/aenm.201601825. URL: https://doi.org/10.1002/aenm.201601825.

[247] H. Liu et al. "A disordered rock salt anode for fast-charging lithium-ion batteries". In: *Nature* 585 (2020). DOI: 10.1038/s41586-020-2637-6. URL: https://doi.org/10.1038/s41586-020-2637-6.

[248] C. -. M. Park et al. "Li-alloy based anode materials for Li secondary batteries". In: *Chem Soc Rev* 39 (2010). DOI: 10.1039/b919877f. URL: https://doi.org/10.1039/b919877f.

[249] Xin Li et al. "Review on comprehending and enhancing the initial Coulombic efficiency of anode materials in lithium-ion/sodium-ion batteries". In: *Nano Energy* 77 (Nov. 1, 2020), p. 105143. ISSN: 2211-2855. DOI: 10.1016/j.nanoen.2020.105143. URL: https://www.sciencedirect.com/science/article/pii/S2211285520307217.

[250] L. Sun et al. "A review on recent advances for boosting initial coulombic efficiency of silicon anodic lithium ion batteries". In: *Small* 18 (2022). DOI: 10.1002/smll.202102894. URL: https://doi.org/10.1002/smll.202102894.

[251] J. Zhou et al. "Wet-chemical synthesis of hollow red-phosphorus nanospheres with porous shells as anodes for high-performance lithium-ion and sodium-ion batteries". In: *Adv Mater* 29 (2017). DOI: 10.1002/adma.201700214. URL: https://doi.org/10.1002/adma.201700214.

[252] H. -. T. Kwon et al. "Silicon diphosphide: a Si-based three-dimensional crystalline framework as a high-performance Li-ion battery anode". In: *ACS Nano* 10 (2016). DOI: 10.1021/acsnano.6b02727. URL: https://doi.org/10.1021/acsnano.6b02727.

[253] R. Reinhold et al. “Silicon monophosphide as a possible lithium battery anode material”. In: *J Mater Chem A* 6 (2018). DOI: 10.1039/C8TA06983B. URL: https://doi.org/10.1039/C8TA06983B.

[254] Ching-Yu Wang et al. “Multi-walled carbon nanotube-wrapped SiP2 as a superior anode material for lithium-ion and sodium-ion batteries”. In: *Journal of Power Sources* 399 (Sept. 2018), pp. 49–58. ISSN: 03787753. DOI: 10.1016/j.jpowsour.2018.07.003. URL: https://linkinghub.elsevier.com/retrieve/pii/S0378775318307122.

[255] J. Saddique et al. “Enhanced silicon diphosphide-carbon composite anode for long-cycle, high-efficient sodium ion batteries”. In: *ACS Appl Energy Mater* 2 (2019). DOI: 10.1021/acsaem.8b02242. URL: https://doi.org/10.1021/acsaem.8b02242.

[256] G. Coquil et al. “Versatile Si/P system as efficient anode for lithium and sodium batteries: understanding of an original electrochemical mechanism by a full XRD-NMR study”. In: *ACS Appl Energy Mater* 1 (2018). DOI: 10.1021/acsaem.8b00567. URL: https://doi.org/10.1021/acsaem.8b00567.

[257] B. H. Park et al. “High-performance silicon diphosphide/nanocarbon composite anode for Li-ion batteries: role of chemical bonding and interfaces in the establishment of cycling stability”. In: *J Power Sources* 434 (2019). DOI: 10.1016/j.jpowsour.2019.226759. URL: https://doi.org/10.1016/j.jpowsour.2019.226759.

[258] H. Yang et al. “Silicon monophosphides with controlled size and crystallinity for enhanced lithium anodic performance”. In: *Nanoscale* 13 (2021). DOI: 10.1039/D0NR07386E. URL: https://doi.org/10.1039/D0NR07386E.

[259] H. Shen et al. “Mechanical robustness two-dimensional silicon phosphide flake anodes for lithium ion batteries”. In: *ACS Sustain Chem Eng* 8 (2020). DOI: 10.1021/acssuschemeng.0c07441. URL: https://doi.org/10.1021/acssuschemeng.0c07441.

[260] R. Reinhold et al. “Surface and electrochemical studies on silicon diphosphide as easy-to-handle anode material for lithium-based batteries-the phosphorus path”. In: *ACS Appl Mater Interfaces* 10 (2018). DOI: 10.1021/acsami.7b18697. URL: https://doi.org/10.1021/acsami.7b18697.

[261] S. Zhou et al. “Doped silicon nanocrystals from organic dopant precursor by a SiCl4-based high frequency nonthermal plasma”. In: *Appl Phys Lett* 105 (2014). DOI: 10.1063/1.4901278. URL: https://doi.org/10.1063/1.4901278.

[262] D. Hanlon et al. “Liquid exfoliation of solvent-stabilized few-layer black phosphorus for applications beyond electronics”. In: *Nat Commun* 6 (2015). DOI: 10.1038/ncomms9563. URL: https://doi.org/10.1038/ncomms9563.

[263] G. -. L. Xu et al. “Facile synthesis of porous MnO/C nanotubes as a high capacity anode material for lithium ion batteries”. In: *Chem Commun* 48 (2012). DOI: 10.1039/c2cc34218a. URL: https://doi.org/10.1039/c2cc34218a.

[264] A. Kovalev et al. "Investigation of the electronic structure of the phosphorus-doped Si and SiO2: Si quantum dots by XPS and HREELS methods". In: *Surface and Interface Analysis: An International Journal devoted to the development and application of techniques for the analysis of surfaces, interfaces and thin films* 36 (2004). DOI: 10.1002/sia.1811. URL: https://doi.org/10.1002/sia.1811.

[265] Y. Domi et al. "Effect of phosphorus-doping on electrochemical performance of silicon negative electrodes in lithium-ion batteries". In: *ACS Appl Mater Interfaces* 8 (2016). DOI: 10.1021/acsami.6b00386. URL: https://doi.org/10.1021/acsami.6b00386.

[266] Xinwei Zhou et al. "In Situ Focused Ion Beam Scanning Electron Microscope Study of Microstructural Evolution of Single Tin Particle Anode for Li-Ion Batteries". In: *ACS Applied Materials & Interfaces* 11.2 (Jan. 16, 2019), pp. 1733–1738. ISSN: 1944-8244, 1944-8252. DOI: 10.1021/acsami.8b13981. URL: https://pubs.acs.org/doi/10.1021/acsami.8b13981.

[267] Ashish Rudola et al. "Opportunities for moderate-range electric vehicles using sustainable sodium-ion batteries". In: *Nature Energy* 8.3 (Mar. 2023). Number: 3 Publisher: Nature Publishing Group, pp. 215–218. ISSN: 2058-7546. DOI: 10.1038/s41560-023-01215-w. URL: https://www.nature.com/articles/s41560-023-01215-w.

[268] D. A. Stevens and J. R. Dahn. "High Capacity Anode Materials for Rechargeable Sodium-Ion Batteries". In: *Journal of The Electrochemical Society* 147.4 (Apr. 1, 2000). Publisher: IOP Publishing, p. 1271. ISSN: 1945-7111. DOI: 10.1149/1.1393348. URL: https://iopscience.iop.org/article/10.1149/1.1393348/meta.

[269] Dequan Chen et al. "Hard carbon for sodium storage: mechanism and optimization strategies toward commercialization". In: *Energy & Environmental Science* 14.4 (Apr. 21, 2021). Publisher: The Royal Society of Chemistry, pp. 2244–2262. ISSN: 1754-5706. DOI: 10.1039/D0EE03916K. URL: https://pubs.rsc.org/en/content/articlelanding/2021/ee/d0ee03916k.

[270] Zhi Li, Jia Ding, and David Mitlin. "Tin and Tin Compounds for Sodium Ion Battery Anodes: Phase Transformations and Performance". In: *Accounts of Chemical Research* 48.6 (June 16, 2015). Publisher: American Chemical Society, pp. 1657–1665. ISSN: 0001-4842. DOI: 10.1021/acs.accounts.5b00114. URL: https://doi.org/10.1021/acs.accounts.5b00114.

[271] V. L. Chevrier and G. Ceder. "Challenges for Na-ion Negative Electrodes". In: *Journal of The Electrochemical Society* 158.9 (July 14, 2011). Publisher: IOP Publishing, A1011. ISSN: 1945-7111. DOI: 10.1149/1.3607983. URL: https://iopscience.iop.org/article/10.1149/1.3607983/meta.

[272] Jiang Wei Wang et al. "Microstructural Evolution of Tin Nanoparticles during In Situ Sodium Insertion and Extraction". In: *Nano Letters* 12.11 (Nov. 14, 2012). Publisher: American Chemical Society, pp. 5897–5902. ISSN: 1530-6984. DOI: 10.1021/nl303305c. URL: https://doi.org/10.1021/nl303305c.

[273] Wen Tao Jing, Chun Cheng Yang, and Qing Jiang. "Recent progress on metallic Sn- and Sb-based anodes for sodium-ion batteries". In: *Journal of Materials Chemistry A* 8.6 (Feb. 11, 2020). Publisher: The Royal Society of Chemistry, pp. 2913–2933. ISSN: 2050-7496. DOI: 10.1039/C9TA11782B. URL: https://pubs.rsc.org/en/content/articlelanding/2020/ta/c9ta11782b.

[274] Ming Chen et al. "Sn Anodes Protected by Intermetallic FeSn2 Layers for Long-lifespan Sodium-ion Batteries with High Initial Coulombic Efficiency of 93.8 %". In: *Angewandte Chemie International Edition* 62.16 (2023). _eprint: https://onlinelibrary.wiley.com/doi/pdf/10.1002/anie.202219177, e202219177. ISSN: 1521-3773. DOI: 10.1002/anie.202219177. URL: https://onlinelibrary.wiley.com/doi/abs/10.1002/anie.202219177.

[275] Yongchang Liu et al. "Ultrasmall Sn Nanoparticles Embedded in Carbon as High-Performance Anode for Sodium-Ion Batteries". In: *Advanced Functional Materials* 25.2 (2015). _eprint: https://onlinelibrary.wiley.com/doi/pdf/10.1002/adfm.201402943, pp. 214–220. ISSN: 1616-3028. DOI: 10.1002/adfm.201402943. URL: https://onlinelibrary.wiley.com/doi/abs/10.1002/adfm.201402943.

[276] Changhyeon Kim et al. "A self-healing Sn anode with an ultra-long cycle life for sodium-ion batteries". In: *Journal of Materials Chemistry A* 6.45 (Nov. 20, 2018). Publisher: The Royal Society of Chemistry, pp. 22809–22818. ISSN: 2050-7496. DOI: 10.1039/C8TA09544B. URL: https://pubs.rsc.org/en/content/articlelanding/2018/ta/c8ta09544b.

[277] Changhyeon Kim et al. "Development and Evaluation of Sn Foil Anode for Sodium-Ion Batteries". In: *Small* 17.50 (2021). _eprint: https://onlinelibrary.wiley.com/doi/pdf/10.1002/smll.202102618, p. 2102618. ISSN: 1613-6829. DOI: 10.1002/smll.202102618. URL: https://onlinelibrary.wiley.com/doi/abs/10.1002/smll.202102618.

[278] Yansong Zhu et al. "Microsized Gray Tin as a High-Rate and Long-Life Anode Material for Advanced Sodium-Ion Batteries". In: *Nano Letters* 22.19 (Oct. 12, 2022). Publisher: American Chemical Society, pp. 7976–7983. ISSN: 1530-6984. DOI: 10.1021/acs.nanolett.2c03334. URL: https://doi.org/10.1021/acs.nanolett.2c03334.

[279] Yansong Zhu et al. "Bimetallic Bi–Sn microspheres as high initial coulombic efficiency and long lifespan anodes for sodium-ion batteries". In: *Chemical Communications* 58.33 (Apr. 21, 2022). Publisher: The Royal Society of Chemistry, pp. 5140–5143. ISSN: 1364-548X. DOI: 10.1039/D2CC00833E. URL: https://pubs.rsc.org/en/content/articlelanding/2022/cc/d2cc00833e.

[280] Yansong Zhu et al. "Voltage-Modulated Structure Stress for Enhanced Electrochemcial Performances: The Case of μ-Sn in Sodium-Ion Batteries". In: *Nano Letters* 21.8 (Apr. 28, 2021). Publisher: American Chemical Society, pp. 3588–3595. ISSN: 1530-6984. DOI: 10.1021/acs.nanolett.1c00489. URL: https://doi.org/10.1021/acs.nanolett.1c00489.

[281] Xiaoqiong Du et al. "Stabilizing Microsized Sn Anodes for Na-Ion Batteries with Extended Ether Electrolyte Chemistry". In: *ACS Applied Energy Materials* 5.2 (Feb. 28, 2022). Publisher: American Chemical Society, pp. 2252–2259. DOI: 10.1021/acsaem.1c03774. URL: https://doi.org/10.1021/acsaem.1c03774.

[282] Jian Yu Huang et al. "In Situ Observation of the Electrochemical Lithiation of a Single SnO2 Nanowire Electrode". In: *Science* 330.6010 (Dec. 10, 2010). Publisher: American Association for the Advancement of Science, pp. 1515–1520. DOI: 10.1126/science.1195628. URL: https://www.science.org/doi/10.1126/science.1195628.

[283] Qianqian Li et al. "In Situ TEM on the Reversibility of Nanosized Sn Anodes during the Electrochemical Reaction". In: *Chemistry of Materials* 26.14 (July 22, 2014). Publisher: American Chemical Society, pp. 4102–4108. ISSN: 0897-4756. DOI: 10.1021/cm5009448. URL: https://doi.org/10.1021/cm5009448.

[284] Binghong Han et al. "Probing the Reaction between PVDF and LiPAA vs Li7Si3: Investigation of Binder Stability for Si Anodes". In: *Journal of The Electrochemical Society* 166.12 (July 5, 2019). Publisher: IOP Publishing, A2396. ISSN: 1945-7111. DOI: 10.1149/2.0241912jes. URL: https://iopscience.iop.org/article/10.1149/2.0241912jes/meta.

[285] Bing-Qing Xiong et al. "In Situ Construction of an Ultrarobust and Lithiophilic Li-Enriched Li–N Nanoshield for High-Performance Ge-Based Anode Materials". In: *ACS Energy Letters* 5.11 (Nov. 13, 2020). Publisher: American Chemical Society, pp. 3490–3497. DOI: 10.1021/acsenergylett.0c02121. URL: https://doi.org/10.1021/acsenergylett.0c02121.

[286] Hanna He et al. "Understanding and improving the initial Coulombic efficiency of high-capacity anode materials for practical sodium ion batteries". In: *Energy Storage Materials* 23 (Dec. 1, 2019), pp. 233–251. ISSN: 2405-8297. DOI: 10.1016/j.ensm.2019.05.008. URL: https://www.sciencedirect.com/science/article/pii/S2405829719304441.

[287] Yeryung Jeon et al. "Flash-induced reduced graphene oxide as a Sn anode host for high performance sodium ion batteries". In: *Journal of Materials Chemistry A* 4.47 (2016). Publisher: Royal Society of Chemistry, pp. 18306–18313. DOI: 10.1039/C6TA07582G. URL: https://pubs.rsc.org/en/content/articlelanding/2016/ta/c6ta07582g.

[288] Xiuqiang Xie et al. "Sn@CNT nanopillars grown perpendicularly on carbon paper: A novel free-standing anode for sodium ion batteries". In: *Nano Energy* 13 (Apr. 1, 2015), pp. 208–217. ISSN: 2211-2855. DOI: 10.1016/j.nanoen.2015.02.022. URL: https://www.sciencedirect.com/science/article/pii/S2211285515000816.

[289] Guanhua Zhang et al. "Tin quantum dots embedded in nitrogen-doped carbon nanofibers as excellent anode for lithium-ion batteries". In: *Nano Energy* 9 (Oct. 1, 2014), pp. 61–70. ISSN: 2211-2855. DOI: 10.1016/j.nanoen.2014.06.030. URL: https://www.sciencedirect.com/science/article/pii/S221128551400144X.

[290] Feng Lin et al. "Synchrotron X-ray Analytical Techniques for Studying Materials Electrochemistry in Rechargeable Batteries". In: *Chemical Reviews* 117.21 (Nov. 8, 2017). Publisher: American Chemical Society, pp. 13123–13186. ISSN: 0009-2665. DOI: 10.1021/acs.chemrev.7b00007. URL: https://doi.org/10.1021/acs.chemrev.7b00007.

[291] Yanjie Cui et al. "(De)Lithiation Mechanism of Li/SeSx (x = 0–7) Batteries Determined by in Situ Synchrotron X-ray Diffraction and X-ray Absorption Spectroscopy". In: *Journal of the American Chemical Society* 135.21 (May 29, 2013). Publisher: American Chemical Society, pp. 8047–8056. ISSN: 0002-7863. DOI: 10.1021/ja402597g. URL: https://doi.org/10.1021/ja402597g.

[292] Christopher J. Pelliccione, Elena V. Timofeeva, and Carlo U. Segre. "Potential-Resolved In Situ X-ray Absorption Spectroscopy Study of Sn and SnO2 Nanomaterial Anodes for Lithium-Ion Batteries". In: *The Journal of Physical Chemistry C* 120.10 (Mar. 17, 2016). Publisher: American Chemical Society, pp. 5331–5339. ISSN: 1932-7447. DOI: 10.1021/acs.jpcc.5b12279. URL: https://doi.org/10.1021/acs.jpcc.5b12279.

[293] Jiangyi Guo et al. "Control over Electrochemical CO2 Reduction Selectivity by Coordination Engineering of Tin Single-Atom Catalysts". In: *Advanced Science* 8.23 (2021). _eprint: https://onlinelibrary.wiley.com/doi/pdf/10.1002/advs.202102884, p. 2102884. ISSN: 2198-3844. DOI: 10.1002/advs.202102884. URL: https://onlinelibrary.wiley.com/doi/abs/10.1002/advs.202102884.

[294] Christopher J. Pelliccione, Elena V. Timofeeva, and Carlo U. Segre. "In Situ X-ray Absorption Spectroscopy Study of the Capacity Fading Mechanism in Hybrid Sn3O2(OH)2/Graphite Battery Anode Nanomaterials". In: *Chemistry of Materials* 27.2 (Jan. 27, 2015). Publisher: American Chemical Society, pp. 574–580. ISSN: 0897-4756. DOI: 10.1021/cm504101h. URL: https://doi.org/10.1021/cm504101h.

[295] Federal Consortium for Advanced Batteries. *Executive summary, National Blueprint for Lithium Batteries 2021–2030*. Executive summary. 2021, p. 54.

[296] Yun Zhao et al. "Recycling of sodium-ion batteries". In: *Nature Reviews Materials* 8.9 (Sept. 2023). Number: 9 Publisher: Nature Publishing Group, pp. 623–634. ISSN: 2058-8437. DOI: 10.1038/s41578-023-00574-w. URL: https://www.nature.com/articles/s41578-023-00574-w.

[297] Peter Slowik, Nic Lutsey, and Chih-Wei Hsu. "How technology, recycling, and policy can mitigate supply risks to the long-term transition to zero-emission vehicles". In: (2020). Publisher: International Council on Clean Transportation. DOI: 10.13140/RG.2.2.30613.35041. URL: http://rgdoi.net/10.13140/RG.2.2.30613.35041.

[298] Meng-Chang Lin et al. "An ultrafast rechargeable aluminium-ion battery". In: *Nature* 520.7547 (Apr. 16, 2015), pp. 325–328. ISSN: 1476-4687. DOI: 10.1038/nature14340.

[299] Chengjun Xu et al. "Energetic Zinc Ion Chemistry: The Rechargeable Zinc Ion Battery". In: *Angewandte Chemie* 124.4 (2012). _eprint: https://onlinelibrary.wiley.com/doi/pdf/10.1002/ange.201106307, pp. 957–959. ISSN: 1521-3757. DOI: 10.1002/ange.201106307. URL: https://onlinelibrary.wiley.com/doi/abs/10.1002/ange.201106307.

[300] Jean-Marie Tarascon. "Na-ion versus Li-ion Batteries: Complementarity Rather than Competitiveness". In: *Joule* 4.8 (Aug. 19, 2020), pp. 1616–1620. ISSN: 2542-4351. DOI: 10.1016/j.joule.2020.06.003. URL: https://www.sciencedirect.com/science/article/pii/S2542435120302403.

[301] Linda Gaines, Kirti Richa, and Jeffrey Spangenberger. "Key issues for Li-ion battery recycling". In: *MRS Energy & Sustainability* 5 (Jan. 2018). Publisher: Cambridge University Press, E14. ISSN: 2329-2229, 2329-2237. DOI: 10.1557/mre.2018.13. URL: https://www.cambridge.org/core/journals/mrs-energy-and-sustainability/article/abs/key-issues-for-liion-battery-recycling/F37D3914A1F5A8FD0ED3EF901664D126.

[302] M. Elena Arroyo-de Dompablo et al. "Achievements, Challenges, and Prospects of Calcium Batteries". In: *Chemical Reviews* 120.14 (July 22, 2020). Publisher: American Chemical Society, pp. 6331–6357. ISSN: 0009-2665. DOI: 10.1021/acs.chemrev.9b00339. URL: https://doi.org/10.1021/acs.chemrev.9b00339.

[303] Contemporary Amperex Technology. CATL. *CATL Unveils Its Latest Breakthrough Technology by Releasing Its First Generation of Sodium-ion Batteries*. 2021. URL: https://www.catl.com/en/news/665.html.

[304] TOB New Energy. *In 2023, the production capacity of sodium-ion batteries will increaseby 10x*. 2023. URL: https://www.tobmachine.com/in-2023-the-production-capacity-of-sodium-ion-batteries-will-increase-by-10x_n662.

[305] S Castillo et al. "Advances in the recovering of spent lithium battery compounds". In: *Journal of Power Sources* 112.1 (Oct. 24, 2002), pp. 247–254. ISSN: 0378-7753. DOI: 10.1016/S0378-7753(02)00361-0. URL: https://www.sciencedirect.com/science/article/pii/S0378775302003610.

[306] M Contestabile, S Panero, and B Scrosati. "A laboratory-scale lithium battery recycling process1This work has been presented as an invited talk at the 4th International Battery Recycling Congress, Hamburg, Germany, 1–3 July, 1998.1". In: *Journal of Power Sources* 83.1 (Oct. 1, 1999), pp. 75–78. ISSN: 0378-7753. DOI: 10.1016/S0378-7753(99)00261-X. URL: https://www.sciencedirect.com/science/article/pii/S037877539900261X.

[307] Michael J Lain. "Recycling of lithium ion cells and batteries". In: *Journal of Power Sources*. Proceedings of the 10th International Meeting on Lithium Batteries 97-98 (July 1, 2001), pp. 736–738. ISSN: 0378-7753. DOI: 10.1016/S0378-7753(01)00600-0. URL: https://www.sciencedirect.com/science/article/pii/S0378775301006000.

[308] Luqman Azhari et al. "Recycling for All Solid-State Lithium-Ion Batteries". In: *Matter* 3.6 (Dec. 2, 2020), pp. 1845–1861. ISSN: 2590-2385. DOI: 10.1016/j.matt.2020.10.027. URL: https://www.sciencedirect.com/science/article/pii/S2590238520305816.

[309] Wei Li et al. "Thermally Depolymerizable Polyether Electrolytes for Convenient and Low-Cost Recycling of LiTFSI". In: *Angewandte Chemie* 134.38 (2022). _eprint: https://onlinelibrary.wiley.com/doi/pdf/10.1002/ange.202209169, e202209169. ISSN: 1521-3757. DOI: 10.1002/ange.202209169. URL: https://onlinelibrary.wiley.com/doi/abs/10.1002/ange.202209169.

[310] Yijie Yin et al. "Fire-extinguishing, recyclable liquefied gas electrolytes for temperature-resilient lithium-metal batteries". In: *Nature Energy* 7.6 (June 2022). Number: 6 Publisher: Nature Publishing Group, pp. 548–559. ISSN: 2058-7546. DOI: 10.1038/s41560-022-01051-4. URL: https://www.nature.com/articles/s41560-022-01051-4.

[311] Arno Kwade et al. "Current status and challenges for automotive battery production technologies". In: *Nature Energy* 3.4 (Apr. 2018). Number: 4 Publisher: Nature Publishing Group, pp. 290–300. ISSN: 2058-7546. DOI: 10.1038/s41560-018-0130-3. URL: https://www.nature.com/articles/s41560-018-0130-3.

[312] Yangtao Liu et al. "Current and future lithium-ion battery manufacturing". In: *iScience* 24.4 (Apr. 2021), p. 102332. ISSN: 25890042. DOI: 10.1016/j.isci.2021.102332. URL: https://linkinghub.elsevier.com/retrieve/pii/S258900422100300X.

[313] Shabbir Ahmed et al. "Energy impact of cathode drying and solvent recovery during lithium-ion battery manufacturing". In: *Journal of Power Sources* 322 (Aug. 1, 2016), pp. 169–178. ISSN: 0378-7753. DOI: 10.1016/j.jpowsour.2016.04.102. URL: https://www.sciencedirect.com/science/article/pii/S037877531630475X.

[314] Paul Nelson et al. *Modeling the Performance and Cost of Lithium-Ion Batteries for Electric-Drive Vehicles, Third Edition*. ANL/CSE–19/2, 1503280, 150624. Mar. 1, 2019, ANL/CSE–19/2, 1503280, 150624. DOI: 10.2172/1503280. URL: https://www.osti.gov/servlets/purl/1503280/.

[315] Heiner Heimes et al. *Lithium-ion Battery Cell Production Process*. Feb. 6, 2019. ISBN: 978-3-947920-03-7.

[316] Chris Yuan et al. "Manufacturing energy analysis of lithium ion battery pack for electric vehicles". In: *CIRP Annals* 66.1 (Jan. 1, 2017), pp. 53–56. ISSN: 0007-8506. DOI: 10.1016/j.cirp.2017.04.109. URL: https://www.sciencedirect.com/science/article/pii/S0007850617301099.

[317] Linda Gaines et al. "Tracking Flows of End-of-Life Battery Materials and Manufacturing Scrap". In: *Batteries* 9.7 (July 2023). Number: 7 Publisher: Multidisciplinary Digital Publishing Institute, p. 360. ISSN: 2313-0105. DOI: 10.3390/batteries9070360. URL: https://www.mdpi.com/2313-0105/9/7/360.

[318] Gavin Harper et al. "Recycling lithium-ion batteries from electric vehicles". In: *Nature* 575.7781 (Nov. 2019). Number: 7781 Publisher: Nature Publishing Group, pp. 75–86. ISSN: 1476-4687. DOI: 10.1038/s41586-019-1682-5. URL: https://www.nature.com/articles/s41586-019-1682-5.

[319] Linda Gaines. "Profitable Recycling of Low-Cobalt Lithium-Ion Batteries Will Depend on New Process Developments". In: *One Earth* 1.4 (Dec. 20, 2019), pp. 413–415. ISSN: 2590-3322. DOI: 10.1016/j.oneear.2019.12.001. URL: https://www.sciencedirect.com/science/article/pii/S2590332219302234.

[320] *America's got a lithium battery problem. Argonne may have the answer.* Chicago Tribune. Mar. 8, 2019. URL: https://www.chicagotribune.com/opinion/editorials/ct-edit-argonne-lithium-battery-recycling-20190311-story.html.

[321] *Nobel prize winner says battery recycling is key to meeting electric car demand.* Automotive News Europe. Section: Suppliers. Oct. 10, 2019. URL: https://europe.autonews.com/suppliers/nobel-prize-winner-says-battery-recycling-key-meeting-electric-car-demand.

[322] Erik Emilsson and Lisbeth Dahllöf. "Lithium-Ion Vehicle Battery Production Status 2019 on Energy Use, CO 2 Emissions, Use of Metals, Products Environmental Footprint, and Recycling". In: (2019). Publisher: IVL Swedish Environmental Research Institute. DOI: 10.13140/RG.2.2.29735.70562. URL: http://rgdoi.net/10.13140/RG.2.2.29735.70562.

[323] Jens F. Peters et al. "The environmental impact of Li-Ion batteries and the role of key parameters – A review". In: *Renewable and Sustainable Energy Reviews* 67 (Jan. 1, 2017), pp. 491–506. ISSN: 1364-0321. DOI: 10.1016/j.rser.2016.08.039. URL: https://www.sciencedirect.com/science/article/pii/S1364032116304713.

[324] Rebecca E. Ciez and J. F. Whitacre. "Examining different recycling processes for lithium-ion batteries". In: *Nature Sustainability* 2.2 (Feb. 2019). Number: 2 Publisher: Nature Publishing Group, pp. 148–156. ISSN: 2398-9629. DOI: 10.1038/s41893-019-0222-5. URL: https://www.nature.com/articles/s41893-019-0222-5.

[325] Marit Mohr et al. "Toward a cell-chemistry specific life cycle assessment of lithium-ion battery recycling processes". In: *Journal of Industrial Ecology* 24.6 (2020). _eprint: https://onlinelibrary.wiley.com/doi/pdf/10.1111/jiec.13021, pp. 1310–1322. ISSN: 1530-9290. DOI: 10.1111/jiec.13021. URL: https://onlinelibrary.wiley.com/doi/abs/10.1111/jiec.13021.

[326] Mengyuan Chen et al. "Recycling End-of-Life Electric Vehicle Lithium-Ion Batteries". In: *Joule* 3.11 (Nov. 20, 2019), pp. 2622–2646. ISSN: 2542-4351. DOI: 10.1016/j.joule.2019.09.014. URL: https://www.sciencedirect.com/science/article/pii/S254243511930474X.

[327] Jennifer B. Dunn et al. "Impact of Recycling on Cradle-to-Gate Energy Consumption and Greenhouse Gas Emissions of Automotive Lithium-Ion Batteries". In: *Environmental Science & Technology* 46.22 (Nov. 20, 2012). Publisher: American Chemical Society, pp. 12704–12710. ISSN: 0013-936X. DOI: 10.1021/es302420z. URL: https://doi.org/10.1021/es302420z.

[328] Jens F. Peters and Marcel Weil. "Providing a common base for life cycle assessments of Li-Ion batteries". In: *Journal of Cleaner Production* 171 (Jan. 10, 2018), pp. 704–713. ISSN: 0959-6526. DOI: 10.1016/j.jclepro.2017.10.016. URL: https://www.sciencedirect.com/science/article/pii/S0959652617323077.

[329] Severi Ojanen et al. "Challenging the concept of electrochemical discharge using salt solutions for lithium-ion batteries recycling". In: *Waste Management* 76 (June 1, 2018), pp. 242–249. ISSN: 0956-053X. DOI: 10.1016/j.wasman.2018.03.045. URL: https://www.sciencedirect.com/science/article/pii/S0956053X18301879.

[330] Jangho Park et al. "Impacts of residual electrolyte components of spent lithium-ion batteries on the physical/electrochemical properties of resynthesized cathode active materials". In: *Journal of Cleaner Production* 379 (Dec. 15, 2022), p. 134570. ISSN: 0959-6526. DOI: 10.1016/j.jclepro.2022.134570. URL: https://www.sciencedirect.com/science/article/pii/S0959652622041427.

[331] Chao Peng et al. "Role of impurity copper in Li-ion battery recycling to LiCoO2 cathode materials". In: *Journal of Power Sources* 450 (Feb. 29, 2020), p. 227630. ISSN: 0378-7753. DOI: 10.1016/j.jpowsour.2019.227630. URL: https://www.sciencedirect.com/science/article/pii/S0378775319316234.

[332] Jian Lu et al. "Surplus energy utilization of spent lithium-ion batteries for high-profit organolithiums". In: *Carbon Energy* 5.6 (2023). _eprint: https://onlinelibrary.wiley.com/doi/pdf/10.1002/cey2.282, e282. ISSN: 2637-9368. DOI: 10.1002/cey2.282. URL: https://onlinelibrary.wiley.com/doi/abs/10.1002/cey2.282.

[333] Panpan Xu et al. "Efficient Direct Recycling of Lithium-Ion Battery Cathodes by Targeted Healing". In: *Joule* 4.12 (Dec. 16, 2020), pp. 2609–2626. ISSN: 2542-4351. DOI: 10.1016/j.joule.2020.10.008. URL: https://www.sciencedirect.com/science/article/pii/S2542435120304979.

[334] Wilkistar Otieno and David S. Wein. "Effects of selected wheel and caster fixture design on the push force: the case of four-wheeled industrial carts". In: *2015 IEEE Great Lakes Biomedical Conference (GLBC)*. 2015 IEEE Great Lakes Biomedical Conference (GLBC). Milwaukee, WI, USA: IEEE, May 2015, pp. 1–4. ISBN: 978-1-4799-1792-1. DOI: 10.1109/GLBC.2015.7158298. URL: http://ieeexplore.ieee.org/document/7158298/.

[335] L.A. Román-Ramírez and J. Marco. "Design of experiments applied to lithium-ion batteries: A literature review". In: *Applied Energy* 320 (Aug. 2022), p. 119305. ISSN: 03062619. DOI: 10.1016/j.apenergy.2022.119305. URL: https://linkinghub.elsevier.com/retrieve/pii/S0306261922006596 (visited on 03/30/2024).

[336] HyukKyun Chang, Jun Lee, and Chang-Wan Kim. "A statistical analysis of thermal characteristics of 55-Ah large-format LIB pouch cell with different tab-type, tab size, and tab position". In: *Case Studies in Thermal Engineering* 30 (Feb. 2022), p. 101777. ISSN: 2214157X. DOI: 10.1016/j.csite.2022.101777. URL: https://linkinghub.elsevier.com/retrieve/pii/S2214157X22000235.

[337] Nathália Vieceli et al. "Solvent extraction of cobalt from spent lithium-ion batteries: Dynamic optimization of the number of extraction stages using factorial design of experiments and response surface methodology". In: *Separation and Purification Technology* 307 (Feb. 2023), p. 122793. ISSN: 13835866. DOI: 10.1016/j.seppur.2022.122793. URL: https://linkinghub.elsevier.com/retrieve/pii/S1383586622023504.

[338] Kevin Knehr et al. *Battery Performance and Cost Modeling for Electric-Drive Vehicles (A Manual for BatPaC v5.0)*. ANL/CSE-22/1, 1877590, 176234. July 1, 2022, ANL/CSE–22/1, 1877590, 176234. DOI: 10.2172/1877590. URL: https://www.osti.gov/servlets/purl/1877590/.

[339] Li-Li Jiang et al. "Inhibiting Solvent Co-Intercalation in a Graphite Anode by a Localized High-Concentration Electrolyte in Fast-Charging Batteries". In: *Angewandte Chemie International Edition* 60.7 (Feb. 15, 2021), pp. 3402–3406. ISSN: 1433-7851, 1521-3773. DOI: 10.1002/anie.202009738. URL: https://onlinelibrary.wiley.com/doi/10.1002/anie.202009738.

[340] Dongdong Wang et al. "Nitrogen, sulfur Co-doped porous graphene boosting Li4Ti5O12 anode performance for high-rate and long-life lithium ion batteries". In: *Energy Storage Materials* 27 (May 2020), pp. 387–395. ISSN: 24058297. DOI: 10.1016/j.ensm.2020.02.019. URL: https://linkinghub.elsevier.com/retrieve/pii/S2405829720300660.

[341] Sujong Chae et al. "A Micrometer-Sized Silicon/Carbon Composite Anode Synthesized by Impregnation of Petroleum Pitch in Nanoporous Silicon". In: *Advanced Materials* 33.40 (Oct. 2021), p. 2103095. ISSN: 0935-9648, 1521-4095. DOI: 10.1002/adma.202103095. URL: https://onlinelibrary.wiley.com/doi/10.1002/adma.202103095.

[342] Tianchan Jiang et al. "Morphology, composition and electrochemistry of a nano-porous silicon versus bulk silicon anode for lithium-ion batteries". In: *Journal of Materials Science* 52.7 (Apr. 1, 2017), pp. 3670–3677. ISSN: 1573-4803. DOI: 10.1007/s10853-016-0599-8. URL: https://doi.org/10.1007/s10853-016-0599-8.

[343] Tiansheng Mu et al. "Scalable mesoporous silicon microparticles composed of interconnected nanoplates for superior lithium storage". In: *Chemical Engineering Journal* 375 (Nov. 1, 2019), p. 121923. ISSN: 1385-8947. DOI: 10.1016/j.cej.2019.121923. URL: https://www.sciencedirect.com/science/article/pii/S1385894719313178.

[344] Wei He et al. "Scalable fabrication of micro-sized bulk porous Si from Fe–Si alloy as a high performance anode for lithium-ion batteries". In: *Journal of Materials Chemistry A* 3.35 (Aug. 25, 2015). Publisher: The Royal Society of Chemistry, pp. 17956–17962. ISSN: 2050-7496. DOI: 10.1039/C5TA04857E. URL: https://pubs.rsc.org/en/content/articlelanding/2015/ta/c5ta04857e.

[345] Jung Sub Kim et al. "Amorphous carbon-coated prickle-like silicon of micro and nano hybrid anode materials for lithium-ion batteries". In: *Solid State Ionics* 260 (July 1, 2014), pp. 36–42. ISSN: 0167-2738. DOI: 10.1016/j.ssi.2014.03.013. URL: https://www.sciencedirect.com/science/article/pii/S0167273814001349.

[346] Ran Yi et al. "Dual conductive network-enabled graphene/Si–C composite anode with high areal capacity for lithium-ion batteries". In: *Nano Energy* 6 (May 1, 2014), pp. 211–218. ISSN: 2211-2855. DOI: 10.1016/j.nanoen.2014.04.006. URL: https://www.sciencedirect.com/science/article/pii/S2211285514000627 (visited on 01/17/2024).

[347] Safa Haghighat-Shishavan et al. "Strong, persistent superficial oxidation-assisted chemical bonding of black phosphorus with multiwall carbon nanotubes for high-capacity ultradurable storage of lithium and sodium". In: *Journal of Materials Chemistry A* 6.21 (May 29, 2018). Publisher: The Royal Society of Chemistry, pp. 10121–10134. ISSN: 2050-7496. DOI: 10.1039/C8TA02590H. URL: https://pubs.rsc.org/en/content/articlelanding/2018/ta/c8ta02590h.

[348] Demao Yuan et al. "Amorphous red phosphorous embedded in carbon nanotubes scaffold as promising anode materials for lithium-ion batteries". In: *Journal of Power Sources* 301 (Jan. 1, 2016), pp. 131–137. ISSN: 0378-7753. DOI: 10.1016/j.jpowsour.2015.10.003. URL: https://www.sciencedirect.com/science/article/pii/S0378775315303906.

[349] Zhaoxin Yu et al. "Phosphorus-Graphene Nanosheet Hybrids as Lithium-Ion Anode with Exceptional High-Temperature Cycling Stability". In: *Advanced Science* 2.1 (2015). _eprint: https://onlinelibrary.wiley.com/doi/pdf/10.1002/advs.201400020, p. 1400020. ISSN: 2198-3844. DOI: 10.1002/advs.201400020. URL: https://onlinelibrary.wiley.com/doi/abs/10.1002/advs.201400020.

[350] Lei Liu et al. "Chemical Vapor Transport Synthesis of Fibrous Red Phosphorus Crystal as Anodes for Lithium-Ion Batteries". In: *Nanomaterials* 13.6 (Mar. 15, 2023), p. 1060. ISSN: 2079-4991. DOI: 10.3390/nano13061060. URL: https://www.ncbi.nlm.nih.gov/pmc/articles/PMC10056364/.

[351] Yunhua Xu et al. "Uniform Nano-Sn/C Composite Anodes for Lithium Ion Batteries". In: *Nano Letters* 13.2 (Feb. 13, 2013). Publisher: American Chemical Society, pp. 470–474. ISSN: 1530-6984. DOI: 10.1021/nl303823k. URL: https://doi.org/10.1021/nl303823k.

[352] Wei Ni, Yabo Wang, and Rong Xu. "Formation of Sn@C Yolk–Shell Nanospheres and Core–Sheath Nanowires for Highly Reversible Lithium Storage". In: *Particle & Particle Systems Characterization* 30.10 (2013). _eprint: https://onlinelibrary.wiley.com/doi/pdf/10.1002/ppsc.201300138, pp. 873–880. ISSN: 1521-4117. DOI: 10.1002/ppsc.201300138. URL: https://onlinelibrary.wiley.com/doi/abs/10.1002/ppsc.201300138.

[353] Li Sun et al. "Double-shelled hollow carbon spheres confining tin as high-performance electrodes for lithium ion batteries". In: *Electrochimica Acta* 321 (Oct. 20, 2019), p. 134672. ISSN: 0013-4686. DOI: 10.1016/j.electacta.2019.134672. URL: https://www.sciencedirect.com/science/article/pii/S0013468619315439.

[354] Jian Qin et al. "Graphene Networks Anchored with Sn@Graphene as Lithium Ion Battery Anode". In: *ACS Nano* 8.2 (Feb. 25, 2014). Publisher: American Chemical Society, pp. 1728–1738. ISSN: 1936-0851. DOI: 10.1021/nn406105n. URL: https://doi.org/10.1021/nn406105n.

[355] Lian-Jie Xue et al. "Lithium storage performance and interfacial processes of three dimensional porous Sn–Co alloy electrodes for lithium-ion batteries". In: *Electrochimica Acta* 56.17 (July 1, 2011), pp. 5979–5987. ISSN: 0013-4686. DOI: 10.1016/j.electacta.

2011.04.103. URL: https://www.sciencedirect.com/science/article/pii/S0013468611006694.

[356] Shufen Fan et al. "Rapid fabrication of a novel Sn–Ge alloy: structure–property relationship and its enhanced lithium storage properties". In: *Journal of Materials Chemistry A* 1.46 (Nov. 5, 2013). Publisher: The Royal Society of Chemistry, pp. 14577–14585. ISSN: 2050-7496. DOI: 10.1039/C3TA13315J. URL: https://pubs.rsc.org/en/content/articlelanding/2013/ta/c3ta13315j.

[357] Yaolin Xu et al. "Reversible Na-Ion Uptake in Si Nanoparticles". In: *Advanced Energy Materials* 6 (Nov. 1, 2015), n/a–n/a. DOI: 10.1002/aenm.201501436.

[358] Qianjin Zhao, Yunhui Huang, and Xianluo Hu. "A Si/C nanocomposite anode by ball milling for highly reversible sodium storage". In: *Electrochemistry Communications* 70 (Sept. 1, 2016), pp. 8–12. ISSN: 1388-2481. DOI: 10.1016/j.elecom.2016.06.012. URL: https://www.sciencedirect.com/science/article/pii/S1388248116301400.

[359] Chek-Hai Lim et al. "Experimental Study on Sodiation of Amorphous Silicon for Use as Sodium-Ion Battery Anode". In: *Electrochimica Acta* 211 (Sept. 1, 2016), pp. 265–272. ISSN: 0013-4686. DOI: 10.1016/j.electacta.2016.06.031. URL: https://www.sciencedirect.com/science/article/pii/S0013468616313482.

[360] Lei Zhang et al. "In Operando Mechanism Analysis on Nanocrystalline Silicon Anode Material for Reversible and Ultrafast Sodium Storage". In: *Advanced Materials* 29.5 (2017). _eprint: https://onlinelibrary.wiley.com/doi/pdf/10.1002/adma.201604708, p. 1604708. ISSN: 1521-4095. DOI: 10.1002/adma.201604708. URL: https://onlinelibrary.wiley.com/doi/abs/10.1002/adma.201604708.

[361] Ying Li et al. "Multilevel Gradient-Ordered Silicon Anode with Unprecedented Sodium Storage". In: *Advanced Materials* n/a (n/a). _eprint: https://onlinelibrary.wiley.com/doi/pdf/10.1002/adma.202310270, p. 2310270. ISSN: 1521-4095. DOI: 10.1002/adma.202310270. URL: https://onlinelibrary.wiley.com/doi/abs/10.1002/adma.202310270.

[362] Yujie Zhu et al. "Red Phosphorus–Single-Walled Carbon Nanotube Composite as a Superior Anode for Sodium Ion Batteries". In: *ACS Nano* 9.3 (Mar. 24, 2015). Publisher: American Chemical Society, pp. 3254–3264. ISSN: 1936-0851. DOI: 10.1021/acsnano.5b00376. URL: https://doi.org/10.1021/acsnano.5b00376.

[363] Jie Sun et al. "A phosphorene-graphene hybrid material as a high-capacity anode for sodium-ion batteries". In: *Nature Nanotechnology* 10.11 (Nov. 2015), pp. 980–985. ISSN: 1748-3395. DOI: 10.1038/nnano.2015.194.

[364] Eric Detsi et al. "Tuning ligament shape in dealloyed nanoporous tin and the impact of nanoscale morphology on its applications in Na-ion alloy battery anodes". In: *Physical Review Materials* 2.5 (May 29, 2018). Publisher: American Physical Society, p. 055404. DOI: 10.1103/PhysRevMaterials.2.055404. URL: https://link.aps.org/doi/10.1103/PhysRevMaterials.2.055404.

[365] Liubin Wang et al. "3D Porous Tin Created by Tuning the Redox Potential Acts as an Advanced Electrode for Sodium-Ion Batteries". In: *ChemSusChem* 11.19 (Oct. 11, 2018), pp. 3376–3381. ISSN: 1864-5631, 1864-564X. DOI: 10.1002/cssc.201801662. URL: https://chemistry-europe.onlinelibrary.wiley.com/doi/10.1002/cssc.201801662.

[366] Bin Luo et al. "Tin nanoparticles encapsulated in graphene backboned carbonaceous foams as high-performance anodes for lithium-ion and sodium-ion storage". In: *Nano Energy* 22 (Apr. 1, 2016), pp. 232–240. ISSN: 2211-2855. DOI: 10.1016/j.nanoen.2016.02.024. URL: https://www.sciencedirect.com/science/article/pii/S2211285516000756 (visited on 01/20/2024).

[367] Jun Liu et al. "Uniform yolk–shell Sn4P3@C nanospheres as high-capacity and cycle-stable anode materials for sodium-ion batteries". In: *Energy & Environmental Science* 8.12 (Nov. 24, 2015). Publisher: The Royal Society of Chemistry, pp. 3531–3538. ISSN: 1754-5706. DOI: 10.1039/C5EE02074C. URL: https://pubs.rsc.org/en/content/articlelanding/2015/ee/c5ee02074c.

[368] Hongshuai Hou et al. "Sb porous hollow microspheres as advanced anode materials for sodium-ion batteries". In: *Journal of Materials Chemistry A* 3.6 (2015), pp. 2971–2977. ISSN: 2050-7488, 2050-7496. DOI: 10.1039/C4TA06476C. URL: http://xlink.rsc.org/?DOI=C4TA06476C.

Appendix A

Appendix A: Supporting Information for Case 1

A.1 Experimental Section

- **Chemicals**. Multiwall carbon nanotube (MWCNT), 2-propanol (IPA), gelatin, Dulbecco's phosphate buffered saline (DPBS), methacrylic anhydride (MA), 2-hydroxy-2 methylpropiophenone (photo initiator, PI), tin (II) chloride dihydrate ($SnCl_2.2H_2O$) and sulfur power were purchased from Sigma-Aldrich without further treatment. Deionized (DI) water was used throughout the experiment.

- **Preparation of GelMA Solution**. We follow the reported method to synthesis GelMA. Briefly, 10g gelatin is dissolved in 100mL DPBS at $50°C$ to form the gelatin solution. 8 mL MA is added to it at a rate of 0.5 mL/min under stirring. After reaction for 3h at $50°C$, the mixture is diluted with 300 mL DPBS to stop the reaction. Then the obtained solution is dialysed in DI water using dialysis tubing at $40°C$ for 1 week, followed by freeze drying for 1 week to generate a white porous foam and stored at $-4°C$ for further use. To functionalize CNT, 1wt.% GelMA aqueous solution with 0.5 vol.% PI was prepared and put into the refrigerator ($-4°C$) for further use.

- **Fabrication of** $SnS_2/NS-CNT$. 20 mg MWCNT is dispersed in 40 mL DI water/IPA mixture (v:v=1:1) by sonicating for 3 h. And 1mL prepared GelMA solution is added into the CNT solution, followed by sonication for 15 min. Then the mixture is exposed to UV light (365 nm, 1.350 W/cm^2) for 15 min to polymerize the GelMA hydrogel on the surface of CNT (GelMA@CNT). Subsequently, 1.34 mL $SnCl_2$ solution of 0.15 M is dropped into GelMA@CNT and kept stirring for 4 h for ion adsorption. After freeze drying, the obtained Sn^{2+}@ GelMA@CNT black powder (70 mg) was mixed with sulfur powder (105 mg) and put at the end of a semi-close tube, and load into the quart tube (1 in diameter) and put at the heating zone. Here the excessive sulfur power is added to ensure the fully sulfurization and lead to S-doping into CNT. Before sulfurization, 200 sccm Ar gas is used to purge for 20 min. Then the furnace is heated up to $550°C$ for 15 min, then cooled by moving the furnace after annealing for 20 min under 50 sccm Ar gas to obtain the final product $SnS_2/NS-CNT$.

- **Materials Characterization**. XRD (PW1830, Philips) with Cu Ka radiation (λ=1.5406 Å) is applied to investigate the crystal structure with the range from $5°C$ *to* $90°C$. Scanning electron microscope (SEM, JEOL 6700) and HRTEM (JEOL 2010F) with EDX are conducted to check the morphology, elemental distribution and crystal structure. The Raman spectrum is measured by Renishaw Raman RM3000 scope (514 nm excitation argon laser). XPS (PHI 5600) is used to collect the elemental information. To calculate the weight percentage of SnS_2, TGA (Q5000) is carried out in air from room temperature to $700°C$ with a heating rate of $2°C\ min^{-1}$. Fourier transform infrared spectroscopy (FTIR, Vertex 70 Hyperion 1000) is applied to check the chemical bonds of GelMA.

- **Electrochemical Test**. To prepare the $SnS_2/NS-CNT$ electrode, the mixture consisting of 70 wt.% active materials, 20 wt.% carbon black (TIMCAL-C45) and 10 wt.% PVDF was spread on a copper foil current collector. After drying in a vacuum oven at $80°C$ for 24 h, the as-prepared $SnS_2/NS-CNT$ electrode was assembled into coin cell (CR2032) to evaluate the electrochemical performance in an-argon-filled glove box with content of moisture and oxygen below 0.5 ppm. The electrode was separated from the sodium counter electrode by a separator (glass fiber, Grade GF/F Glass Microfiber Filter Binder Free, circle, 125 mm) with 1 $M\ NaPF_6$ in propylene carbonate (PC) with 2 vol.% fluoroethylene carbonate (FEC) as the electrolyte. The mass loading is estimated to be 1.0 $mg\ cm^{-2}$, and the specific capacities were calculated based on the mass of active material in $SnS_2/NS-CNT$ electrode.

- **Synchrotron Sn K-edge XANES and In Operando SAXS Characterization**. The synchrotron XANES on the Sn K-edge during electrochemical cycling was carried out in transmission mode at Beamline 20-BM-B of the Advanced Photon Source (APS) at Argonne National Laboratory. The incident beam was monochromatized by using a Si (111) fixed-exit, double-crystal monochromator. In operando synchrotron SAXS was carried out at sector 12-ID-B of the APS. The results were presented in X-ray scattering intensities verse momentum transfer, q ($q = 4\pi\sin\vartheta/\lambda$, where ϑ is one-half of the scattering angle, and $\lambda = 0.886$ Å is the wavelength of the X-ray at 12-ID-B).

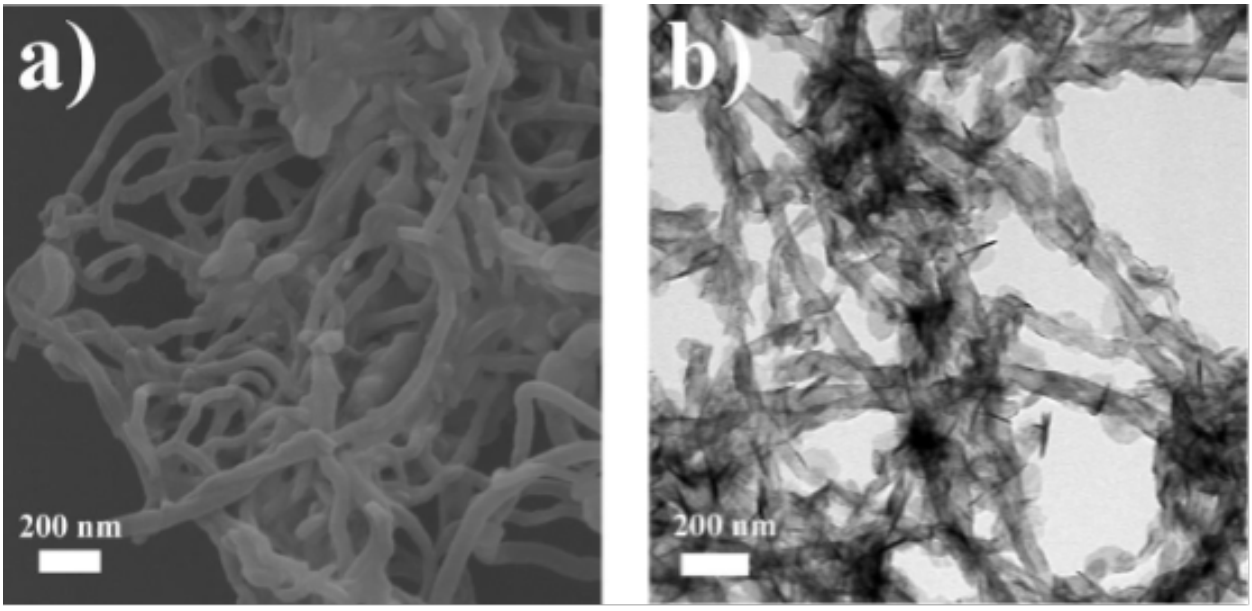

Figure A.1: Low magnified SEM (a) and TEM (b) images of $SnS_2/NS-CNT$.

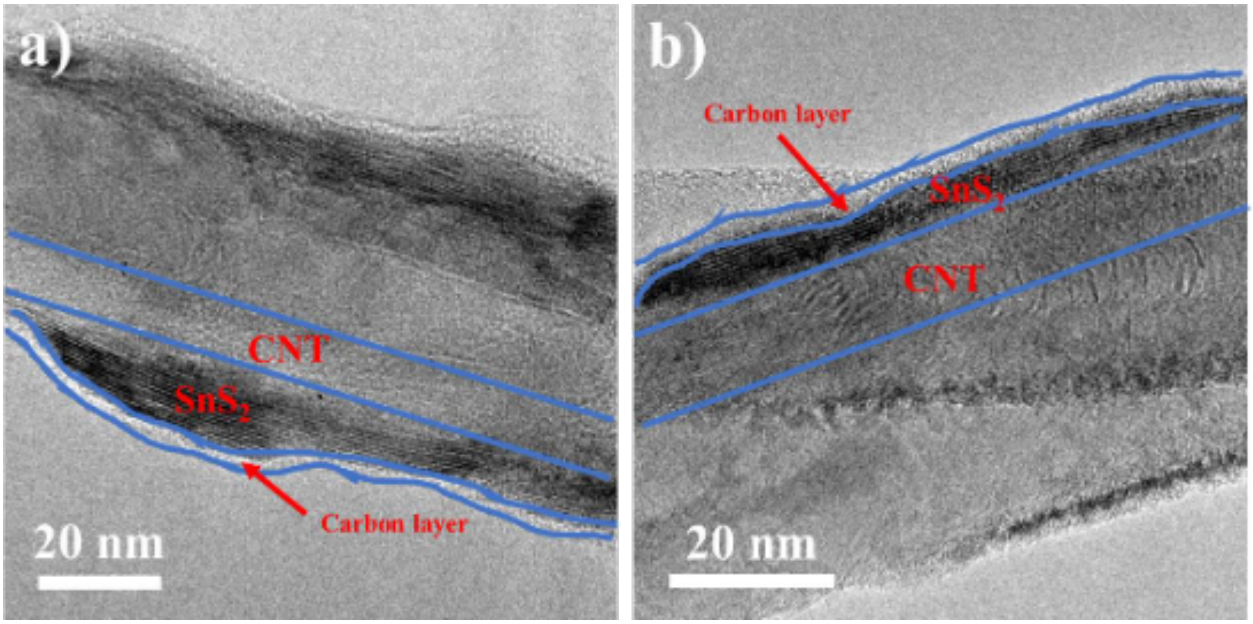

Figure A.2: High-magnified TEM images (a-b) illustrating the $carbon/SnS_2/NS-CNT$ sandwich-like structure.

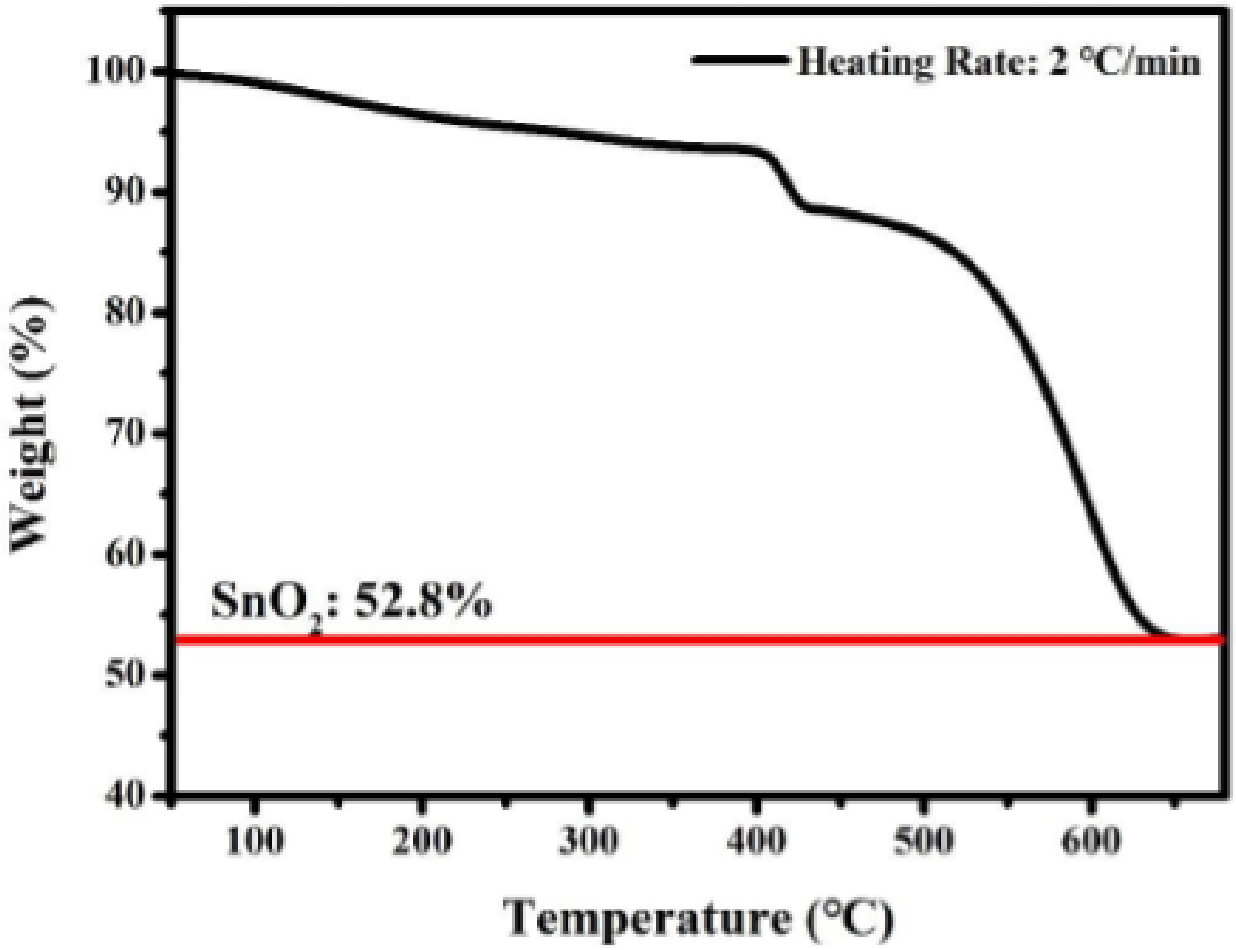

Figure A.3: TGA analysis of the weight percentage of SnS_2 *in* $SnS_2/NS-CNT$ electrode

- Since all SnS_2 will be converted into SnO_2 by heating $SnS_2/NS-CNT$ in the air from room temperature to $700°C$, the weight percentage of SnS_2 is calculated to be:

$$52.8\% \ . \ \frac{Molecular\ weight\ of\ SnS_2}{Molecular\ weight\ of\ SnO_2} = \ 64\%.$$

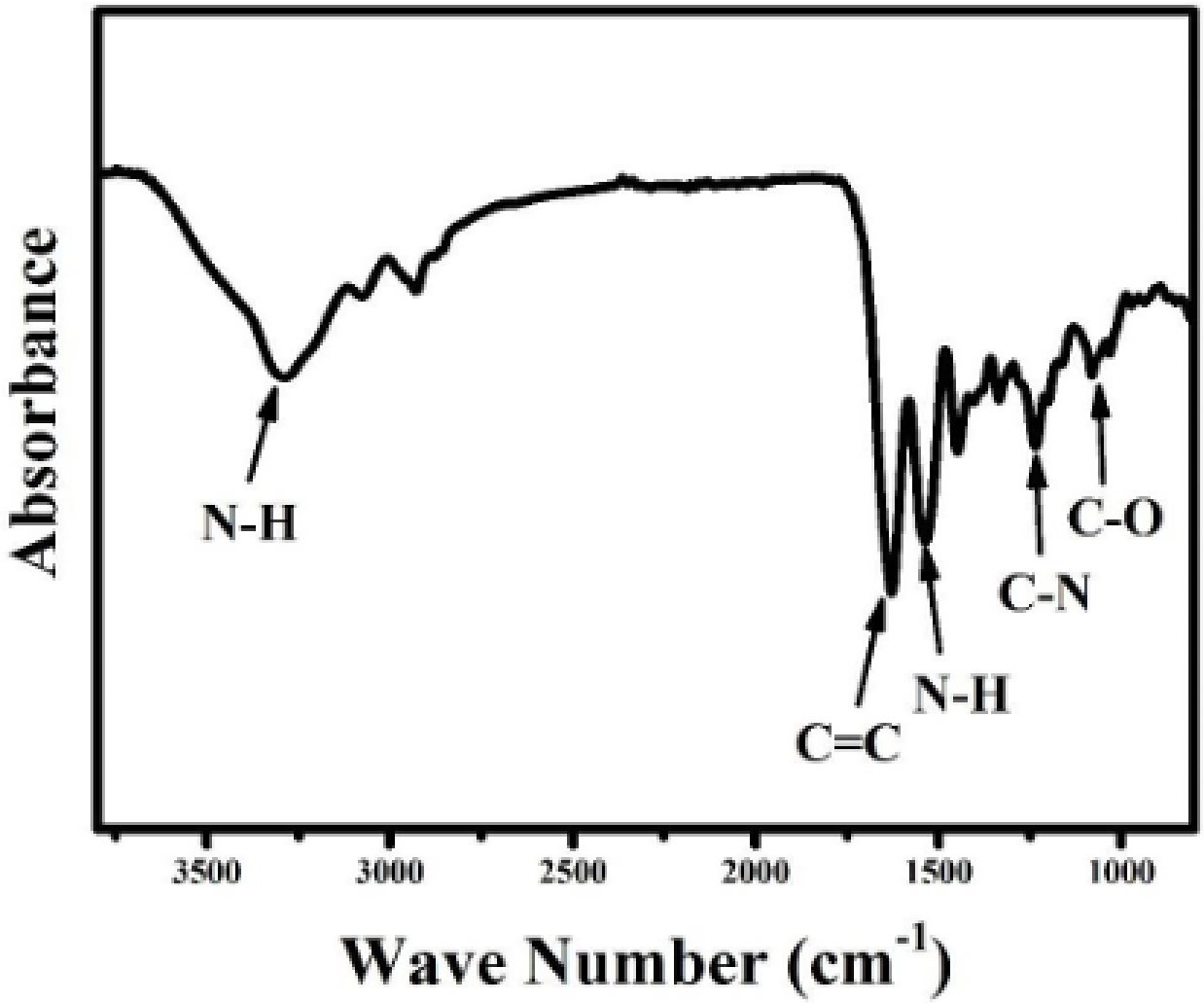

Figure A.4: FTIR spectra of GelMA.

Appendix B

Appendix B: Supporting Information for Case 2

Table B.1: **The parameters of cathode and anodes used to estimate the energy density**

	Specific Capacity (mAh/g)	**Average working voltage**	**ICE**
$LiNi_{0.6}C_{0.2}Mn_{0.2}O_2$	180	3.6V	>90%
Graphite	360	0.2V	>85%
SiO	1000	0.4V	<80%
BPC	2000	0.7V	91%

The energy density of lithium-ion batteries can be estimated using the following equation:

$$E = \frac{C_{cathode} * m_{cathode}}{m_{cathode} + m_{anode}} * (V_{cathode} - V_{anode})$$

where E represents energy density of cell, C represents capacity, m represents the mass of cathode or anode, V represents average working voltage of electrode materials.

With a fixed negative ratio of 1.1, the energy density of NMC622/Graphite, NMC622/SiO and NMC622/BPC are calculated to be 395, 480 *and* 474 $Whkg^{-1}$, respectively. As shown, NMC622/BPC cell chemistry shows higher energy density than NMC622/Graphite, and is comparable with NMC622/SiO. One of the merits of our BPC anode is their high reversible specific capacity, which can significantly lower the mass of anode materials required in the full cells. In addition, our BPC anode has high ICE (91%), which do not need extra prelithiation; while most of the Si-based anode suffer from low ICE (< 80%). Taking together, our BPC is a practical anode material for the next generation lithium-ion batteries.

Appendix C

Appendix C: Supporting Information for Case 3

C.1 Experimental Section

- **Materials synthesis:** Synthesis of Si-P/Ketjenblack-MWCNTs Composites. The micrometer-sized (325 mesh) and nanometer-sized silicon powder were purchased from Sigma-Aldrich. The bulk black phosphorus (BP) (99.998%) used in this work was purchased from Smart Elements. Ketjenblack (EC-600JD) with a high surface area of $1400 m^2/g$ was purchased from AkzoNobel. MWCNTs (SMW 200X) were provided by SouthWest Nanotechnologies. Typically, the mSPC composite was prepared by mixing micrometer-sized silicon, BP, Ketjenblack, MWCNTs in a stainless-steel jar under an argon atmosphere with a mass ratio 33.2:36.8:25:5. And then the mixture was ball-milled for 700 minutes using a ball-milling instrument (800D Mixer/Mill, SPEX Sample Prep.) The weight fraction of the balls to the mixture was maintained in the ratio (10:1), typically 1g of the mixtures of SiP, KB, and MWCNTs versus 10 of balls. The synthesis of nSPC was similar to that of mSPC except using nanometer-sized silicon to replace micrometer-sized silicon. Synthesis of SiC composite is also similar to that of mSPC except without adding black phosphorus and the mass ratio between m-Si:KB:MWCNTs is 35:25:5.

- **Structure characterization:** Synchrotron XRD was measured at Beamline 11-ID-C of the Advanced Photon Source at Argonne National Laboratory. The X-ray wavelength is 0.117418 Å. Scanning electron microscopy and transmission electron microscopy were conducted by HITACHI S-4700-II and focused FEI Talos F200 X TEM/STEM systems, respectively. Raman was measured using a Renishaw inVia microscope spectrometer. X-ray photoelectron spectroscopy was examined using a PHI 5000 VersaProbe II XPS Microprobe (Physical Electronics).

- **Electrochemical measurement:** The SPC or SiC laminates were prepared by spreading a slurry consisting of 70% wt.% active material, 20 wt.% of carbon black, and 10 wt.% sodium alginate (2 wt.% in water) onto a copper foil current collector. The as-prepared laminates were then dried at $80°C$ in a vacuum oven for 24 h and then

punched into electrodes with a diameter of 9/16 inch. The loading of active materials in the electrodes was controlled at about $1.0 - 1.5\ mg.cm^{-2}$. The electrochemical performance was tested by assembling them into coin cells (type CR2032) in an argon-filled glove box under conditions such that the moisture and oxygen contents were both below 1.0 ppm. The anode electrode was separated from a lithium counter-electrode by a separator (Celgard 2325). We use GEN II electrolytes ($1.2M\ LiPF_6$ in a mixture of ethylene carbonate and ethyl methyl carbonate (3/7, v/v)) with 10 wt.% fluoroethylene carbonates as additive for electrochemical testing. The cells were charged and discharged in a MACCOR system with a voltage range of 0.02-2.0 V (vs. Li/Li^+). Cyclic voltammograms were recorded on a Solartron Analytical 1470 System between 0.01 and 2.0 V (vs. Li/Li^+) at 0.1 mV/s.

- **In situ single particle charge/discharge inside a scanning electron microscope:** In situ FIB-SEM during charge/discharge of single mSPC particle was conducted on a Zeiss NVision 40 FIB-SEM system at Center for Nanoscale Materials of Argonne National Laboratory. We have used this setup to probe the volume changes of many battery materials, including layered oxide cathode [1], Germanium-anodes [2, 3], and Phosphorus-anodes [4, 5]. Typically, we used a tungsten probe to get single particle via ion beam carbon deposition and serves as the positive electrode. The electrolyte used in the experiments was ionic liquid-based electrolytes (ILE) consisting of lithium bis (trifluoromethylsul-fonyl) imide (LiTFSI), in a solvent of 1-butyl-1-methylpyrrolidinium bis (trifluoromethylsulfonyl) imide (P14TFSI). Li metal was used as reference electrode and attached on a SEM stage. The cell was charged/discharged using a Keithley 6430 Sub-Femtoamp Remote SourceMeter® from Tektronix within 0.02-2.0 V at 300 pA, 600pA, and 1500pA. During cycling, the particle was immersed in the ILE drop which was placed on top of the Li metal, then lifted out for imaging at different states of charge and discharge. The voltage window was between 0.02 and 2.0 V. To visualize the microstructural change of the particle, the imaging area was polished by a focused ion beam to remove the ILE from the Surface

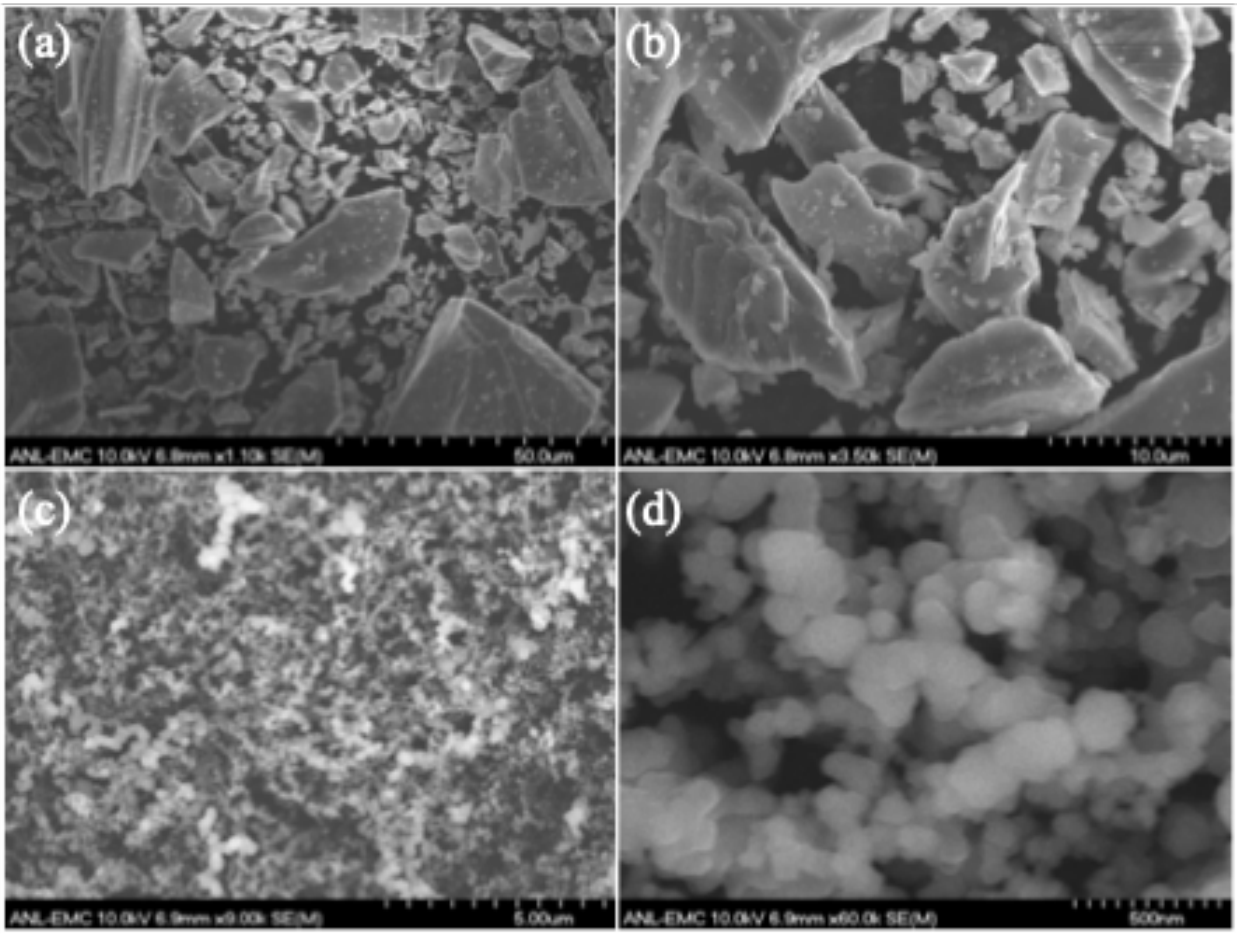

Figure C.1: (a, b) SEM images of micrometer-sized Si. (c, d) SEM images of nanometer-sized Si.

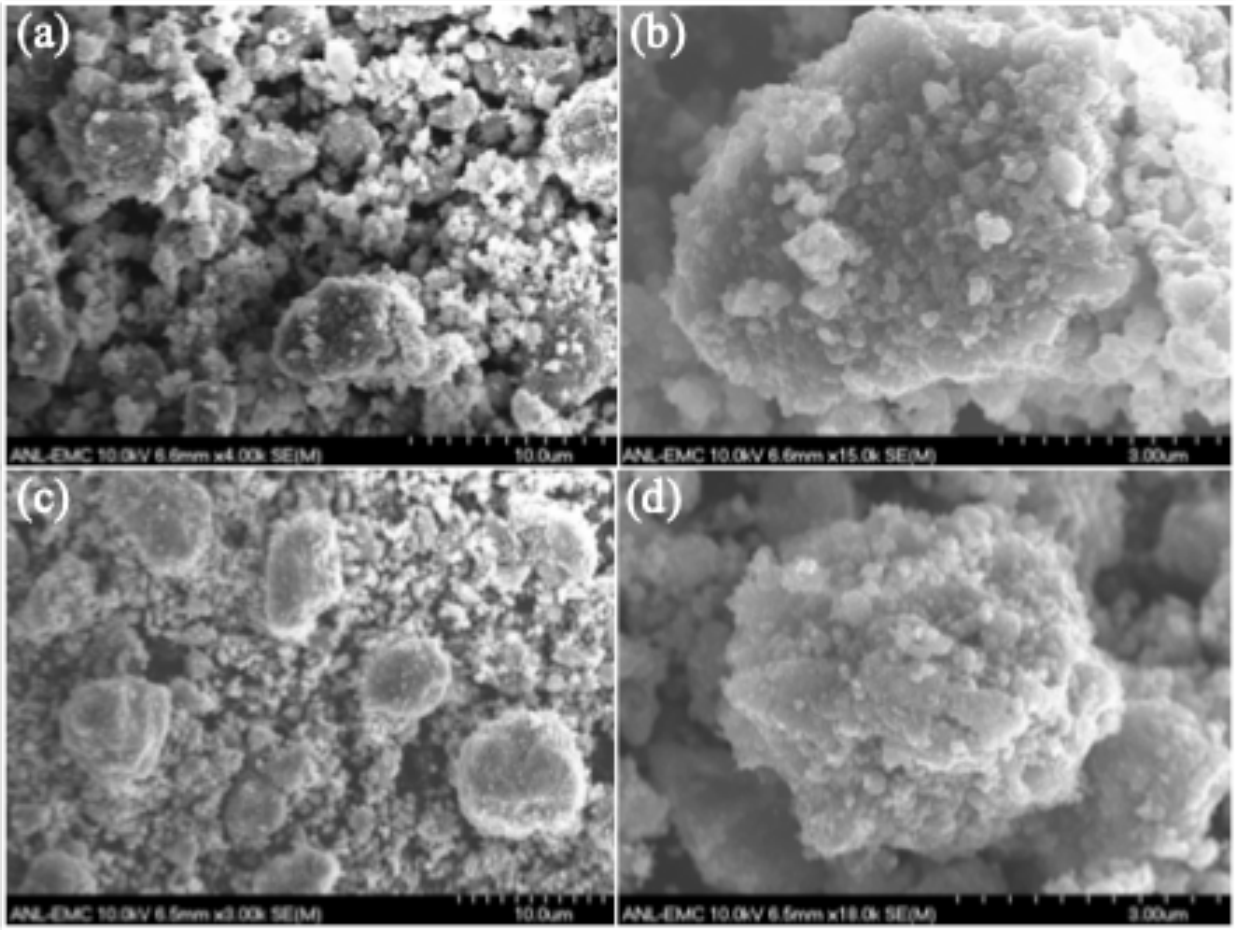

Figure C.2: (a, b) SEM images of the mSPC composite. (c, d) SEM images of the nSPC composite.

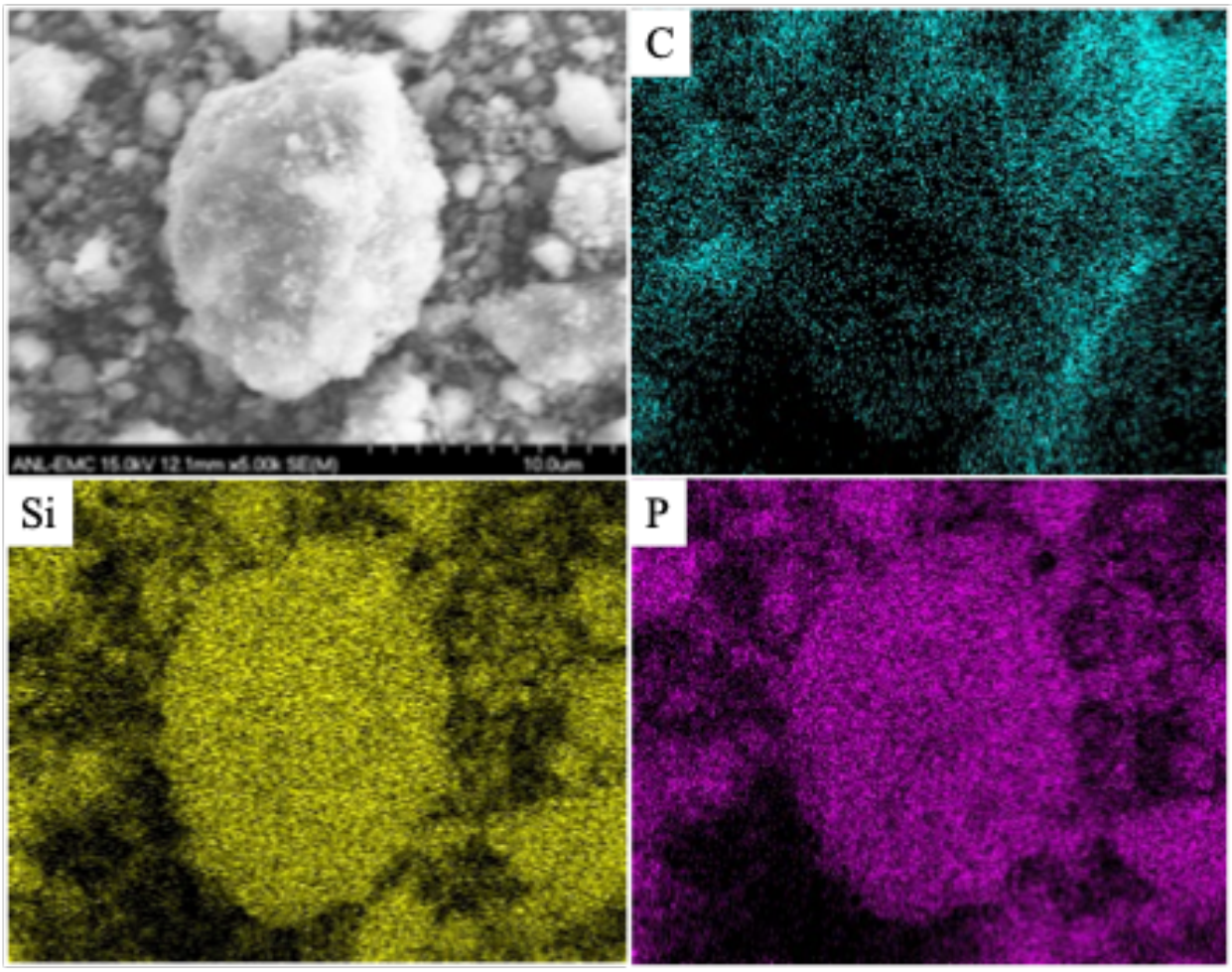

Figure C.3: SEM image and the corresponding EDX mapping of nSPC.

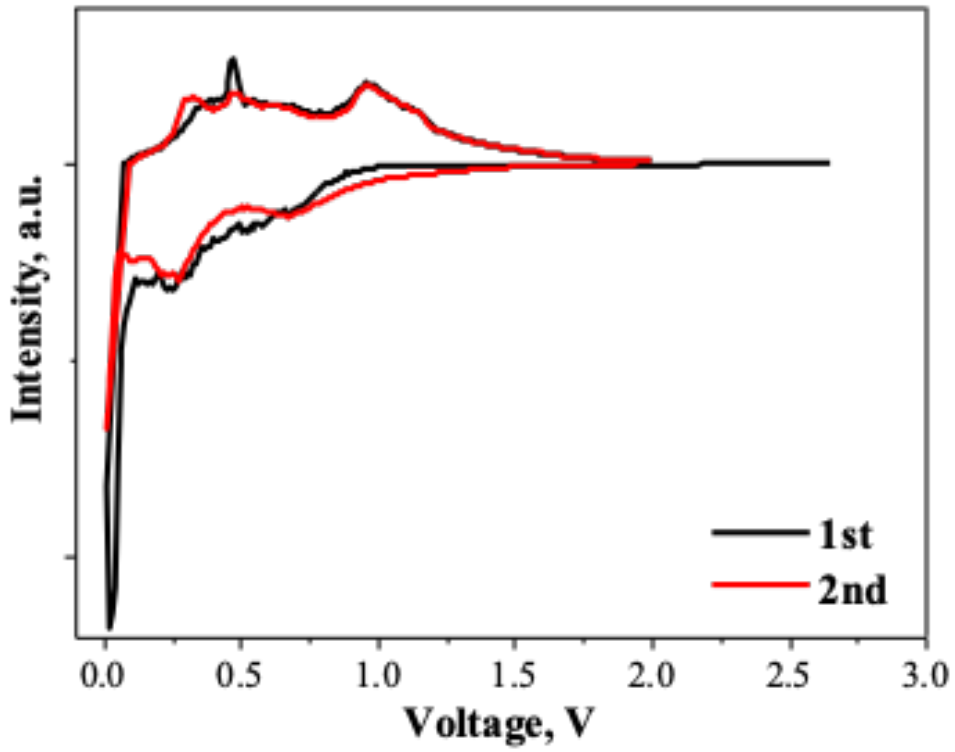

Figure C.4: dQ/dV curves of mSPC in the first two cycle of charge/discharge at 0.2 C.

Table C.1: Comparison on the electrochemical performance of mSPC anode with other Si-P anodes in the literatures

Materials	**1^{st} Specific capacity mAh/g (Current density)**	**Voltage plateau**	**Voltage Window**	**ICE**	**Cycling performance/ Retention rate@cycle number, last specific capacity**	**Rate performance**	**Material fabrication**	**Ref**
mSPC	2140/1700 (680 mA/g)	0.3V	0.01-2.0V	84%	95% @ 120cycles, 1600mAh/g	1000mAh/g @15.3 A/g	Ball milling for 12 h	This work
SiP2/C	1999/1661 (100 mA/g)	0.8V	0.0-2.0V	83%	45%@ 100cycles, 738mAh/g	800mAh/g @3.3 A/g	Ball milling for 20 h	[252]
SiP2(redP)	2750/1800 (50 mA/g)	0.5V	0.0-1.2V	65%	20%@ 10cycles, 370mAh/g	NA	Ball milling for 3 h	[260]
SiP	3125/1000 (100 mA/g)	0.5V	0.01-1.2V	32%	55%@ 50cycles, 550mAh/g	300mAh/g @0.5 A/g	Transport reaction of Si-RedP using Iodine	[253]
MWCNTs/ SiP2	2642/2131 (500mA/g)	0.7V	0.01-2.0V	80%	76%@ 100cycles, 1622mAh/g	500mAh/g @30 A/g	Three-steps Ball milling for 13 h	[254]
SiP2/carbon	2258/1987 (100mA/g)	0.6V	0.0-2.0V	88%	75%@ 100cycles, 1515mAh/g	661mAh/g @10 A/g	Ball milling for 48 h	[257]
2D SiP Flake	1650/1326 (200 mA/g)	0.4V	0.005- 3.0V	87%	53%@ 10cycles, 700mAh/g	400 mAh/g @2A/g	Exfoliation method	[259]
SiP	2644/1612 (100mA/g)	0.7V	0.0-1.5V	61%	38%@ 200cycles, 615mAh/g	320mAh/g @5 A/g	Chemical vapor Transportation	[258]
SiP2	2730/2055 (148mA/g)	0.5V	0.0-1.5V	75%	38%@ 200cycles, 615mAh/g	NA	Ball milling for 16 h	[256]

Table C.2: Comparison on the electrochemical performance of mSPC anode with other types of anode

	ICE	**Discharge Working Potential (V)**	**Specific Capacity (mAh/g)**	**Fast charging mAh/g@A/g**	**Ref**
mSPC	84%	0.3	2000	1000@15	This work
Graphite	>90%	0.1	340	220@1.5	[339]
$Li_4Ti_5O_{12}$	>90%	1.6	180	120@17.5	[340]
Silicon	NA	0.45	2500	NA	[341]
$Li_{3+x}V_2O_5$	73%	0.6	250	125@10	[247]
Phosphorus	76%	0.75	2538	700@13	[222]

Appendix D

Appendix D: Supporting Information for Case 4

Video 1 Appendix D : https://ars.els-cdn.com/content/image/1-s2.0-S2211285523005906-mmc1.mp4

Appendix E

Appendix E: Supporting Information for Chapter 5

Software Names:

- Battery Performance and Cost Model, BatPaC-Version 5.1.By: Argonne National Laboratory. OPEN SOURCE LICENSE.
- MINITAB Statistical software.

Table E.1: The 8 BATPAC default configurations

	Pack configurations							
	1	**2**	**3**	**4**	**5**	**6**	**7**	**8**
Cells per module	20	12	12	12	20	12	12	40
Cells in parallel	2	4	2	3	2	3	4	4
Modules in row	5	5	5	6	4	5	6	5
Rows of modules per pack	4	4	4	4	4	4	4	2
Modules in parallel	2	1	1	1	2	1	1	1

Analysis of Variance of MAXIMUM BATTERY COST

Source	DF	Seq SS	Contribution	Adj SS	Adj MS	F-Value	P-Value
Model	30	10123772	100.00%	10123772	337459	961.08	0.026
Linear	5	9734269	96.15%	9734269	1946854	5544.62	0.010
Yield	1	2065528	20.40%	2065528	2065528	5882.60	0.008
Fast Charging	1	939820	9.28%	939821	939821	2676.60	0.012
Phosphorus	1	6480000	64.01%	6480000	6480000	18454.97	0.005
Anode	1	3570	0.04%	3570	3570	10.17	0.193
Cathode Chem	1	245350	2.42%	245350	245350	698.75	0.024
2-Way Interactions	10	339004	3.35%	339004	33900	96.55	0.079
Yield*Fast Charging	1	990	0.01%	990	990	2.82	0.342
Yield*Phosphorus	1	8256	0.08%	8256	8256	23.51	0.129
Yield*Anode	1	392	0.00%	392	392	1.12	0.482
Yield*Cathode Chem	1	50	0.00%	50	50	0.14	0.770
Fast Charging*Phosphorus	1	84050	0.83%	84050	84050	239.37	0.041
Fast Charging*Anode	1	38226	0.38%	38226	38226	108.87	0.061
Fast Charging*Cathode Chem	1	18145	0.18%	18145	18145	51.68	0.088
Phosphorus*Anode	1	180300	1.78%	180300	180300	513.49	0.028
Phosphorus*Cathode Chem	1	7626	0.08%	7626	7626	21.72	0.135
Anode*Cathode Chem	1	968	0.01%	968	968	2.76	0.345
3-Way Interactions	10	41305	0.41%	41305	4130	11.76	0.223
Yield*Fast Charging*Phosphorus	1	171	0.00%	171	171	0.49	0.612
Yield*Fast Charging*Anode	1	242	0.00%	242	242	0.69	0.559
Yield*Fast Charging*Cathode Chem	1	288	0.00%	288	288	0.82	0.531
Yield*Phosphorus*Anode	1	1352	0.01%	1352	1352	3.85	0.300
Yield*Phosphorus*Cathode Chem	1	760	0.01%	760	760	2.17	0.380
Yield*Anode*Cathode Chem	1	703	0.01%	703	703	2.00	0.392
Fast Charging*Phosphorus*Anode	1	22578	0.22%	22578	22578	64.30	0.079
Fast Charging*Phosphorus*Cathode Chem	1	8128	0.08%	8128	8128	23.15	0.130
Fast Charging*Anode*Cathode Chem	1	1250	0.01%	1250	1250	3.56	0.310
Phosphorus*Anode*Cathode Chem	1	5832	0.06%	5832	5832	16.61	0.153
4-Way Interactions	5	9195	0.09%	9195	1839	5.24	0.320
Yield*Fast Charging*Phosphorus*Anode	1	882	0.01%	882	882	2.51	0.358
Yield*Fast Charging*Phosphorus*Cathode Chem	1	761	0.01%	760	760	2.17	0.380
Yield*Fast Charging*Anode*Cathode Chem	1	703	0.01%	703	703	2.00	0.392
Yield*Phosphorus*Anode*Cathode Chem	1	351	0.00%	351	351	1.00	0.500
Fast Charging*Phosphorus*Anode*Cathode Chem	1	6498	0.06%	6498	6498	18.51	0.145
Error	1	351	0.00%	351	351		
Total	31	10124123	100.00%				

Figure E.1: Analysis of Variance of MAXIMUM BATTERY COST.

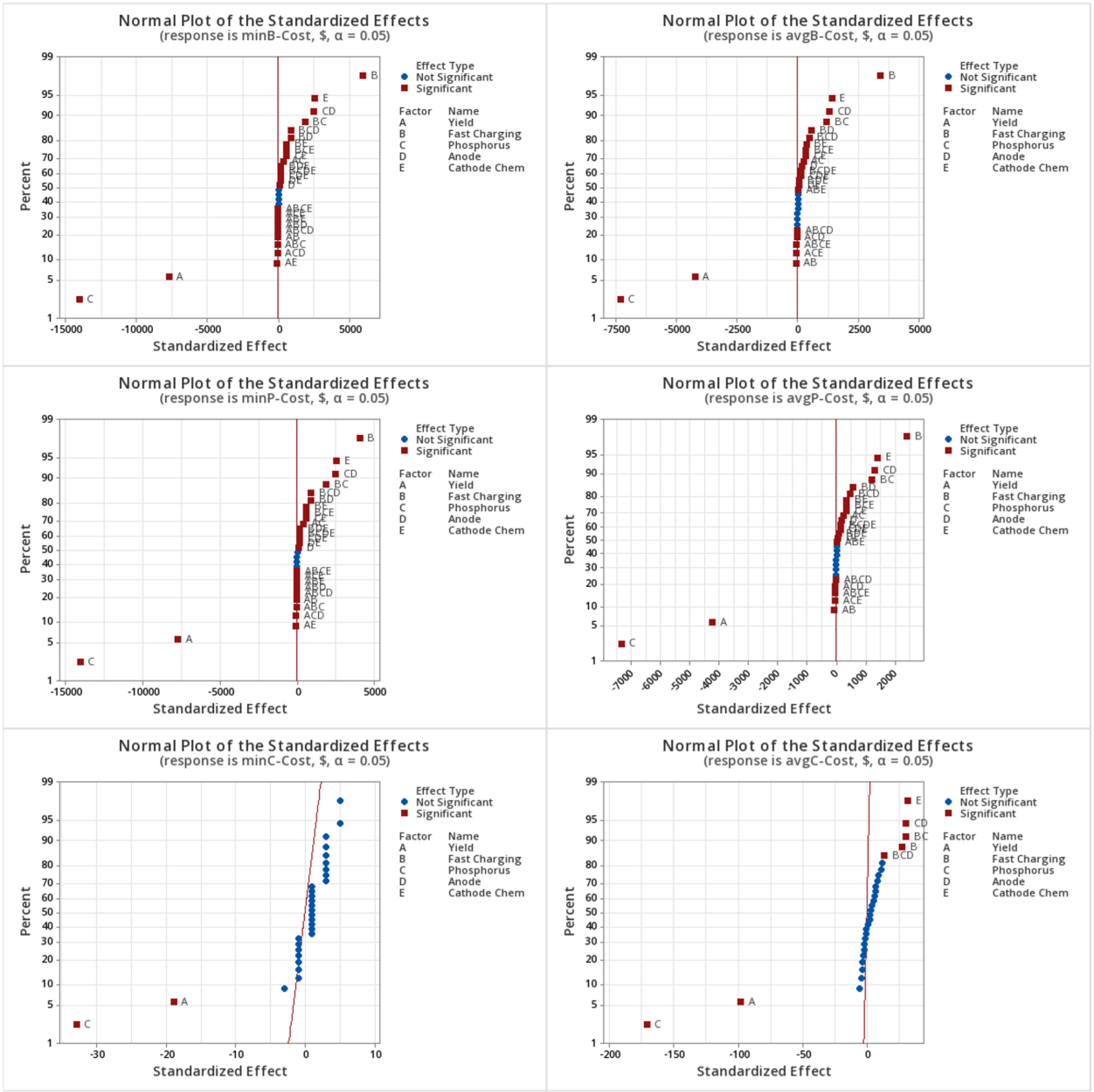

Figure E.2: Normal plots of the standardized effect for minimum and average costs of the battery system, the pack, and the cell.

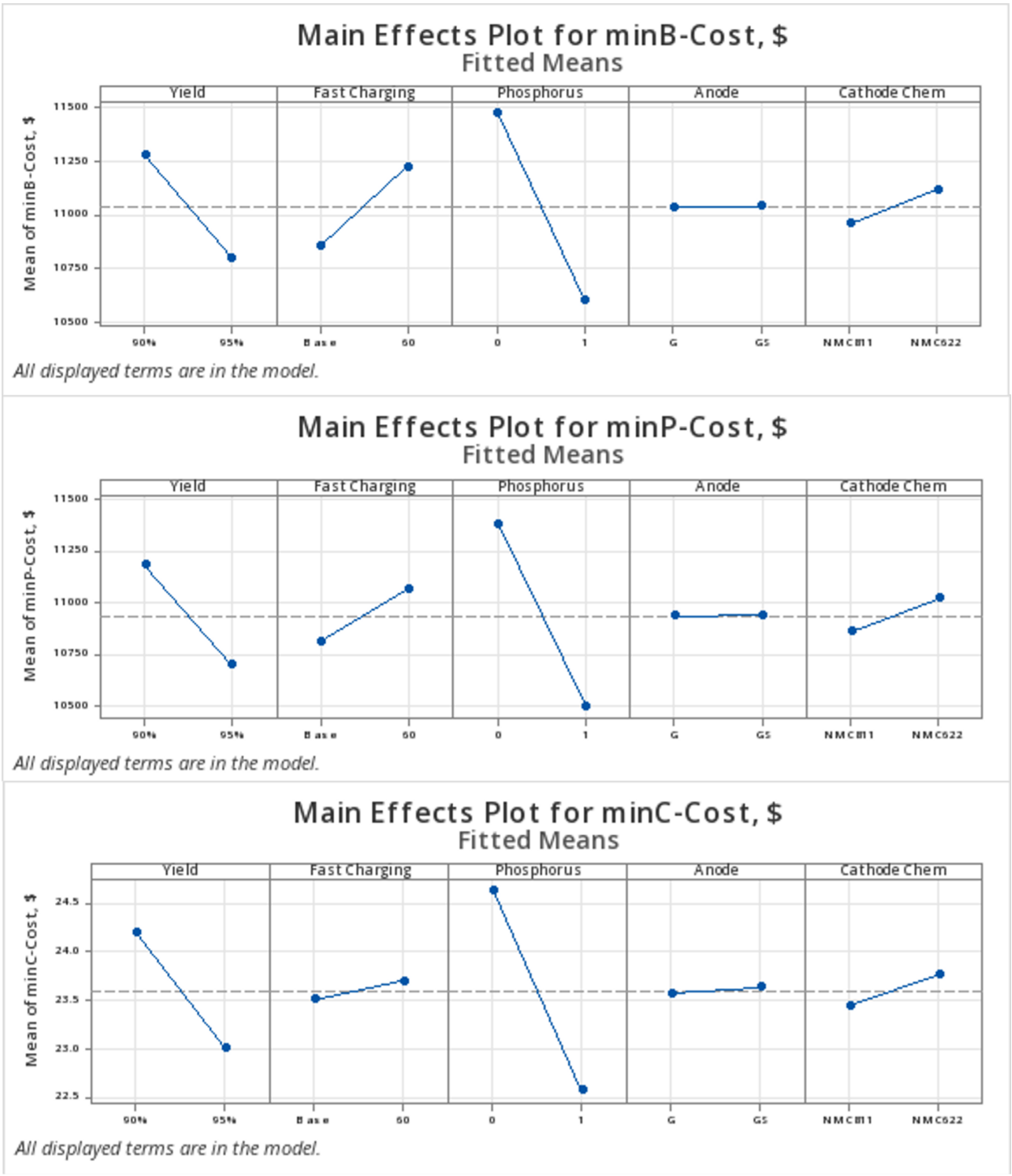

Figure E.3: Main effects plots for the minimum cost of the battery system, the pack, and the cell.

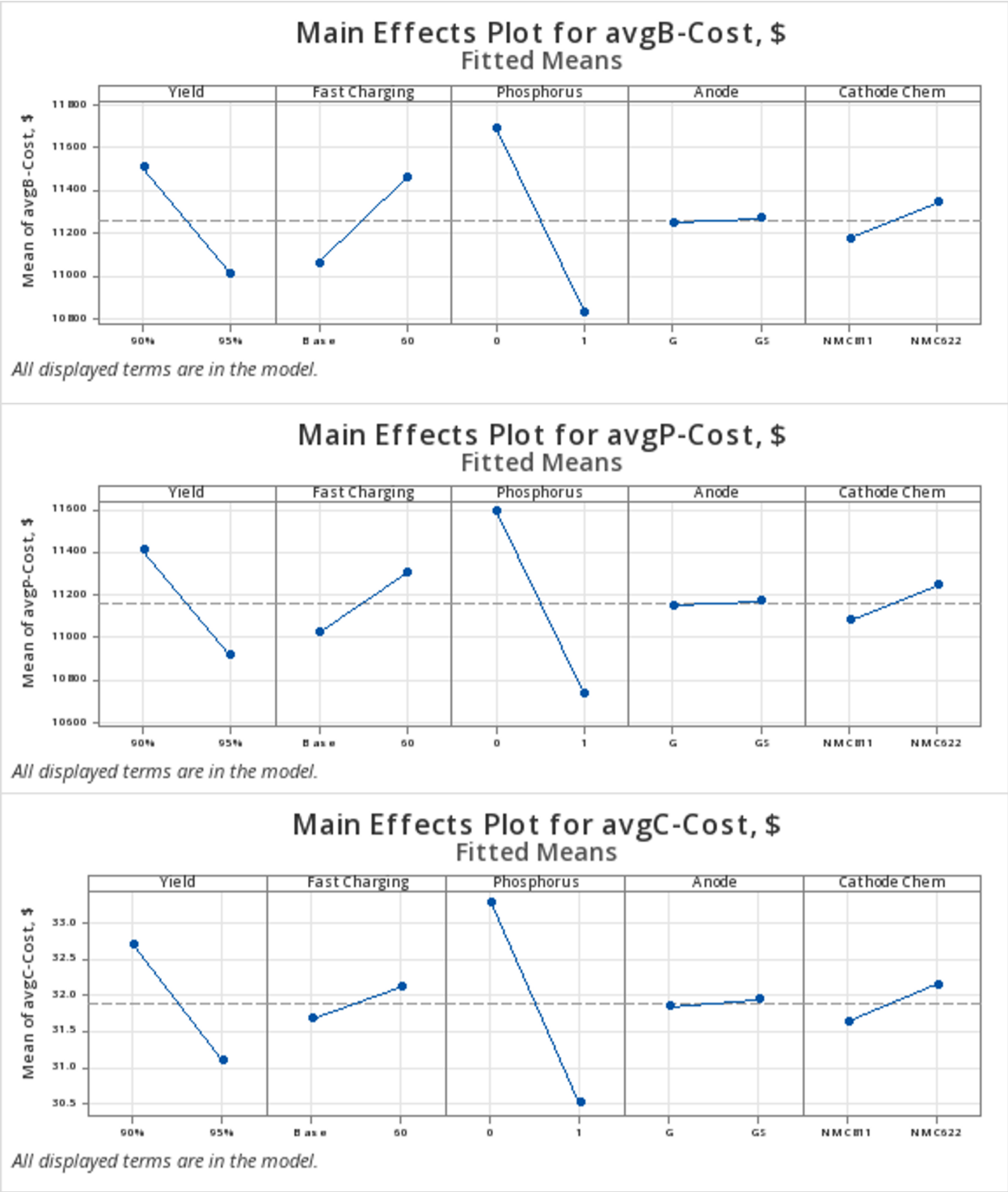

Figure E.4: Main effects plots for the average cost of the battery system, the pack, and the cell.

Appendix F

Appendix F: Supporting Information for the literature review

Table F.1: Summary of different alloy anodes for LIBs (part1)

Anode Materials	**1^{st} Discharge capacity (mAh/g) [Current density]**	**ICE**	**Retention rate @ cycle no.**	**Fast Charging (MAh/g @ A/g)**	**Synthesis method**	**ref**
Nano-Porous-Si	2600 [0.06 A/g]	86%	62% @ 60 cycles	-	HCl etching	[342]
Microparticle-Si	3100 [0.1 A/g]	85.1%	40% @ 360 cycles	1183 @ 1	Magnesiothermic reduction	[343]
Microsized bulk Porous Si	2222 [50 mA/g]	88.1%	63% @ 100 cycles	558 @ 5	Ball milling and acid etching	[344]
Prickle-like Si@C	2300 [0.4 A/g]	87.5%	65% @ 100 cycles	1400 @ 4	Metal-assisted chemical etching and chemical vapor deposition (CVD)	[345]
Microsize Si-C composite	2004 [0.4 A/g]	77.2%	97.8% @ 50 cycles	700 @ 12.8	Etching and Carbon filling	[346]
Hierarchical micro/nanostructures Black Phosphorus Carbon composite (BPC)	2775.2 [0.52 A/g]	91%	87% @ 100 cycles	1637 @ 6.24	High Energy Ball Milling (HEBM)	[244]
Cross-linked BP-CNT	2000 [0.52 A/g]	70%	87.5% @ 400 cycles	1098 @ 11.7	HEBM	[347]
Red P/CNT	2870 [0.11 A/g]	74.3%	46% @ 50 cycles	816.6 @ 1.1	Planetary ball milling	[348]
Red P-Graphene	2517 [130 mA/g]	84%	74% @ 200 cycles	1100 @ 7.8	HEBM	[349]
Fibrous Red P	2500 [0.2 A/g]	81%	80% @ 80 cycles	1316 @ 2	Chemical Vapor Transport (CVT)	[350]

Table F.2: Summary of different alloy anodes for LIBs (part 2)

Anode Materials	1^{st} **Discharge capacity (mAh/g) [Current density]**	**ICE**	**Retention rate @ cycle no.**	**Fast Charging (MAh/g @ A/g)**	**Synthesis method**	**ref**
Nano-Sn/C composite	1029 [0.2 A/g]	69%	98% @ 130 cycles	600 @ 15.12	Aerosol spray pyrolysis	[351]
Sn@C yolk-shell	1414 [0.2 A/g]	69%	44% @ 800 cycles	-	CVD	[352]
Micro-size porous Sn	818 [0.2 A/g]	65%	37% @ 10 cycles	-	Dealloying	[181]
Double-shelled hollow Carbon spheres-Sn	2267 [0.1 A/g]	62%	77.8% @ 130cycles	430 @ 5	Chemical Etching	[353]
Graphene networks anchored with Sn@graphene	1803 [0.2 A/g]	69%	87.5% @ 100 cycles	459 @ 5	CVD	[354]
Hierarchical micro/nanostructures Silicon Black Phosphorus Carbon composite (SPC)	2140 [0.68 A/g]	84%	95% @ 120 cycles	1000 @ 15.3	HEBM	[73]
2D SiP Flake	1650 [0.2 A/g]	87%	53% @ 10 cycles	400 @ 2	Exfoliation Method	[259]
3D micro-Sn-Sb-Co alloy	816 [0.13 A/g]	83%	90% @ 100 cycles	500 @ 16	Electrodeposition	[355]
SiP2/C	1999 [0.1 A/g]	83%	45% @ 100 cycles	800 @ 3.3	HEBM	[252]
Micro-Sn-Ge flake like ribbons	1242 [0.14 A/g]	85%	94% @ 60 cycles	500 @ 7.15	Melt Spinning	[356]

Table F.3: Summary of different alloy anodes for SIBs (part 1)

Anode Materials	**1^{st} Discharge capacity (mAh/g) [Current density]**	**ICE**	**Retention rate @ cycle no.**	**Fast Charging (MAh/g @ A/g)**	**Synthesis method**	**ref**
Si nanoparticles	1027 [20 mA/g]	26%	91% @ 100 cycles	90 @ 0.5	CVD	[357]
Micro-Si-graphite	650 [0.1 A/g]	54.4%	79% @ 100 cycles	170 @ 1	Grinding	[358]
Amorphous Si	420 [36 mA/g]	60%	56% @ 100 cycles	143 @ 0.725	Mechanical fusion	[359]
c-Si/C hybrid	813.7 [50 mA/g]	53.8%	100.3% @ 200 cycles	269 @ 5	Electrospinning and Etching	[360]
Multilevel Gradient-Ordered Si	950 [50 mA/g]	-	40% @ 20 cycles	108 @ 1	Electrochemical reconstruction	[361]
Hierarchical micro/nanostructures Black Phosphorus Carbon composite (BPC)	2206 [0.416 A/g]	91.1%	90% @ 50 cycles	982 @ 3	HEBM	[224]
Hierarchical micro/nanostructures Red Phosphorus Carbon composite (RPC)	2300 [0.416 A/g]	87.8%	77% @ 50 cycles	-	HEBM	[224]
Red P / SWCNT	985 [50 mA/g]	68%	80% @ 2000 cycles	300 @ 2	Vaporization-Condensation method	[362]
BP/AB Composite	2125 [125 mA/g]	76%	91% @ 23 cycles	500 @ 25	HEBM	[62]
Sandwiched BP/Graphene	3050 [50 mA/g]	80%	85% @ 100 cycles	645 @ 26	Liquid-phase exfoliation	[363]

Table F.4: Summary of different alloy anodes for SIBs (part 2)

Anode Materials	**1^{st} Discharge capacity (mAh/g) [Current density]**	**ICE**	**Retention rate @ cycle no.**	**Fast Charging (MAh/g @ A/g)**	**Synthesis method**	**ref**
Porous nano-Sn	550 [40 mA/g]	90.9%	55% @ 95 cycles	300 @ 0.2	Dealloying	[364]
3D Porous Sn	850 [0.2 A/g]	96%	85% @ 400 cycles	700 @ 6.5	Replacement reaction	[365]
Microsized Sn (Glyme)	920 [0.25 A/g]	92%	90% @ 100 cycles	622 @ 1.69	HEBM	[70]
Microsized Sn (Diglyme)	900 [0.085 A/g]	84%	80% @ 300 cycles	300 @ 1.6	HEBM	[69]
Sn@Graphene	730 [0.1 A/g]	60%	95% @ 100 cycles	106 @ 3.2	Hydrogen assisted thermal reduction method	[366]
Yolk-shell Sn_4P_3@C	1804 [0.1 A/g]	43%	65% @ 50 cycles	421 @ 3	Solvothermal	[367]
Micro/nano SB-RP@MWCNT-KB	2801 [0.86 A/g]	88%	96% @ 70 cycles	1179 @ 5.2	HEBM	[58]
Sb porous Microspheres	981.7 [0.1 A/g]	64.6%	97.2% @ 100 cycles	312.9 @ 3.2	Templates method	[368]